Electronic Effects in Radiation Damage Simulations in Metals

Alexis Rutherford

Department of Physics and Astronomy
London Centre of Nanotechnology University College London

2009

Thesis submitted for the degree of Doctor of Philosophy

I, Alexis Rutherford, confirm that the work presented in the thesis is my own. Where information has been derived from other sources, I confirm that this has been indicated in the thesis.

Alexis Rutherford

Abstract

Radiation damage has traditionally been modelled using classical molecular dynamics, in which the role of the electrons is confined to describing bonding via the interatomic potential. This is generally sufficient for low radiation energies. However high energy atoms lose a significant proportion of their energy to electronic excitations, therefore a simulation of the relaxation of a metallic lattice after a high energy event requires a description of the energetic interaction between atoms and electrons. The mechanisms of inelastic collisions between electrons and ions, coupling between electrons and phonons and the diffusion of energy through the electronic system to the rest of the lattice become significant.

We have coupled large scale MD simulations of the lattice to a continuum model for the electronic temperature evolution. Energy lost by the atoms due to elastic and inelastic electronic collisions is gained by the electronic system and evolves according to a heat diffusion equation. The electronic energy is coupled to the lattice via a modified Langevin thermostat, representing electron-phonon coupling.

Results of the simulation of both displacement cascades and ion tracks, representing the low and high extremes of incident ion energy respectively, are presented. The effect of annealing of pre-existing damage by electronic excitation is studied and the behaviour under swift heavy ion irradiation in iron and tungsten is compared. In simulations of displacement cascades, the strength of coupling between the atoms and electrons emerges as the main parameter determining residual damage. Our new methodology gives rise to reduced damage compared to traditional methods in all cases. Ion track simulations demonstrated that the relaxation dynamics, and hence the residual damage, was dependent on the magnitude and temperature dependence of the electronic thermal parameters.

Acknowledgements

I extend my thanks to my supervisor Dr Dorothy Duffy, not least for offering a fascinating and stimulating project, but for remaining actively involved in my work throughout my PhD and for always being available to give me guidance and support. Her careful supervision was critical to this work. I am also very lucky to have had the opportunity to work with Dr Sascha Khakshouri whom I thank for never hesitating to apply his keen mind to various problems and impasses I came across. I am also grateful for the following members of the CMMP group for help in matters computational, technical and academic; Alastair Dunn, Professor Ian Ford, Dr Che Ganarelli, Andy Gormanly and Dr Tony Harker.

I am indebted to the following friends and colleagues for inspiring me with their intelligence and motivating me with their support; Colin Angus, Abigail Caldwell, Emma Dimond, Alastair Dunn, Roland Fairman, Stuart Fraser, Oliver Gray, Alex Grimwood, Tim Howitt, Nikki Lee, Martin Reilly, Sam Robson, Maria del Mar Rodriguez Yebra, David de Sancho and Tandeep Sohi.

I would also like to thank my family for always encouraging me to pursue my interests, never refusing to buy me a book and indulging me years of unintelligible, one-sided conversations about science. In particular I would like to thank my mother, Mary Adams, to whom I dedicate this thesis.

Contents

Chapter 1

Introduction

1.1 Background

In recent years fusion power has emerged as an increasingly viable energy source. As the environmental, political and economic consequences of fossil fuel reliance become more and more obvious and advances continue to be made in plasma and reactor technology, fusion power can be identified as a very credible long term solution to growing energy requirements [1]. The advantages over nuclear fission are manyfold. The reactants can be extracted from heavy water by electrolysis in the case of deuterium and mined in the case of lithium and both sources are relatively abundant. Fusion reactions depend far more sensitively on the reaction environment than fission reactions, the former requiring a very delicate balance of temperature, pressure and magnetic field so that the plasma may release net energy. Any disruption of the optimal operating conditions will result in a rapid decrease in output energy or complete shutdown of the fusion process, consequently there is no risk of a runaway chain reaction or meltdown. Further the primary products and reactants of the reaction do not have long radioactive half lives, although energetic neutrons produced by the reaction may lead to radioactive activation in the reactor materials.

It is not hyperbole to state that

> *Fusion power plant first wall and blanket systems arguably represent the single greatest structural materials challenge of all time*[2]

. The difficulty of containing a reaction, similar to that which takes place in the core of a star, under laboratory conditions cannot be overestimated. Stoneham et al noted that it is unlikely that any one material will be able to provide the necessary materials requirements, several different materials may be used to provide separate functionality [3]. There are many different considerations to be taken into account when choosing materials to perform different functions in the design of a fusion reactor aside from resistance to radiation damage; high thermal stress capacity, a long lifetime, good safety and environmental behaviour and compatibility with other materials. In addition practical considerations such

as the ease of fabrication must be considered.

1.2 Fusion Materials and Radiation Damage

Plasma facing materials are exposed to the most severe environment in a reactor; they will have to withstand temperatures of order $10^3 K$ and high fluxes of both ions and neutrons. Carbon based materials such as graphite and diamond-like carbons have been suggested to this end. However sputtering, the ballistic modification of a surface by ion bombardment, causes erosion and structural damage [4], therefore even this class of materials will experience damage and degredation.

Materials surrounding the plasma facing layer will have to withstand transmutation and radiation induced effects caused by highly mono-energetic neutrons with energies centred at $14.1\,MeV$, which are not contained by magnetic confinement due to their charge neutrality. Unfortunately there are many transmutation reactions with energies in the range $15\,MeV > E > 2\,MeV$ [5]. Special reduced activation ferritic/martensitic (RAFM) steels have been developed which demonstrate reduced nuclear activation but problems persist in terms of embrittlement and swelling, whereby vacant lattice sites agglomerate into voids and nucleate forming local regions of low density. Transition metals are often used in structural materials as they are characterised by high tensile strength and melting temperatures attributable to the high density of states close to the Fermi level which leads to stronger bonding.

RAFM steels are strong candidates for blanket structural materials due to the low rate of activation by neutrons and an intrinsically low rate of swelling. A moderate proportion of martensite can strengthen the steel without embrittlement. Alloying with different metals can also lead to more desirable properties such as better swelling resistance when alloyed with Ni, increased strength at high temperatures with 9% Cr impurities and reduced nuclear activation rate [6].

Tungsten has recently begun to be considered for use as a functional material in the divertor, the function of which is to allow removal of waste materials. This is due to exceptionally high thermal conductivity, low sputtering rate and high strength at high temperatures. Tungsten has a disadvantage in that it is expensive to manufacture.

Not only will candidate materials have to *withstand* hostile operating conditions, to be practically useful in a realistic reactor scenario functionality must not suffer on long time scales. Irradiation leads to individual atomic displacements and defects (creation of vacant lattice sites and interstitial atoms). Interstitials migrate towards sinks leaving

a saturated region of vacant lattice sites which can precipitate into voids. The presence of helium in high concentrations produced in the fusion reaction is seen to enhance void swelling. This is the basis of macroscopic damage and degradation.

The effect of irradiation depends strongly on the mass and energy of the incident particle. For example optical irradiation, such as that from lasers, strongly modifies electronic properties as the electronic system absorbs this energy at first. On the other hand a large particle with a low velocity will give rise to very different effects, a large proportion of energy being dissipated in the atomic system. It is the effect of irradiation which this thesis studies.

Fusion neutrons have a highly monochromatic energy spectrum centred at $14.1 MeV$ with a spread of $\approx 0.5 MeV$ for a D-T plasma [7]. On collision with an iron lattice, this will impart an energy of up to $1.0\,MeV$ to a single iron nucleus with a mean of $500\,keV$. In this high energy regime the energy loss of an Fe ion in bulk Fe due to inelastic collisions with electrons is comparable to that due to atomic collisions (see Fig. (1.1) evaluated using the SRIM code using the LSS model (see section 1.5.1) [8]).[1] A relatively low energy ion will impart its energy into the lattice since the nuclear stopping cross-section is much higher than the electronic stopping cross-section and the dynamics are dominated by collisions between atoms. This is known as a **displacement cascade**. At energies far beyond the scale shown in Fig. (1.1), for example using a swift heavy ion, the proportion of energy lost by an incident ion to electrons is much greater than that lost to collisions with the atoms. Although some energy is lost to the electrons in a cascade, a distinction is made between this situation and when incident ion energies exceed $\approx 10\,MeV$ which is known as an **ion track**.

It is clear from the above discussion that the energy loss to the electrons is significant for high energy radiation events. However the incident ion's motion will not only be affected by a simple frictional force due to inelastic scattering causing electronic excitations. Energy is also *exchanged* between the lattice and the electrons via electron-phonon coupling at lower energies, close to equilibrium. The mechanisms of stopping and coupling are described in more detail in section 1.5. Since the electrons have well defined thermal properties of their own, the energy deposited into the electron system will also be stored and redistributed and fed back into the lattice, influencing atomic dynamics at later times and far from the site of the event.

Upon irradiation, sufficient energy may be given to one atom, the primary knock-on atom (PKA), for it to be displaced from its lattice position and a displacement cascade

[1] Throughout this thesis 'ion' will be used to refer to any single free particle incident on a bulk material whether charged or uncharged, whereas 'atom' is reserved for nuclei within the bulk material.

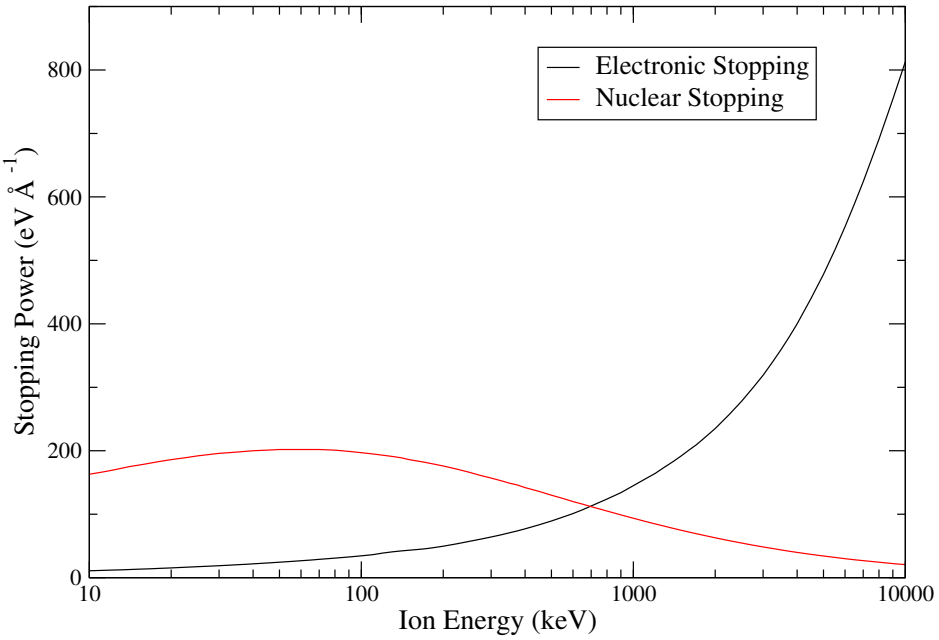

Figure 1.1: Electron and nuclear stopping as a function of incident energy [8] for an Fe ion incident on bulk Fe.

will result [9]. If an atom acquires a kinetic energy greater than the depth of its local potential well it will move through the lattice colliding with other bound atoms. Brinkmann introduced the concept of the displacement spike to describe this [10, 11] [2]. Brinkmann suggested that as ion energies increased and the mean free path between collisions increased, approaching the atomic spacing of target atoms, displaced atoms are forced away from the incident ion's path leaving a core of vacancies with an outer shell of interstitials in its wake.

During this time, in the case of both a cascade or an ion track, although the temperature of the core may be poorly defined, these atoms may have an energy density above that of melting. As a result the atoms will be able to move freely past one another and the core will effectively be liquid. This behaviour is confirmed by ion beam mixing experiments [12]. This phase will last until all atoms have a kinetic energy less than that to displace an atom from its lattice site. Once the energy begins to be shared amongst the atoms via lattice vibrations (typical time scales for this are $\approx 0.1 - 1.0ps$), they will be described by a Boltzmann distribution and a local temperature may be defined.

Once the atoms have insufficient kinetic energy to leave their positions, whether a regularly spaced lattice site or an interstitial site, they will be bound into position but will

[2] Animation of the ballistic phase of a displacement cascade observed in simulation of a $60\,keV$ cascade can be accessed in .avi form at http://www.box.net/shared/8y46kyp448. Only interstitial atoms and vacant sites are visualised, the simulation length is $20\,fs$ and the PKA range is $\approx 70\mathring{A}$.

undergo thermal vibrations with energy $\approx k_B T$. This will allow Frenkel pairs to begin to recombine and as a result the disorder formed in the initial phase may be annealed out. However if the energy is removed on a very short time scale, the atoms will be 'frozen' into position. The rate at which energy is removed from the collision region will determine the proportion of primary damage which persists as residual damage.

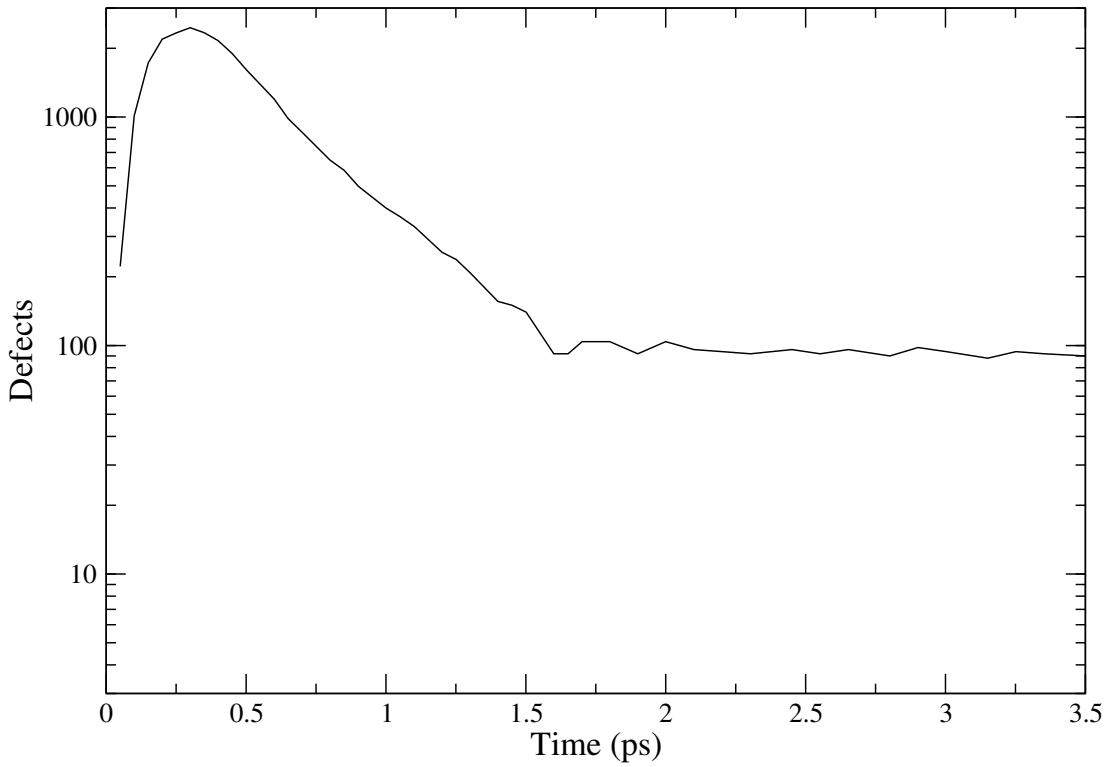

Figure 1.2: Atomic displacements over time during a test simulation of a 10 keV cascade in iron.

Guinan and Kinney first observed the collisional (or displacement spike), thermal spike and relaxation stages of a cascade by measuring the number of atomic displacements over time in molecular dynamics (MD) simulations [13]. Fig. (1.2) shows the number of displaced atoms with time (defined as an atom $1.0\mathring{A}$ from a vacant lattice site), and Fig. (1.3) the various stages of a cascade observed in a simulation. A highly disordered core forms in the early stages which spreads through the lattice as the energy is transferred to neighbouring atoms. Examination of the number of Frenkel pairs during this time shows a collisional period up to $0.5\,ps$ during which the number of displacements increases dramatically. The majority of defects relax and recombine, although some remain as residual defects and continue to migrate. Only atoms displaced by more than $1.0\dot{A}$ from a regular lattice site are shown; the blue spheres represent vacant lattice positions and the red spheres represent interstitial atoms. Snapshots taken at $0.05\,ps$ after the collision event, $0.65ps$, $0.95ps$ and $1.25ps$ are shown.

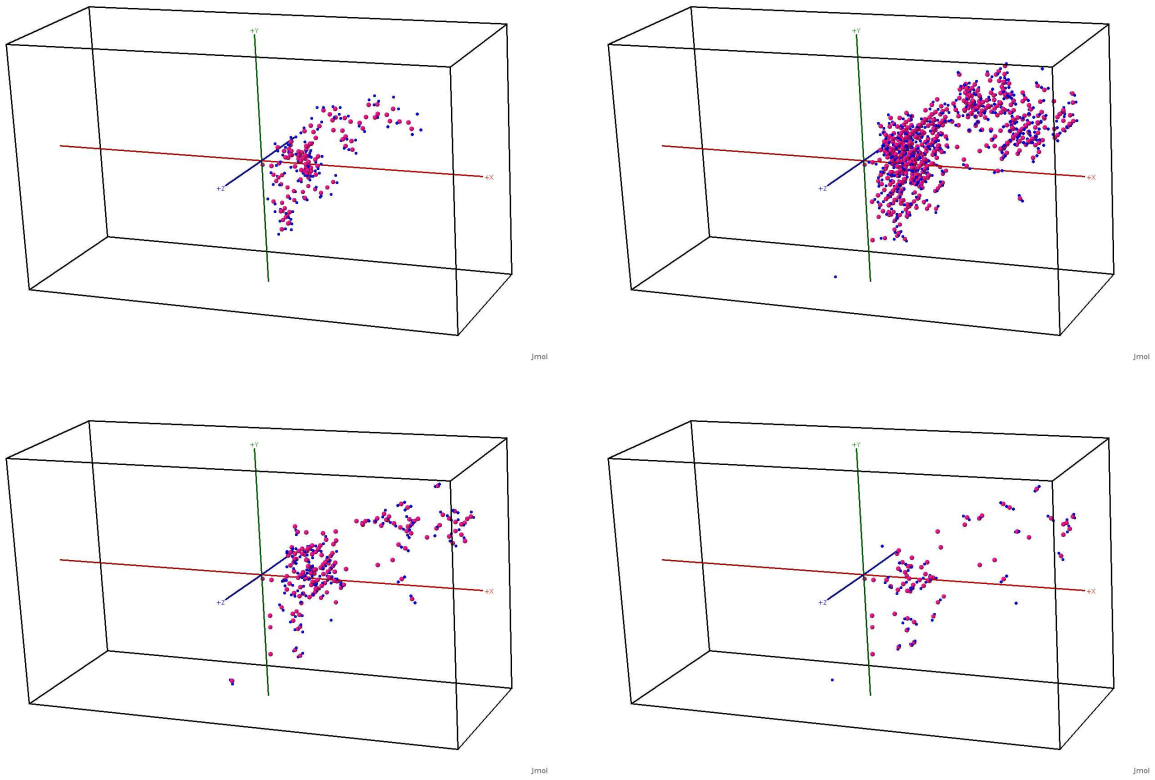

Figure 1.3: Visualisation of the test simulation of a 10 keV cascade. From left to right, top to bottom at 0.05, 0.65, 0.95 and 1.25 ps. Vacancies are shown in red and interstitials in blue. The length of the simulation box is

The residual damage is that which persists long after the event, in contrast to, for example, the local temporary melting of the core of a displacement cascade making up the primary damage state caused by the irradiation which quickly solidifies. However some defects will remain as interstitials and vacancies after the temperature has dropped below the melting temperature. The model of vacancy-intersititial recovery put forward by Schilling et al describes relaxation in several stages [14]. Initially, at the elevated temperatures, such as those experienced in the core of a displacement cascade or ion track, a large concentration of vacancies and interstitials exist in dynamic equilibrium. Closely spaced Frenkel pairs will begin to recombine. At any non zero temperature Frenkel pairs may spontaneously recombine and the range over which this may occur is known as the spontaneous recombination volume which increases with temperature.

Next vacancies and interstitials, which survive recombination, migrate and begin to nucleate and form clusters. These clusters may then collapse to form energetically favourable dislocation structures such as dislocation loops. Although it would be expected that an attractive force would exist between vacancies and interstitials, due to strain fields of opposite signs, thermal activation leads not to annihilation but movement of interstitials

from the core region, due to greater ease of migration than vacancies. This difference in mobility is due to a lower transition energy barrier allowing replacement collision sequences, whereby interstitials displace neighbouring atoms and occupy the newly vacated lattice site allowing the defect to leave the core region very efficiently, normally along close packing directions and migration. As a result interstitials are more readily available for annihilation at sinks leading to a 'production bias' of vacancies as described by Woo and Singh [15]. This mechanism of vacancy and interstitial separation was postulated [16] and later observed in simulations [17].

1.3 Experimental Observations of Radiation Damage

Various experimental studies have been undertaken which have investigated radiation damage. In many cases electronic effects have been concluded as being significant, so for this reason these works are reviewed here.

Direct experimental observation of atomic dynamics in radiation damage is challenging for several reasons, not least as there is no intense source of $14\,MeV$ neutrons currently available. The time and length scales involved are extremely small and the isolation of single events is difficult. In the past probes of radiation damage have been limited to bulk resistivity measurements which are restricted to final defect configurations, although the early stages of disorder may be frozen in by performing the experiment at very low temperatures thereby reducing thermal recovery. Further, absolute values of resistivity rely upon knowledge of the resisitivity of an individual Frenkel pair which often limits results to comparison of *changes* in resistivity.

Only very recently have observations of atomic scale dynamics been possible using high voltage electron microscopy. Ishino and co-workers have observed the migration of clusters indirectly by measuring defect sinks and size effects using tunnelling electron microscopy (TEM) [18]. Also diffraction by x-rays with femtosecond temporal precision has allowed resolution of electronic processes such as inner shell electron dynamics and lattice-electron interactions, and atomic processes such as ultra-fast, 'non-thermal' melting [19]. In this case the size of lattice vibrations are large fractions of the interatomic spacing, but the average displacement is still zero, chacteristic of a crystalline state [20]. More recently Lindberg et al observed very short lived transition states between solid and liquid phases in which phonon modes are softened to the extent that atoms move along a flat potential energy surface [21].

The temperature dependence of the defect yield resulting from displacement cascades following irradiation of Cu was investigated using TEM by Daulton et al [22]. The defect yield was seen to steadily decrease as the temperature was increased above $573\,K$. This was

attributed to several non-independent annealing mechanisms, including the loss of point defects and loops from sinks and surfaces as well as simple thermally activated recombination of interstitials and vacancies. At long times the defect evolution was dominated by the behaviour of stacking fault tetrahedra, whereas vacancy loop-loss mechanisms dominated at short times. Arrhenius type plots of the rate constants of each of these mechanisms confirmed the presence of an energy barrier to be crossed by thermal activation.

Rauch et al were able to analyse the correlation of interstitials produced in displacement cascades in Zn doped Al and Cu using X-ray diffraction [23]. The influence of incomplete knowledge of the PKA energies was avoided by analysing the Fourier transform of the defect correlations in terms of the actual PKA energy spectrum (the maximum of which was at $0.1\,MeV$). It was observed that dilute cascades were formed in Al with many subcascades forming, acting to spread the energy over a large volume. In contrast, the cascades in Cu were very compact with a high energy density. The high energy density in the latter was found to encourage recombination and agglomeration, as seen by residual resistivity measurements after irradiation.

Although not directly related to electronic properties, damage under soft phonon modes, whereby atoms undergo violent displacements at low energy, has been observed experimentally [24]. Strong coupling between electrons and phonons, allowing swift transfer of energy between electrons and the lattice, has been attributed to a high d-band density of states at the Fermi level. This is to be contrasted with inelastic collisions between electrons and ions which allow a one-way transfer of energy at high energy. The strength of this interaction is characterised by the stopping strength (see section 1.5.1). The damage under irradiation of several different metals both with and without a large density of states was observed. While there was no trend found with coupling strength, a large degree of damage was found in Zr, Co and Ti which all undergo a transition via a displacive transformation due to soft phonon modes. It was concluded that energy transffered to the lattice in a coherent way, whether via redistribution of charge leading to repulsion of bare nuclear charges or simple thermal expansion under electronic heating, can lead to displacements with individual energies below the usual threshold displacement energy in the presence of such modes.

The degree of damage observed was compared to the following ratio

$$\zeta = \frac{\sigma}{\sigma_{calc}} \tag{1.1}$$

where σ_{calc} is a number of defects predicted theoretically by the Kinchin and Pease [25] or Norgett, Robinson and Torrens [26] (NRT) picture and σ is the number observed in experiment. As discussed in section 1.4.1 this is likely to overestimate the real degree

of damage for several reasons; the value of the displacement energy E_D determines the number of defects formed but this value is highly anisotropic. Further any recombination of defects will be ignored. However the trend of ζ with stopping power is of more interest than absolute values.

It has been found that tracks of high density electronic excitations can give rise to diverse effects in metals such as melting, phase transitions, amorphisation and plastic flow [27]. For example, experiments on NiTi using many different incident ions were observed using X-ray diffraction [28]. TEM measurements showed that tracks were formed, when the electronic energy loss was above $46keVnm^{-1}$, with an amorphous structure in their centre. The outer cylindrical shells underwent a martensitic to austenitic transition at a temperature dependent on the rate of energy deposition. The complicated behaviour and the formation of several different phases was attributed to the generation of a shock wave and the different structures of the various phases.

Dufour et al analysed the observations of swift heavy ion irradiations of Bi, Fe and Ti using bulk resistivity measurements and TEM methods. Some simple relationships were found in various elements. For example the track radius increased as the energy required for melting increased and the threshold stopping power for track formation increased as the electron-phonon coupling strength decreased. It was suggested that knowledge of two out of track radius, coupling strength and threshold stopping power will allow predictions of the third and so behaviour under swift heavy ion irradiation [29].

Audoard et al [30] irradiated Ni_3B ribbons with ions in the GeV energy range. The atomic structure was probed in situ during the experiment via resistivity measurements and the final configuration at room temperature via electron diffraction was examined. This material was chosen as it has a crystalline to amorphous phase transition at ≈ 0.1 displacements per atom by nuclear collisions and so the experiments would address the question of whether electronic energy loss could lead to the same effect. Some degree of amorphisation was seen in the core of the track although it had some crystalline character. It was suggested that full amorphisation would require very high levels of energy deposition, since the mobility of the electrons in metallic solids allows the swift dissipation of energy.

van Kampen et al used a pump-probe laser experiment to study electron thermalisation and electron-phonon equilibration in Ni. Measurement of the reflectivity was used as a direct probe of the rate of electron thermalisation and a time scale of $\tau_{th} = 80fs$ was found. The measurement of strain waves in the lattice allowed calculation of the electron-phonon relaxation time scale as $\tau_{ep} = 0.7 - 1.0\ ps$, while using the reflectivity data and de-coupling electron and lattice components gave $\tau_{ep} = 0.3 - 0.5\ ps$. The diffi-

culty of analysing highly non-equilibrium electronic effects in terms of simple models in transition metals such as Ni with a high d-band density of states close to the Fermi level in comparison to noble metals was noted [31].

Experiments have shown different behaviour among pure metals under swift heavy ion irradiation. Inelastic collisions of the swift heavy ion with electrons causes damage production in some metals while in others enhanced defect recovery and annealing is observed. Iwase and Iwata coined the phrase 'radiation annealing' to describe this latter phenomenon. Several different fcc metals were studied under bombardment with ions in the range $1 - 100MeV$ and defect recovery was measured via bulk resistivity measurements [32]. The defect production cross-section was given by

$$\sigma_d^{exp} = [dC/d\Phi] = (1/\rho_F)(d(\delta\rho)/d\Phi)_{\Phi\to 0} \tag{1.2}$$

Here C is the atomic concentration of Frenkel defects, Φ is the ion fluence, $\delta\rho$ is the increase of electronic resistivity following irradiation and ρ_F is the resistivity increase per unit concentration of Frenkel defects. The experimental cross-section was compared to the theoretical cross-section calculated from a screened Coulomb interaction and a modified Kinchin-Pease type formula. Very different behaviour was observed in Ni compared to Cu. The damage efficiency is much lower in Ni which was attributed to a stronger interaction between electrons and lattice atoms. As a result damage produced by elastic collisions is annealed out by electronic agitation. In Cu, on the other hand, insufficient energy is transferred to the lattice from the electrons to anneal defects produced by other means. In fact higher fluences led to increased damage due to more elastic nuclear collisions. The damage produced at higher fluences in metals with strong lattice-electron interactions was found to depend on the rate at which energy is deposited into the electrons, (S_e) as $S_e^{1.7}$ and $S_e^{1.5}$ in Cu and Ag respectively. This near quadratic dependence suggests its origin is from a screened mutual Coulomb repulsion of atoms.

Similar results were found in experiments in Fe using an undamaged lattice. Low levels of electronic stopping led to less damage than that predicted solely by atomic collisions due to annealing of primary damage caused by atomic collisions [33, 34]. At high levels of electronic stopping ($(\frac{dE}{dx})_e > 40keV\,nm^{-1}$), the damage efficiency was higher than that calculated theoretically. A microscopic model was developed describing the redistribution of charge driving collective and coherent atomic recoils leading to easy coupling to phonons causing permanent atomic displacements. This was a modified version of the form developed by Dettmann et al [35]

$$\frac{d\widehat{c}}{d\Phi} = \overbrace{\sigma_e(1 - 2\nu_0\widehat{c})}^{(1)} - \overbrace{\sigma_r\widehat{c}}^{(2)} \tag{1.3}$$

Here $\widehat{c}$ is the average defect concentration, ν_o is the volume in which defects may spon-

taneously recombine, σ_e is the defect production cross-section due to electronic excitation and σ_r is the cross-section due to defect recombination. (1) describes defect production and spontaneous annihilation, while (2) describes recombination due to additional lower energy events.

The implications of this model were validated using MD; a proportion of the atoms in an MD cell corresponding to a cylinder of $10\mathring{A}$ were given radial velocities between $0.5 - 2.0eV$/atom. In this case a damage cross-section comparable to experiment was found, however using recoil velocities with random orientations, no defect creation was found. The authors emphasised the importance of the coherence of the excitations. As an extension of the simulations, Frenkel pairs were introduced into the cell and recombination was seen with recoil energies as low as $0.2eV$/atom.

The situation of doping a sample with defects before undergoing irradiation was later developed by the same group [36]. Following irradiation in the range $10 - 170MeV$ in which the majority of energy was deposited into the lattice, Fe showed annealing of defects produced by cascades under self-ion irradiation with energies of $500MeV$ in which inelastic collisions dominated. Defect annealing due to the collapse of disordered zones into vacancy dislocation loops or simple recombination of Frenkel pairs was attributed to the transfer of electronic energy into the lattice atoms. The authors concluded that electronic processes must be taken into account to study radiation damage in metals with strong coupling.

Stuchbery and Bezakova measured changes in the magnetic fields experienced by implanted heavy ions into Fe [37]. The hyperfine magnetic field within the solid is quenched while the local temperature exceeds the Curie temperature. Measurements of the recovery of the magnetic field suggest that the thermal spike following such an event, in which several keV is deposited into the atomic system, persists for $\approx 6\,ps$.

It should be noted that the situation described for a displacement cascade or an ion track is similar to that which arises using various ballistic materials modification techniques [38]. In both cases a large amount of energy is initially deposited into either the electrons (e.g. laser ablation) or the atoms (e.g. ion beam mixing, sputtering). The subsequent dynamics of the transition to equilibrium from an initial state far from equilibrium will determine the accuracy with which the atomic or electronic structure may be modified and damage controlled. This represents a useful potential application of the work described in this thesis.

1.4 Modelling Radiation Damage

There are several different approaches to the modelling of individual radiation damage events. Each of these techniques captures different information, meaning that each is suitable to capturing different aspects of the event. The binary collision approximation, atomistic simulation and two-temperature models are described and their successes and failures are discussed.

1.4.1 Binary Collision Approximation

Computer simulations of radiation damage were first performed within the binary collision approximation (BCA) (e.g. [39]), using the ideas of Bohr [40]. Bohr addressed many problems which are crucial in modern stopping theories which describe inelastic collisions between ions and electrons. These include polarisation of of the target medium by distortion of the electron plasma, the effect of finite ion size, the screening of the Coulomb interaction and relativistic considerations. Further Bohr considered atomic structure by introducing electronic velocities derived from optical spectra.

In the BCA a cascade is approximated as a series of two-body collisions, and atoms are assumed to follow asymptotic trajectories between collisions in straight lines. Lattice models use the geometry of the crystal cell to determine the positions of other atoms with which to scatter, whereas Monte-Carlo algorithms are used to calculate collision rates from probability distributions in amorphous materials. The primary knock on atom (PKA) collides elastically with a second atom in its path. If it imparts an energy greater than the cohesive energy E_c the second atom joins the cascade and as the simulation progresses the positions of the mobile atoms are followed. The cohesive energy is input as a parameter to this model and losses to the electrons may be included as a frictional force. In order to balance the energy, the following relation is imposed

$$E_{PKA} = E_i + E_d + E_k \tag{1.4}$$

This represents the initial energy given to the PKA being given to electronic energy losses (E_i), atoms with energies below the cut off (E_d) and the kinetic energy of the other atoms being followed (E_k). The output of this model is the position and velocity of each atom still in motion. Thus the range of an incident atom can be calculated as the distance the atom travels before its kinetic energy, up to the cut off for atomic displacements, is dispersed.

The SRIM (stopping and range of ions in matter) code developed by Ziegler et al, is a code within the BCA which calculates stopping powers and ranges from comprehensive descriptions of atomic and nuclear interactions [8]. Statistical algorithms are used to interpolate between calculated collisions and the ion and atoms experience a screened

Coulomb interaction, including exchange and correlation interactions between overlapping electron shells. The excitations and plasmons created within the electronic system by the ion are included, as is the interatomic bond structure. The effective charge of the ion is calculated using a velocity dependent charge state and long range screening by the electron sea. SRIM was the succesor of the TRIM (transport of ions in matter) program, which allows calculation of the final distribution in 3-D of the atoms and ion, as well as kinetic phenomena including sputtering, damage and phonon production.

This method does not include many body effects which must be considered when neighbouring atoms are likely to be affected by the collision between two atoms. This limit corresponds to energies of the order $10\,eV$ per atom [41]. Although this renders the method unsuitable for full simulation of highly energetic events it has been used frequently to model the collisional phase of a cascade and so to calculate starting configurations for full atomistic simulations.

Caro et al used the output of the binary collision code MARLOWE to construct a discretised heat conduction equation and so predict the volume of the melted zone [42] in cascade simulations. $5keV$ cascades in Cu and Ni were simulated ignoring electronic energy losses, and compared to MD simulations. The radial energy distributions in both BCA and MD simulations compared well. The main variable parameter is the cut off energy E_c, however it was found that, while this affected the number of atoms set in motion, the distribution of energy deposition was insensitive to it. Despite these successes, the authors suggested several reasons why MD should be used in modelling cascade events, rather than binary collision codes. Firstly, a large proportion of energy is carried away from the core by radial expansion and coherent atomic motion, leaving less energy available for atomic heating. Secondly the density fluctuation caused by this expansion will give rise to high pressures affecting the melting temperature of the material. Such effects will become more important as higher energies are considered and many-body and non-linear effects cannot be ignored.

Jakas and Harrison investigated sputtering yields using a modified version of the TRIM code within the BCA [43, 44]. The effect of inelastic collisions was considered in implantation of $3keV$ ions as a frictional drag force given by LSS theory [45, 46, 47], which was included above a cut-off velocity. The effect of including such an energy loss for both incident ions and for the lattice atoms was investigated by measuring sputtering yield. It was found that the yield was sensitive to electronic energy losses by atoms but not by the incident ion.

Norgett et al [26], after Kinchin and Pease [25], proposed an empirical formula for the number of Frenkel pairs formed after irradiation of a low energy PKA with an energy

E_{PKA}, lying in the nuclear stopping regime

$$N_{FP} = 0.8E_{PKA}/2\overline{E_D} \tag{1.5}$$

Here E is defined as the damage energy, which is the PKA energy, less any losses due to electronic collisions, and $\overline{E_D}$ is the threshold displacement energy for Frenkel pair formation averaged over all crystallographic directions. While this formula accurately describes the mechanism of damage formation at low PKA energies, its range of validity is restricted to the BCA. In the NRT picture of binary collisions, the number of defects increases linearly with the damage energy; the PKA will transfer an energy above E_D to a greater number of atoms. In the binary collision approximation these displaced atoms are removed from the lattice sites with no way to annihilate with their own vacant sites or that of any other interstitial. In this picture the crystal structure remains largely unchanged apart from a small proportion of atoms displaced in two body collisions.

1.4.2 Atomistic Simulation

Molecular dynamics (MD) simulation is a technique that is particularly well suited to radiation damage, as individual atomic information can be obtained. There are various experimental methods to measure final damage configurations, such as X-ray diffraction, electrical resistivity measurements, various microscopy and spectroscopy methods as well as mechanical measurements but these are limited. This type of observation is not ideal as the irradiation environment is very dynamic and will create interstitials in continuous production and annihilation. The processes between impact and the static final damage state will not be captured.

Following considerable advances in the theory and experimental observation of crystal defects and damage [48], and Alder et al's first use of the MD technique [49], MD was used to model the individual motion of a knock on atom within a crystal lattice some 50 years ago by Gibson et al[50]. However, these pioneering studies were limited by the available computational power to low energies of the order $10eV$. This simulated only the early stages of a cascade or avoided direct simulation of large numbers of atoms by modifying the interatomic forces to model the presence of the surrounding lattice. Following the advent of the supercomputer and parallel computing, systems with sizes orders of magnitude larger than these early simulations can now be simulated explicitly. MD allows an atomistic treatment of displacement cascades, and the resulting radiation damage, by imparting one atom with a large velocity and following the subsequent dynamics by modelling each atom in the system [51, 52, 53].

These early simulations contributed greatly to the understanding of damage formation and evolution. For example, an early understanding of cascade dynamics led to a calcula-

tion of the anisotropy of the energy required to displace an atom from its lattice site [54]. Also the importance of replacement collision sequences was highlighted, whereby an energetic atom displaces a neighbour and occupies its vacant lattice site, which provides an efficient mechanism for interstitial atoms to leave the core of a cascade [50]. Such chains of collision and replacement are most readily observed along close packing directions. The sensitive dependence of the stages following collisional, ballistic behaviour of a cascade upon the crystal structure was observed by moving beyond a simplified picture of binary collisions.

A different effect, known as chanelling, also affects the dynamics of energetic ions due to the crystal structure. An incident ion may be steered into the open space or channels between atomic planes by the repulsion of the atomic potentials. The ion will avoid close impact collisions and thus lose energy at a much lower rate. As a result the range of penetration of the ion will be greatly increased. Although chaneling is hard to characterise, some theories exist which allow the calculation of the critical angle of incidence to the atomic planes required for channeling. Typical values are $3 - 5^o$ [9]. Many stopping theories are based on the assumption that materials are amorphous, thus only an atomistic treatment will capture such effects.

The high energy and highly non-equilibrium nature of radiation damage challenges many of the assumptions underlying classical MD. Interatomic potentials are fitted to equilibrium properties of atoms and ground state properties of electrons, therefore care must be taken to ensure that any potential used also describes the full regions of phase space to be simulated, including regimes far from equilibrium. At realistic fusion energies local melting occurs and a liquid core is formed, thus it is not possible to model very high energy events as a simple perturbation of the atoms in a perfect lattice. Fig. (1.4) shows the dynamics of atoms in a low energy ($400eV$) cascade from [50] [3], motion along close packing directions can be seen but overall disturbance of the lattice is limited. This is to be compared with the much higher degree of damage, and local melting observed in Fig. (1.3) under a $10\,keV$ PKA.

In MD simulations of cascades in Si and several metals, Nordlund and Averback investigated the motion of pre-existing defects [55]. The defects were introduced with a Gaussian distribution centred where the previous cascade core would have been. PKA energies of $5keV$ were used and electronic energy loss ignored. The state of the lattice and the presence of interstitials were characterised by structure factor analysis. Several distinct mechanisms of defect annealing were found; most annealing took place in the

[3]Reprinted figure with permission from J.B. Gibson, A.N. Goland, M. Milgram and G.H Vineyard, Physical Review, 120, 1229, 1960. Copyright 2008 by the American Physical Society. http://tinyurl.com/58fx7z

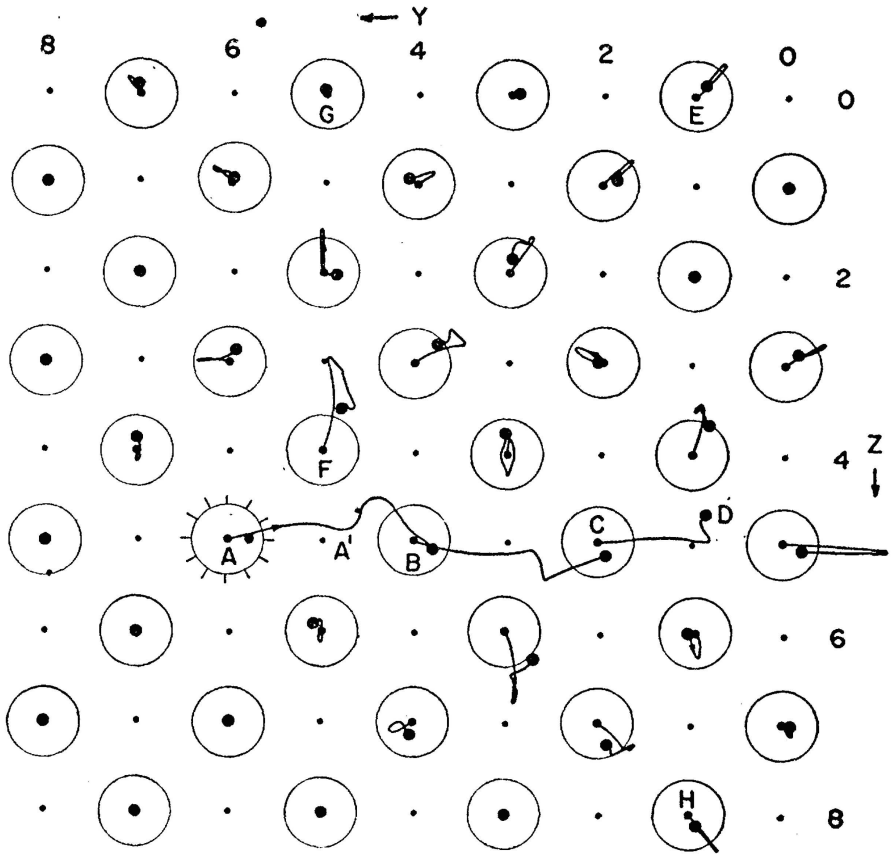

Figure 1.4: Visualisation of the loci of atoms in a low energy MD simulation [50].

liquid zone formed. Interstitial atoms are able to recombine with vacancies easily under local melting. Secondly, thermal migration outside the melted zone encouraged annealing although the degree of movement was found to be sensitive to the shape of the initial defect distribution. Differences were observed between the behaviour of Si and metals which were attributable to differences in the nature of the bonding. Later investigation of ion beam mixing [56] found the degree of atomic rearrangement to be very different between crystalline and amorphous materials and between semiconductors and metals. This was again attributed to differences in bonding and also to the short range structural order. Comparison of the results from simulation to experiment were made and the exclusion of electron-phonon coupling highlighted as a possible cause of disagreement.

The same group performed large scale MD simulations of $200keV$ collision cascades in order to compare the degree of mixing in Ni, Pd and Pt directly with experiment [57]. Since such high energy events form a liquid-like core and electronic effects act to cool this melt and reduce mixing, such a comparison was used as a probe of the importance of this interaction. Experiments using a 'marker' layer of a different atomic species which is as chemically similar as possible were considered, the disruption of this layer gives a measure

of the degree of atomic re-arrangement [58].

The range and number of primary recoils of the implanted ion were derived from range calculations and the evolution of the resulting sub-cascades modelled using full MD. The atoms experienced no electron-phonon coupling, but above a cut off kinetic energy ($E_{kin} > 10eV$) they experienced a frictional force which represented electronic stopping. The total of the squared atomic displacements was compared and excellent agreement found with experiment over 3 orders of magnitude of energy. It was concluded that the small differences observed represented an upper limit of the influence of electron-phonon coupling as 30%. Despite Ni, Pd and Pt having very high electron-phonon coupling strengths, the role of this interaction in the dynamics of collision cascades was assumed to be negligible.

In later work Nordlund and co-workers performed a comparative study of cascades in semiconductors and fcc metals [59]. By performing cascades with energies in the range $400\,eV$ to $10\,keV$ in each material, the effect of mass, melting temperature, material strength and crystal structure were investigated. It was concluded that crystal structure gave rise to differences in damage production processes; the close packed fcc structure promoted swift regeneration of the damaged lattice while the open nature of the diamond structure in Si enhanced mixing and damage. Atomic mass and density determined the spatial extent of cascades and their breakdown into sub-cascades. Further the mechanism of interstitial cluster formation by interstitials being pushed to the periphery of the liquid core under high pressure was identified.

Caro et al investigated the thermodynamics and mass transport in collision cascades. The authors noted in previous work that when the temperature is well above that of melting, linear and reversible thermodynamics will not suffice. In order to model the formation of a melted zone and the presence of the solid-liquid interface the usual equations for heat flux were used along with the Onsager relations for mass transport. Estimates of the parameters in these equations were derived from MD simulations in which the initial spatial and energetic distribution of atoms set in motion following the collisional phase were derived from MARLOWE [60].

Bacon and co-workers reviewed a number of results of MD simulations of cascades [61]; in particular the effect of crystal structure and irradiation temperature were considered. The fits of defect numbers according to (1.6) were compared in materials with structures as disparate as fcc, bcc, hcp and $L1_2$, and no systematic difference was seen with different structures, although the parameters did vary from material to material.

$$N_{FP} = A\,(E)^m \tag{1.6}$$

Here A and m are material dependent parameters with values of 5.67 and 0.779 respectively for Fe when E is expressed in keV. The exponent m is of most interest here as the prefactor A will be sensitive to the method of classification of defects and other details of the MD simulation, such as the manner in which the potential is stiffened at small atomic seperations. In this range the NRT equation can be seen to overestimate the number of defects at a given energy (Fig. (1.5)). This difference can be ascribed to an annealing process which the binary collision approximation cannot describe. Above energies of around $1keV$ sufficient atomic displacements are caused that the core has some liquid like characteristics. Evidence for this can be derived from ion beam mixing experiments [12, 62] and simulations [56, 63].

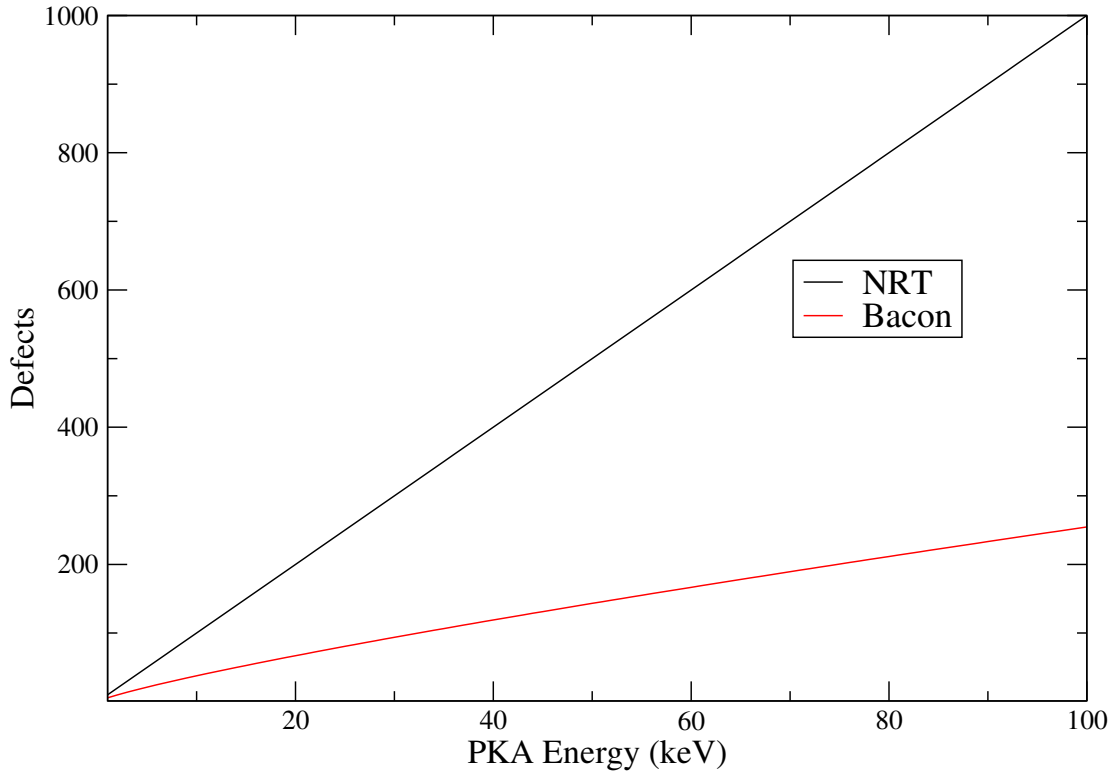

Figure 1.5: Functional forms for defect fits after Bacon et al and Norgett et al.

This picture of damage represents a different paradigm to that of Norgett et al. The proportion of primary damage which persists as residual damage is now determined by the degree of annealing of the liquid core, which is in turn determined by the dynamics of energy transfer to the electrons, since this is the most efficient means to remove energy from the region. The rate of cooling will determine the degree to which defects may diffuse, their lifetime before annihilation and subsequent clustering. The damage calculated within the BCA will depend sensitively on focussed collision sequences. However in many-body atomistic simulations, the annealing of damage is determined by the thermal spike stage following the collisional phase, which is dominated by liquid-like behaviour.

Differences were also found between metals with different atomic masses; lighter elements are more prone to form diffuse sub-cascades which give rise to more damage than a single cascade with the same energy, due to a lower liklihood of recombination. Therefore the exponent m in (1.6) is closer to unity for the lighter elements, giving a defect production efficiency closer to that within the BCA where defect recombination is excluded.

In the intermediate energy regime considered by Bacon et al, between that governed by the binary collision approximation and realistic fusion energies, the only material parameters which enter are A and m, which quantify the extent of sub-cascade formation and their spatial overlap. However the need for inclusion of electron-phonon coupling to describe the lifetime of the thermal spike was later noted [64]. In a more complete description of radiation damage, these constants would be expected to be related to the strength of electron-phonon coupling in the material. This work was extended by Stoller et al [65] to energies up to $50keV$, it was found that the number of defects obeyed a power law but with an exponent that varied between 3 different regimes. A large divergence from the NRT value was observed at $20keV$ which was attributed to the beginning of sub-cascade formation.

The addition of alloying elements with different masses was also seen to affect the degree of disorder and the duration of the thermal spike. The presence of gold in a concentration of 15% in copper was seen to reduce the length of focussed displacement events in $2keV$ cascades [66] due to the differing atomic masses in the alloying elements. In contrast little difference was seen in Fe-Cu alloys, due to the similar masses [67].

Finally an increase in the ambient temperature was seen to significantly prolong the thermal spike leading to increased annealing and reduced defect numbers [68]. This also increased the proportion of defects in clusters at the end of the simulation as an elevated temperature allowed more time for thermally assisted diffusion. This is in agreement with results obtained by Hsieh et al in simulations of $3keV$ cascades in Cu. They examined the diffusion coefficients as the ambient temperature was varied between $0 - 700\,K$ and they observed a four-fold increase [69]. Since they used an unphysical potential function this result was purely qualitative.

Despite the successes of radiation damage modelling, several shortcomings of current MD approaches have been noted. Potentials need to be developed for this purpose and so should reproduce many-body effects such as magnetism and at the very least recover important quantities such as defect creation energies and migration energies [70, 71]. Further, the role of electrons has been confined to the interatomic potential, which ignores the heating of the electrons in the vicinity of the radiation event leading to energy storage and redistribution in space and time. These shortcomings suggest that simulations of

energetic collisions must move beyond simple 'billiard ball' models of atomic dynamics [72].

1.4.3 Thermal Spike and Two Temperature Models

The subsequent thermal relaxation of an initial temperature impulse following irradiation may be described by the thermal spike model. In this picture the energy initially deposited is quickly distributed among neighbouring atoms in a spherical region, raising the local temperature. The temperature of the hot zone subsequently decreases as the heated zone expands and the initial energy impulse is partitioned among neighbouring atoms. This was originally applied to metals by Seitz et al [73]. Although the thermal spike is most readily applicable to an ion track, it can also describe the diffusive transport of energy from the collision site in a displacement cascade.

The thermal spike model is often formulated in terms of a two temperature model. This is described by two coupled differential equations representing the evolution of the temperatures of the electronic and atomic systems in space and time [74]. Each is described as a continuum with well defined thermal parameters and temperatures. The initial impulse is represented as a source term in the thermal diffusion equations. This allows calculation of the spatial and temporal distribution of the electronic and atomic temperatures.

$$C_e(T_e(r,t))\frac{\partial T_e(r,t)}{\partial t} = \nabla.(\kappa_e \nabla T_e(r,t)) - g[T_e(r,t) - T_a(r,t)] + A(r,t) \tag{1.7}$$

$$C_a(T_a(r,t))\frac{\partial T_a(r,t)}{\partial t} = \nabla.(\kappa_a \nabla T_a(r,t)) + g[T_e(r,t) - T_a(r,t)] + B(r,t) \tag{1.8}$$

Here T_e, T_a, C_e, C_a, κ_e, κ_a are the temperatures, specific heats and thermal conductivities of the electronic and atomic subsystems respectively. g accounts for heat transfer due to electron-ion interactions and $A(r,t)$ and $B(r,t)$ are source terms representing the energy deposited due to the incident particle. Integration of the source terms over all space will give the total stopping power.

Energy is transferred between the two subsystems at a rate which depends on the temperature difference and coupling strength and it diffuses away at a rate dependent on the electronic thermal conductivity. The dynamics of the system will be determined by the amount of energy initially deposited in each subsystem, a number of processes which act to return the system to thermal equilibrium and the time scales on which they proceed [72, 75]. The diffusivity in each system is determined by the ratio of the thermal

conductivity and specific heat.

$$\frac{C}{\kappa} = \alpha_{diff} \tag{1.9}$$

Beuve et al used a two temperature model coupled to an MD simulation to model sputtering following irradiation by a swift heavy ion in the electron-stopping regime. The energy deposited in the electrons is transferred to the atoms within the cylindrical track at a rate given by the coupling strength, while electronic damping of the atoms was considered a secondary effect. The sputtering yield was sensitive to both the coupling time scale and the amount of energy deposited by the ion's passage. When energy was transferred on a time scale comparable to the Debye period the yield was reduced at low rates of energy deposition, but above a certain threshold of stopping power it was increased. Similarly, when the stopping power was increased above a certain threshold, the sputtering yield was seen to increase [76].

1.4.4 Multi-scale Modelling

The purpose of modelling radiation events using MD is to investigate the residual damage. This is an inherently multi-scale problem [77]; ab-initio methods allow determination of defect formation energies and other useful information [78]. While pure ab-initio methods are unsuitable for simulating the dynamics of large systems, there are mixed quantum-classical techniques which introduce some quantum degrees of freedom into classical atomic simulation and can therefore model forces other than those within the Born-Oppenheimer approximation [79, 80]. Due to computational complexity the energy range accessible with such techniques is limited.

To simulate larger systems, robust potentials are parameterised using this information for MD simulations on ps time scales. From these simulations information can be derived on the number of defects formed per radiation event and their subsequent clustering [81], which can inform coarse grained models such as defect dynamics [82], stochastic annealing [83], rate theory approaches [84, 85], and kinetic Monte-Carlo simulations [86, 87, 88]. At this point comparison may be made with experimental observations. In turn, information can be fed into finite element models to simulate matter on macroscopic time and length scales. Thus the microscopic details of damage formation can be related to evolution on engineering time and length scales. In some cases these different techniques are simultaneously coupled together [78, 79, 89]. The relevant time and length scales of these various techniques can be seen in Fig. (1.6) [82].[4]

[4]Reprinted from Nuclear Instruments and Methods B, 103-111, B.D. Wirth, G.R. Odette, J. Marian, L. Ventelon, J.A. Young-Vandersall and L.A. Zepeda-Ruiz, Multiscale Modelling of Radiation Damage

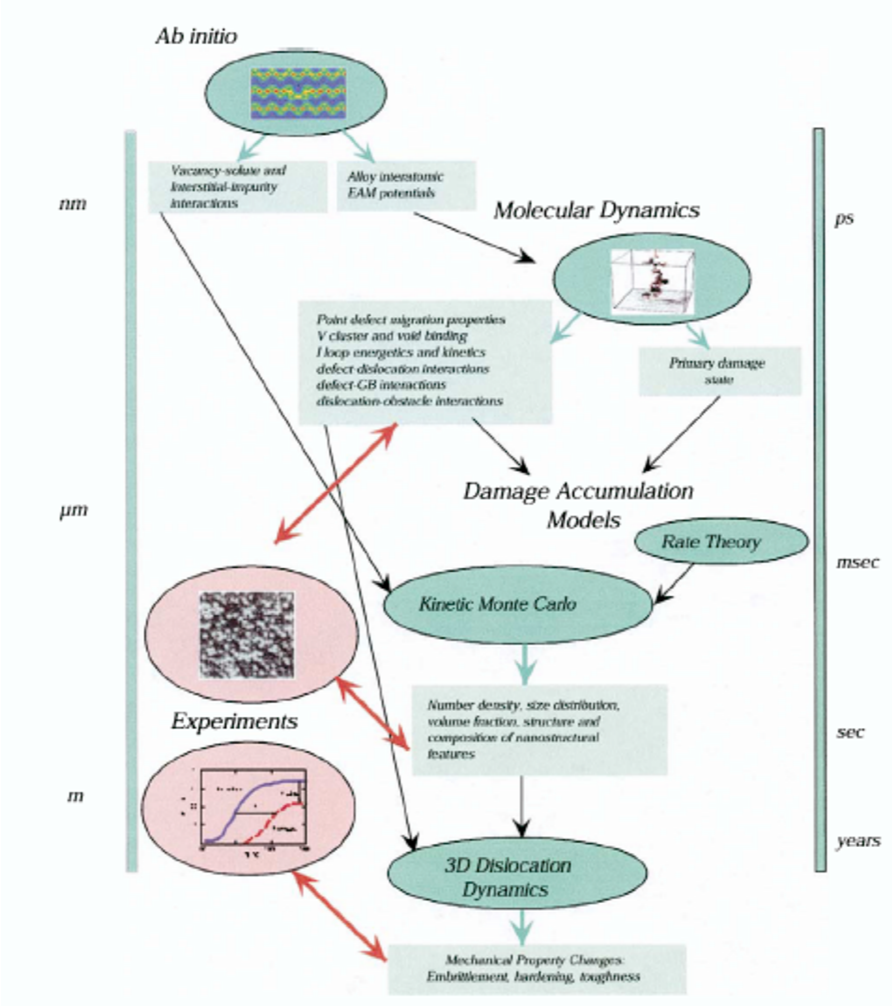

Figure 1.6: The range of scale of damage simulation techniques. [82]

Soneda and de la Rubia investigated the migration of self-interstitial clusters in Fe [88]. The diffusivities of clusters of differing sizes from single interstitial atoms to 20 atom clusters were calculated using MD and Arrhenius plots showed migration to be a thermally activated process. A kinetic Monte-Carlo scheme was in agreement with the MD results and experiment. Very low migration energies were observed, $0.17\,eV$ for a single interstitial. Migration may in fact involve many different processes such as successive reorientations. The importance of reliable starting defect configurations for higher energy cascades from MD simulations was noted. The role of temperature in cascade clustering is complicated. On the one hand a high temperature will encourage thermal diffusion and nucleation. Conversely a high temperature will lead to vibrations with a large mean squared atomic displacement, causing less efficient transfer of energy through replacement collision sequences [90]. However energies of a certain threshold are needed for replacment

in Fe-based Alloys in the Fusion Environment, 329-333, Copyright 2008, with permission from Elsevier. http://tinyurl.com/58fx7z

collision sequences, and so these are not likely to be important at low PKA energy.

1.5 Electronic Effects

Molecular dynamics simulation has traditionally been, and continues to be, an essential tool for understanding radiation damage. However the realm of application of the technique is limited by several assumptions. Within the molecular dynamics picture, the atoms evolve according to Newton's equations of motion and interact according to an interatomic potential function. This is the only part of the simulation where the electrons enter, and often this function is fit to ground state properties. Low energy events are overwhelmingly dominated by nuclear energy losses of the incident ion and atomic collisions and so are well described by MD, however as increasing computing power allows higher energy events to be simulated, these traditional approximations are challenged. While some methods allow simulation of electronic effects (such as two-temperature models and binary collision codes as discussed in sections 1.4.1 and 1.4.3), these do not capture atomic scale information necessary for meaningful quantitative comparison of damage. We therefore seek to include such effects into a classical molecular dynamics formalism. For this reason the mechanisms of electron stopping, electron-phonon coupling, thermal conduction and heat storage are now examined in detail.

1.5.1 Electron Stopping

A free ion moving through a solid will lose energy to the electron sea via inelastic collisions. Bohr first developed the theory of ion stopping by collisions within a solid in order to explain the differences observed between tracks produced by uranium fission fragments and lighter alpha particles and protons [40]. Ion-solid interactions are also of interest within nuclear physics, materials modification and medical physics. The main practical parameter of use is the range within the material defined by

$$R = \int_{E_o}^{E_1} -\frac{\mathrm{d}E}{\frac{\mathrm{d}E}{\mathrm{d}x}} \tag{1.10}$$

Here E_o is the initial ion energy, E_1 is the energy at which the ion may no longer move through the solid and $\frac{\mathrm{d}E}{\mathrm{d}x}$ is the rate of energy loss, related to the stopping power (S) by

$$S = \frac{\frac{\mathrm{d}E}{\mathrm{d}x}}{N} \tag{1.11}$$

Here S is the stopping power and N is the atomic density. S has two distinct contributions; one due to elastic collisions between the ion and other atoms, where kinetic energy is conserved, and the other due to inelastic collisions between the ion and electrons, where

some kinetic energy is lost to excitations of the electrons.

$$\frac{\mathrm{d}E}{\mathrm{d}x} = \frac{\mathrm{d}E}{\mathrm{d}x}_{nuclear} + \frac{\mathrm{d}E}{\mathrm{d}x}_{electronic} \tag{1.12}$$

The relative importance of these two terms depends sensitively on the energy and type of incident particle and target.

Two regimes of electronic stopping may be identified; Bohr's description based on the Thomas-Fermi model in the range $\nu < \nu_o$ and Bethe behaviour when $\nu > \nu_o$ where ν_o is the Bohr velocity of an inner shell electron in Hydrogen ($\approx 2.2 \times 10^7 ms^{-1}$). The different behaviours may then be characterised by the state of ionisation of the projectile ion. Bohr gives the charge fraction as

$$\frac{Z^*}{Z} = \left(\frac{\nu_1}{\nu_o Z_1^{2/3}}\right) \tag{1.13}$$

Here Z is the total number of electrons in the ground state (equal to the atomic number) and Z^* is the partial charge on the ion, ν_1 is the ion velocity. Thus when

$$\nu < \nu_o Z_1^{2/3} \tag{1.14}$$

The ion is not fully stripped of its electrons, and when

$$\nu >> \nu_o Z_1^{2/3} \tag{1.15}$$

the ion is fully stripped to a bare nucleus. Several models with different motivations have been suggested to describe the former regime by Fermi and Teller [91] and Firsov [92]. These both predict a stopping cross-section directly proportional to ion velocity.

In the high energy regime the ion is essentially a bare nucleus and interactions with target electrons are Coulombic. Bohr derived an expression for this based on the classical picture of momentum exchange, with relativistic corrections this is known as the Bethe formula. In this case the stopping power is given by

$$\frac{\mathrm{d}E}{\mathrm{d}x}_e = \frac{2\pi Z_1^2 e^4}{E} N Z_2 \left(\frac{M_1}{m_e}\right) ln\left(\frac{2m_e\nu^2}{I}\right) \tag{1.16}$$

Where $Z_1 e$ and M are the charge and mass of the incident ion respectively, Z_2 is the atomic number of the bulk ion, N is the number density of the atoms respectively and I is the average excitation energy of the electrons.

It is clear that the relative importance of various mechanisms such as momentum exchange between the ion and free electrons, electron capture, ionisation of target atoms and collective excitations forming plasmon quasi-particles depends on ion velocity [45]. The theory developed by Lindhard and co-workers was based on statistical models of

atom-atom collisions and combined these different mechanisms into a single unified model using accurate interpolation schemes allowing the calculation of stopping and ranges of ions [46, 47]. The so called LSS theory is based on the Thomas-Fermi picture of the atom, therefore is most accurate for atoms with an intermediate velocity so that the atom is neither fully stripped nor neutral. Nevertheless the range of ions in solids was predicted to within a factor of two over the full energy regime within a single model.

1.5.2 Electron-Phonon Coupling

Coupling between electronic and atomic motion can lead to long and short range order effects. Each atom partially polarises the surrounding electrons so that their motions are correlated to a degree. Thus, the electronic motion takes some of the momentum of the atomic vibrations with it. This is the basis of long range electronic order which leads to superconductivity [93].

At low energy the lattice will support well defined phonons and the electron-ion interactions are between electrons and the phonons. At high temperatures the core will be liquid like and atomic motion will be essentially random. The interactions at extremes of energy are fundamentally the same, yet the mechanisms differ and operate on different timescales so for this reason a distinction is made between the two in this work. Thermal vibrations disrupt crystal periodicity and so affect the efficiency with which energy can be transported out from the core. Suppression of energy transport can lead to the localisation of low-energy cascades and suppression of sub-cascade formation [94].

The interaction between atoms and electrons is complex; electron-phonon coupling allows an electronic subsystem and an atomic subsystem close to equilibrium to reach thermal equilibrium, while electron stopping represents inelastic collisions between higher energy ions and electrons. Koponen used a rate equation for the exchange of momentum and energy between a coupled valence electron-ion system out of equilibrium to describe electron-phonon coupling and electron stopping. These two distinct processes were shown to be equivalent in the low and high energy limit, although the crossover between the two will be abrupt. This approach had the shortcoming that it used mean transport parameters derived from equilibrium. In the thermal spike regime it was suggested that band structure effects and correlated ionic motion may be important and could be captured using kinetic transport equations [95].

The form arrived at for the electronic stopping regime was shown to be consistent with a Boltzmann equation approach for a heavy ion being slowed down by a homogeneous electron gas. This is true when the effect of band structure and correlations of the ionic

motion can be ignored, however the energy loss due to the electron-ion interaction has the second moment of the atomic structure factor as a parameter. Therefore this will take a different form in a solid compared to a liquid. The rate of atomic energy loss was given as

$$\dot{U}_a = \frac{2m_e}{M_i}\tau_{ei}^{-1}\Gamma[1 - \frac{T_e}{T_L}]E_{ther} \tag{1.17}$$

$$\dot{U}_a = \frac{\partial E}{\partial t} = \mathbf{F_a^{friction}}.\nu_\mathbf{a} = \gamma\nu_a^2 \tag{1.18}$$

Here E_{ther} is the thermal energy per atom in the cascade, τ_{ei} is the electron-ion collision time and $\Gamma = N(E_F)_{band}/N(E_F)_{free}$ is the ratio of the band density of states to the free electron density of states at the Fermi level. This rate of energy loss can be related to the frictional force acting on each atom $F_a^{friction}$. This is in turn determined by the velocity of the atom and the friction co-efficient γ. Although (1.17) is a comprehensive description of electron-ion dynamics, in general approximations have to be made as the atomic structure factor and band structure are prohibitively complex to model. Koponen later investigated the mechanism of equilibration of electrons with a distribution of phonons characterised by a fractal distribution soon after excitation and found that the rate of energy transfer was increased [96].

Allen [97] extended the early work by Spitzer [98] and Landau [99] which described weakly coupled plasmas, to dense crystalline systems. A formula for the strength of the electron-phonon interaction was derived from the Bloch-Boltzmann-Peierls formula as

$$\frac{1}{\tau_{epc}} = \chi_{epc} = 3\hbar\frac{\lambda\langle\omega^2\rangle}{\pi k_B T_e} \tag{1.19}$$

Here $\chi_{epc} = \frac{1}{\tau_{epc}}$ is the inverse of the time scale for electron-phonon coupling and $\lambda\langle\omega^2\rangle$ is the product of the low temperature linear specific heat coefficient and the mean square phonon frequency and is a familiar factor from the theory of superconductivity [100]. This approach makes the assumption that electron diffusion is negligible and that the lattice structure is not disturbed.

Volkov and Borodin [101] used a perturbative approach to derive the following expression for the rate of heat transfer between electrons and ions in laser excitation experiments on the basis of a heated Fermi gas considering only conduction electrons.

$$q = \frac{4LZne^4m^2}{\pi M\hbar^3[1+\exp(-\mu/T_e)]}\left(\frac{T_i}{[1+\exp(\mu/T_e)]-T_e}\right) \tag{1.20}$$

Here M and Z are the mass and effective ionisation factor of the ion, μ is the chemical potential and $L \approx 1$ is the Landau integral. q can be related to the rate of change of

electronic energy

$$q = C_e \frac{\partial T_e}{\partial t} = \frac{\partial E_e}{\partial t} \tag{1.21}$$

As a result, the electron-ion heat transfer will be non-linear above the Fermi energy and so deviates from the predictions of other models of electron-phonon coupling. Since initial electron temperatures of $1 < T_e/T_F < 10$ correspond to an increase in the lattice temperature of $\approx 700K$, this will have consequences for melting in metals.

Mason et al investigated the rate of transfer of energy from an isolated copper atom to the electron subsystem using time-dependent tight binding [79]. The importance of the form of the density of states at the Fermi level was noted, and the use of a simplified s-band Hamiltonian found to underestimate the rate of very energetic transitions. The value of the coupling was observed to be independent of the frequency of atomic oscillation at high electronic temperature, but the directional dependence of damping at interstitial points was seen to vary considerably. The authors suggested that a tensor form of the damping coefficient would represent a considerable improvement in accuracy.

Some indirect experimental measurements of the electron-phonon coupling strength have been made. Gilmore et al developed a framework to relate the electron-phonon coupling strength in metals to quantities measureable by time-domain spectroscopy. The quantities used to characterise the coupling strength and phonon density of states are the transport weighted electron-phonon coupling constant, a parameter controlling the temperature dependence of the electron-phonon mass enhancement and the plasma frequency which relates exclusively to the electronic degrees of freedom. A laser pulse was used which gave information on the complex conductivity. Measurements were made in a lead thin film which gave estimates, although with large uncertainties, of the above parameters in agreement with published values [102].

Groeneveld et al used a combination of fs optical reflectivity measurements and surface-plasmon polariton resonance techniques to probe the electron distribution in laser heated gold and silver [103]. The electron-phonon coupling time scale was seen to decrease with temperature in the range $710 - 530\,fs$ and $830 - 530\,fs$ for gold and silver respectively when the temerature was in the range $10 - 300\,K$. Some disagreements were found between these results and predictions based on the two-temperature model which were attributed to incomplete thermalisation of the electron system. By introducing the finite rate of electron-electron scattering into a model based on the Boltzmann equation, a consistent description of the experimental data was made.

Tas and Maris also reached the conclusion that the non-thermal nature of an electron

distribution can be significant [100]. Ultrasonic pulses following a laser pulse were studied which are influenced by the distance that hot electrons may diffuse before losing energy to the lattice. Experimental data in Al was better fit by a model in which the non-thermal character was considered since the electron-electron scattering process greatly enhances the rate of energy transfer to the lattice.

Eidmann et al performed simulations of Al under ultrashort laser irradiation which drives the metal to a plasma state, using a combination of a two-temperature model and Maxwell's hydrodynamical equations [104]. The duration of the state of non-equilibrium of electrons and ions was highlighted in such a simulation where the time for equilibration greatly exceeds the pulse length. Their results were fitted to experimental absorption measurements with an electron-ion coupling time scale of $10 - 20\,ps$.

1.5.3 Thermal Conduction

In solids the total thermal conductivity, κ is given by a lattice component due to phonon heat transport and an electronic component.

$$\kappa = \kappa_a + \kappa_e \tag{1.22}$$

Here κ_e and κ_a are the electronic and atomic thermal conductivity respectively. However in high purity solid metals, κ is dominated by the electron contribution as the electrons are less susceptible to scattering and have higher velocities. Alloying metals with impurities reduces thermal and electrical conductivities since impurity atoms disrupt crystalline symmetry and act as scattering centres. As a result, κ_e is closely related to the electron mean free path, the temperature dependence of which will be very complex between the extremes of a cold, highly degenerate Fermi liquid, and a plasma, where the mean free path is determined by Coulomb collisions.

At low temperatures the thermal and electrical conductivity are related according to the Wiedemann-Franz law [105]. Although this law has a large range of applicability, it begins to break down at high temperature as the assumption that collision times limiting electrical and heat currents are the same starts to fail. Using elementary kinetic theory the thermal conductivity and mean free path are related according to

$$\kappa_e = \frac{1}{3} C_v v_e \lambda_e \tag{1.23}$$

Here C_v is the constant volume specific heat and v_e is the electron velocity. The characteristic velocity v_e is normally approximated as the Fermi velocity, and λ_e is the electron mean free path. At high temperatures v_e deviates from v_F due to a high kinetic

energy contribution according to

$$v_e = (v_F^2 + k_B T_e/m_e)^{\frac{1}{2}} \tag{1.24}$$

This is equal to the Fermi velocity in the cold limit and tends to $(k_B T_e/m_e)^{\frac{1}{2}}$ in a hot plasma. The main unknown entering into (1.23) is the electron mean free path which will have a complicated temperature dependence.

The mechanism of electron-phonon coupling is intimately related to thermal conduction in metals. As noted by Flynn and Averback [106], to carry energy efficiently away from a hot region with a size R, the electrons must be able to scatter from a phonon in the hot region and scatter again outside the heated region. This means that the electron-phonon mean free path must be comparable to R, or the electrons will scatter very many times before leaving the heated region. Then, for effective energy transfer that is *diffusive* in nature, the electron-electron mean free path must not be so small that energy becomes localised nor so large that electronic motion is ballistic.

In the hot plasma limit, the electron dynamics will be dominated by Coulomb collisions with one another. As a result the collision frequency is dependent on T_e as given by Spitzer's result [107]

$$f_{Spitzer} = \frac{4}{3}(2\pi)^{\frac{1}{2}} \left(\frac{Z_{av} e^4 m_e n_e}{(m_e k T_e)^{\frac{3}{2}}} \right) \ln(\Lambda) \tag{1.25}$$

Where Z_{av} is the average ionic charge, n_e is the electron number density and $\ln(\Lambda)$ is the Coulomb logarithm which is determined by the parameters of electron-electron collisions.

Rinker amended the work of Lampe [108] to calculate transport coefficients at plasma temperatures and densities [109], however the phase of iron varies greatly between the energy range of $10^{-2} - 10^4 eV$ (equivalent to $\approx 10^2 - 10^8 K$) and the density range of $10^{-4} - 10^5 g\,cm^{-3}$. The behaviour varies between the standard state observed at standard temperature and pressure, insulator, liquid-gas quantum plasma, classical plasma and a non-degenerate electron gas. As a result the phase plots of the transport co-efficients are complex. Nevertheless these have been tabulated for the entire periodic table [110]. Unfortunately these results are not readily applicable to the situation observed in radiation damage. In this case the lattice and electrons will be far from thermal equilibrium during the period most important for determining damage. In the situation where the lattice is effectively liquid following local melting the electronic structure may still be relatively unchanged for times $t < \tau_{epc}$, likewise if the electrons are initially excited to the point that they only weakly feel the lattice potential, the lattice atoms may still be highly ordered. It is not obvious that either of these situations are adequately described by a fully or

partially ionised plasma in which electrons and ions are in thermal equilibrium.

Many numerical simulations of laser excitations have used two temperature models to determine the temperatures reached by the lattice. The atomic and electronic systems are assumed to each have a well defined temperature which varies in space and time according to a heat diffusion type equation with a term describing coupling. This is described in more detail in section 1.4.3. The initial excitation features as a source term in the electronic system and often simple models of the temperature dependence of the thermal parameters included. In simulations of laser excitation of gold, Wang et al [111] used a formula for the electron collision frequency, after MacDonald [112] and Kaveh et al [113] given by

$$f = \frac{1}{\tau} = BT_a + AT_e^2 \tag{1.26}$$

Here f represents the frequency of electron collisions. The term in T_a represents phonon scattering and the term in T_e represents electron-electron scattering. The form of the latter contribution can be shown to be true for a Fermi sphere of non-interacting electrons scattering on the Fermi surface [114]. This formula is valid for $T_e > T_{Debye}$ and is dominated by the phonon term linear in T_a below $\approx 10^3 K$. Chen et al also found an expression for temperature dependent electron-phonon coupling in terms of the constants same A and B since the mechanism of thermal conduction is intimately related to electron-phonon coupling as both are determined by the frequency of collisions between electrons and phonons [115].

Eidmann et al modified a code for the hydrodynamical simulation of sub-ps lasers with cold Al [104]. Two regimes were interpolated between; a low temperature regime with a collision frequency based on (1.26) but omitting the electron scattering term and the hot plasma limit given by Spitzer's result. By taking the harmonic mean of these two regimes it was found that, at the point of highest collision frequency, the electron mean free path is considerably lower than the interatomic distance. To avoid the unphysical situation of 'resistivity saturation' [116] whereby electrons would become constrained to a single ion the following condition was imposed

$$f < \frac{\nu_e}{r_o} \tag{1.27}$$

Here r_o is the ion sphere radius and the characteristic velocity ν_e is given by (1.24).

Antaki [117] showed the importance of using a non-equilibrium form of the thermal conductivity in the context of sub-ps laser heating of metals. Using the Boltzmann transport equation a particularly simple form of the temperature dependence of κ was found

$$\kappa_{neq} = \frac{T_e}{T_a}\kappa_{eq} \tag{1.28}$$

which can be arrived at by ignoring the T_e^2 term in (1.26) and using a specific heat linear in T_e (see section 1.5.4). It was shown that using this form for the non-equilibrium of the two sub-systems in short-pulse laser heating led to better agreement with experimental desorption measurements. [118].

There exist estimates [119, 120] of the mean free paths as a function of temperature for various metals including Fe, as well as a model for the temperature dependence of the mean free path [121], however this model makes use of an unreliable interpolation between high and low temperature regimes which is complicated due to band structure effects. This temperature range is likely to be of greatest importance in determining damage. Also experimental data for the thermal conductivity has been fit up to the melting temperature for various metals, [122] however a robust functional form for the thermal conductivity over a suitable temperature range, and under non-equilibrium between electrons and atoms, has not yet been arrived at.

1.5.4 Heat Storage

Heat capacity measures the amount of energy required to raise the temperature of a material, and in general this is given as

$$C_e(T) = \frac{\partial U}{\partial T} \tag{1.29}$$

Classical statistical mechanics predicts an energy of $\frac{1}{2}k_BT$ for each degree of freedom with a squared energy dependence giving a constant value of $C_e = \frac{3}{2}k_B$ per electron in 3 dimensions. However at low temperatures the heat capacity of a system of electrons is observed to be much lower than this. This problem was not explained until the discovery of the Pauli exclusion principle which limits the number of electrons that can be excited to higher energy states. Thus, in a system of electrons in the quantum mechanical regime, C_e depends on the precise form of the density of states at the Fermi level as

$$C_e = \int_0^\infty (E - E_F)\frac{\partial f(E, \mu, T_e)}{\partial T_e} g(E) \mathrm{d}E \tag{1.30}$$

Here μ is the chemical potential and $g(E)$ is the density of states at energy E. $f(E, \mu, T_e)$ is the Fermi-Dirac distribution given by

$$\frac{1}{e^{(E-\mu)/k_BT} + 1} \tag{1.31}$$

However, making the approximation that $k_BT \ll E_F$, it can be shown, by considering the increase in energy of a free electron Fermi gas of N electrons, that the heat capacity is given by [123]

$$C_e = \frac{1}{2}\pi^2 N k_B \frac{T_e}{T_F} \tag{1.32}$$

$$C_e = \Gamma T_e \tag{1.33}$$

Here Γ is the low temperature specific heat coefficient. This approximation is known as the Sommerfeld expansion, and the linear temperature dependence at low temperatures is in agreement with experimental observations. Values of Γ have been measured experimentally for many different metals.

When evaluating (1.30) for a system with a complicated band structure, such as for electrons in a solid metal, care must be taken to ensure that the correct chemical potential is used. The chemical potential is equal to the Fermi energy at $0K$, but at higher temperatures is determined by normalising the integral of the product of the density of states and the Fermi-Dirac distribution to the total number of electrons

$$N = \int_0^\infty g(E) f(E, \mu, T) \mathrm{d}E \tag{1.34}$$

The density of states as a function of energy in W is plotted in Fig. (1.7) [124]. The electron energy is shown relative to the Fermi energy. Since the d-band is partially filled in transition metals the chemical potential decreases steadily with temperature for a 3 dimensional Fermi gas since the density of states increases with energy at all times. The chemical potential is seen initially to decrease with temperature in W since the density of states is larger immediately above the Fermi energy than below it. However, as the temperature increases further the chemical potential increases slightly as the Fermi-Dirac distribution begins to flatten and the contribution to the integral in (1.34) due to the large peak at $\approx -3eV$ is given less weighting.

Lin et al have used density functional theory to calculate the density of states of transition metals. Some of which show the opposite trend to that of free electron type metals such as Ag, which demonstrate an increase in the chemical potential at high temperatures. As a result the electronic heat capacity is lower in Fe than that predicted by the Sommerfeld expansion (but higher in W due to the precise form of the density of states around the Fermi level). Comparison of these two forms can be seen in Figures (1.8) [125] and (1.9) [126], the Sommerfeld form approximates ab-initio data well at low temperatures but above $\approx 2000K$, a saturated value is reached. Calculations from this density of states information have given tables of values for the heat capacity and also thermal conductivity and electron-phonon coupling strength as a function of T_e for various transition metals [127, 128]. The increase in electron-phonon coupling strength was seen to agree with recent electron diffraction experiments and it was found that commonly used approximations for the thermal parameters overestimate the time for the onset of melting.

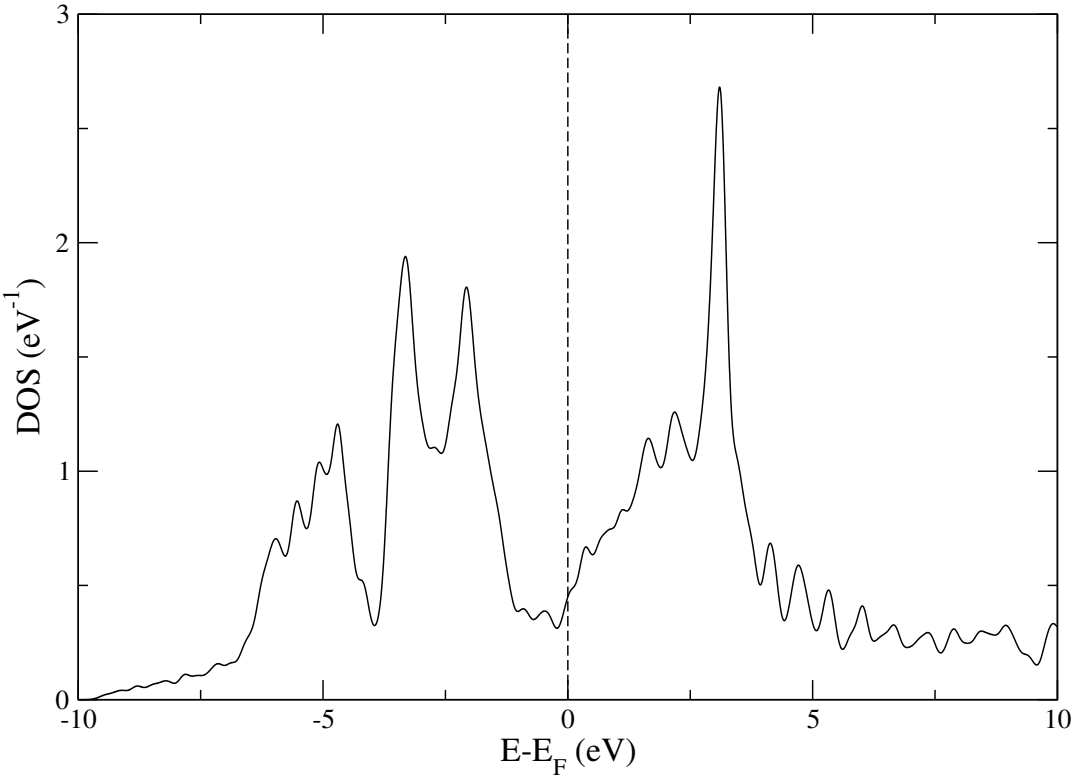

Figure 1.7: Density of states as a function of energy in tungsten.

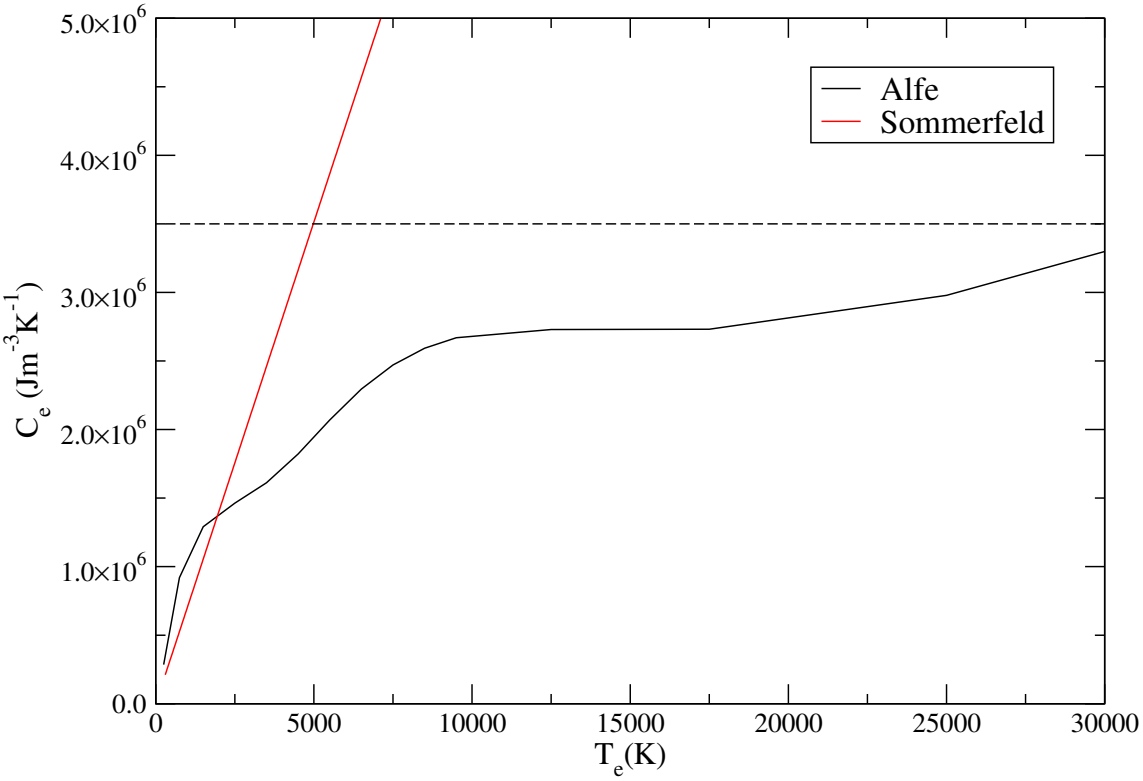

Figure 1.8: Electronic specific heat in non-magnetic bcc iron as a function of electronic temperature as calculated by Alfe [125] and as given by the Sommerfeld expansion. The dashed line shows the classical value assuming 2 electrons contribute to specific heat per atom

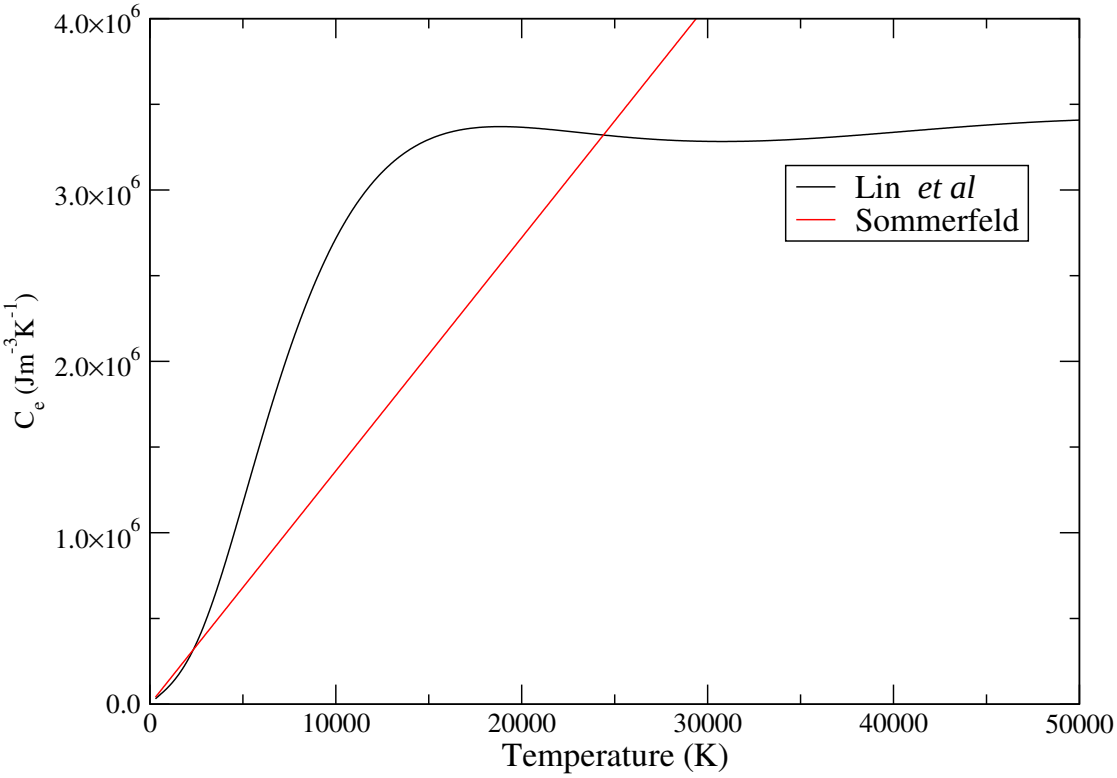

Figure 1.9: Electronic specific heat in tungsten as a function of electronic temperature as calculated by Lin *et al* and as given by the Sommerfeld expansion.

1.6 Including Electronic Effects In Radiation Damage Simulations

There have been some attempts in the past to model the effects of electrons in radiation damage, and these are reviewed in this section. These have been in the context of radiation damage, both in classical atomistic simulation of displacement cascades but also continuum, two-temperature approaches to describe ion tracks. Also the modelling of laser ablation has motivated some consideration of electronic effects, and since the situation of an intense, localised excitation of the electronic subsystem has many parallels with an ion track, these techniques are reviewed. Approaches including some kind of frictional damping of atomic motion into MD assume the effect of the electronic temperature rise to be negligible, while those which define a local electronic temperature neglect the feedback of electronic energy to the atomic degrees of freedom.

1.6.1 Displacement Cascades

The question of whether electron-phonon coupling affects the progression of displacement cascades was first addressed by Flynn and Averback [106]. It was concluded that the rate of cooling of hot atoms by electrons was dependent on the ratio λ_e/r_{TS} where λ_e is the electron mean free path and r_{TS} is the radius of the hot region. If the electron mean free path is small compared to the heated region, electrons will not be able to leave the hot zone via diffusive transport and transfer energy away; in this case heat diffusion will be dominated by the atoms. Conversely, when the electron mean free path is very large, such as in Cu, the electrons are not able to collide in the spike region and transport energy away. As a result electron-phonon coupling does not play a part in cascade dynamics. By extrapolating the harmonic approximation of lattice vibrations above the melting temperature the electron mean free path was calculated for several metals. It was concluded that the mean free path was comparable to the dimensions of the heated zone in Ni, Co and Fe. For these metals electron-phonon coupling will act as an efficient heat sink, cooling the cascade.

Both the mechanisms of electron-phonon coupling and electronic stopping were first included in a unified picture by Caro and Victoria using a Langevin formalism [129]. This is able to describe a frictional force on the atoms and thermal agitation by the electrons due to the feedback of energy into the atomic system. The two forces represent the interactions between the atoms and electrons and have an intuitive interpretation as the effect of a heat bath. Electron stopping corresponds to when the systems are far from equilibrium and electron-phonon coupling when close to equilibrium, so there is a cut off ionic velocity and switch over between the two behaviours. The frictional force in each case is linear in velocity while the force feeding energy back to the ions is stochastic with

a Gaussian distribution with mean zero and a second moment proportional to the interaction strength via the fluctuation-dissipation theorem. The electronic temperature enters into the distribution of the random force and is assumed to be constant. The authors noted that this approximation will fail when the electron mean free path is comparable to the cascade dimensions as energy will not be removed efficiently as the electrons must scatter many times to leave the cascade region. In this case a description of the electronic temperature evolution will be necessary.

Finnis *et al* [130] derived coupled differential equations for the heat flow in the electronic and atomic systems in terms of the local temperatures and various material parameters. The expressions derived for the heating of, and energy dissipation within, the electron system were found to be consistent with the Flynn and Averback analysis [106]. Making the approximations that the electronic temperature remains constant, justified by the swift heat conduction within the electron system, and ignoring phonon diffusion as negligible in comparison to electron diffusion led to the following expression for the rate of change of the atomic temperature

$$\frac{\mathrm{d}T_a}{\mathrm{d}t} = -\alpha(T_a - T_e) \tag{1.35}$$

Where the time constant for the cooling of the lattice by the electrons α is given by

$$\alpha = \frac{3\Theta_D \gamma_e T_e \nu_F}{\pi^2 r_o \sigma \rho T_o} \tag{1.36}$$

Here Θ_D is the Debye temperature, γ_e is the coefficient of electronic heat capacity, ν_F is the Fermi velocity, r_o is the Wigner-Seitz cell radius, σ is the specific heat capacity and ρ is the density. Electron-phonon coupling was included into MD simulations via a frictional force in the atomic equation of motion. When comparing Ni and Cu they found that the strong coupling in the former reduced the number of residual defects compared to the latter, and also noted the importance of the electron-phonon mean free path and the coefficient of electronic heat capacity.

Kapinos and Bacon [131] extended the work of Finnis et al [130] to investigate the effect of electron-phonon coupling on the degree of melting and the formation mechanism of concentrated regions of vacant lattice sites known as depleted zones. The atomic velocities within an MD simulation were scaled at each timestep according to the time scales for cooling given in [130]. It was found that a strong coupling interaction limited the formation of a liquid-like zone and decreased the average vacancy concentration due to reduced thermal gradients. In later work this model was developed by solving the heat diffusion equations to scale the atomic temperatures at each timestep. The initial temperature and defect distributions were calculated using the MARLOWE code in the BCA. It was found that strong electron-phonon coupling in Ni and Fe caused amorphisation

and no melting respectively. Whereas weak coupling in Cu led to a core with a vacancy concentration above a threshold at which recrystallization gives way to amorphisation of the core, preventing collapse into vacancy dislocation loops [132, 133].

Gao et al[134] developed the model put forward by Finnis and Agnew [130] to model displacement cascades using a hybrid of atomistic MD with a frictional drag force and the continuum two temperature model. Their investigations of higher energy events showed the production of more defects as the coupling strength increased, consistent with the picture of defects being quenched into the final configuration.

Zhurkin and Kolesnikov considered the effect of both electron-stopping and electron-phonon coupling in simulations of self-ion sputtering in Ni and Al [135]. This was included as a frictional force acting on the atoms, the crossover between elastic and inelastic interactions, corresponding to the coupling and stopping interaction respectively, is at the velocity corresponding to two times the cohesive energy. In comparison to identical simulations excluding electron-ion interactions it was concluded that stopping had a negligible influence on the collisional phase of the cascade and coupling affects the cooling phase reducing the thermal spike lifetime and suppressing non-additive effects in sputtering.

The same technique was used by Spaczer and co-workers [136] to investigate the kinetics of disordering and amorphisation processes in three intermetallic compounds. The strength of the electron-phonon coupling was varied and amorphisation was studied in 5 and $15keV$ cascades. In the former case no amorphisation was seen, but in the latter case the final state of the crystal was dependent on the strength of the electron-ion interaction. With no coupling the system was able to form a highly disordered state. The size of this region was reduced with weak coupling. In the case of strong coupling a highly ordered state resulted. The probability of amorphisation was found to be dependent upon the degree of short range order in the molten state. If this was similar to the crystalline state the atoms are able to relax back to the crystalline phase without any energetically expensive, displacive transitions. The speed with which the molten region is quenched by electron-phonon coupling emerged as a key factor driving amorphisation.

When considering ionisation probabilities following a displacement cascade, Duvenbeck et al[137] considered inhomogeneities in the electronic temperature. The atomic system was modelled using a classical MD simulation, and monitoring the energy lost to the electrons by every atom in the simulation. In this case the feedback of energy from the electrons back to the ions was neglected, since the level of excitation was low, and the evolution of the excitation energy density was calculated using a Green's function formalism. Diffusion within the electronic system is governed by the electron mean free path which was initially fixed at $4.2\,nm$, appropriate for the highest electronic temperatures

seen in the simulations. Significant differences were seen when compared to simulations using a diffusion coefficient which decreased linearly in time to model the gradual transition from an ordered lattice to complete amorphisation. The decrease in the efficiency of the diffusion mechanism led to a increase in the electronic temperature.

1.6.2 Ion Tracks

When a swift heavy ion is incident on a material, the majority of the deposited energy is imparted to the electron subsystem since electronic stopping will be greater than nuclear stopping. This will cause some excitation of the electrons and some proportion of this energy will be transferred to the lattice. Under certain circumstances, and above a certain threshold stopping power, this may lead to observable macrodefects known as tracks, which may be regions which have undergone local amorphisation, melting or a phase transformation. These can be observed in metals, insulators and semiconductors, although the processes leading to track formation in these different materials are diverse and will be dependent upon structural properties as well as electronic properties [27].

Several mechanisms have been suggested to explain track formation. The first is the Coulomb explosion, whereby electrons undergo collisions with the incident ion and are given fast radial velocities leaving bare nuclear charges which mutually repel. There will be some degree of expansion and the spread of a melt front from the track axis before the charges recombine [138]. The creation of an ionised cylindrical region around the path of an energetic heavy particle was described by Fleischer [139]. These tracks form above a critical value of electronic stopping power. Such a mechanism is probably not appropriate in metals due to high electron mobility leading to swift charge neutralisation, although this is could be of considerable importance in insulators as charge inhomogeneities can persist for several *ps*. It has been observed that under swift heavy ion irradiation, some ionic crystals do not undergo amorphisation. Swift heavy ion irradiation may give rise to a complex damage morphology and collective electronic excitations above a threshold energy loss [140].

Bringa and Johnson simulated a Coulomb explosion using MD in simulations of sputtering in a Lennard-Jones (LJ) material with parameters pertinent to astronomical applications [141]. A number of randomly selected atoms, proportional to the stopping power and so ionisation density, experienced an ionised potential given by

$$V = (e^2/r)\exp(-r/a) \tag{1.37}$$

Here a is an average screening constant and r is the radial distance from the track axis. There was an instantaneous switch between the standard LJ potential and the modified

potential to simulate the Coulomb explosion and the number of ions (n_{ions}) were reduced according to

$$n_{ions} \propto \exp\left[-t/\tau\right] \tag{1.38}$$

to simulate charge recombination with a time scale of τ. Analysis of the energy of sputtered atoms gave an energy distribution which differed from the later stages of the event suggesting Coulomb explosion and thermal spike mechanisms are the early and late stages of the event respectively. In later work it was concluded that charge neutralisation times of greater than one tenth of a Debye period are needed for Coulomb explosion mechanism to be effective in heating the lattice [142]. It should be noted that a typical Debye frequency is $\approx 10fs$ while the typical time scale for recovery of charge homogeneity in a metal is $\approx 1fs$ [31].

Ryazanov et al compared simulations of damage in the amorphous material $Fe_{85}B_{15}$ and Cu according to the thermal spike and Coulomb explosion models [143]. The heat diffusion equations for the thermal spike were formulated and solved by numerical methods while the kinetic energy transferred to the atoms by the electric field set up by the Coulomb explosion were also solved to give comparable temperatures. The total number of point defects produced by the irradiation was calculated as

$$N = N_o f_D 2\pi \int_0^{r_o} r\mathrm{d}r \int_o^{\tau} \exp \frac{-E_f}{k_B T(r,t))} \mathrm{d}t \tag{1.39}$$

Here N_o is the number density of host atoms in the lattice, f_D is the Debye frequency, r is the distance from the track axis and E_f is the vacancy formation energy. The temperature changes in each system were examined and the point defects produced compared to experimental data. It was concluded that the Coulomb explosion predicted stronger atomic heating and more accurate point defect concentrations.

Ossi and Pastorelli compared calculations using the segregation-charge transfer model based on the Coulomb explosion to experimental data. The dissociation of an atom into a species with net charge was described; the ionised atoms experienced mutual repulsion and frictional forces from the surrounding neutral lattice atoms. The cohesive energy enters as a parameter to this model. The energy cost to introduce such a partially ionised atom into the lattice was calculated and qualitative differences were found between metals which undergo different structural changes such as amorphisation and those that do not [144].

In addition to the Coulomb explosion, the lowering of E_D (the energy to displace an atom from its lattice position) due to electronic excitation may lead to phonon mode softening and violent displacements at low energy. Efforts have been made to simulate [145]

this effect using a modified Finnis-Sinclair type potential form. Rather than using a rectangular form as an approximation to the density of states and a rectangular distribution function appropriate to $0K$, a realistic, temperature dependent Fermi-Dirac distribution was used. Preliminary simulations of laser excitation demonstrated that changes in the repulsive energy due to the elevated electronic temperature affected the rate of ablation of atoms from the surface.

Using the thermal spike model and a modified two-temperature model, Wang and colleagues calculated the maximum lattice temperature reached following irradiation, using the number of valence electrons as a free parameter [146]. Temperature dependent thermal parameters were used derived from experiment and the models of Allen [97] and Kaganov [74] used to derive the electron-phonon coupling parameter. It was assumed that the maximum lattice temperature was reached at a time (τ) equal to

$$\tau = \frac{C_e(T_e)}{g(T_e)} \tag{1.40}$$

where $g(T_e)$ is the electron phonon coupling strength. It was concluded that the sensitivity of a metal to electron stopping was most closely linked to the melting temperature and the coupling strength. Using a rate theoretical approach for the creation and annealing of defects within Fe, a threshold stopping power of $S_e = 15keVnm^{-1}$ was derived for the electronic annealing of defects formed through nuclear collisions. From consideration of the nuclear stopping power the number of defects produced was calculated within the Kinchin and Pease picture [25], then the jump frequency for an interstitial atom into a vacant lattice site was calculated from the atomic temperature as

$$f(r,t) = f_o \exp\left(-\frac{Q_a}{k_B T_a(r,t)}\right) \tag{1.41}$$

Here $f_o = k_B T_D/h$ and Q_a is the activation energy of defect annealing. The value of $S_e = 15keVnm^{-1}$ for Fe was in agreement with experimental observations.

Toulemonde also used a two-temperature model to describe swift ion irradiation, and in particular to model phase transitions within amorphous materials following melting [147]. An approximation was made for the source term in the atomic system consisting of a Gaussian spatial term and an exponentially decaying temporal term.

$$S(r,t) = \frac{\mathrm{d}E}{\mathrm{d}x}\exp(-t/\tau)B(r)/\tau \tag{1.42}$$

Where τ is the electron-ion interaction time scale and B is the spatial term given by

$$B(r) = A\exp(-r^2/4\sigma^2) \tag{1.43}$$

σ^2 gives a measure of the energy diffusivity within the electronic system. The only free parameter which enters into the analysis is the length scale characterising the movement

of the electrons. By assuming melting when the atomic temperature exceeds the melting temperature, the radius of the melted zone was calculated. This predicted track radius agreed with experiment using a value of $\lambda = 14\,nm$ for this free parameter. It should be noted that this is two orders of magnitude higher than estimates of the diffusive mean free path, although since this is describing ballistic transport this is to be expected.

Tombrello described the situation in MeV ion irradiations where the initial energy distribution is given by collisions between ions and electrons which are emitted as δ rays with known radial ranges [148]. From this, the range over which there is sufficient energy to break atomic bonds can be calculated. The total damage produced by irradiation is modified by electronic excitation; the defect cross-section is given by

$$\frac{\sigma_d}{\sigma_n} = \overbrace{M^{'}(1 - e^{-(a_c/R)^2})^M}^{(1)} + \overbrace{e^{-(a_c/R)^2}}^{(2)} \tag{1.44}$$

Where a_c is the radial range over which there is sufficient energy to break atomic bonds, R is the radial extent of recoil damage, M is the number of excited bonds and $M^{'}$ is the number of bonds following partial self-annealing. (1) is due to annealing of defects and (2) due to the transformation of an existing defect into a permanent displacement. Good agreement was found with experimental results in Fe, Ti, Zr, Co, Nb and Pt within this model although further investigation of the various parameters within the model using MD and TEM was suggested .

1.6.3 Laser Ablation

The interaction of femtosecond duration laser pulses resembles the situation in ion tracks very closely. A large amount of optical energy is deposited into the electronic system in a short amount of time, following which a number of processes act to return the system to equilibrium. These can be divided into *athermal processes* which act up to $1\,ps$, and *thermal processes* after $1\,ps$ [149].

- $\approx$ **10fs** Excited electrons expelled from the core will recover spatial homogeneity and so local charge neutrality, and electron-hole pairs will recombine allowing recovery of a local thermal distribution at an elevated temperature.
- $\approx$ **0.1 − 0.5ps** Energy will begin to diffuse away from the collision region by thermal conductivity.
- $>$ **1ps** The electronic subsystem will equilibrate with the lattice.

Jeschke et al performed a theoretical study of the graphitisation of diamond on a fs time scale [150]. The transition of the electrons from a non-thermal to a thermal distribu-

tion via electron-electron collisions was modelled and used to derive the modified forces between atoms and so the changing potential energy surface. Determination of the reflectivity during laser induced melting agreed well with experiment which was attributed to the excited state contribution.

Most attempts to simulate electronic excitations in ion tracks or laser simulations have used continuum two temperature models [151] as there has been no consistent way to model energy exchange between excited electrons and the lattice. However Yamashita et al, coupled an MD cell to an electron continuum by scaling atomic velocities simulating laser ablation [152]. Temperature was removed in two different methods; by scaling according to a two-temperature model and the removal of heat on the boundary limited by elastic transport. It was concluded that electronic heat transport dominated total heat transport over the first few *ps*, after which a thermal shock wave and phonon transport became important once the electrons and atoms had reached equilibrium.

Wellershoff and co-workers investigated the threshold fluence required for melting of various metals [153]. Calculations using a modified two-temperature model were fit to experimental data in order to estimate the electron-phonon coupling strength. Diffusion within the phonon system was considered negligible in comparison to electronic diffusion on the short time scales involved. The ballistic transport of electrons is significant in noble metals, so must be included using a modified source term, although it can be ignored in transition metals. It was concluded that for short, femtosecond pulses, unlike nanosecond pulses, electron-phonon coupling is important in determining damage as the diffusion length is strongly dependent upon this parameter. The good agreement between the model and experiment demonstrated that damage formation under laser pulses is predominantly a thermal process.

Chen et al considered the thermomechanical response of metal films to fs laser heating [154]. By coupling thermal diffusion within the two temperature model to the classical equations of thermoelasticity, both the transfer of energy from the electrons to the lattice and the momentum transfer due to hot electrons were described. The formulation of this model was made in one and two dimensions and compared. It was found that the 1-D formulation overestimated electronic and atomic temperatures.

1.7 Overview of Thesis

Previous attempts to model electronic effects in molecular dynamics simulations of radiation damage have either used Langevin equations of motion to include frictional damping of the atoms, but neglected the thermodynamics of the electrons and imposed

a constant electronic temperature, or have used a two temperature model to describe the electron temperature but neglected the feedback of electronic energy into the atomic subsystem. It has been noted by several authors that the roles of thermal properties, electron-phonon coupling and electronic excitations need to be examined in greater detail [3, 32, 36, 42, 43, 51, 64, 70, 155]. It is clear that a consistent model of electronic excitations and energy exchange is necessary.

In this chapter we have discussed the mechanisms of electron stopping, electron-phonon coupling, electronic heat storage and thermal conductivity, along with methods that include these effects into radiation damage simulations and their observation in experiment. The method of molecular dynamics is described in detail (chapter 2). In particular numerical integration schemes, methods to impose constant temperature and descriptions of interatomic bonding are discussed, as well as limitations of these techniques. The two-temperature model is also discussed.

In chapter 3 a new model is described. An atomistic simulation using classical molecular dynamics for the atomic system is coupled to a heat diffusion equation for the electrons, which describes the evolution of a local electronic temperature. The atomic equation of motion is a Langevin equation with a coupling that is a function of the local electronic temperature. The atomic dynamics are dependent on the local temperature difference and the whole system is driven to the ambient temperature. Thus electron phonon coupling and electronic stopping are included, which gives rise to a spatially varying electronic temperature and feedback of this energy loss back into the atomic system.

A full investigation of the role of electronic effects in displacement cascades is presented in chapter 4. The electron-phonon coupling strength emerges as the main unknown parameter in our model, so a systematic study is made of the effect of the strength of this parameter compared to less sophisticated models. The temperature and defect evolutions during the simulation and residual defect configurations are examined. It is shown that the overall dynamics of the system and, most importantly, the final damage state is determined by several non-independent mechanisms and the time scales on which they operate.

The first atomistic simulations of ion tracks in iron are presented in which the initial excitation is of the electronic system (chapter 5.1). In contrast to displacement cascades, the dynamics are always dominated by diffusion in the electron system. Consequently the electronic thermal parameters emerge as critical for determining the dynamics of energy transfer and so damage formation. A range of values of these parameters is investigated. The effect of electronic excitation on an existing defect configuration is examined and compared to experiment and the evolution of the defect distribution is monitored. Finally comparisons are made between ion tracks in tungsten and iron. A temperature dependent

specific heat, derived from density functional theory, is used and compared to a model extrapolated from low temperature behaviour. The defect distributions and the presence of shock waves are investigated in detail.

Chapter 2

Numerical Modelling Techniques

We seek to model both the lattice and electron subsystems during a radiation event. Since information on microscopic damage is required, the lattice must be modelled atomistically to access these length scales. The highly excited electron system is prohibitively complex and computationally expensive to model quantum-mechanically, on this scale, and so it is treated as a continuum. By coupling the two subsystems together, the effect of energy exchange between the lattice and electrons and energy storage and diffusion within the electrons are introduced in a consistent manner and their effects on atomic dynamics modelled. The techniques for simulating each subsystem are examined in this section.

2.1 Thermal Diffusion Equation and Two Temperature Models

The heat diffusion equation is derived from Fourier's law of heat flow and the conservation of energy. It is a partial differential equation relating the first time derivative of heat energy or temperature to its second spatial derivative and may be expressed as

$$C\frac{\partial T}{\partial t} = \overbrace{\nabla\kappa\nabla T}^{diffusive} + \overbrace{S(\mathbf{r},t)}^{source} \tag{2.1}$$

The diffusive term describes the propagation of heat energy in the presence of a temperature gradient and the source term describes energy being added to the system over time. There exist some elementary solutions to (2.1) in 1 dimension; with an initial condition given by

$$T(x,0) = T_o\,\delta(x - x_o) \tag{2.2}$$

The temperature profile at a later time is then given by

$$T(x,t) = T_o\frac{1}{\sqrt{4\pi\alpha t}}\exp\left(-\frac{(x-x_0)^2}{\alpha t}\right) \tag{2.3}$$

Where $\alpha = \frac{\kappa}{C}$ is the diffusivity. Plots of the relaxation of such an initial condition over time can be seen in Fig. (2.1); each dataset is characterised at different times by the diffusion length scale which represents the standard deviation of the temperature profile and is defined as

$$L_{diff} = \sqrt{\alpha t} \tag{2.4}$$

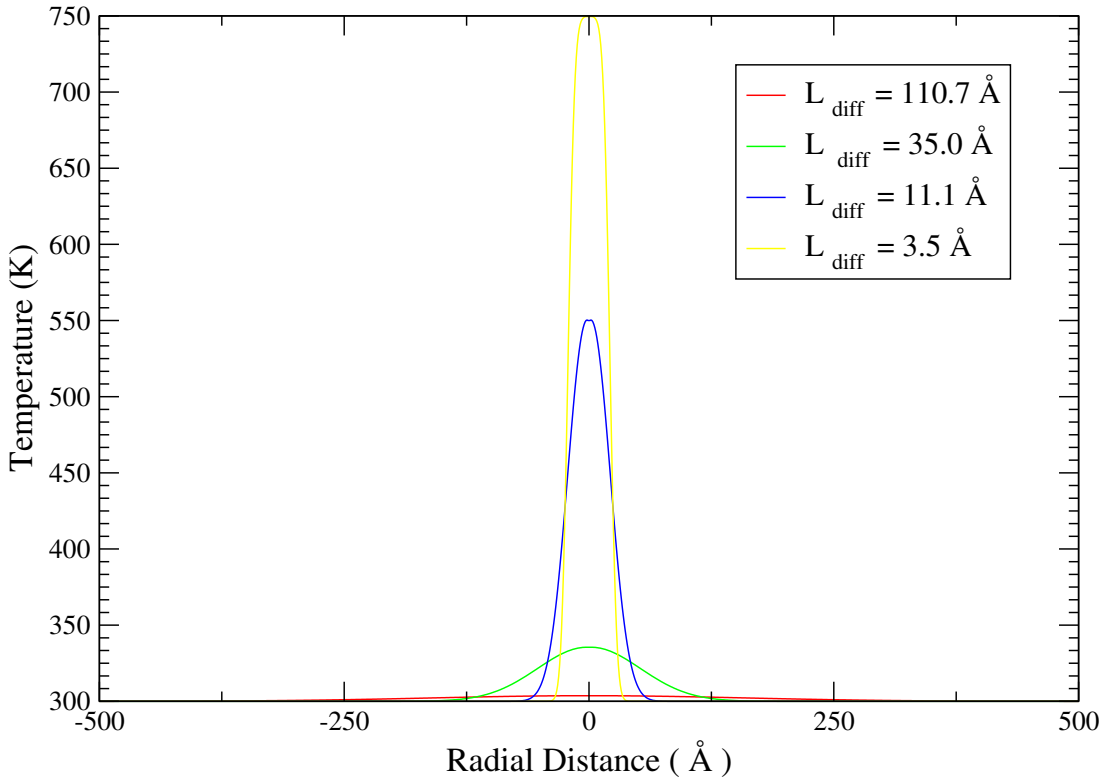

Figure 2.1: The relaxation of a temperature spike by thermal diffusion

However, for general initial conditions, temperature dependent thermal parameters or for coupled systems, the heat diffusion equations cannot be solved analytically, so a numerical method must be used.

The simplest example of a Runge-Kutta type integration algorithm is the explicit method. The derivative information at the beginning of a timestep is used to advance the solution through Δt. This approach is is not as accurate as other methods using an equivalent timestep, as the error introduced at each step is $O(\Delta t)^2$.

$$x(t + \Delta t) = x(t) + (\Delta t)\dot{x}(t) \tag{2.5}$$

Here x is the position variable, which is calculated from its first derivative and value at the previous timestep. (3.3) can be solved for the case of constant thermal parameters and assuming no source term by discretising and writing the finite-difference equation explicitly

in 3-D. The temperature can at timestep i can be calculated from the temperature at the previous timestep by assuming a 3-D grid of equal spacing, as

$$T^{i+1}(x,y,z) = T^{i}(x,y,z) + \frac{\kappa}{C}\frac{1}{(\Delta x)^2}\left[T^{i}\left(x+\Delta x,y,z\right) + T^{i}\left(x-\Delta x,y,z\right) + \right.$$
$$\left. T^{i}\left(x,y+\Delta y,z\right) + T^{i}\left(x,y-\Delta y,z\right) + T^{i}\left(x,y,z+\Delta z\right) + T^{i}\left(x,y,z-\Delta z\right) - 6\,T^{i}\left(x,y,z\right)\right]\Delta t \tag{2.6}$$

When the explicit method is applied to the heat diffusion equation with an equal grid spacing, the condition for convergence is given by

$$F_{om} = \alpha\frac{\Delta t}{(\Delta x)^2} < \frac{1}{2d} \tag{2.7}$$

Where F_{om} is the Fourier mesh number and d is the dimensionality. This gives a timestep for convergence of

$$\Delta t_{FourierMesh} < \frac{(\Delta x)^2}{2\,d\,\alpha} \tag{2.8}$$

The timestep given by (2.8) is a criterion for convergence using the explicit method for the diffusive part of (2.1). Fig. (2.2) shows the core electronic and atomic temperatures as a function of time in a continuum two temperature model of an ion track as a function of time using the heat flow equations (2.9) and (2.10) describing coupled systems. The source terms were set to zero and only the diffusion within and exchange between systems was considered in 1 dimension as below.

$$C_e\frac{\partial T_e}{\partial t} = \kappa_e\frac{\partial^2 T_e}{\partial x^2} - g[T_e - T_a] \tag{2.9}$$

$$C_a\frac{\partial T_a}{\partial t} = \kappa\frac{\partial^2 T_a}{\partial x^2} + g[T_e - Ta] \tag{2.10}$$

An ambient temperature of $300K$ was used with constant values of the thermal parameters and coupling strength appropriate to this temperature in Fe. The initial conditions used were an elevated temperature in the centre of the electronic system typical of an ion track. A square temperature profile and a smeared, more continuous profile with comparable energy were compared; more formally the two conditions are, respectively

$$T_e(x,0) = (T_{exc} - T_{ambient})\delta(x) + T_{ambient} \tag{2.11}$$

$$T_e(x,0) = (T_{exc} - T_{ambient})N(0,\Delta x) + T_{ambient} \tag{2.12}$$

Where T_{exc} is the excited temperature , $T_{ambient}$ is the ambient temperature (300K) and Δx is the grid spacing.

It can be seen from Fig.(2.2) that as the timestep is increased very slightly, complete divergence sets in after very few iterations and in fact ($0.8\Delta\, t_{FourierMesh}$) is needed for convergence. The discontinuous initial condition gives rise to large local errors, which challenge the assumptions of the explicit method; that all functions are smooth.

Fig. (2.3) plots atomic and electronic temperatures in the ion track axis as a function of time and shows the results for which the integration scheme has converged. The addition of coupling terms of the form $g\,(T_e - T_a)$ will give an additional criterion for convergence related to the coupling strength and specific heat

$$\Delta\, t_{convergence} < \frac{C_e}{g} \tag{2.13}$$

Here g is the coupling strength in units of $Wm^{-3}K^{-1}$. In practice this time scale is much longer than the constraint due to diffusion as $\frac{C_e}{g}$ is of the order of ns. If temperature dependent thermal parameters are considered this condition will become a function of temperature. Additionally there is a limit to which the the 'discretisation error' of using finite-difference integration schemes can be quantified since there is no exact analytical solution to complex, non-linear or many body dynamics to which a numerical solution may be compared [156].

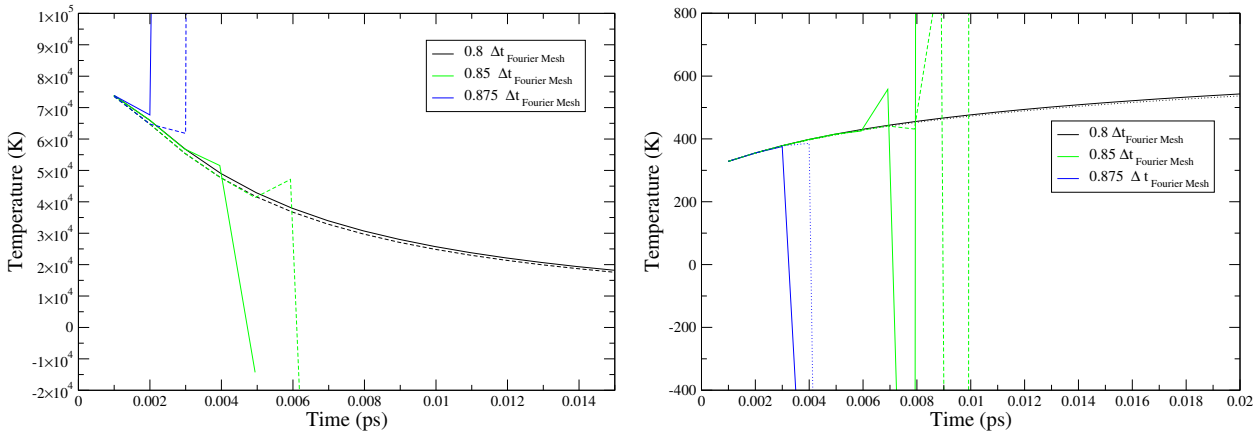

Figure 2.2: The performance of the explicit integration algorithm in continuum simuations of a ion track with two different initial conditions. A Lorenztian temperature profile (full line) and smeared profile (dashed line). Electron temperature profile (left) and atomic temperature (right).

2.2 Classical Molecular Dynamics

Molecular dynamics (MD) allows the calculation of the trajectories of a number of classical degrees of freedom through phase space, according to the equations of motion

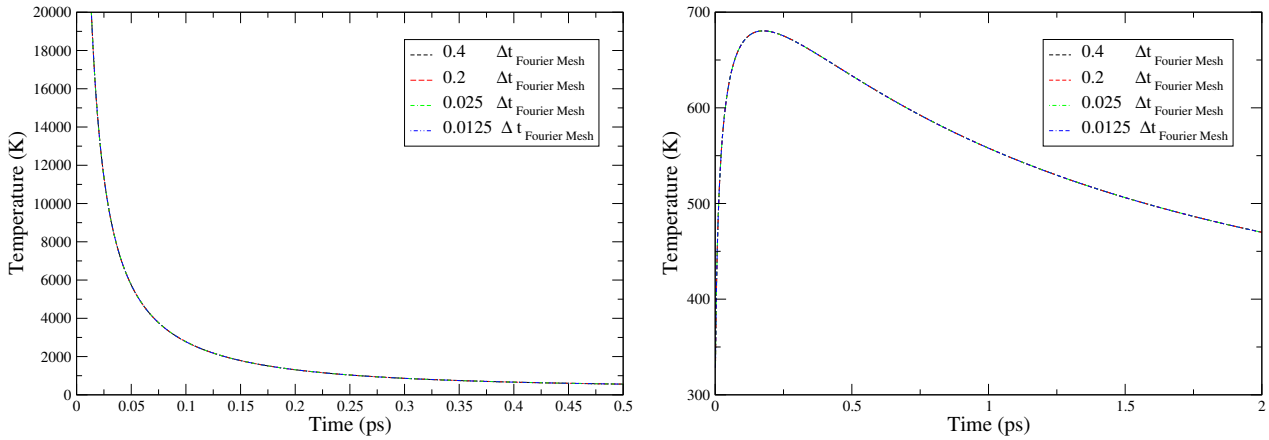

Figure 2.3: The behaviour of the explicit integration algorithm with varying timestep once convergence has been achieved

and the interatomic forces. There is a choice of how accurately the interatomic forces are calculated from the behaviour of the electrons, giving a spectrum of techniques. At one extreme there is ab-initio MD developed by Carr and Parinello [157] in which the forces are found by solving the electronic structure problem explicitly. The ground state wave-function is found by minimisation of the Kohn-Sham energy functional using a method of simulated annealing based on the importance sampling technique pioneered by Metropolis et al [158]. The other extreme is *classical* MD in which purely empirical potentials are used; in this case the behaviour of individual electrons is averaged out.

Despite continuing increases in computing power and the development of order N computer codes [159] the current upper size limit of systems which can be modelled using ab-initio techniques is of the order 10^4. However this number is even lower for metallic systems as codes scaling linearly with system size are not generally applicable, due to long range correlations.

Given that the system size necessary to contain the cascade scales roughly as 20 atoms per eV of energy of the primary knock-on atom (PKA) [160] it is obvious that to model cascades with energies approaching those of fusion neutrons, classical MD must be employed. Nordlund, however, formulated a method of 'Recoil Interaction Approximation' for calculating the ranges of high energy ions, using a hybrid method of the binary collision approximation and MD. This allows a single ion of interest to be simulated as if it were in a full atomic environment despite having a range many times that of the size of the MD cell. Consequently both self-interaction and use of a large MD cell can be avoided [161].

In MD the microscopic state of the system is completely described by the positions

and momenta of the d-dimensional array of N particles of the system. The system's evolution represents a trajectory through $2Nd$ dimensional phase space, which is prescribed by the iteration of the equations of motion over a number of timesteps. While, in theory, this involves simply the solution of an, albeit large, set of coupled differential equations, care must be taken to ensure ergodicity, convergence of numerical integration and energy conservation.

Using the Born-Oppenheimer approximation the Hamiltonian of the system can be expressed in terms of the nuclear variables and separated into terms depending on momentum $\mathbf{p}$ and position $\mathbf{r}$.

$$H(\mathbf{r}, \mathbf{p}) = H(\mathbf{p}) + V(\mathbf{r}) \tag{2.14}$$

Where $H(\mathbf{r}, \mathbf{p})$ is the full energy operator, $H(\mathbf{p})$ is the momentum operator and $V(\mathbf{r})$ is the potential energy term. In classical MD, $V(\mathbf{r})$ averages out the electron motion to give an effective potential which is fitted to certain material parameters (see section 2.5).

An MD simulation starts with an initial configuration specified by positions $[\mathbf{r}_i]$ and velocities $[\dot{\mathbf{r}}_i]$ chosen appropriately to allow swift relaxation of the system to a realistic state. These are often sampled from the Boltzmann distribution in such a way that there is no overall momentum. A period of equilibration is necessary to ensure that the system has no memory of its initial configuration [162].

During the course of the simulation, the $2Nd$ microscopic quantities are sampled regularly to give time averages of the macroscopic thermodynamic properties of the system. If we make the ergodic hypothesis, these time averages are equivalent to ensemble averages, whereby the state of the system is sampled from a distribution of points in phase space consistent with macroscopic constraints on at least three of, for example, particle number, pressure, temperature, volume, chemical potential, entropy and stress.

The evolution, as a whole, of an ensemble of classical degrees of freedom through phase space can be described theoretically by the Liouville equation [163] for Hamiltonian systems,

$$\widehat{\mathbf{L}}[f] = \widehat{\mathbf{C}}[f] \tag{2.15}$$

Here $\widehat{\mathbf{L}}$ is the Liouvillian operator, f is the probability distribution and $\widehat{\mathbf{C}}$ is the collisional operator. $\widehat{\mathbf{C}}$ describes collisions with particles other than those in the distribution function f. Now each point represents a system evolving in time along a trajectory through phase space. These trajectories cannot cross, as this would represent a branching of identical systems and the specification of the $2dN$ position and momenta evolving under

deterministic dynamics must uniquely describe distinct systems.

Consideration of the collision term leads to the Boltzmann equation. Written in full for a collisionless system

$$\widehat{\mathbf{L}}f = \frac{\partial f}{\partial t} + \frac{\mathbf{p}}{m}.\nabla_{\mathbf{q}}f + \mathbf{F}.\nabla_{\mathbf{p}}f = 0 \tag{2.16}$$

Or equivalently,

$$\frac{df}{dt} = 0 \tag{2.17}$$

This is analogous to the continuity equation; the density in phase space must be conserved. This constraint is equivalent to time symmetry. It can also be shown that under Hamiltonian flow (i.e. evolution of the equations of motion over time) that the integral of the measure, represented by the probability distribution, over the total phase space volume is invariant, leading to ergodicity.

In order to simulate a macroscopic piece of material one would ideally model of the order 10^{23} atoms. However, since this is currently beyond the upper limit of available computational resources, it is necessary to simulate a smaller system representing a region of interest. In order that this smaller simulation will reproduce the behaviour of the macroscopic system, surface effects arising from the finite size of the system must be eliminated [164]. This can be done by imposing periodic boundary conditions so that the system topology is represented by a torus.

This effectively gives rise to an infinite number of *image systems* each containing an image particle for each real particle in the real system. When one particle leaves the real system from one side into an image system from the left, it is replaced by a particle leaving an image system placed to the right to enter the real system. It is not necessary, however, to store infinite details of the image particles; only the real system need be simulated. This can be seen schematically in Fig. (2.4)

In order to avoid real particles interacting with their conjugate particle in a nearby image cell, the interaction must drop off as $V\alpha\, r^{-\mu}$ where $\mu > d$, the dimensionality of the system.

2.3 Verlet Integration Schemes

In MD the implementation of an appropriate algorithm for integration of the equations of motion at each timestep is crucial for the accurate description of the system's evolution

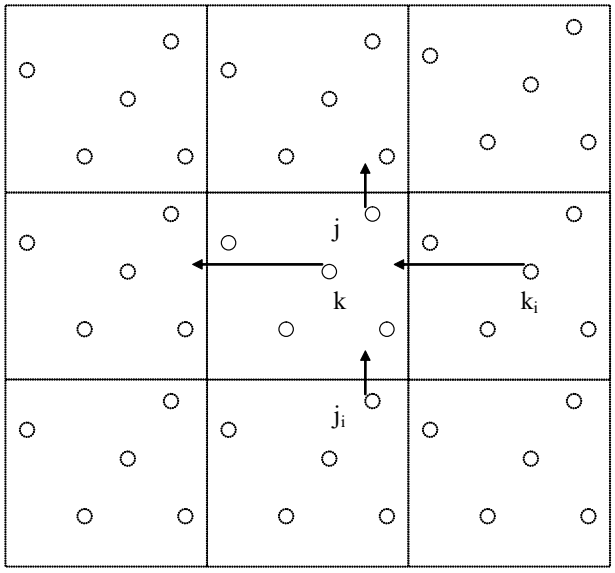

Figure 2.4: The image cell convention in MD.

and conservation of energy. Rounding errors introduced by limits of the precision of the computer and truncation errors in expansions of the position variable can cause the simulated system to diverge exponentially from the true system. It is possible, by considering terms $O(n)$, to achieve an accuracy $O(n+1)$. However the implementation of complex higher order algorithms are prohibitively costly in terms of computing time.

One example is the predictor-corrector algorithm, which extrapolates from previous stored values of the solution to predict the value at the new timestep correcting the value using derivative information at that point. This approach lends itself better to systems following smooth trajectories rather than those observed in highly non-equilibrium situations. Although the predictor-corrector algorithm has potentially higher accuracy and can deal with more complex systems, the fact that it stores a large amount of data as it progresses renders it unsuitable for large systems [165]. This method is also time-asymmetric; since succesive values are predicted from the history of the trajectory. If the simulation is reversed the initial starting configuration will not be recovered. Although macroscopic irreversibilty is the norm for large systems, even if the components obey reversible microscopic dynamics in agreement with increasing entropy, it is preferable to have an integration scheme which obeys time symmetry.

It is necessary to find a balance between complexity of the algorithm and efficiency of its implementation. Since the calculation of forces is the most computationally intensive task in any MD simulation, many numerical methods used to solve differential equations can be be dismissed since they require many calculations per timestep [166, 167].

It is also preferable that an integration algorithm for conservative equations of motion conserve the volume of an element in phase space. The Jacobian for the transformation from $t_o \longrightarrow t$, according to Newton's equations, is equal to unity, so Newton's equations solved exactly conserve phase space volume. All symplectic integration schemes conserve phase space volume. However the term symplectic means more than just this condition [167]. A symplectic integrator for N particles is guaranteed to preserve N Poincare integral invariants, the N^{th} being the total phase space volume [168]. Few integration schemes can be considered as a sequence of time evolutions generated directly by simple Hamiltonians and so retain symplecticity of the exact equations of motion in MD.

2.3.1 Verlet Algorithm

The Verlet algorithm [169, 170] is the most popular integration algorithm used for the solution of the equations of motion in MD

Writing two third order Taylor expansions of $\mathbf{r}(t)$, one forward in time and one backwards in time, gives

$$\mathbf{r}(t+\Delta t) = 2\mathbf{r}(t) - \mathbf{r}(t-\Delta t) + \ddot{\mathbf{r}}(t)(\Delta t)^2 + O(\Delta t)^4 \tag{2.18}$$

Although this evolves the particles position at each timestep, it does this without explicitly calculating the velocities, which are needed to calculate the kinetic energy and so the temperature. The velocity can be calculated from $\mathbf{r}(t+\Delta t)$ and $\mathbf{r}(t-\Delta t)$ according to

$$\frac{\mathbf{r}(t+\Delta t) - \mathbf{r}(t-\Delta t)}{2\Delta t} + O(\Delta t)^2 \tag{2.19}$$

The steps in the Verlet algorithm can be seen schematically; the stored values are shown in grey and the arrows indicate how the unknown terms are calculated.

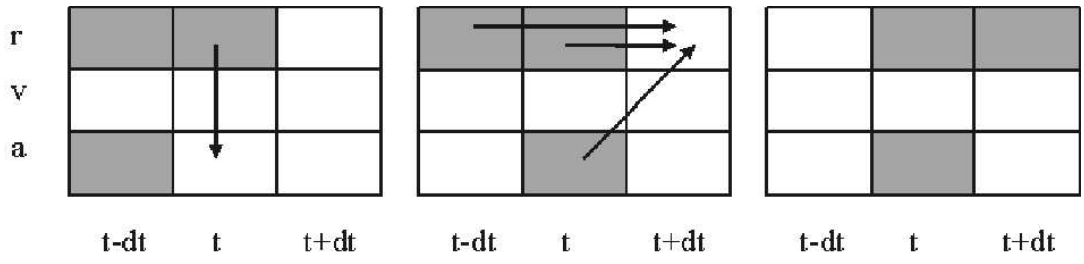

Figure 2.5: The Verlet integration algorithm

2.3.2 Velocity and Leapfrog Verlet

There are several variants of the Verlet scheme such as the Leap-Frog Verlet (LFV) [171] and Velocity Verlet (VV) algorithms [172].

The VV algorithm obtains the position at the next timestep by first calculating the velocity at a half timestep

$$\dot{\mathbf{r}}(t+\frac{\Delta t}{2}) = \dot{\mathbf{r}}(t) + \frac{\Delta t}{2}\frac{\mathbf{F}(t)}{m} + O(\Delta t)^2 \tag{2.20}$$

Here $\mathbf{F}$ is the force and m is mass. The full timestep position is calculated from

$$\mathbf{r}(t+\Delta t) = \mathbf{r}(t) + \Delta t\dot{\mathbf{r}}(t+\frac{\Delta t}{2}) + O(\Delta t)^3 \tag{2.21}$$

Using the new position, the force at the next full timestep is obtained, and from this the full timestep velocity can be calculated

$$\dot{\mathbf{r}}(t+\Delta t) = \dot{\mathbf{r}}(t+\frac{\Delta t}{2}) + \frac{\Delta t}{2}\frac{\mathbf{F}(t+\Delta t)}{m} \tag{2.22}$$

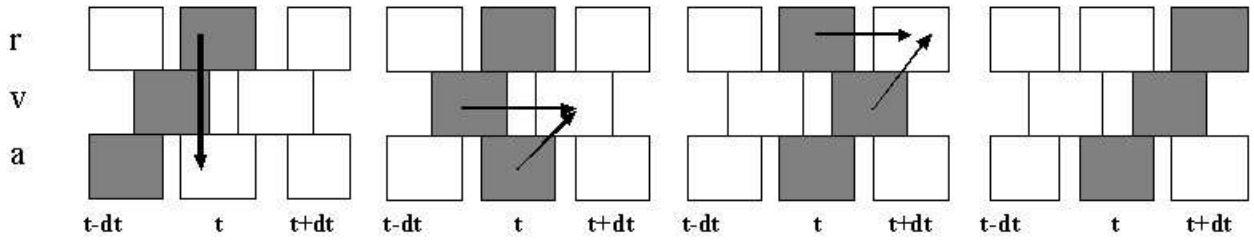

Figure 2.6: The velocity Verlet integration algorithm

While the LFV algorithm is algebraically equivalent to the Verlet algorithm, it has the advantage that it calculates the position and velocity of each particle at the same time. Writing

$$\mathbf{r}(t+\Delta t) = \mathbf{r}(t) + \Delta t[\dot{\mathbf{r}}(t) + (\frac{\Delta t}{2})\ddot{\mathbf{r}}(t)] + O(\Delta t)^3 \tag{2.23}$$

The term in square brackets is simply $\dot{\mathbf{r}}(t+\frac{\Delta t}{2})$. Subtracting from $\dot{\mathbf{r}}(t+\frac{\Delta t}{2})$ the corresponding equation for $\dot{\mathbf{r}}(t-\frac{\Delta t}{2})$ gives

$$\dot{\mathbf{r}}(t+\frac{\Delta t}{2}) = \dot{\mathbf{r}}(t-\frac{\Delta t}{2}) + \Delta t\ddot{\mathbf{r}}(t) \tag{2.24}$$

$$\mathbf{r}(t) = \mathbf{r}(t) + \Delta t\dot{\mathbf{r}}(t+\frac{\Delta t}{2}) \tag{2.25}$$

Although co-ordinates and velocities are evaluated at different times, an estimate for $\dot{\mathbf{r}}(t)$ is given by

$$\dot{\mathbf{r}}(t) = \dot{\mathbf{r}}(t \mp \frac{\Delta t}{2}) \pm (\frac{\Delta t}{2})\ddot{\mathbf{r}}(t) \tag{2.26}$$

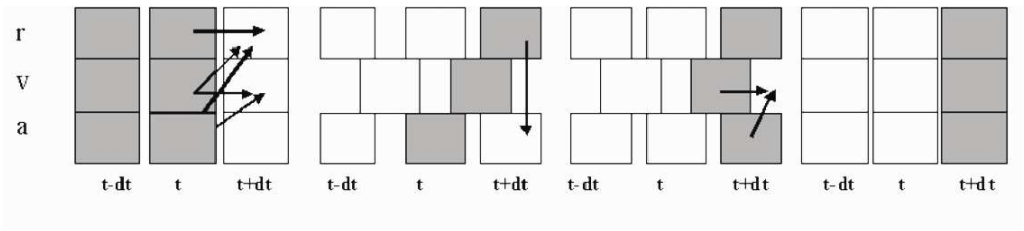

Figure 2.7: The leapfrog Verlet integration algorithm

The general rule for the length of the timestep to use in the Verlet algorithm is such that the fastest moving particle does not travel more than 5 percent of the nearest neighbour distance [173].

$$\Delta t\, \dot{r}_{max} < \frac{r_{NN}}{20} \tag{2.27}$$

These difficulties are unavoidable in MD; in reality it is impossible to use an algorithm that describes the system's trajectory precisely. While small errors in the early stages of the simulation will undoubtedly sensitively affect the system's subsequent trajectory through phase space, we can still extract useful statistical information from the results. The behaviour of a system, in this respect, can be quantified by the Lyapunov exponent. Consider two points in phase space $\mathbf{Z_1}$ and $\mathbf{Z_2}$ which are separated by an infinitesimally small increment $\Delta\mathbf{Z_o}$. If these are used as initial conditions for two different trajectories evolving under identical dynamics, the difference between them $\Delta\mathbf{Z} = \mathbf{Z}_1(t) - \mathbf{Z}_2(t)$ diverges over time t according to

$$|\Delta\mathbf{Z}| \propto e^{\lambda t}\Delta\mathbf{Z_o} \tag{2.28}$$

Here λ is the Lyapunov exponent. If $\lambda < 0$ the two trajectories converge over time to a common basin of attraction, if $\lambda = 0$ the two trajectories remain at a fixed separation in phase space and the system is linear and additive since the two trajectories are independent. If $\lambda > 0$ the system is chaotic and two closely located initial conditions will quickly diverge. In a many body system, even with completely deterministic dynamics, it is common for λ to be very large. In an MD simulation this can arise from small thermal fluctuations, which mean that otherwise identical simulations can arrive at very different points in phase space. However, while the trajectories will differ, the macroscopic, time averaged properties, such as temperature, will be identical within the ergodic approximation.

For this reason it is common to take an average, in non-equilibrium situations, over several trajectories from equivalent, but not identical, inital conditions [174]. For example, by averaging defect distribution data resulting from several cascades formed with different PKA directions, statistically significant average quantities can be derived.

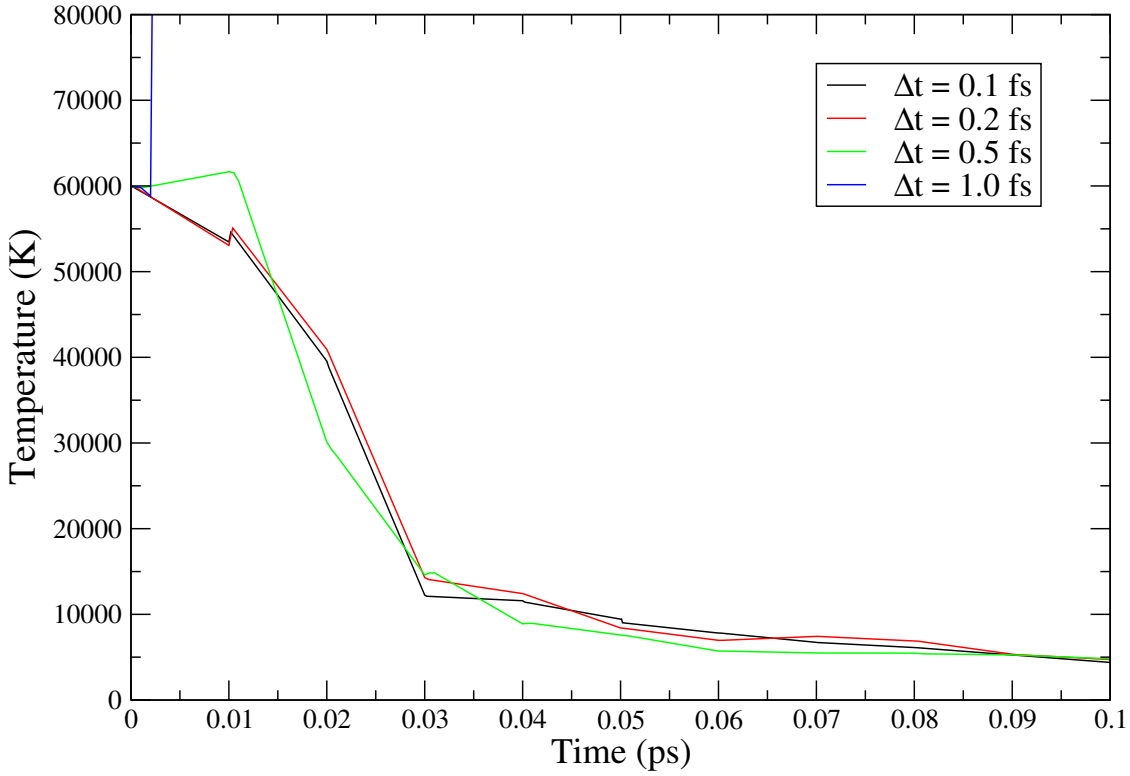

Figure 2.8: Core atomic temperature in $2.5keV$ displacement cascades using a Langevin thermostat.

Figure (2.8) demonstrates this. Otherwise identical MD simulations of $2.5keV$ displacement cascades in Fe performed with different timesteps are compared. The MD cell is divided into cubic temperature cells of $\approx 25\mathring{A}$ dimension and the temperature of the central cell containing the PKA is examined. It can be seen that the fluctuations are very different in each case since the different trajectories cannot be compared after a few iterations of the equations of motion, the general shape of the cooling curves are the same. As long as a timestep is used which is sufficiently small that the dynamics are stable the macroscopic details of the simulation may be considered an accurate approximation to the many-body dynamics. It can be seen that the integration of the equations of motion is not converged with a timestep of $1.0fs$, and the atomic temperature diverges.

2.4 Thermostats

When simulating radiation damage it is often necessary to remove energy from the simulation cell to model the return to the ambient temperature. Since such a large amount of energy is introduced into the system, a significant increase in the average temperature is seen as the PKA energy is shared amongst all atoms, so this energy must, at some point, be removed. Therefore a physically motivated model for driving the lattice atoms to a fixed ambient temperature is required. A constant energy ensemble has been used to model low energy events however. This is justified by the small overall increase in temperature.

There are several methods to produce MD sampling the constant temperature ensemble. This can be done by scaling of individual particle velocities [175]. However this does not accurately reproduce the equilibrium canonical distribution, since a constant temperature is achieved by restriction of the total *kinetic energy* of the system. While the *potential energy* of the system is allowed to fluctuate the system can only sample a portion of the true canonical ensemble. In this case the ergodic hypothesis fails as the system cannot ever fully sample the canonical ensemble due to the constraint on total kinetic energy.

A second constraint method [176, 177, 178] introduces an extra term to the equations of motion in proportion to the particles momenta. The Hamiltonian in this case is mathematically consistent, but it does not correspond to a real physical system. While both these schemes produce a constant temperature, the extended system methods of Nose [179] and Hoover [180] are preferred as they give a canonical distribution in both configuration and momentum space. Berendsen et al formulated a method to weakly couple an MD cell to an external heat or pressure bath using a deterministic velocity scaling approach with variable time constants [181].

Pseudo-thermostating techniques have also been used to impose a target temperature in MD simulations [68, 182, 183]. Atoms within a fixed distance from the boundary of the cell are thermostatted to a given temperature by the application of stochastic and viscous forces, as in a Langevin formalism, or by simple velocity rescaling. The speed of relaxation is limited by thermal conduction of the atoms in the cell.

A different approach was formulated based on the Langevin equation describing frictional losses to, and random thermal agitation, by some virtual particles which may be treated statistically in a unified picture. The net effect of this is to drive the system to a fixed temperature.

2.4.1 Nose-Hoover Thermostat

The Nose-Hoover thermostat introduces an extra *virtual* degree of freedom to the system, corresponding to the action of the heat bath on the real degrees of freedom. Since the real system is now coupled to a heat bath allowing exchange of energy the real system can now sample the true canonical ensemble, while the extended system samples the micro-canonical ensemble. This is in contrast to earlier constraint methods which drive the system to a reference temperature by fixing the total kinetic energy,

The modified Lagrangian equation of motion gives rise to deterministic dynamics described by the following equations of motion for position, momentum and friction coefficient η [167].

$$\frac{d\mathbf{r}_i}{dt} = \frac{\mathbf{p}_i}{m_i} \tag{2.29}$$

$$\frac{d\mathbf{p}_i}{dt} = \mathbf{F}_i - \eta\mathbf{p}_i \tag{2.30}$$

$$\frac{d\eta}{dt} = \frac{1}{Q}\left(\Sigma_i \frac{p_i^2}{m_i} - gk_BT_{therm}\right) \tag{2.31}$$

Where g is the number of *real* degrees of freedom. The system relaxes to equilibrium by negative feedback at a speed given by Q, which represents the inertia associated with the extra degree of freedom. This parameter of the virtual degree of freedom has the units of $[Energy][Time]^2$ as it determines the second time derivative of an energy change and it is related to the characteristic time scale for thermostating τ_{therm}

$$Q \propto k_BT_{therm}\tau_{therm}^2 \tag{2.32}$$

This formalism allows energy loss to be incorporated as a damping term. As a result the temperature undergoes oscillations about the mean temperature, the amplitude of which has a negative exponential envelope. This is analogous to a damped classical harmonic oscillator with an equation of motion of the form $x(t) = A\ cos(\omega t)\ e^{-Bt}$. While this incorporates frictional energy loss, it neglects the feedback of energy; the systems evolution will thus be completely specified by the value of Q and the initial value of η.

Fig. (2.9) shows the average atomic temperature in a $2.5\,keV$ displacement cascade as a function of thermostating time scale. There is an initial spike in the temperature due to the PKA energy, after which there are sinusoidal fluctuations about an exponentially decreasing curve, the frequency of which are determined by the strength of coupling between atoms and the heat bath. Such a 'mean field' formalism, where damping is applied to all atoms uniformly depending on a global average of the energy, is not appropriate to model

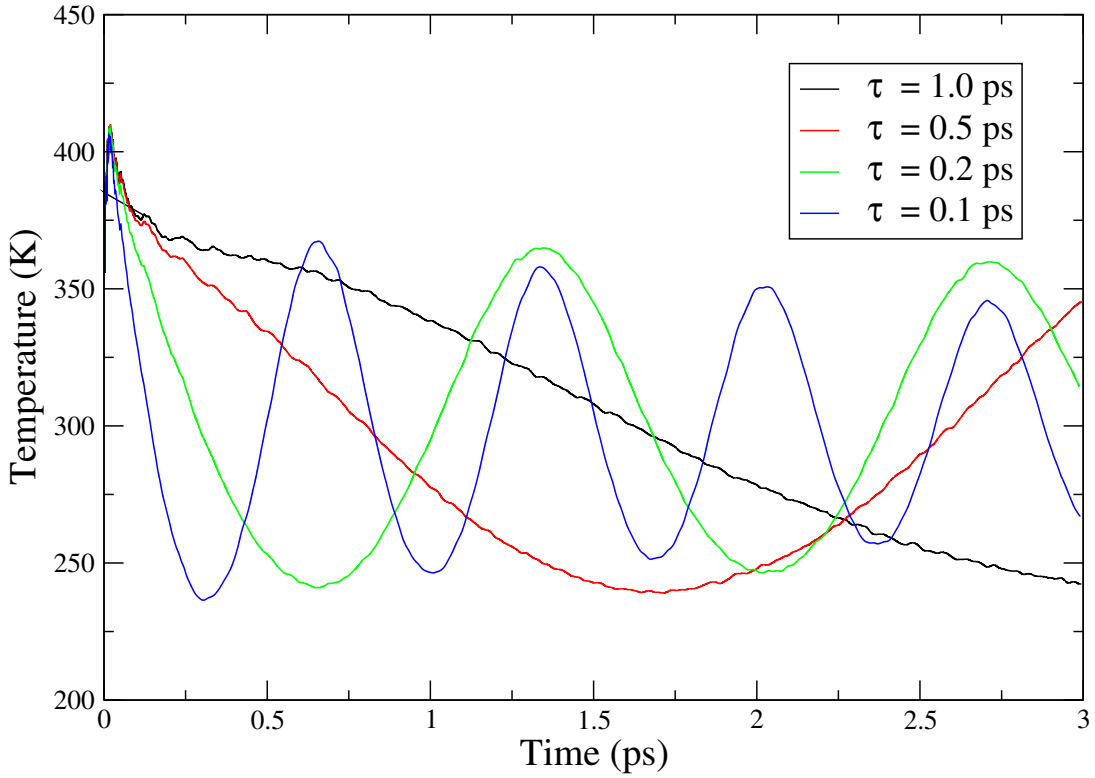

Figure 2.9: Average atomic temperature in a 2.5 keV displacement cascade in iron as a function of coupling time scale using the Nose-Hoover thermostat.

the damping in radiation damage as the energy is initially partitioned very hetrogeneously. The Langevin thermostat has the advantage that the frictional force is directly proportional to the individual atomic velocity and so damps atomic motion at an individual rate.

2.4.2 Langevin Thermostat

Langevin dynamics combines deterministic MD, governed by Newton's equations of motion, with the Monte Carlo technique [184]. The particle's equations of motion are modified to describe frictional losses to, and random thermal agitation by some virtual particles as in Langevin's description of Brownian motion [185]. This allows time efficient treatment of motion on long time scales while including motion on short time scales, which is not of great interest, in terms of a statistical average.

Mori [186, 187] and Zwanzig [188] described a system in which motion takes place on two very different time scales. This allows the evolution matrix describing the system to be separated into a product of terms for motion on each time scale. When applied to the

momentum of a single particle this gives

$$\dot{p}(t) = -\int_0^t M(t^{'})p(t-t^{'})dt^{'} + \widetilde{p}(t) \tag{2.33}$$

Where $\widetilde{p}(t)$ is a rapidly varying fluctuation and $M(t)$ is the normalized auto-correlation matrix of the projected force and contains information of the history of the system. Thus $M(t)$ is also known as the memory function. Since the memory function for a stochastic force drops off much more quickly than that of a deterministic force, $M(t)$ in this case may be approximated statistically as $\widetilde{p}(t)$ is Brownian and so independent of the value of $\widetilde{p}$ at earlier times. For this reason it is not neccesary to integrate over time as for the deterministic force.

$\widetilde{p}$ is postulated to be Gaussian distributed, with 2nd moment given by

$$\left\langle \widetilde{p}(t)\widetilde{p}(t^{'}) \right\rangle = 2mkT\gamma\delta(t-t^{'}) \tag{2.34}$$

Integration of the delta function in (2.34) for the auto-correlation matrix allows (2.33) to be written as the classical position Langevin equation

$$m\ddot{\mathbf{r}} = \mathbf{F} - \gamma\dot{\mathbf{r}} + \widetilde{\mathbf{F}} \tag{2.35}$$

$\mathbf{F} = -\nabla(V(\mathbf{r}))$ is the deterministic force, γ represents frictional loss and is equal to χm. The inverse of χ is the time scale for equilibration of the ghost particles with the atoms. The statistical properties of $\widetilde{\mathbf{F}}$ are now given by

$$\left\langle \widetilde{\mathbf{F}} \right\rangle = 0 \tag{2.36}$$

$$\left\langle \widetilde{\mathbf{F}}^2 \right\rangle = 3\gamma k_B T \tag{2.37}$$

where T is the temperature. In practise a random force is found by randomly sampling a uniform probability distribution using a standard computational technique and scaling according to the temperature and friction coefficient.

It was noted by Andersen [189] that the addition of stochastic moves to the equation of motion of the whole system could simulate the effect of a surrounding solvent driving a region of interest to a particular temperature. The deterministic terms of the Hamiltonian allow the system to move across a constant energy surface in phase space as the Newtonian equations of motion conserve energy. Each collision moves the system to another constant energy surface allowing exploration of trajectories with constant temperature, volume and particle number; the $[NVT]$ ensemble.

It is necessary that the frequency of the collisions be carefully chosen so as to ensure ergodicity. If the velocities are modified too frequently, the systems dynamics will be dominated by the effect of the heat bath, the net result of which is that the system will explore configurational space too slowly. Whereas if the particles collide too slowly, the system will not fully sample the canonical energy distribution. In both cases the validity of the ergodic hypothesis is threatened [162].

Written in an incremental form equation (2.35) becomes

$$m\, d\dot{\mathbf{r}} = \mathbf{F}\, dt - \gamma\, d\mathbf{r} + \widetilde{\mathbf{F}}\, dt \tag{2.38}$$

Since successive collisions are uncorrelated, the incremental change $d\,\dot{\mathbf{r}}(= \frac{\widetilde{\mathbf{F}} dt}{m})$ due to thermal agitation is an increment in a Weiner process and the system's position in phase space as a function of time is a Markov process [190]. That is to say the state of the system at $(t + dt)$ depends only on the state of the system at time t.

The Langevin thermostat, in general, represents the atomic system coupled to a heat bath which represents everything outside the system of interest with an assumed infinite heat capacity. This is shown schematically in Fig. (2.10). Caro and Victoria modelled the electrons as a heat bath, with the strength of the interaction given by electron-ion interactions [129]. The effect of interactions with the heat bath is again included via a frictional term in the atomic equation of motion which is directly proportional to velocity. However, unlike the Nose-Hoover thermostat, the atoms are now also subjected to a stochastic force in accordance with Einstein's fluctuation-dissipation theorem [191]. This force is described by a Gaussian distribution and allows energy to be exchanged between the bath and the ions until they are in thermal equilibrium. The balance of these two forces allows the temperature of the atoms to be maintained at a given average value. The dynamics described by (2.35) do not conserve the energy of the whole system since the heat bath is assumed to have an infinite heat capacity. In addition time reversibility is lost, as only information about the *moments* of $\widetilde{\mathbf{F}}$ are known. As a result the integration of the atomic equations of motion will now not be symplectic. However, since the exact Hamiltonian equations of motion for the Langevin thermostat do not conserve energy this condition will in any case be violated, as indeed it will be by any ensemble other than $[NVE]$. The collisional term on the right hand side of the Liouville equation (2.15) will not be zero as the atoms now undergo collisions with the ghost particles in the bath. Figure (2.11) shows the system temperature as a function of time for a range of coupling time scale.

It should be noted that while $\widetilde{\mathbf{F}}$ in (2.35) randomly samples a Gaussian distribution, the application of the Langevin thermostat on a computer is in fact only pseudo-random.

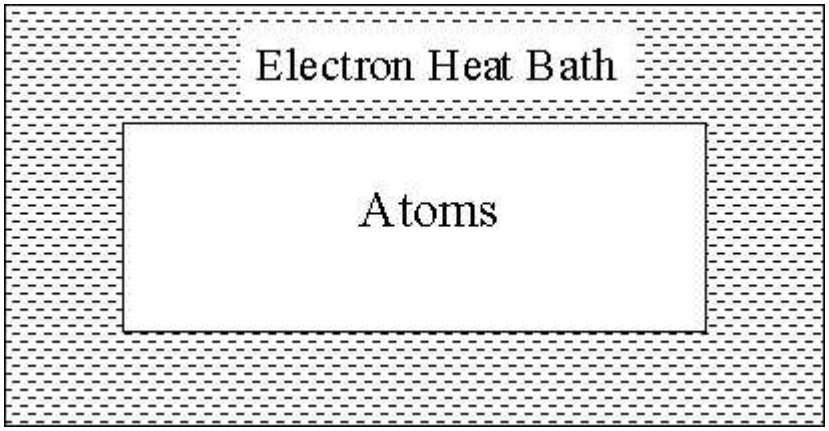

Figure 2.10: Thermodynamic coupling under Langevin thermostat.

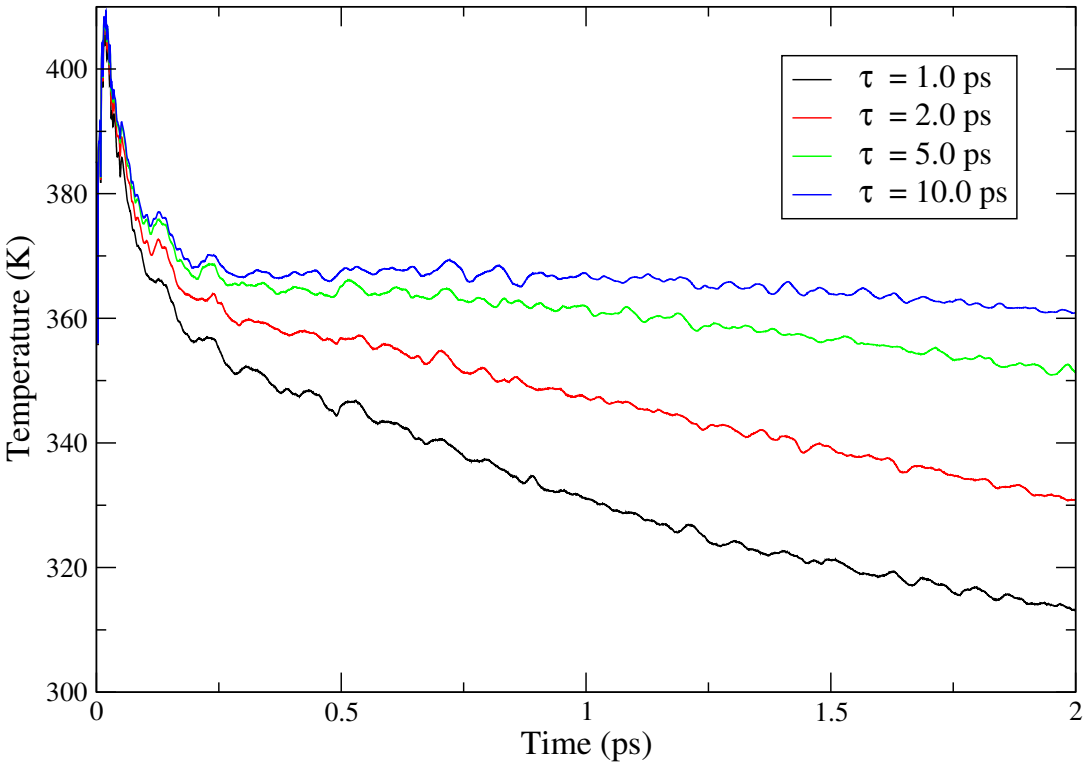

Figure 2.11: Average system temperature as a function of coupling time scale in a $2.5keV$ cascade using a Langevin thermostat.

The algorithm for random number generation on a computer requires a seed number, any particular value of which will produce the same sequence of random numbers with each implementation. Although this algorithm is highly chaotic, $\widetilde{\mathbf{F}}(t)$ is deterministic with respect to this number. As a result, any simulation which uses the same seed and initial conditions and the same computer architecture will be identical when repeated.

2.5 Interatomic Potentials

The interatomic potential in (2.14) represents the essential physics of an MD simulation. The accurate reproduction of bulk cohesion from the quantum mechanical behaviour of the electrons is the hardest part of the simulation of a system of atoms. As discussed in section 2.2 there is a range of methods to model the electrons and thus describe the cohesion between atoms, as always there is a trade off between accuracy of the model and the time scale or length scale that can practically be simulated [192].

One of the simplest realistic interatomic potential is the Lennard-Jones (LJ) 6-12 potential which has the following form

$$V^{LJ}(\mathbf{r}) = 4\epsilon((\sigma/r)^{-12} - (\sigma/r)^{-6}) \tag{2.39}$$

The LJ potential is an example of an empirical potential; σ and ϵ must be fitted to experimental data rather than being calculated from first principles. It is mostly only suitable for modelling organic molecules and systems of inert gases with no electrons available for bonding due to its simplicity, however it demonstrates the salient features a potential should reproduce.

- At short distances the potential form gives a strongly repulsive force due to the close approach of ion cores. This causes the electron clouds of the approaching atoms to begin to overlap giving rise to an increase in the system energy by the Pauli exclusion principle and so a strong repulsive force. This is assumed to be $\propto (r)^{-12}$ due to the computational efficiency of its calculation as the square of $(r)^{-6}$.

- There is long ranged attraction, in this case due to van der Waals forces, accounting for cohesion in purely covalent and inert systems such as the noble gases. The form of this can be argued for dispersion interactions and fluctuations in the electron clouds present in all systems regardless of the nature of the bonding. However the form of this potential does not describe other types of bonding such as in ionic or metallic systems.

- At intermediate distances there is an approximately harmonic potential well centred at the equilibrium position at $r = 1.122\sigma$. At thermal equilibrium, and at low temperatures, the atoms will oscillate about this position, due to thermal fluctuations, with energy $\approx k_B T$.

2.5.1 Pair Potentials

In general interatomic potentials feature terms depending on the co-ordinates of atom pairs, triplets, higher order terms and any external potential with the following form [162]

$$V = \nu_{ext}(\mathbf{r_i}) + \sum_i \sum_{i>j} \nu_2(\mathbf{r_i}, \mathbf{r_j}) + \sum_i \sum_{j>i} \sum_{k>j>i} \nu_3(\mathbf{r_i}, \mathbf{r_j}, \mathbf{r_k}) + \dots \tag{2.40}$$

Truncation of terms above ν_4 is usually necessary for practical application on a computer. These extra terms are included using an effective pair potential or sometimes by including bond angle or dihedral angle terms.

$$V = \sum_i \nu_1(\mathbf{r_i}) + \sum_i \sum_{i>j} \nu_{eff}(\mathbf{r_i}, \mathbf{r_j}) \tag{2.41}$$

This approximation ignores many body effects. The force between atom i and j is now independent of the position of atom k which is unrealistic in some systems.

The shortcomings of this approximation can be seen from examination of various material parameters [193].

System	$\frac{E_v}{E_c}$	$\frac{C_{12}}{C_{44}}$
Cu	0.33	1.5
Ag	0.36	1.9
Pt	0.26	3.3
Au	0.25	3.7
LJ	$\approx$1	1

Table 2.1: Table showing material parameters calculated experimentally in comparison to those predicted by the Lennard Jones potential for 4 different metals.

Here E_c is the cohesive energy, E_v is the vacancy formation energy and C_{12} and C_{44} are elastic constants. Simple two body models predict values for the ratio of cohesive energies to thermal energies roughly a factor of 3 below those observed experimentally or via ab-initio calculations. Thus the pairwise potential model is unable to account for the extra cohesion present in metals. The Cauchy relation between elastic constants $C_{12} = C_{44}$ can be proved analytically for two body systems, but deviations are commonly observed in metals. While this dichotomy can be resolved by adding a term dependent on the macroscopic volume to the pair potential total energy, this is unsatisfactory. In particular the bulk modulus predicted by the methods of homogeneous deformation and long waves will differ. Furthermore, stacking fault energies, surface structure and relaxation properties are not correctly reproduced [194].

In contrast embedded atom potentials allow the calculation of atomic forces from the local electron density with a contribution from each neighbouring atom. However, since the individual contributions to the electron sea are assumed to superimpose linearly,

they may be treated in a similar way to a pair potential within a simulation. Also, the contribution to the electron sea allows the band structure of the atomic species to enter on a phenomenological level [195].

2.5.2 Embedded Atom Potentials

The Finnis-Sinclair [196] (FS) and Sutton-Chen [197] (SC) potentials were formulated to describe the transition metals and the ten fcc elemental metals respectively, and belong to the class of embedded atom method (EAM) potentials.

EAM potentials were initially proposed [198] and subsequently developed [199] by Daw *et al.* This approach draws on density functional theory in its quasi-atom approach [200] in which an impurity ion plus its electron screening cloud, together considered as one unit, are embedded into the host electron cloud. EAM potentials also draw on the effective-medium theory of Norskov [201] which proposed that the inhomogeneous host density is replaced with a homogeneous electron gas with an effective density equal to that at the impurity site. The effect of the impurity's presence is approximated using first order perturbation theory. Such a formalism is seen to approximate experimental values of binding energies well [202].

In the EAM the energy to embed an atom in a lattice depends on the electronic density at that lattice site. The electron density is a linear superposition of the electronic densities of all background atoms. The cohesive term is described by a functional of this electron density at the atomic site I ($F[\rho_I]$) while the repulsive part is modelled by a pair potential form. The embedding functional is unique to the identity of the atom and independent of the source of the background density, allowing a large degree of transferability e.g. to alloy systems, while the contribution of background atoms to the local density is a measure of the degree of delocalisation. Thus in the EAM the total energy is of the form

$$E^{EAM} = \sum_i F_i[\rho_{h,i}] + \frac{1}{2}\sum_i \sum_{j \neq i} \phi_{ij}(r_{ij}) \tag{2.42}$$

Here $\rho_{h,i}$ is the host electron density due to atom i and ϕ_{ij} is the pairwise potential between atoms i and j.

By making the assumption that the electron density for the whole quasi-atom is constant, the so called uniform density approximation, a degree of universality is achieved since the quasi-atom energy depends only on the host electron density regardless of its source.

EAM potentials are in the class of empirical potentials, as the variables in the models must be parameterized in terms of material properties [203]. There is no fixed proce-

dure for doing this however, as some fitting schemes will capture some properties well and not others. Mishin and co-workers have attempted to construct a database and consistent methodology for fitting interatomic potentials for monatomic metals [204]. They suggested compiling both experimental and many ab-initio data from various crystalline phases for fitting, weighting bulk properties more than surface properties. By examining the root mean square difference between desired and calculated properties derived from the potential, the data available can be split into that used for fitting and that used for testing. As long as this difference decreases, more fitting parameters should be used, but if no further accuracy is gained the use of extra parameters for fitting should be avoided. The advantage of using ab-initio data over experimental data is that ab-initio data can sample large regions of phase space not acessible in experiment and so increase the degree of transferability of the potential between diverse systems and conditions.

2.5.2.1 Finnis-Sinclair Potentials

The Finnis-Sinclair (FS) potentials were proposed to model the cohesion in transition metals [196]. In this case the embedding functional is proportional to the square root of the co-ordination number motivated by the second moment approximation of the tight binding model in which the cohesive energy of an atom scales with the square root of its atomic co-ordination number. In the tight binding model electronic wavefunctions are based on atomic sites and fall away rapidly. Cohesion is attributed to the overlap of these wavefunctions. Since the band energy term can be written in terms of the density of states, cohesion can be interpreted in terms of the form of this function. This function can be of any form provided it has the required moments, although it is often assumed to be Gaussian-like [205]. The zeroth moment represents normalisation (transition metal d bands are normalised to 10), and the first moment fixes the mean energy and the second moment represents the bandwidth of the local density.

This leads to a real space second moment approximation of the form

$$E^{FS} = \overbrace{\frac{1}{2}\sum\sum_{i\neq j}\phi(r_{ij})}^{U_{pair}} - \overbrace{c\sum_{i}\sqrt{\rho_i}}^{U_{band}} \tag{2.43}$$

FS potentials are empirical potentials. The above model must be parameterised by fitting the cohesive energy, equilibrium volume and all three independent elastic moduli for the bcc transition metals. A typical form of the embedding functional in U_{band} appropriate for the [100] surface, restricting the ranges of each term to first and second neighbours, was found by Finnis and Sinclair to be

$$f = (8\phi_1 + 6\phi_2)^{1/2} \tag{2.44}$$

Where ϕ_1 and ϕ_2 are given in terms of the lattice parameter a as

$$\phi_1 = \phi(\sqrt{3a/2}) \tag{2.45}$$

$$\phi_2 = \phi(a) \tag{2.46}$$

There are several different interpretations of the FS formalism. Within the tight-binding picture U_{band} is the band energy, which is bonding in nature, while U_{pair} represents core-core repulsion and so is repulsive in character. Within the embedded atom picture, ρ_i is the local electronic density at site i constructed by linear superposition of neighbouring atomic charge densities. Further, ρ_i may be interpreted as a measure of the local density of atomic sites and so U_{bond} is a volume dependent energy term.

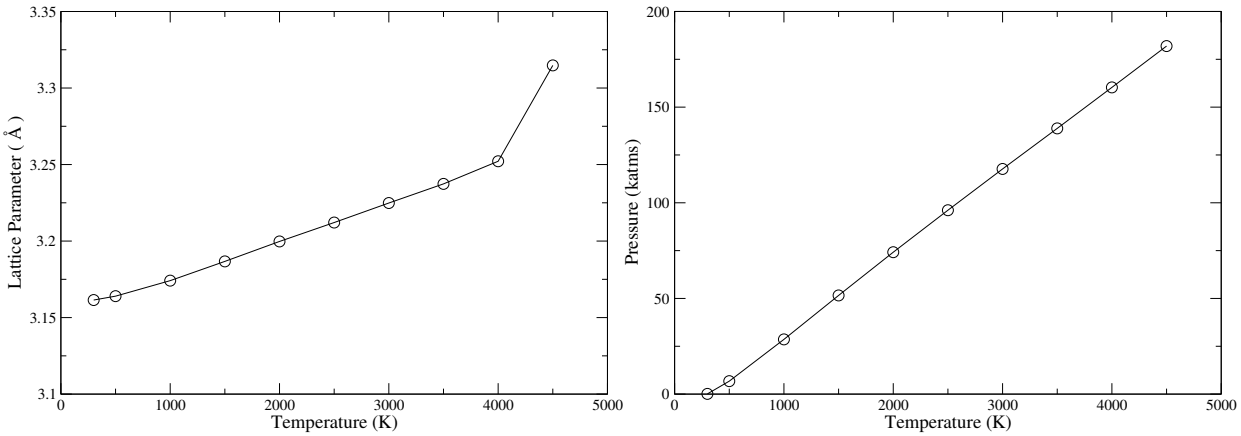

Figure 2.12: Pressure and volume as a function of temperature using the FS tungsten potential.

Figure (2.12) shows the thermal properties of W using a Finnis-Sinclair potential. The left hand figure shows heating at [NPT] under which the volume of the cell may fluctuate. The right hand figure demonstrates heating at [NVT] allowing fluctuations in pressure. Melting is seen in the [NPT] simulation at $\approx 4000K$ (Compared to the experimental value of 3695K [206]) accompanied by a rapid increase in volume. The [NVT] simulations shows a monotonic increase in pressure with temperature.

2.5.2.2 Sutton-Chen Potentials

The Sutton-Chen potentials [197] were proposed to describe metallic clusters which interact via van der Waals forces at large separations. They proposed a potential of the

form

$$E^{SC} = \epsilon \left[\frac{1}{2} \sum \sum_{i \neq j} \phi(r_{ij}) - c \sum_{i} \sqrt{\rho_i} \right] \tag{2.47}$$

Where the repulsive potential is given by

$$\phi(r_{ij}) = \left(\frac{a}{r_{ij}} \right)^n \tag{2.48}$$

and the density at atomic site i is given by

$$\rho_i = \sum_{i \neq j} \left(\frac{a}{r_{ij}} \right)^m \tag{2.49}$$

Where ϵ and a are charateristic energy scales and length scales respectively and n and m are integers with $n > m$. Choosing $m = 6$ gives rise to an attractive van der Waals tail suitable for describing surface relaxation.

2.5.3 Zeigler, Biersack and Littmark (ZBL) Potential

As noted by Sutton and Chen, in shock situations the potential may need to be amended at high energies when the ions approach each other very closely. This is of particular interest in high energy displacement cascade simulations as potentials, which are often fitted to properties derived at equilibrium, must be transferable to situations far from equilibrium. In this case the ions scatter elastically from each other and the interaction is essentially Coulombic, with the electron clouds acting to screen the nuclear repulsion. Ziegler et al suggested a potential with the following form [207]

$$V(r) = \frac{1}{4\pi\epsilon_o} \frac{Z_1 Z_2}{r} \varphi(r) \tag{2.50}$$

Where $\varphi(r)$ is a screening function which tends to 1 as r tends to 0 and Z_1 and Z_2 are the nuclear charges. (2.50) is fitted to experimental nuclear stopping data and $\varphi(r)$ has been calculated for a large number of atom pairs [208]. It is common for a potential function to be 'stiffened' by interpolating between the the equilibrium potential function and the ZBL form at short distances. The manner in which the potential is stiffened at intermediate interatomic distances has been found to significantly affect cascade development in MD simulations of iron [51]. Eckstein et al also found differences in the sputtering yield and reflection coefficient in Si between three different repulsive potentials (including ZBL) in simulations using a modified form of the TRIM code [209].

A ratio of interest is S/R where R is defined as the interatomic distance at which the interaction energy is equal to $30eV$ and S is the stiffness, the gradient at that point. A high value of this ratio describes a stiff potential, leading to an increase in the number of replacement collision sequences, whereas a low value leads to a dense cascade and long

recombination times [210]. Nordlund et al concluded that the damage production is more sensitive to the exact form of the repulsive potential in simple metals when atomic dynamics are strongly ballistic as expected [211]. The accuracy of the form of the repulsive part of the potential was also improved from the ZBL form by using various ab-initio methods.

2.5.4 α -Fe and Fe Alloy Potentials

$\alpha - Fe$, iron in its most common ferritic, bcc phase, and its alloys are of great importance in modelling radiation damage due to low rate of neutron induced activation when alloyed and low swelling under irradiation[3, 70, 6] (see section (1.2)). Consequently much work has been done to develop suitable potentials for their simulation via MD. Becquart et al [90] compared four different interatomic potentials for iron.

- Derived by Harrison et al [212] and stiffened for use in cascades by Turbatte [213].
- Derived by Haftel et al [214] and stiffened by Vascon [215].
- Derived by Simonelli et al [216] and stiffened by Raulot [217].
- Derived by Finnis et al [196] and stiffened by Calder et al [218].

The melting temperature, structural stability and displacement energies were examined and cascade simulations performed with each. It was concluded that the choice of potential sensitively affected the primary damage state and the form developed by Simonelli et al was determined to be most suitable, due to the accurate thermal behaviour and defect efficiency. However Malerba later found that the defect production efficiency in each case converged with increasing energy [51].

While the different approaches each predict vacancy migration and formation energies, melting temperatures and structural stabilities with varying degrees of accuracy; the choice of potential must consider, and be fully tested under, the circumstances in which it will be used to determine whether it will be suitable [52]. However each potential function, in particular the manner in which it is stiffened and the value of defect mobility it produces, will affect the cascade morphology and defect clustering.

Low activation martensitic steels are formed by alloying iron with low concentrations of chromium and tungsten. Difficulties persist in formulating robust potentials for alloy systems as there is less data, both ab-initio and experimental, available for parameterisation and the bonding is necessarily more complex and difficult to capture with potentials based on simple models. Further, very small percentage concentrations of an alloying element can have a significant effect on defect energies. To describe an alloy system using

an EAM type method, a pair potential is required for each element and a cross potential for each combination of these elements as well as an embedding functional for each element.

Such a potential has been developed by fitting the mixed potential to ab-initio calculations of mixing enthalpies and suceeded in producing the correct ordering of $< 110 >$ and $< 111 >$ interstitial energies by relaxing conditions on the pressure-volume relation at short interatomic separations. Cascade simulations using low concentrations of Cr showed that the presence of chromium does not affect the collisional stage of a cascade, due to the similar atomic masses, but it does affect residual damage configurations. This was ascribed to more stable Fe-Cr and Cr-Cr dumbell interstitial formation, which persist during prolonged cascade cooling and also hinder recombination of Fe defects [219, 220, 221].

2.5.5 Dudarev bcc Metal Potential

Derlet and co-workers have addressed the problem of describing the low observed values of defect activation energies in the non-magnetic bcc metals and the correct ordering of the $\langle 111 \rangle$ and $\langle 110 \rangle$ crowdion configurations. From examination of ab-initio calculations of the density of states, it was concluded that the use of a FS 2nd moment approximation formalism was sufficient to capture the relevant bonding mechanism. Using the usual physical properties; cohesive energy, lattice constant, elastic constants, vacancy formation energies and interstitial defect energies, as well as the zero temperature isotropic thermal expansion coefficient, potentials were constructed for vanadium, niobium, tantalum, molybdenum and tungsten. The potentials were later used to investigate the magneto-elastic fields of dislocation loops and the thermally activated migration of point defects [222].

Despite having the strength of the correct description of defect energies, the Dudarev formalism has some flaws. In particular the thermal properties are unphysical in places as can be seen from Figs. (2.14) and (2.13). As W is heated at constant pressure the cell is seen to contract slightly before expanding and finally melting at $\approx 4000K$. Likewise, when heated at constant volume, negative pressures are observed up to $\approx 3000K$. This unphysical behaviour renders the potential unsuitable for the simulation of cascades since the expansion of the cascade core affects the transport of interstitial atoms, which is strongly ballistic and depends strongly on and the final damage state. Also, since the temperature in the cell will at times be highly inhomogeneous, some parts of the cell will expand while others contract.

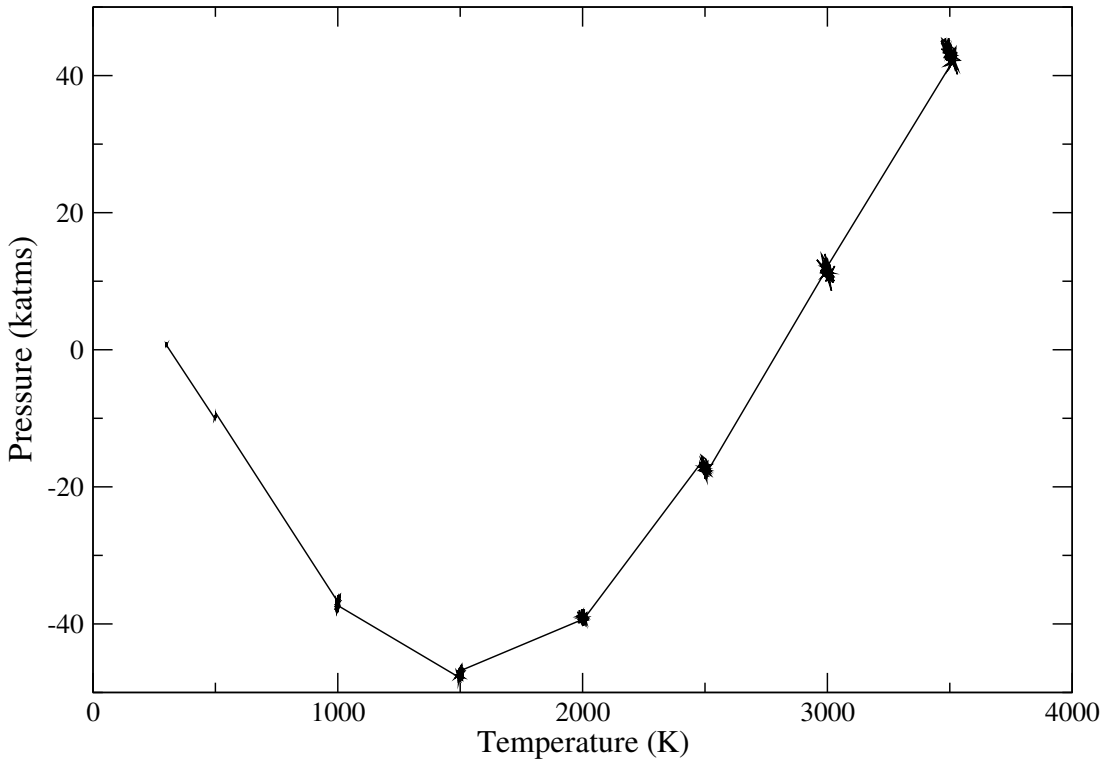

Figure 2.13: Pressure as a function of temperature using the Dudarev tungsten potential.

2.5.6 Dudarev Magnetic Fe Potential

A successful potential model is one which is able to account for many body effects without including the higher order terms present in (2.40). It is therefore necessary to include the effects of magnetism in ferromagnetic materials such as iron and its alloys on a phenomenological level [70].

A "magnetic" potential suitable for MD simulations of iron has been developed by Dudarev et al based on the EAM [223]. This potential adds a term derived from the Stoner and Ginzburg-Landau (G-L) models to the embedding functional of FS.

The effect of magnetism is to include an extra degree of freedom for each particle. In the case of iron, which has two spin eigenvalues, there are now two energy surfaces corresponding to a magnetised and a non-magnetised state for each configuration of atoms below the Curie temperature. The G-L model of phase transitions describes this symmetry breaking.

The G-L theory leads to an embedding functional given by

$$F[\rho] = -A\sqrt{\rho} - B\frac{\left(\sqrt{\rho_c} - \sqrt{\rho}\right)^2}{\left(\nu + \sqrt{\rho_c} - \sqrt{\rho}\right)}\Theta(\rho_c - \rho) \tag{2.51}$$

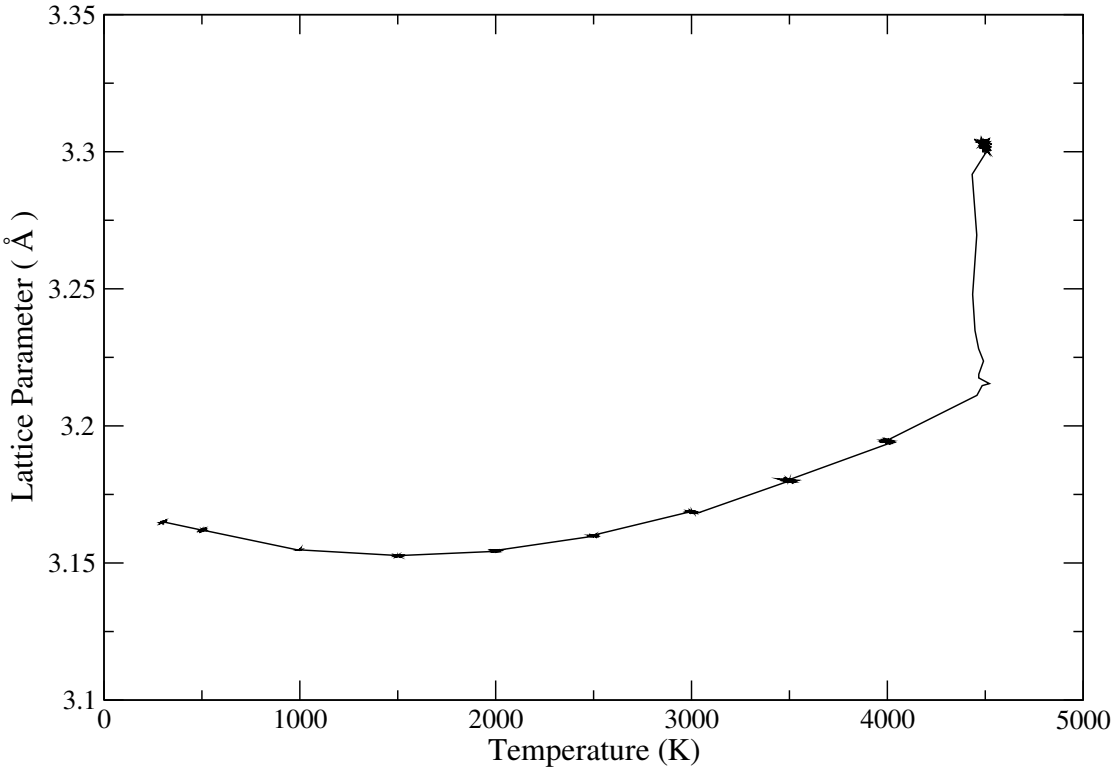

Figure 2.14: Lattice parameter as a function of temperature using the Dudarev tungsten potential.

Here A and B are constants, ρ_c is the critical value of effective density at which magnetism vanishes, ν is a small positive constant and Θ is the Heaviside function. The potential function is parameterised according to case study I in [223] and the interpolation function according to appendix I.

The forms of both the pairwise repulsive potential $V(r_{ij})$, and the pairwise density radial function $f(r_{ij})$ which describes the contribution to the electronic density from each atom are fitted using ab-initio values of the bulk cohesive energy, lattice constants, defect energies and elastic constants of the bcc and fcc magnetic and non-magnetic phases and the temperature that this transition takes place at. Magnetic effects give rise to an important contribution to the bulk cohesive energy, this contribution affects different interstitial energies to different degrees. Consequently the Dudarev potential has the advantage over other bcc iron potentials that the $\langle 111 \rangle$ interstitial configuration is correctly predicted as having a lower energy than the $\langle 110 \rangle$ configuration. [51].

Finally (2.51) is modified to give the ZBL form at interatomic distances below $r_1 = 1.8\,\dot{A}$ with an interpolation function beetween r_1 and $r_2 = 2.0\,\dot{A}$. These values were chosen to ensure that the regime of $10 - 100\,eV$, which corresponds to the threshold displacement energy of iron, is governed by the physical potential form rather than an arbitrary inter-

polation function. This makes the potential particularly suited to simulating high energy events.

Fig. (2.15) shows the behaviour of the lattice parameter as a function of temperature during an $[NPT]$ simulation, a heating timescale of $1.0\,ps$ was used and the lattice allowed to equilibrate for $15\,ps$ at each temperature interval. It can be seen that there are two phase transitions, in both cases accompanied by a rapid change in temperature and volume. The lower at $\approx 1500\,K$ is due to the magnetically driven structural phase transition from a bcc to an fcc structure. The lattice parameter in the plot was calculated from the cell volume, which is seen to decrease due to lower volume per atom in the fcc phase, and the number of unit cells assuming a bcc structure. If, however an *fcc* structure is assumed above the transition temperature, the corresponding lattice parameter is seen to increase to $\approx 3.7\,\mathring{A}$. This is to be compared to the fitted value of $3.49\,\mathring{A}$ in the magnetic fcc phase.

The transition at $\approx 2500\,K$ is simple melting accompanied by a drop in temperature and volume as the atomic structure changes before the volume increases rapidly in the liquid phase. At constant volume no phase transition is observed as the necessary expansion is not permitted. The cell size used was 8192 atoms corresponding to $(16)^3$ unit cells.

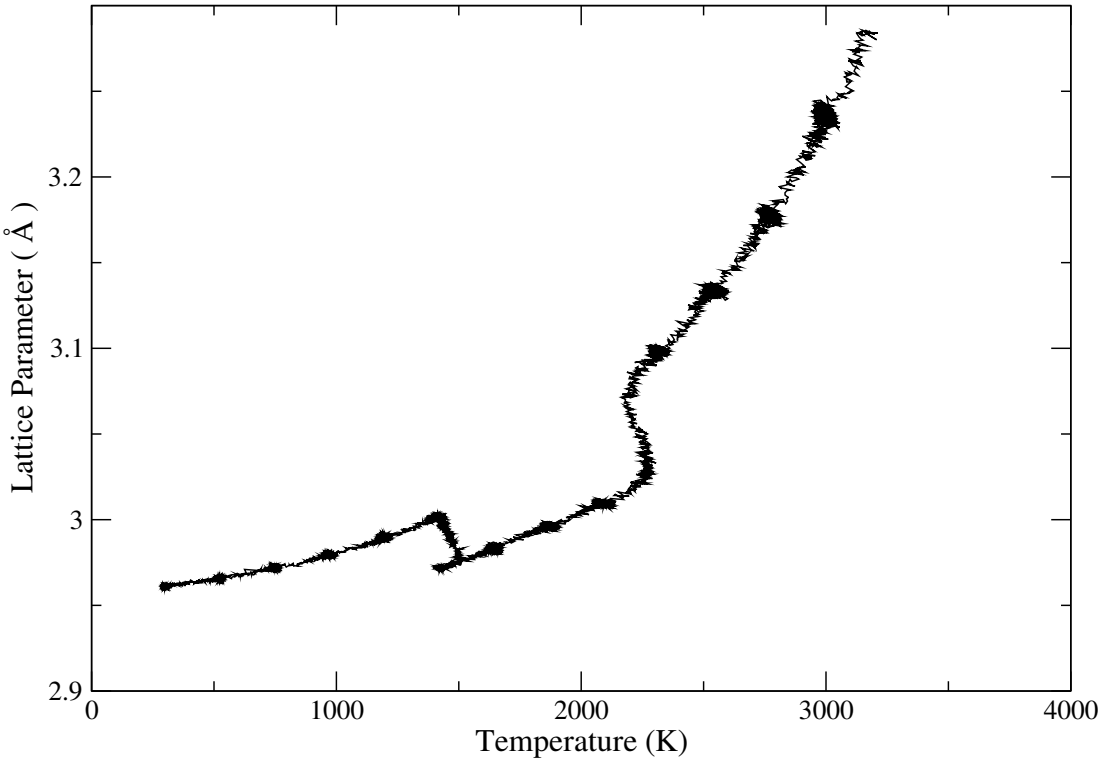

Figure 2.15: Lattice parameter as a function of temperature using the Dudarev magentic potential in Fe.

Although the bcc-fcc transition is observed under slow heating so that the atoms may sample the reaction pathways to the fcc structure, it is unlikley that such a transition will be observed in a cascade. In a cascade, a liquid core is formed surrounded by solid metal. As the melt cools there will always exist a boundary between the two phases with a large energy cost causing the melt to preferentially revert to the low temperature phase. The presence of displacive phase transitions have been postulated to provide a low energy pathway to defect formation during heavy ion irradiation [224], however the bcc-fcc phase transition observed here is not an activated process. The presence of an activation energy is normally required to cause violent atomic displacements to be quenched into the lattice. Also the lattice heating in a cascade is not only highly inhomogeneous but also very swift; heating with a thermostat time scale of $1.0ps$ captures the bcc-fcc phase transition, but faster heating with a time scale of $0.05ps$ does not, suggesting that the atoms need a finite amount of time to undergo the transition.

Chapter 3

Methodology

In this section our model for a modified Langevin thermostat is presented, which couples a continuum model for the electrons, evolving according to a heat diffusion equation, to an MD simulation imposing a heat bath with an inhomogeneous temperature distribution. The method by which these two models are coupled together, and its physical interpretation are discussed together with the technical details of energy conservation and convergence of numerical integration routines. Several physical parameters enter into our model; the choice of values and, where appropriate, functional forms of these are outlined.

3.1 Inhomogeneous Langevin Thermostat

In the past attempts to include electronic effects using a Langevin approach have considered hot atoms being damped to a constant electronic temperature. Although this includes the frictional damping of atomic motion by electron-phonon coupling and its subsequent feedback, it neglects any heating of the electrons and the spatial temperature distribution. This is highly inhomogeneous in the early stages of a displacement cascade or an ion track. In contrast two-temperature models describe the exchange of energy between the two sub-systems but fail to capture atomic information. The description of our model appears in [225].

In order to model the thermal properties of the electrons we introduce a hybrid technique; an atomistic simulation using Langevin dynamics is coupled to an open continuum model for the electronic energy in such a way that energy is conserved between the two subsystems. This is done by coupling the atoms to the electrons in the vicinity of the collision event. The electrons are in turn coupled to the infinite heat capacity bath representing the rest of the lattice, allowing energy to be removed from the simulation. The atoms are still coupled to a perfect heat bath, though now indirectly. The effect of electron stopping is included as a one way energy transfer process from highly energetic atoms above a cut off velocity. The exchange of energy can be seen schematically in Fig. (3.1)

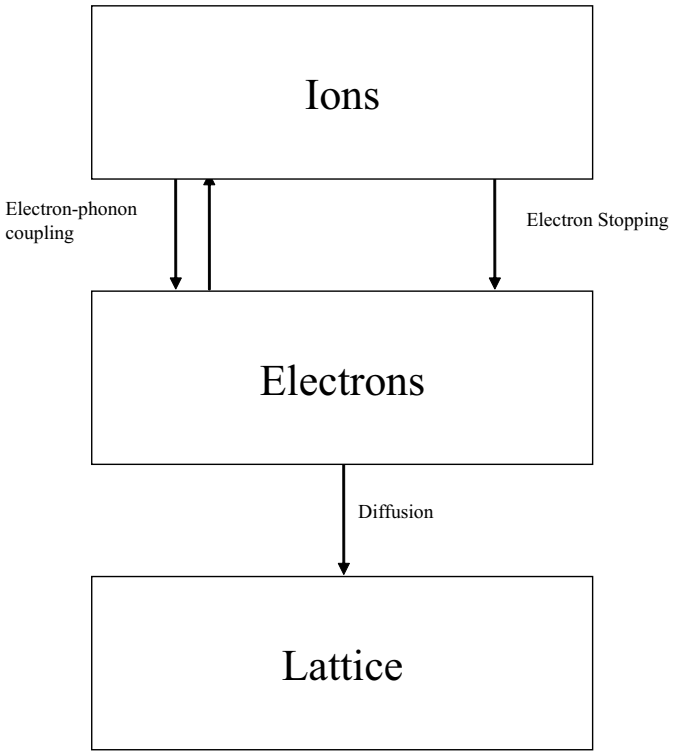

Figure 3.1: Schematic of energy exchange for inhomogeneous Langevin thermostat.

In the two temperature model cylindrical symmetry of the elevated temperature along the ion track axis is often assumed and writing in general terms for an event which may deposit energy into both the electrons and atoms the temperature evolution is described by;

$$C_e(T_e)\frac{\partial T_e}{\partial t} = \nabla.(\kappa_e(\nabla T_e)) - g[T_e - T_a] + A(r,t) \tag{3.1}$$

$$C_a(T_a)\frac{\partial T_a}{\partial t} = \nabla.(\kappa_a(\nabla T_a)) + g[T_e - Ta] + B(r,t) \tag{3.2}$$

Here T_e, T_a, C_e, C_a, κ_e, κ_a are the temperatures, specific heats and thermal conductivities of the electronic and atomic subsystems respectively. g accounts for heat transfer due to electron-ion interactions and $A(r,t)$ and $B(r,t)$ are source terms representing the energy deposited due to the incident particle. In our model, the evolution of the atomic subsystem as described by (3.2) is replaced by an explicit atomistic simulation.

Within our model the electronic subsystem evolves according to

$$C_e\frac{\partial T_e(x,y,z)}{\partial t} = \overbrace{\nabla(\kappa_e\nabla T_e(x,y,z))}^{1} - \overbrace{g_1[T_e(x,y,z) - T_a(x,y,z)]}^{2} + \overbrace{g_2T_a^{'}(x,y,z)}^{3} \tag{3.3}$$

Here g_1 and g_2 are coefficients related to the strength of the electron-phonon interaction and electronic stopping respectively. $T_a^{'}$ has the units of temperature and is derived from a subset of the atoms and is defined below.

(1) simply represents the diffusion of heat through the electron subsystem. (2) is the standard electron-phonon coupling term from the two temperature model and is a function of the local temperature difference, as it represents local thermal equilibration of the electronic and atomic subsystems. The sign of (2) determines whether the electrons act as a heat source or heat sink and g_1/C_e determines the time scale on which equilibrium is reached.(3) is solely a function of $T_a^{'}(x, y, z)$ (defined below) and is related to the electronic stopping power.

The atomic motion is described by the following Langevin type equation after Caro and Victoria [129]

$$m_i \ddot{\mathbf{r}}_i = \overbrace{\mathbf{F_i}(t)}^{1} - \overbrace{\gamma \dot{\mathbf{r}}_\mathbf{i}}^{2} + \overbrace{\widetilde{\mathbf{F}}}^{3} \tag{3.4}$$

Here γ is given by

$$\gamma = \gamma_1 + \gamma_2 \tag{3.5}$$

γ_1 and γ_2 represent the strength of the frictional forces due to electron-phonon interactions and electron stopping respectively.

(1) represents the usual deterministic force due to the interatomic potential in MD ($= -\nabla V(\mathbf{r_i})$). (2) is a frictional force felt by the atoms moving through the background electronic medium, losing energy to the electrons, while (3) is a stochastic force which returns energy from the electrons to the atoms.

The frictional and stochastic forces can be seen to be intimately related. Given that the atoms interact energetically with the electrons with which they are embedded, this interaction is assumed to be manifested by Brownian collisions at a rate related to the strength of the electron-phonon coupling strength. If an atom has a non-zero velocity the net force due to the electrons will no longer be Brownian distributed in the frame of the atom. As the atom moves through the medium it will experience stronger collisions anti-parallel to its velocity than parallel to the velocity, simply by relativity of the two particles velocities. Thus the frictional force can be seen to originate from the random thermal agitation in agreement with the fluctuation-dissipation theorem. When an atom has a very large velocity, (2)>(3) and its overall energy is reduced. However for an atom with a small velocity (2)<(3) and thus the overall energy of the atoms is increased. The definition of an atom with a 'large' or 'small' velocity is relative to the temperature of the

electronic system and determines the size of thermal movement. In this way the average temperature of an ensemble of atoms can be maintained at a given value. The strength of the electron-phonon interaction determines both the magnitude of the frictional force and the strength of the stochastic collisions (although the magnitude of the stochastic forces are also proportional to the temperature of the bath); a stronger interaction allows thermostating on a shorter timescale.

The interaction described above is due to electron-phonon coupling which allows an exchange of energy. In contrast, electronic stopping represents a one way transfer of energy from the atoms to the electrons. The electron stopping interaction is unrelated to the local temperature difference. Atoms in the stopping regime simply lose energy to the electrons at a constant rate given by the electronic stopping friction coefficient. This energy loss is not fed back directly to the atoms as with the electron-phonon coupling. Both coupling and stopping make a contribution to the frictional term (2).

In order to couple the continuum model for the electrons to the MD simulation a grid is superimposed on the MD cell. The atoms within each cell of this grid are used to define a spatially varying atomic temperature across the MD cell, and the same grid is also used as the mesh for the finite-difference solution of the electronic heat diffusion equation. In each cell, the energy lost by the atoms is gained in the electronic system via the coupling and stopping terms in (3.3). Likewise energy lost from the electrons is gained by the atoms via the stochastic term in (3.4).

In contrast to a homogeneous Langevin thermostat, the atoms must now reach *local* equilibrium with the electrons which are in turn thermostatted to the ambient temperature. This is included by fixing the electronic temperature at the ambient level on the boundary of the electronic simulation cell, which is much larger than the MD cell. This is shown schematically in Fig. (3.2). The electronic and atomic subsystems will eventually both be driven to the ambient temperature, but the time for this to happen will depend on the respective initial temperatures and thermal properties of the subsystems. The fact that energy can only be removed through the electron subsystem is justified by the much slower atomic heat diffusion, thus the atomic thermal excitation will be contained by the length scale of the simulation cell. Here the lattice represents the material far from the cascade region to which energy is lost.

The electron system was extended beyond the size of the atomic system (The atomic system corresponded to $9\Delta x$ cells in each dimension in the atomic system and the electron system $100\Delta x$, where Δx is the size of a temperature cell) to ensure that the boundary conditions on T_e did not drive the temperature of the system down unrealistically quickly. Our model assumes that energy can only be removed through the electronic system due

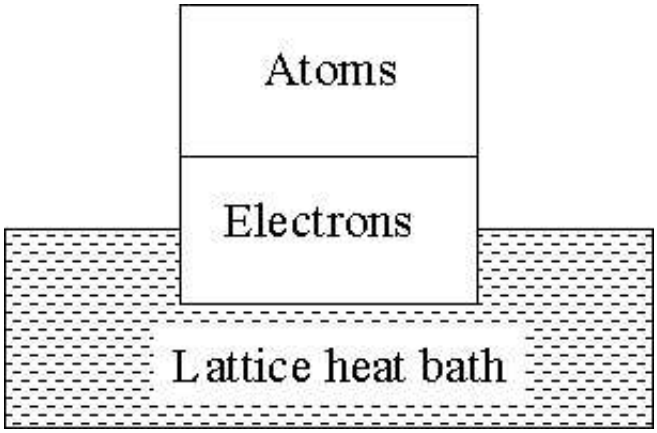

Figure 3.2: Thermodynamic coupling under the inhomogeneous Langevin thermostat.

to a higher thermal conductivity in comparison to the atoms, in reality the electronic temperature would be expected to relax to the ambient level over an infinite length scale. Fixing the temperature at the ambient level on the edge of the MD cell assumes that T_e can be assumed to have relaxed to $300K$ at this point, whereas the temperature will remain elevated much further from the collision event. Thus the atomic system is effectively embedded in a larger electron sea. Since the electron system is modelled as a continuum, this represents only a small increase in computational cost. Fig. (3.3) shows a schematic of the coupled systems with the number of cells reduced for clarity. This allows a diffusive profile to be set up over a much larger distance than the length scale of the MD cell. Periodic boundary conditions were used in the MD cell.

The boundary conditions used to solve (3.3) are given by

$$\begin{aligned} T_e(0,y,z) &= T_e(L,y,z) = T_e^{ambient} \\ T_e(x,0,z) &= T_e(x,L,z) = T_e^{ambient} \\ T_e(x,y,0) &= T_e(x,y,L) = T_e^{ambient} \end{aligned} \tag{3.6}$$

Where $T_e^{ambient}$ is the temperature of the surrounding lattice away from the collision event to which the whole system is driven once local thermal equilibrium has been established (assumed to be $300K$ in our model) and L is the length of the cubic electron system.

3.2 Energy Conservation

The atomistic and continuum models are coupled by discretising the spatial variation of the atomic temperatures as follows; each subsystem is divided into a series of equally sized cubic temperature cells with a size that varied in the range $(15.5 - 25.1\mathring{A})$ across

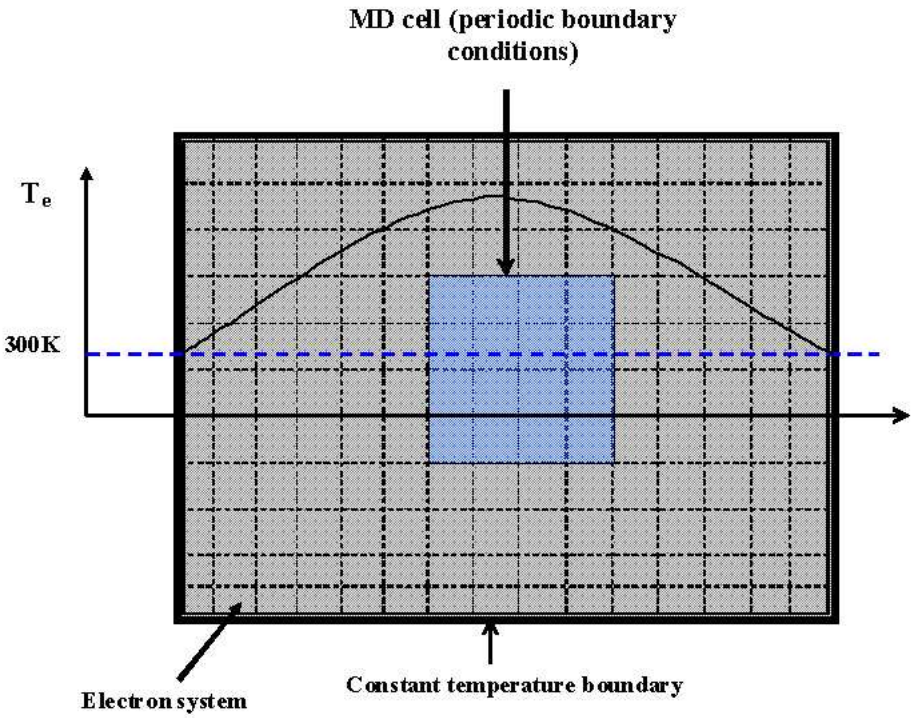

Figure 3.3: 1-D Schematic of simulation cell.

the range of systems considered, corresponding to an occupation of $(10^2 - 10^3)$ atoms. The electronic temperature is assumed to be constant in these cells while a temperature is defined for the atoms for each cell.

The heat diffusion equation is solved numerically and iterated at each MD timestep Δt. At each such timestep the electronic energy gain ΔE_{eg} in (3.3) of each temperature cell of volume ΔV is

$$\Delta E_{eg} = g_1 \, T_a \, \Delta V \, \Delta t + g_2 T_a^{'} \, \Delta V \, \Delta t \tag{3.7}$$

At each timestep in the MD system the frictional energy loss ΔE_i of atom i moving with a velocity $\dot{r}_i$ due to a friction force $\mathbf{F}_i^f$ ((2) in (3.4)) is given by

$$\Delta E_i = \mathbf{F}_i^f . \dot{\mathbf{r}}_i \, \Delta t = \gamma_i \, \dot{r}_i^2 \, \Delta t \tag{3.8}$$

Therefore the total frictional energy loss (ΔE_l) in each temperature cell J at each timestep is given by

$$\Delta E_l = \Delta t \sum_{i \in J} \gamma_i \dot{r}_i^2 = \Delta t \sum_{i \in J} \gamma_1 \dot{r}_i^2 + \Delta t \sum_{i' \in J} \gamma_2 \dot{r}_{i'}^2 \tag{3.9}$$

The sum in the final term is restricted; a distinction is now made between atoms with a velocity above the cut off velocity $\dot{r}_c$, which are in the electronic stopping regime. Only

these atoms make a contribution to the second term in (3.9). Equating ΔE_{eg} with ΔE_l we find

$$\sum_{i \in J} \gamma_1 \dot{r}_i^2 = g_1 \, T_a \, \Delta V \tag{3.10}$$

$$\sum_{i' \in J} \gamma_2 \dot{r}_{i'}^2 = g_2 \, T_a^{'} \, \Delta V \tag{3.11}$$

In order to conserve energy transferred between the two systems, two atomic temperatures for all the N atoms T_a and the subset of $N^{'}$ atoms in the electronic stopping regime $T_a^{'}$ must be defined

$$\frac{3}{2} k_B T_a = \frac{1}{N} \sum_{i \in J} \frac{1}{2} m \dot{r}_i^2 \tag{3.12}$$

$$\frac{3}{2} k_B T_a^{'} = \frac{1}{N'} \sum_{i' \in J} \frac{1}{2} m \dot{r}_{i'}^2 \tag{3.13}$$

However since the 'temperature' $T_a{'}$ may in theory be defined only by the energies of very few atoms which lie in the stopping regime of a given temperature cell, care must be taken when referring to this quantity as a statistically significant average.

This leads to the following equations for the electron-phonon coupling and stopping strengths

$$g_1 = \frac{3 \, N \, k_B \, \gamma_1}{\Delta V \, m} \tag{3.14}$$

$$g_2 = \frac{3 \, N^{'} \, k_B \, \gamma_2}{\Delta V \, m} \tag{3.15}$$

The quantity $\frac{3Nk_B}{\Delta V}$ represents the lattice heat capacity per unit volume while $(\frac{\gamma_\alpha}{m})$ is an inverse time scale for the interaction. Therefore both g_1 and g_2, can be considered as a time scale for the rate of 'energy flow' when multiplied by a temperature difference as in (3.3).

The stochastic force in the Langevin equation of motion gives rise to an energy gain in the atomic system ΔE_{ag} which can be calculated from stochastic calculus

$$\Delta E_{ag} = \Delta t \sum_{i \in J} \frac{\gamma_1 \, 3 \, k_B \, T_e}{m} = \frac{\Delta t \, N \, 3 \, k_B \, T_e \, \gamma_1}{m} \tag{3.16}$$

Equating the energy loss of the electronic system ($(-g_1 \, T_e(x,y,z))$ in (3.3)) to this energy gain in the atomic system due to the stochastic force

$$\Delta E_{ag} = \frac{\Delta t \, N \, 3 \, k_B \, T_e \, \gamma_1}{m} = \Delta t \Delta V g_1 T_e \tag{3.17}$$

This recovers (3.14). There is in practise some mismatch in energy between systems; the explicit scheme has accuracy of order $(\Delta t)^2$ whereas Verlet of the order $(\Delta t)^4$. This mismatch is further complicated by the stochastic term in (3.4) and any temperature dependence of the thermal parameters in (3.3). While such a small drift is significant for simulations close to equilibrium with small temperature gradients, in a situation far from equilibrium and over *ps* time scales it is negligible.

The first moment of $\widetilde{\mathbf{F}}$ in (3.4) is given by

$$\left\langle \widetilde{\mathbf{F}} \right\rangle = 0 \tag{3.18}$$

as for the standard Langevin formalism described in section 2.4.2. The second moment is now related to the electron-phonon friction coefficient γ_1 and the *local* electronic temperature $T_e(x, y, z)$. Therefore the strength of the random collisions depends on the local electronic temperature.

$$\left\langle \widetilde{\mathbf{F}}(t^{'})\widetilde{\mathbf{F}}(t) \right\rangle = 2\gamma_1 k_B T_e(x, y, z)\delta(t^{'} - t) \tag{3.19}$$

Thus the atomistic simulation is coupled to the continuum description of the electrons; the material parameters $g_1, g_2, \gamma_1, \gamma_2$ and temperatures $T_a, T_a^{'}, T_e$ can be related to the MD quantities $[\dot{r}_i], [m_i], \Delta V, \Delta t$. Unlike the action of a homogeneous thermostat which removes energy from the atoms uniformly over the lattice, the electrons now have explicit temperature dependent coupling to the atoms, while electron-phonon coupling is included in a unified picture and high energy ions lose energy via inelastic collisions.

3.3 Cascades

When ion energies are relatively low energy events, the majority of the energy is imparted to a single atom. This atom (the PKA) will, provided it has sufficient energy to leave it's lattice site, move through the lattice colliding with other bound lattice atoms and losing some energy to the electron subsystem. This was simulated by giving a velocity, corresponding to a given value of the PKA energy. The resulting atomic and electronic temperatures are followed and the final defect distribution investigated.

Plots of the surface temperature in the plane of the PKA velocity in the two subsystems can be seen below in a displacement cascade using a $10keV$ PKA; Fig. (3.4). Note that the scale has been fixed for meaningful comparison between different times, obscuring the peak core temperature in each system which is at $T_a \approx 2 \times 10^5 K$ and $T_e \approx 5 \times 10^3 K$. The length of the electronic system is around 10 times larger than the atomic MD cell. The difference in diffusivity can be seen between the two systems, the electronic temper-

ature profile settles into a very smooth curve immediately while the atomic temperatures do not, due to fluctuations in velocity and cell populations. The temperature rise in the atomic system is negligible on the boundary of the cell demonstrating that the initial excitation may be contained by the system size.

The number of temperature cells used to describe the whole simulation cell needs to be chosen carefully, a large number is required so that the size of each is small enough to ensure convergence of the explicit integration algorithm (see section (2.3)). However the description of macroscopic diffusion is based on an average distance travelled by an electron which scales as $\propto \sqrt{t}$. On a shorter length scale, between collisions, electron transport is ballistic and distance simply scales linearly with time ($\propto \nu t$ where ν is the velocity). In order that the assumption of Brownian type motion holds, there must be several collisions in the time taken for an electron to traverse one temperature cell. Written more formally

$$\Delta x \geq \lambda_{MFP} \tag{3.20}$$

The mean free path of an electron in Fe at $300K$ can be estimated from experimental thermal conductivity values [226] and elementary kinetic theory [105] as $6.6\mathring{A}$, and it decreases sharply at higher temperatures. This is to be compared to the size of a temperature cell in the range $(15.5 - 25.1\mathring{A})$. Therefore the assumption of diffusive behaviour is satisfied even at the lowest temperatures under consideration.

The electronic heat diffusion equation (3.3) is solved using the explicit integration method at each MD timstep. Evaluating (2.8) at $300K$ for an average system size gives a maximum timestep of $\approx 2fs$ to ensure convergence in Fe. This can be calculated from (2.8) using the length of a constant temperature cell and the electronic thermal parameters. As the temperature increases from the ambient level, C_e will increase, leading to a lower diffusivity and so a higher upper limit for the timestep. Thus, provided the MD timestep stays below $2fs$ (3.3) will always converge.

A cut-off velocity to determine the electronic stopping regime was imposed. $\gamma_2 \rightarrow 0$ below a cut off velocity $\dot{r}_c$ corresponding to an energy of $2E_{co}$.($= 4.28eV \rightarrow 38.46\mathring{A}ps^{-1}$ [227])

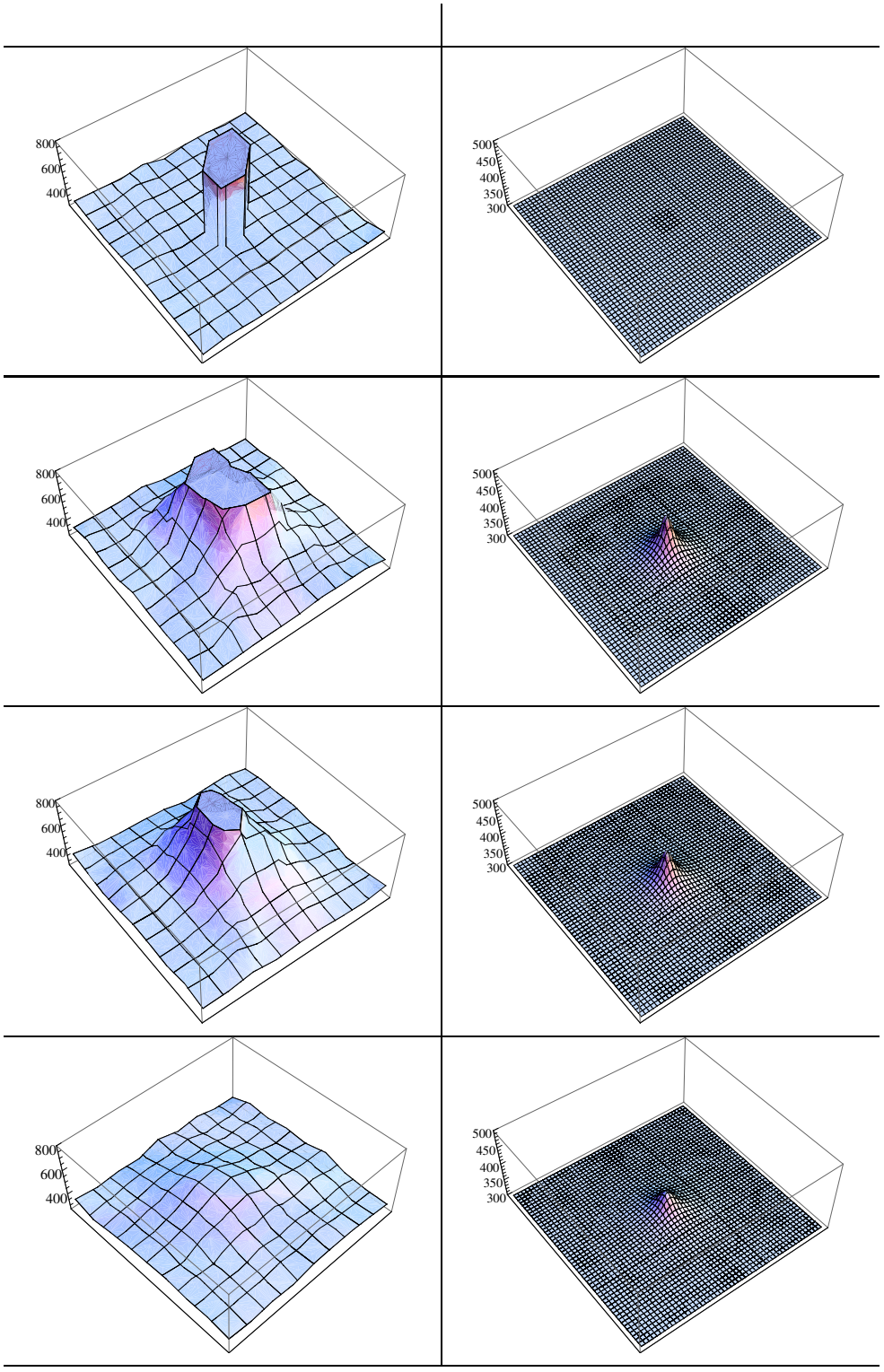

Figure 3.4: Surface temperature plots, in the plane of the PKA, of atomic (left) and electronic (right) temperatures in a $10keV$ displacement cascade. From top to bottom at $0.01fs$, $0.5ps$, $1.0ps$ and $2.0ps$. The atomic cell size is $140\mathring{A}$ in each dimension, and $1555\mathring{A}$ in the electronic system. The temperatures are in Kelvin.

3.4 Ion Tracks

Under highly energetic irradiation, when incident ion energies are $> 10MeV$, the majority of energy is deposited into the electron system. However, before the incident ion comes to rest, large amounts of energy are deposited into the lattice via energetic nuclear collisions. To model such an event as a series of atomic collisions would be prohibitively costly as the necessary system size is proportional to the PKA energy. In this case the ion range is of the order of microns. Therefore the aftermath of the path of a swift heavy ion is modelled. As energy is lost to the electronic system, a track of excited electrons is left in its wake. Above a threshold rate of electronic energy loss, dependent on the strength of coupling of energy between electrons and atoms, atoms will be displaced from their lattice sites and a track of melted solid will be left along the ion's path. There is a critical difference between a cascade and an ion track. In the former energy is initially deposited in one single atom and energy is transferred to other atoms through ballistic nuclear collisions, whereas in the latter, rapid electronic thermalisation means that energy propagates through the electron cloud very quickly. As a result a larger region of lattice atoms is heated uniformly.

This effect was included in the simulations by setting a central column of temperature cells in the electron system to an elevated temperature. Numerical integration was used to determine $T_e^{excited}$ such that (3.21) is satisfied, so that equivalent stopping powers may be compared for different temperature dependences for $C_e(T_e)$.

$$S = ((\Delta x)^2) \int_{300}^{T_e^{excited}} C_e(T_e) \mathrm{d}T_e \tag{3.21}$$

Where Δx is the length of a temperature cell and S is the required stopping power.

In order to impose cylindrical symmetry along the path of the ion, the boundary conditions were made periodic in the z direction (the ion track axis) of the electronic subsystem allowing radial diffusion away from the track axis. It was necessary to increase the system size to contain the larger initial excitation, to 986,078 atoms (78 unit cells in each dimension). Due to computational restrictions, it was necessary to reduce the size of the electronic system to $50 \times 50 \times 9$ temperature cells representing a length scale of $\approx 10^3 \mathring{A}$. The simulations were initiated by setting each electronic temperature cell in the centre of the x-y plane along the z-axis to an elevated temperature, representing the path of a swift ion in the z direction.

Plots of the temperature profiles in the plane perpendicular to the the track axis, in each of the two subsystems can be seen in Fig. (3.5). Note that the scale has been fixed for meaningful comparison between different times. The electronic system is ≈ 10 times larger than the atomic MD cell. The initial temperature of the central cell is $234,000\,K$

corresponding to a stopping power of $35\,keVnm^{-1}$.

It was necessary in tungsten to execute several iterations of the thermal diffusion integration per MD step, effectively using a smaller timestep in the electronic temperature evolution. This is because the thermal conductivity in tungsten is ≈ 2 times larger than in iron, and so the minimum timestep needed for convergence as given by (2.8) is comparable to $1\,fs$ which is the smallest MD timestep which may be used at $300K$ with realistic computer resources. Test simulations showed that when the integration of the thermal diffusion is broken into a number of smaller steps (n) each of length $\frac{\Delta t_{MD}}{n}$ that convergence was achieved for $n > 20$.

Due to the extremely high thermal conductivity in tungsten, the condition for diffusive behaviour in (3.20) is not satisfied until $\approx 700K$. Therefore it can be assumed that our model does underestimate the rate of thermal conduction. Although the problem of calculating electron transport on a length scale shorter than the mean free path has been addressed by including ballistic effects into the diffusion equation to approximate the Boltzmann equation [228], we recognise this as a limitation of our model.

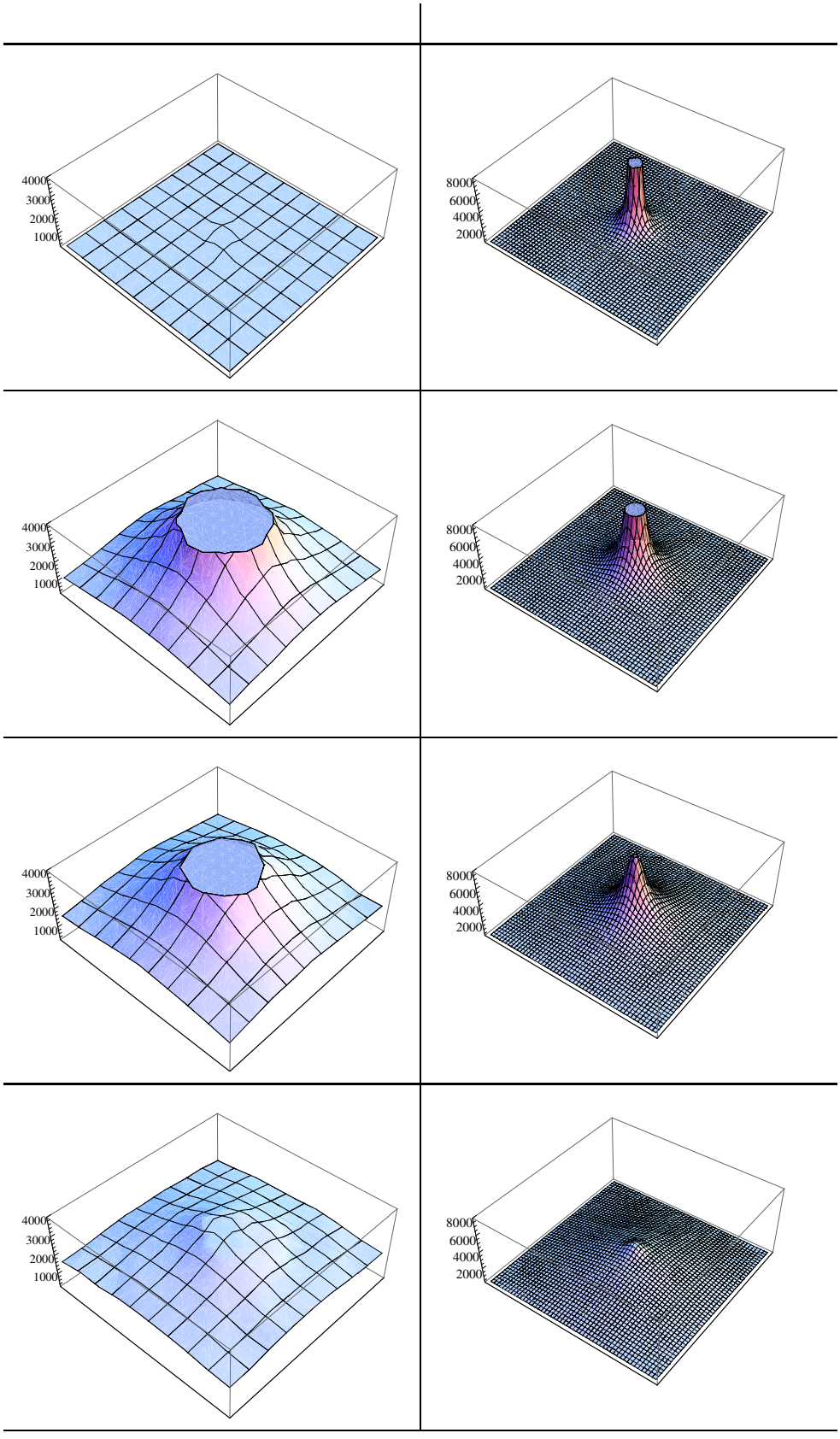

Figure 3.5: Surface plots of atomic (left) and electronic (right) temperatures in the plane perpendicular to the track axis in a $35\,keVnm^{-1}$ ion track in tungsten. From top to bottom at 0.001, 0.5, 1.0, 2.0 ps. The atomic cell size is $250\mathring{A}$ in each dimension, and $1388\mathring{A}$ in the electronic system.

3.5 Parameters

3.5.1 Electron-Phonon Coupling

The strength of the interactions are characterised by the time scale τ_α. From equation (3.14)

$$\tau_\alpha = \frac{3nk_B}{\gamma_\alpha} \tag{3.22}$$

here n is the number of atoms per unit volume.

Allen formulated a model for the rate of energy transfer at low energy in terms of $\lambda\left\langle\omega^2\right\rangle$, used in the theory of superconductivity, using the Bloch-Boltzmann-Peierls formula to describe the rate of change of the electron and phonon distributions [97]. Wang et al used this approach to arrive at a value of $g \approx 144 \times 10^{16}\, Wm^{-3}K^{-1}$ for Fe using the number of free electrons as the only free parameter [146]. This corresponds to an electron-phonon coupling time scale of $\tau_1 = 0.06\, ps$

Gao et al developed the model put forward by Finnis and Agnew to describe displacement cascades using a hybrid of atomistic MD and the continuum two temperature model [134]. A value of $5438 \times 10^{16}\, Wm^{-3}K^{-1}$ was arrived at. This corresponds to a value of $\tau_1 = 2.4\, ps$.

Attempts have been made to probe the electron-phonon coupling strength experimentally using femtosecond laser experiments. An intense laser pulse is split into two to stimulate the sample, while the second pulse is used to probe the excited electron distribution. This gives a value of $\approx (2-4) \times 10^{16}\, Wm^{-3}K^{-1}$ corresponding to $\tau_1 \approx 0.1\, ps$ for transition metals [229].

Fujimoto et al investigated multiphoton and thermally enhanced photoemission [230], and specifically the role of non-equilibrium between electrons and atoms, from a W surface using a pump-probe laser experiment. Electron temperature data from these experiments led to an estimate of $5 \times 10^{17} - 1 \times 10^{18}\, Wm^{-3}K^{-1}$ for the electron-phonon coupling strength. This corresponds to a time scale of $\tau_1 = 0.07 - 0.26\, ps$.

Lin et al used DFT to calculate the density of states in W, from which they calculated the coupling strength as a function of electronic temperature [127, 128]. This varied between a value $\approx 2 \times 10^{17} - 10^{18}\, Wm^3K^{-1}$, equivalent to a time scale in the range $0.07 - 0.3\, ps$.

3.5.2 Thermal Conductivity

The two contributions to the frequency of electronic collisions, which determines thermal conductivity may be expressed as

$$f = \frac{1}{\tau} = \overbrace{BT_a}^{1} + \overbrace{AT_e^2}^{2} \tag{3.23}$$

Here (1) is the phonon scattering term and (2) is the electron-electron scattering term.

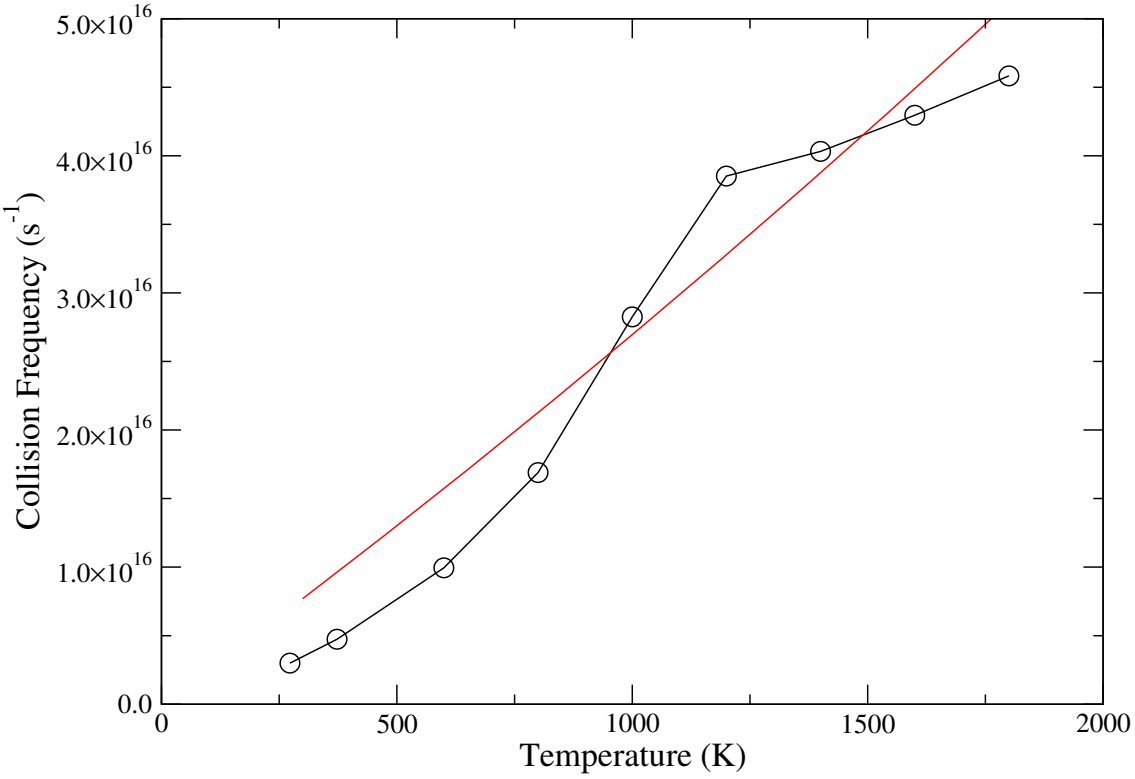

Figure 3.6: Experimental values (black) and fit (red) for electron collision frequency in iron.

Using experimental values [226] of thermal conductivity in the temperature range 300K-1800K [$T_m = 1810K$] and theoretical values of the heat capacity, following the well known Sommerfeld expansion [114], values of $1.85 \times 10^9 K^{-2}s^{-1}$ and $2.51 \times 10^{13} K^{-1}s^{-1}$ were fitted for A and B respectively in iron using the same procedure as in [111] . Due to the relative sizes of A and B, thermal relaxation is likely to be dominated by electron-phonon coupling at low temperatures giving a roughly linear temperature dependence of κ_e and above $T_e = 1eV$ will be dominated by electron-electron scattering [115].

Fig. (3.7) shows the collision frequency as given by (3.24) and the condition given by (3.25) (Discussed in section (1.5.3)) and assuming equilibrium, i.e. $T_e = T_a$. The

convergence of (3.24) to (3.25) is seen at $537K$.

$$f = \frac{1}{\tau} = BT_a + AT_e^2 \tag{3.24}$$

$$f < \frac{\nu_e}{r_o} \tag{3.25}$$

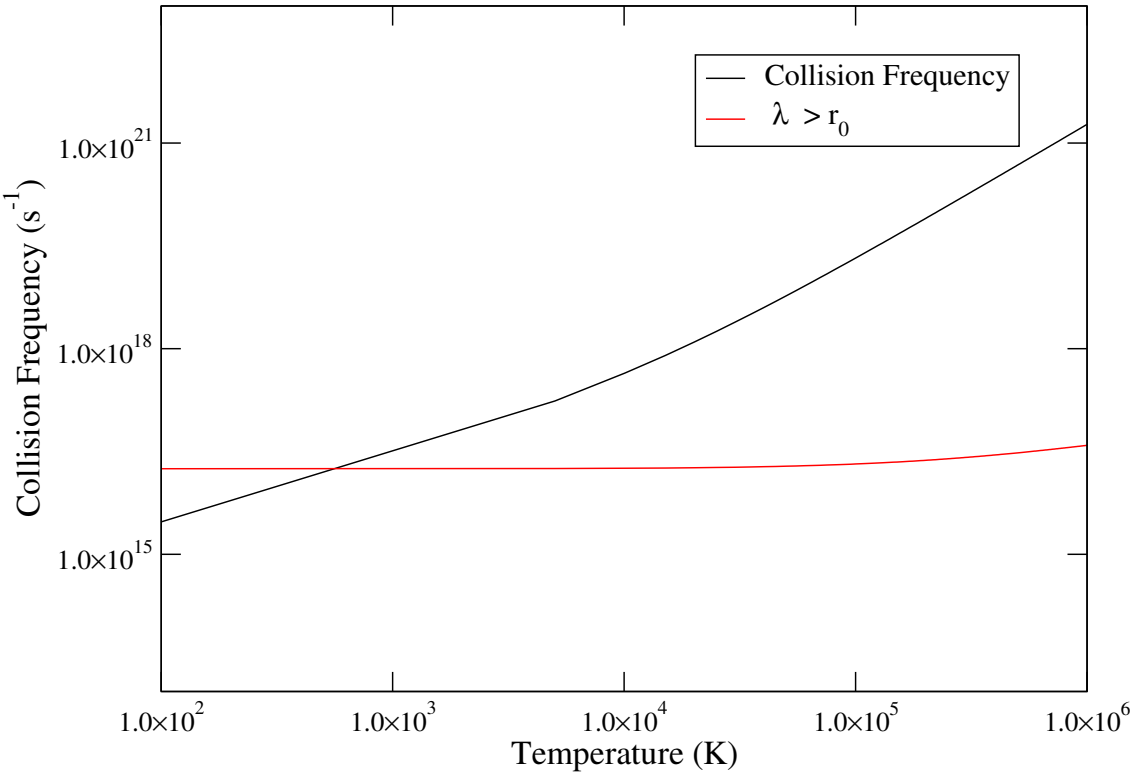

Figure 3.7: The electron collision frequency fit in iron (black) as given by e-e scattering and e-phonon scattering and the upper limit of the collision frequency dictated by the condition $\lambda_e > r_o$(red).

The high temperature part of the collision frequency was set to saturate at the limit given by (3.25). However, as can be seen, the condition of resistivity saturation arises at $\approx 600K$, while the experimental values predict a mean free path which continues to decrease to $0.3r_0$. This apparent unphysical violation of the resistivity saturation condition, is due to deviation from free electron behaviour and over-simplification of the scattering mechanism. For this reason a fixed value of thermal conductivity appropriate to $300K$ was used equivalent to $80\,Wm^{-1}K^{-1}$ in iron and $177\,Wm^{-1}K^{-1}$ in tungsten [206].

3.5.3 Electron Stopping

The SRIM code includes all stopping effects and predicts a stopping strength $\lambda = 0.1093 eV \mathring{A}^{-1}$ [8] in Fe. From Lindhard's model [45] the rate of energy loss for a single atom can be written as

$$m\frac{d\nu}{dt} = \lambda \left(\frac{m}{2}\right)^{\frac{1}{2}} \nu \tag{3.26}$$

Comparing this to the frictional term in (2.35)

$$\chi_2 = \frac{\gamma}{m} = \lambda \left(\frac{m}{2}\right)^{\frac{1}{2}} \tag{3.27}$$

This is equivalent to an inverse stopping time scale of $1.0\, ps^{-1}$.

There will be a threshold kinetic energy above which electron stopping will dominate and below which it can be ignored as ions will not be moving fast enough to inelastically collide. Intuitively this will be related to the displacement energy E_D necessary for an atom to leave a lattice site. Various values have been proposed; a threshold of energy loss of $50-55 keV nm^{-1}$, a kinetic energy equivalent to the cohesive energy [44], two times the cohesive energy [135] and a constant value of $10\, eV$ [57] (equivalent to $\nu_{co} = 4763.62 \mathring{A}^2\, ps^{-2}$).

A cut-off velocity of $\nu_{co}^2 = 2981.16 \mathring{A}^2\, ps^{-2}$ ($T_{co}^2 = 9.94 \times 10^4 K$) was used corresponding to two times the cohesive energy.

3.5.4 Heat Capacity

A tanh function was used of the form below to interpolate between low temperature linear behaviour and high temperature classical behaviour.

$$C_e(T_e) = 3k_B \tanh(\Gamma\, T_e / 3k_B) \tag{3.28}$$

This gives a monotonic increase at low temperature in proportion to Γ which tends to the classical value at $T_{sat} \approx 20,000K$. Only the contribution of the d electrons are considered at the temperatures under consideration in this study, 2 in the case of Fe.

Γ has been accurately determined as $4.98 \times 10^{-3} Jmol^{-1}K^{-2} = 702.400\, Jm^{-3}K^{-2}$ for Fe and $1.3 \times 10^{-3} Jmol^{-1}K^{-2} = 136.17\, Jm^{-3}K^{-2}$. [123]

In tungsten a tanh functional form was derived as for iron, demonstrating linear behaviour at low temperatures with a gradient given by [123]. At high temperatures saturation occured at the classical value of $3\, k_B$. The DFT data provided by Lin and Zhigilei [126]

was used to fit the high temperature regime. Agreement was found when a value of 2.47 electrons per atom contributing to electronic specific heat was used.

It was found that the Sommerfeld expansion considerably underestimated the specific heat when compared to DFT data at low temperatures. Therefore a tanh function was fit to this data using the low temperature specific heat co-efficient Γ_e as free parameters amd fixing the number of electrons contributing to the specific heat at 2.47. It can be seen that there is a decrease in the DFT data at $\approx 17000K$, however saturation was imposed as given by the dashed line as it was suspected that this decrease was due to neglect of contributions to the density of states at high energy which become important at high temperatures. These three functional forms are plotted below in Fig. (3.8).

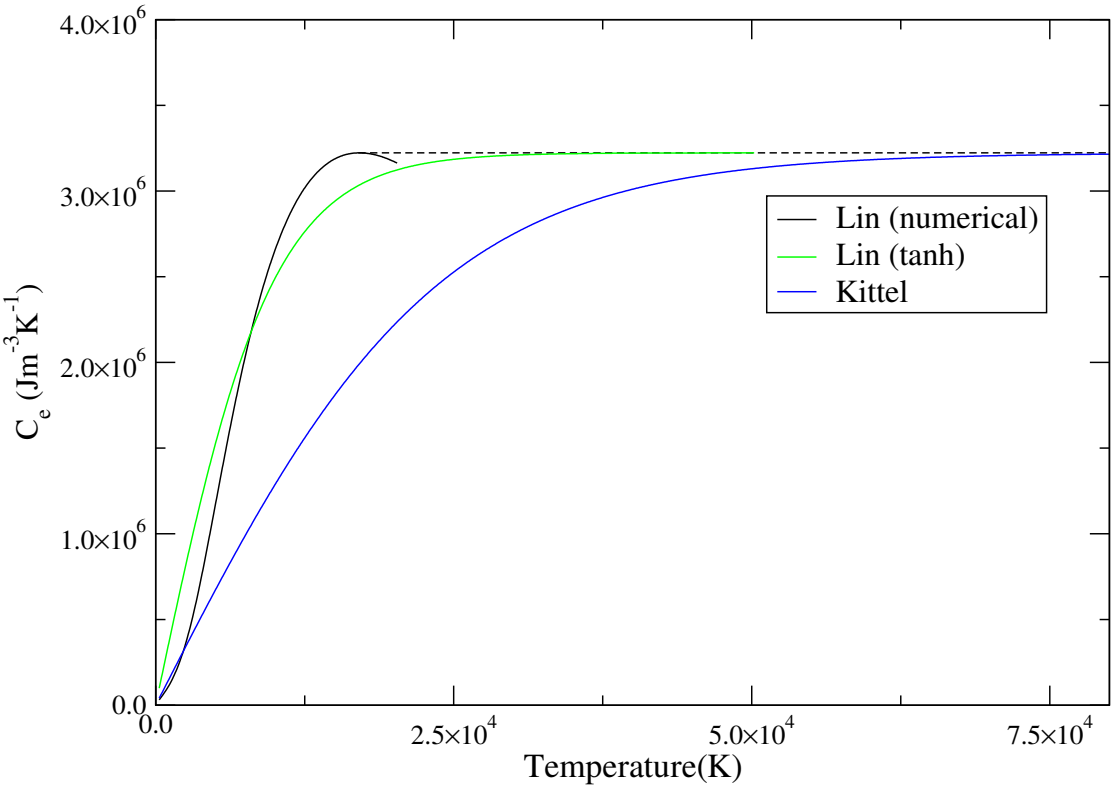

Figure 3.8: Specific heat in tungsten as a function of electronic temperature as fit to DFT data, numerical DFT data and extrapolation of low temperature expansion.

Chapter 4

Cascade Results

In this chapter results are reported of an investigation of displacement cascades in Fe using our inhomogeneous thermostat. The effect of the strength of electron-phonon coupling and electronic stopping is investigated in $10\,keV$ events. The inhomogeneous thermostat is seen to affect residual defect distributions, cascade evolution and the degree of disorder, however two distinct mechanisms have been introduced. In order to decouple the effects of stopping and coupling some investigation of the the neglect of electronic stopping is undertaken to determine, solely, the effect of a varying electronic temperature. Events with energies in the range $1 - 12.5\,keV$ are then simulated to determine how these effects scale with energy. Since the homogeneous thermostat describes the situation in a low energy event accurately, it is likely that the differences between the homogeneous and inhomogeneous thermostats become more pronounced as energies increase.

The model outlined in chapter 3 was implemented using modified code from the DLPOLY package [182] version 3 incorporating a domain decomposition parallelisation architecture. The electron-phonon coupling time scale $\tau_1(=\frac{1}{\chi_1})$ emerges as our main variable parameter as the various models predict a range of values; χ will refer to χ_1 unless otherwise specified from now on. The following technical details apply for all simulations unless otherwise specified.

A variable timestep was used, determined by the speed of the most energetic atom, such that it travels no more than $0.025\mathring{A}$. A constant value of κ_e was used which corresponds to the experimental value at $300K$ ($80\,Wm^{-1}K^{-1}$), while the specific heat capacity was modelled using a tanh function linear in temperature until saturation at the classical value of $3k_B$ at $\approx 20,000K$, as described in section 3.5.4. A default value of the electronic stopping strength $\chi_2 = 1.0\,ps^{-1}$was used corresponding to $g_2 = 1.12 \times 10^{13} Wm^{-3}K^{-1}$ or a rate of electronic energy loss of $\approx 0.11\,eV\,\frac{1}{2}\mathring{A}^{-1}$. The Dudarev magnetic potential [223] was used with a cut-off of $4.1\mathring{A}$. Interstitial atoms are defined as any atom more than $1.0\mathring{A}$ from a lattice site.

A system of 235,298 Fe atoms was used, corresponding to 49 cubic unit cells in each dimension. This cell was split into temperature cells of $15.5\,\mathring{A}$ containing on average ≈ 322 atoms. The cascades were initiated with a single PKA with an energy of $10\,keV$ corresponding to a velocity of $1859.15\,\mathring{A}ps^{-1}$. Some of the results presented in this chapter also appear in [231] and [232].

4.1 10 keV Displacement Cascades in Iron

4.1.1 Effect of Electron-Phonon Coupling Strength

In this section the coupling strength is investigated by performing $10\,keV$ cascades using a coupling strength in the range $0.05 - 30\,ps^{-1}$. The extreme values are outside of the experimental range measured for transition metals, but comparison of the homogeneous and inhomogeneous thermostats over this large range gives a better understanding of the role of electron-phonon coupling.

Fig. (4.1) shows the evolution of the temperature of the hottest atomic temperature cell, containing the PKA, during displacement cascades with values of $\chi(=\gamma/m)$ in the range $0.05-30.0\,ps^{-1}$, representing the inverse time scale of electron-phonon equilibration. The rapid decay of an initial high atomic temperature ($\approx 2.4\times10^5K$) can be seen as the energy is transferred to electrons in the vicinity and is also partitioned among neighbouring atoms at a slower rate due to a lower thermal conductivity than in the electron system.

With weak coupling ($\chi = 0.05ps^{-1}$) the core temperature decays more slowly in the homogeneous thermostat than the inhomogeneous thermostat. In this case electronic stopping (the strength of which is determined by the value of χ_2) will have a very large effect since $\chi_1 << \chi_2$ acting to quench the cascade more quickly using the inhomogeneous thermostat than in the homogeneous thermostat in which stopping is not included. The effect of electronic stopping is exacerbated as the rate of energy transfer is independent of the local temperature difference. With strong coupling ($\chi = 30.0ps^{-1}$) this trend is reversed. In this case $\chi_1 >> \chi_2$ and coupling is the dominant mechanism. The electrons heat up very rapidly leading to a reduction in the local temperature difference and, consequently, a much slower decay of temperature in comparison to the homogeneous thermostat, which has a constant $300K$ thermostat.

The peak electronic temperature over time, relative to $300K$, with a range of coupling strengths is shown in Fig. (4.2). Local electronic heating can be observed and even at these relatively low PKA energies, the temperature rise is significant above $300K$, the

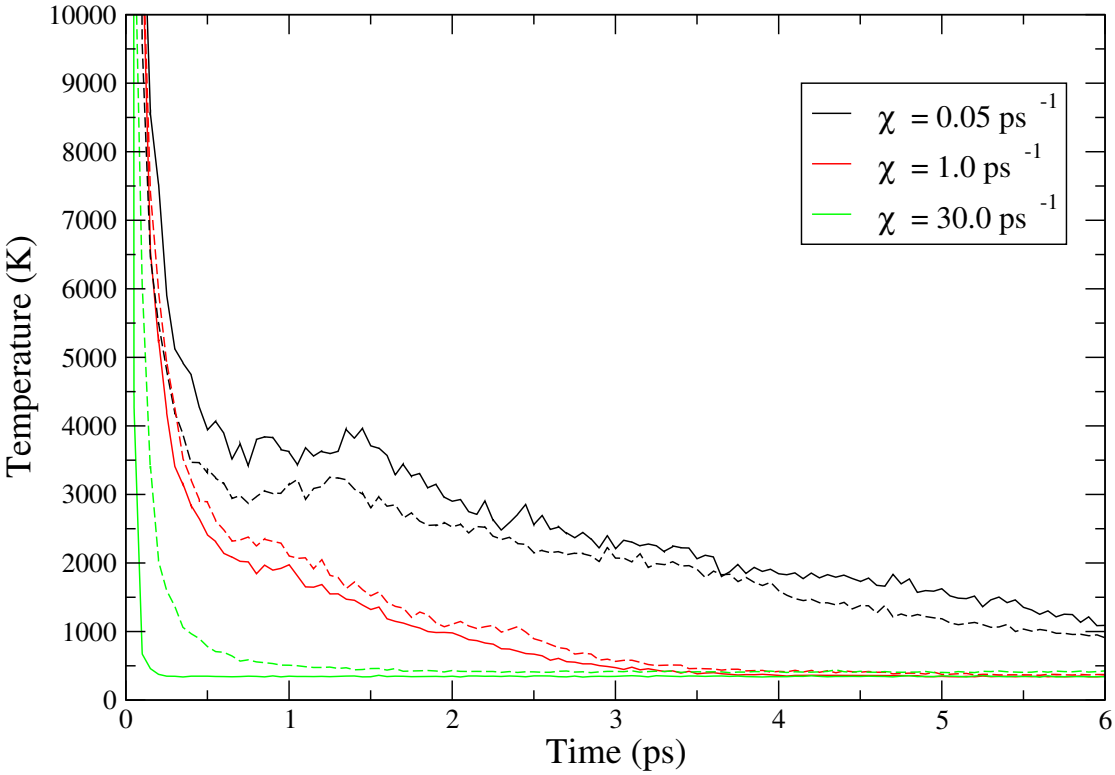

Figure 4.1: Peak atomic temperature in a single 10 keV displacement cascades using inhomogeneous (dashed line) and homogeneous (solid line) thermostat as a function of coupling strength.

electronic temperature assumed by the homogeneous thermostat. Both the peak in the temperature and the rate of decay are sensitive to χ. There is no comparable electron temperature data for the homogeneous thermostat as the electron temperature is assumed to be constant. The fact that these results demonstrate considerable electronic heating before electronic diffusion begins to act suggests that electronic effects are significant.

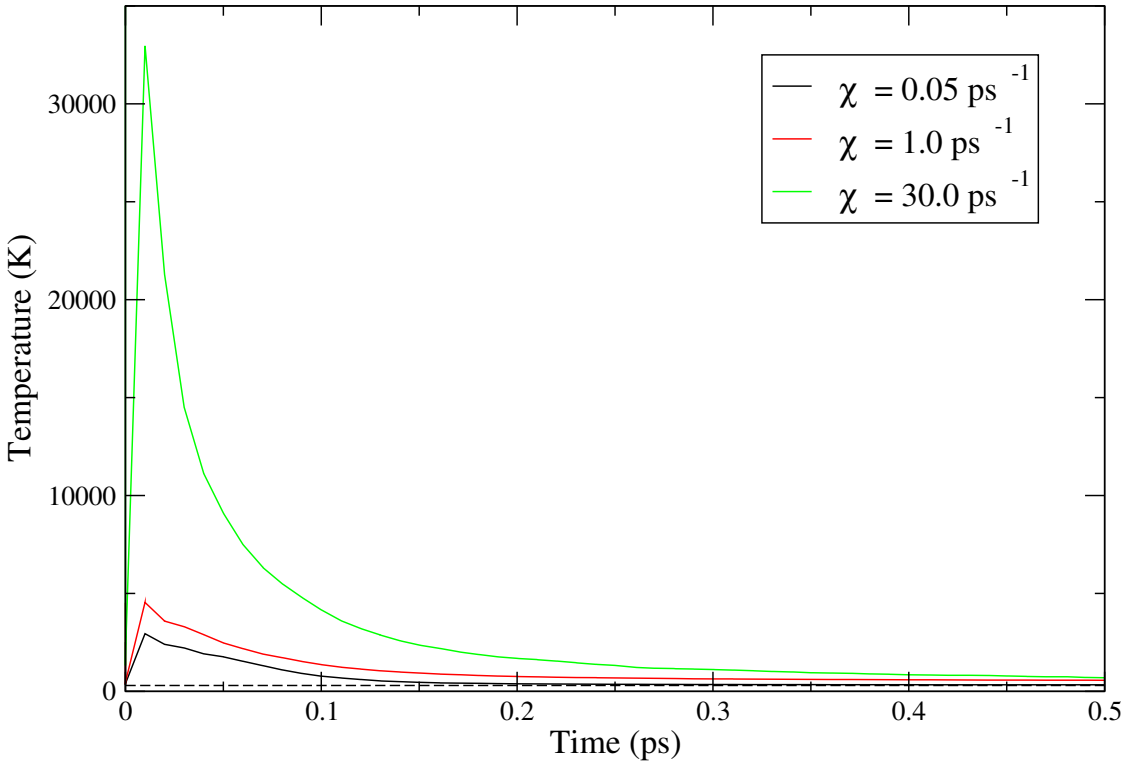

Figure 4.2: Peak electron temperature in a single 10 keV displacement cascade using inhomogeneous thermostat as a function of coupling strength. The dashed line represents a constant electronic temperature of $300K$

4.1.2 Effect of Electronic Stopping

The main parameter in the model is the strength of the coupling constant χ_1 since this has the most uncertainty in its experimental measures and variation with temperature, and the strength of electronic stopping can be calculated accurately using the SRIM code. It is nevertheless informative to investigate the trend in the cooling curves with this parameter.

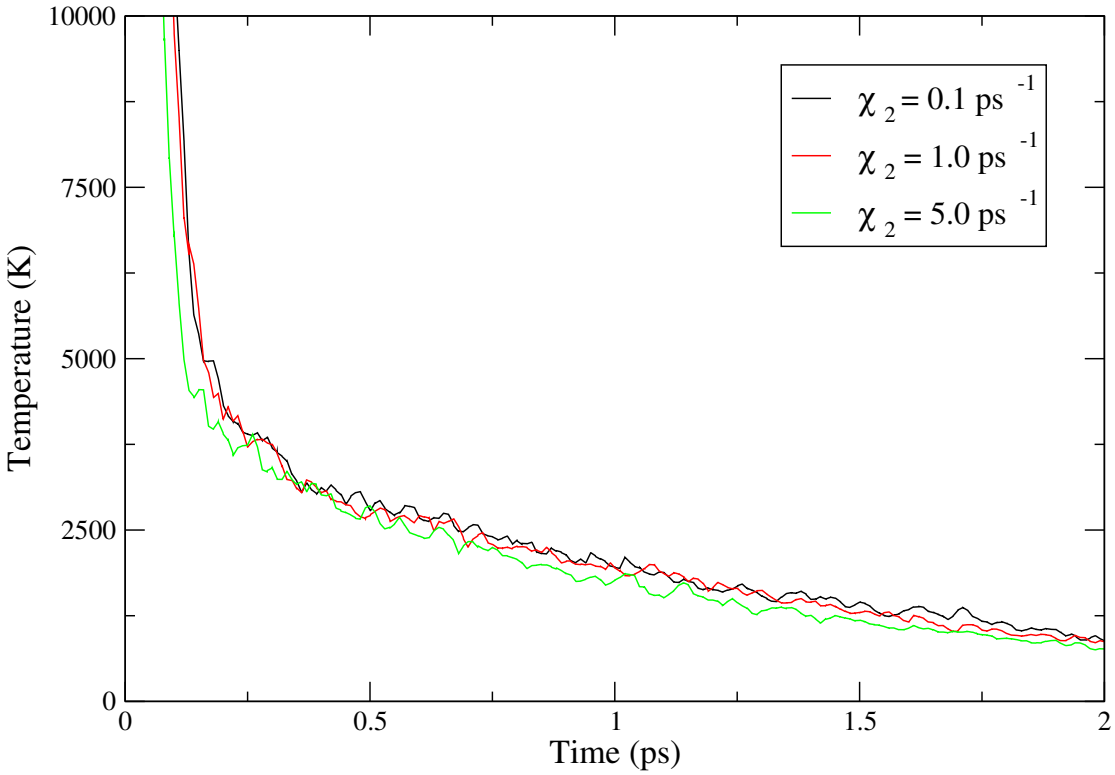

Figure 4.3: Peak atomic temperature in a single 10 keV displacement cascade as a function of stopping strength.

Figures (4.3) and (4.4) show the core atomic and electronic cooling curves over time with varying stopping strength. Fig. (4.3) demonstrates swifter quenching of the cascade with stronger stopping. From Fig. (4.4), as expected, the peak core electronic temperature rises sharply with stopping strength as energy is absorbed more quickly, at a rate *independent of the local temperature difference*. Fig. (4.4) is logarithmic to resolve the trend at later times. Strong quenching of the cascade allows the whole system to relax to the ambient temperature more swiftly. Conversely a weak interaction leads to heating of the electrons by the atoms over a longer time, causing the cross over of the trend at $\approx 0.2\,ps$. Small differences are seen in the initial rate of cooling of the atoms, but they are obscured after $\approx 0.3\,ps$ by fluctuations.

The effect of stopping strength is also reflected in the number of displacements in time

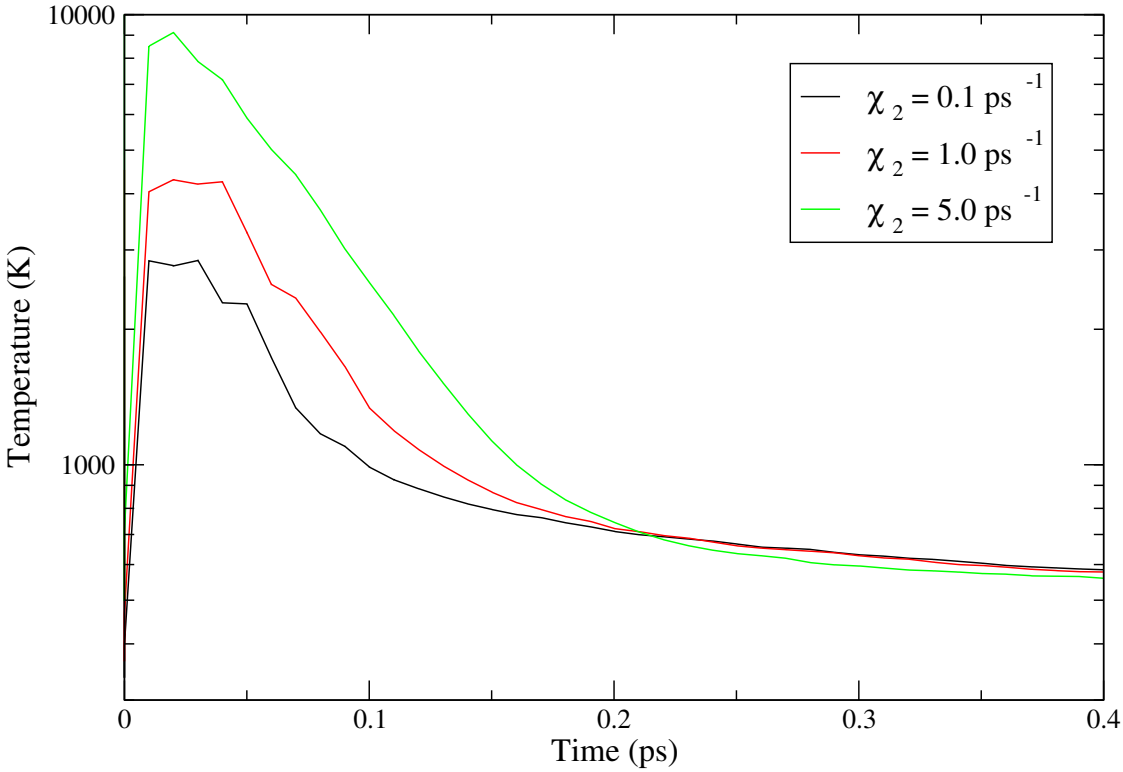

Figure 4.4: Peak electron temperature in a single 10 keV displacement cascade as a function of stopping strength.

during simulations (Fig. (4.5)). The extent of the disorder formed is strongly dependent on the electronic stopping strength and the residual defect numbers to a lesser extent; stopping strongly supresses the ballistic stages of the cascade leading to much a smaller degree of disorder.

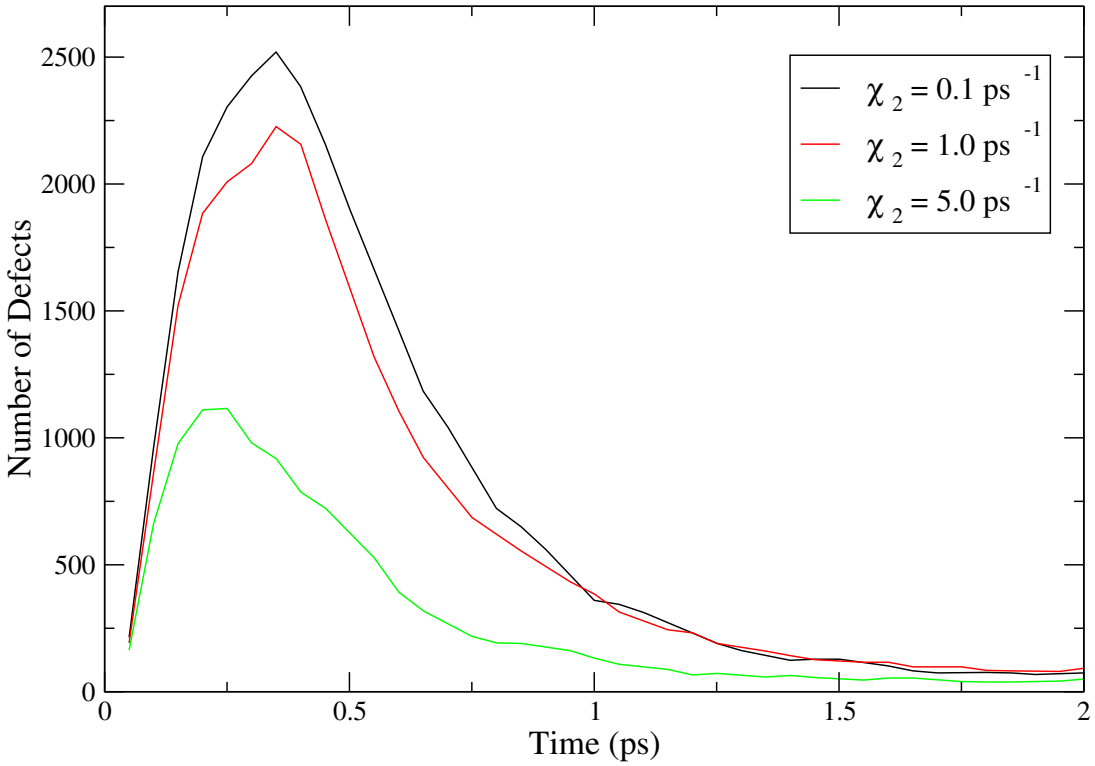

Figure 4.5: Defect numbers in a single 10 keV displacement cascade as a function of stopping strength.

4.1.3 Residual Defects

The most important data from a radiation damage simulation is quantitative information about the residual damage, as it is this persisting damage which will determine damage on a macroscopic scale. The number of atomic displacements, and so residual defects, as a function of coupling strength, both with and without electronic stopping is investigated.

Fig. (4.6) shows a plot of the number of isolated interstitial atoms (equal to the number of vacancies) averaged over 4 distinct PKA directions ($\langle 100\rangle, \langle 010\rangle, \langle 001\rangle$ and $\langle 110\rangle$ with both positive and negative velocities), as a function of coupling strength. The error bars represent the standard error over these simulations. In this plot the standard homogeneous thermostat is compared to an inhomogeneous thermostat. We have not included electronic stopping so that the mechanisms of coupling and stopping may be to some extent decoupled. This is labelled as 'no stopping' in the legends of this, and subsequent plots for brevity. A logarithmic scale is used for clarity as the range of coupling values considered is very large.

Some difficulties exist when counting residual defect numbers. Clusters of interstitial atoms located close to vacant lattice sites are likely to be lower energy configurations of smaller clusters which have relaxed. For example, it is energetically favourable for a single interstitial atom to form a dumbell configuration in which two atoms 'share' a single vacant lattice site. Such a configuration would be considered equal to one interstitial atom. Defect configurations are always interpreted in this way unless otherwise specified.

The general form of the data can be understood as follows; in the limit of zero coupling which is equivalent to an $[NVE]$ simulation in which the only mechanism quenching the cascade is the gradual partition of the initial PKA energy among the other degrees of freedom in the atomic system, a number of defects n_o are found. Using a constant energy ensemble, an average number of defects of 15.5 ± 1.5 is found to which both lines can be seen to approach within statistical scatter. As coupling is increased, less and less time is available for thermally assisted recovery of displaced atoms as energy is rapidly transferred to the electrons where it quickly disperses, so the number of residual defects increases from n_o. This trend persists until a maximum in the number of defects is reached. Above this point coupling is so strong that it acts to quench the cascade at the beginning of the collisional phase before a disordered zone is formed reducing the size of the resulting thermal spike region. This same trend was observed by Pronnecke et al [183]. Since increased quenching usually gives rise to more defects [132, 131, 134], the above result may at first seem counterintuitive. This assumes that the same melt is considered to start with, however in this case the quenching acts on the system *as* the disorder and melted zone is

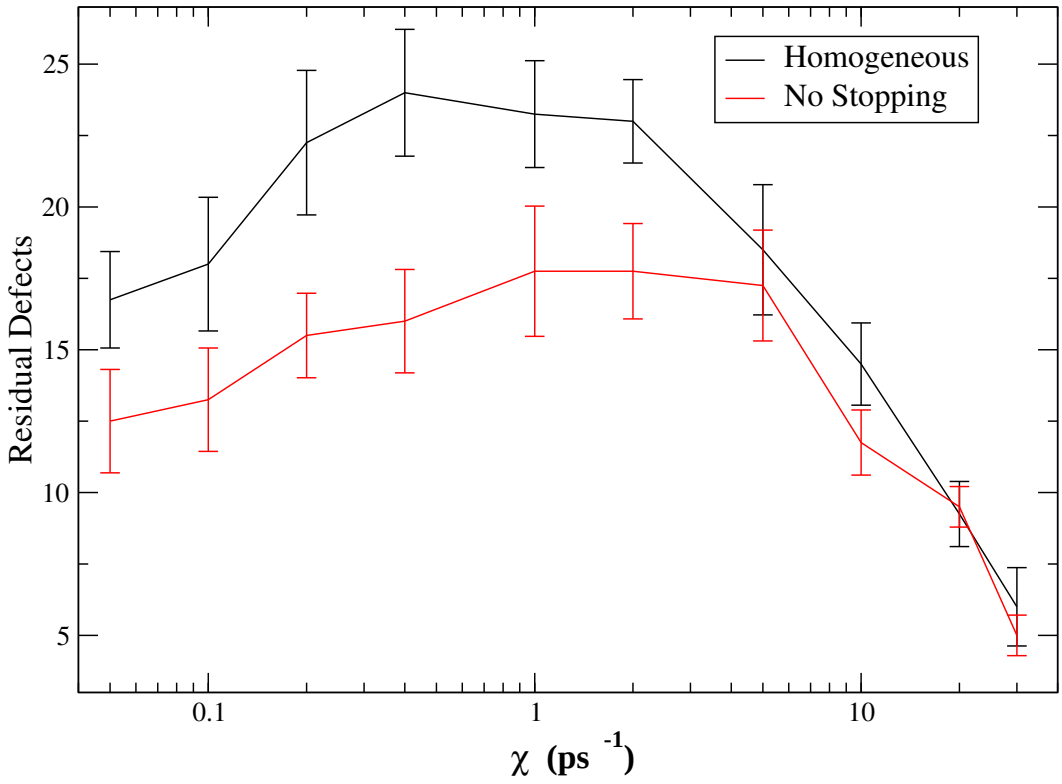

Figure 4.6: Residual defects as a function of coupling strength for 10 keV PKA displacement cascades using an inhomogeneous thermostat without stopping.

forming. Thus two distinct regimes exist; at low coupling ($\chi_1 < 1.0ps^{-1}$) the situation in the cascade is that of a liquid core being quenched. While at high coupling ($\chi_1 > 1.0ps^{-1}$) the situation is of a brief ballistic phase being quenched. As a result there is a degree of convergence between the thermostats at extremely high coupling, as the cascade is so strongly suppressed such that the details of the model become unimportant.

It should be noted that in many of these simulations the electronic sub-system is acting as a very efficient heat sink. Although significant increases are seen in the local electronic temperature, these are much smaller than the temperatures in the core of the lattice. This is attributable to swift electronic diffusion which removes energy to the boundary very quickly. In particular when $\tau_{diff} << \tau_1, \tau_2$, the parameter which limits the rate of relaxation of the cascade is the rate at which energy is transferred between sub-systems. Also, in this situation, feedback of energy via the stochastic force in (3.4) becomes less important, as any spike in the electron temperature quickly dissipates over the time scale for feedback into the lattice. At different cascade energies it is likely that the crossover between the regimes described above will differ; the final state of the system is determined by the relative time scales of diffusion, coupling and stopping, as well as the PKA energy.

The examination of the number of defects during the course of the cascade shows that

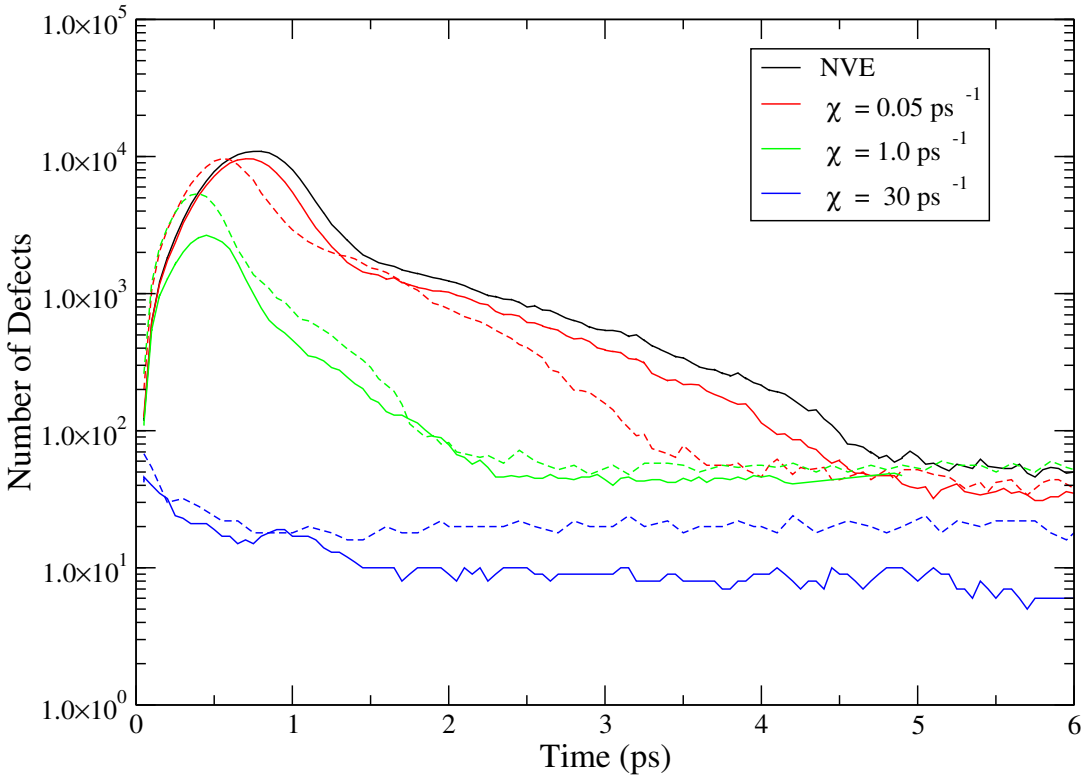

Figure 4.7: The number of defects in 10 keV PKA displacement cascades as a function of time for homogeneous thermostat (solid line) and inhomogeneous thermostat without stopping (dashed line).

the situation is in fact very subtle. Fig. (4.7) shows the number of atomic displacements as a function of time for weak, intermediate and strong coupling compared with a homogeneous and inhomogeneous thermostat without electronic stopping. This demonstrates the general trend of decreasing peak disorder as coupling increases from zero ($[NVE]$). With weak coupling (low χ) the peak disorder is comparable in the homogeneous thermostat and the inhomogeneous thermostat without stopping, the disorder is steadily annealed to comparable levels of residual damage. This is faster in the inhomogeneous thermostat without stopping dataset as the electron temperature is slightly elevated, encouraging recombination of defects. For strong coupling (high χ), much less disorder is formed by the homogeneous thermostat. These observations are both consistent with the two different pictures at extremes of coupling. With weak coupling the diffusive timescale is much smaller than the coupling timescale, therefore any electronic temperature spike quickly dissipates. As a result there is little significance in modelling the finite heat capacity of the electrons as the temperature does not rise much above $300K$, and for both models the rate of relaxation of the system is limited by coupling. Conversely when $\tau_{diff} >> \tau_{epc}$ and the cascade is quenched in the *ballistic* phase, the rate of quenching is limited by diffusion, as strong coupling quickly leads to saturation of the electronic temperature and so a reduction in the local temperature difference. Since the homogeneous thermostat

effectively has infinitely fast diffusion, the ballistic atoms are quenched to $300K$ and any formation of disorder is considerably limited. While this early stage is limited by the finite diffusion rate for the inhomogeneous thermostat without stopping, it is sufficiently fast that there is little opportunity for annealing, leaving the small amount of disorder created quenched into the lattice.

In order to obtain an estimate of the crossover between the diffusion-limited and coupling-limited regimes the relative sizes of τ_{diff} and τ_{epc} may be compared. Using the electronic diffusivity with a characteristic length scale given by the size of a temperature cell ($= 15.6\,\mathring{A}$), τ_{diff} may be estimated as

$$\tau_{diff} = \frac{L_{cell}^2}{\alpha_e} = \frac{C_e\, L_{cell}^2}{\kappa_e} \tag{4.1}$$

The difficulty in evaluating (4.1) arises in the temperature dependence of C_e; within our model τ_{diff} is at a maximum in the classical regime at high temperature ($= 3.5\,ps$) and decreases at low temperature ($= 0.58\,ps$ at $T_e = 300K$). Also, since the temperature distribution is highly inhomogeneous, the rate of diffusion will vary across the cell. Further, stronger coupling will lead to stronger electron heating which will in turn change the electronic thermal parameters. It is clear that the time scales of several key mechanisms are critical in determining the system's behaviour, namely coupling, diffusion and, as discussed in more detail later, stopping. However since these mechanisms are mutually dependent and temperature dependent they will combine synergistically, giving behaviour which is not easily predicted in an intuitive manner. Therefore it is not straightforward to partition the parameter space into two clearly defined regimes with predictable behaviours.

In order to investigate the effect of stopping, the same information is compared between the inhomogeneous thermostat, that is with just the effect of coupling as considered above, and with the combined effect of stopping and coupling. This can be seen in Fig. (4.8) showing the instantaneous number of atomic displacements over time for a range of coupling strength compared between inhomogeneous thermostats with and without stopping. With weak coupling, the inclusion of stopping quenches the ballistic stages of the cascade significantly giving reduced peak disorder and residual damage. As coupling increases, the system's evolution becomes diffusion limited. The presence of a stopping mechanism, which removes energy at early times at a rate independent of the local temperature difference, causes the saturation of the electron temperature and so less effective removal of energy by coupling and diffusion at later times. As a result greater disorder is formed. This situation can be clarified by examining the atomic (Fig. (4.9)) and electronic (Fig. (4.10)) temperature evolution with and without stopping for strong, weak and intermediate coupling. The inclusion of stopping gives rise to a stronger temperature spike in the electron system, although there is some convergence between the two datasets as

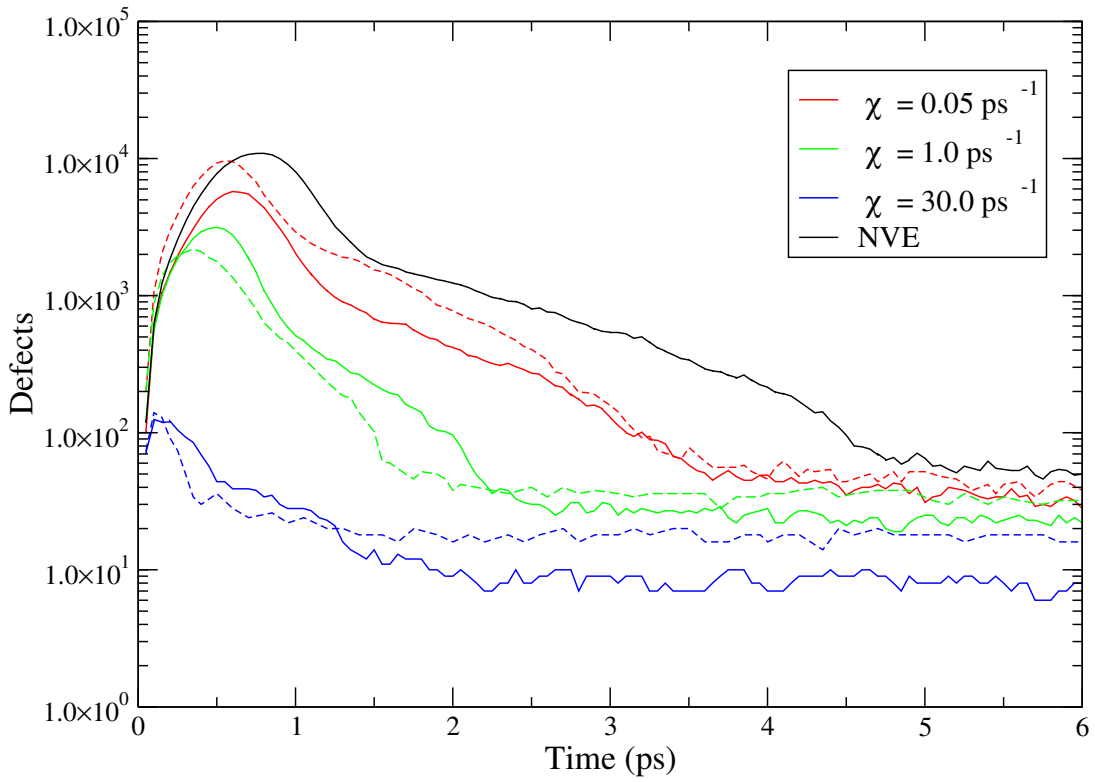

Figure 4.8: The number of defects in single 10 keV PKA displacement cascades as a function of time for inhomogeneous thermostats with (solid line) and without stopping (dashed line).

coupling becomes large and $\tau_1 << \tau_2$ so that the details of the model become insignificant. Stopping causes more efficient atomic cooling at low coupling, but at higher coupling the atoms cool more efficiently without stopping, as this causes the swift heating and saturation of the electronic temperature in and around the core, and so slower relaxation by diffusion.

While some differences are seen in the final, stable defect numbers for a single simulation in Fig (4.8), it can be seen from the averaged residual defect numbers as a function of coupling strength plotted in Fig. (4.11) that there are some *systematic* differences in averaged results. Below $\chi = 1.0ps^{-1}$ the inclusion of stopping gives more defects, while when $\chi > 1.0ps^{-1}$ stopping gives fewer residual defects. When dynamics are coupling limited, stopping removes energy more quickly reducing the time for annealing. As the coupling strength increases the cascade becomes quenched in the ballistic phase; diffusion-limited behaviour. The stopping mechanism allows the formation of a disordered core to be supressed very strongly, reducing damage.

It can be concluded from the differences between the three curves that the overall trend in residual defects is primarily attributable to coupling between the atomic and electronic

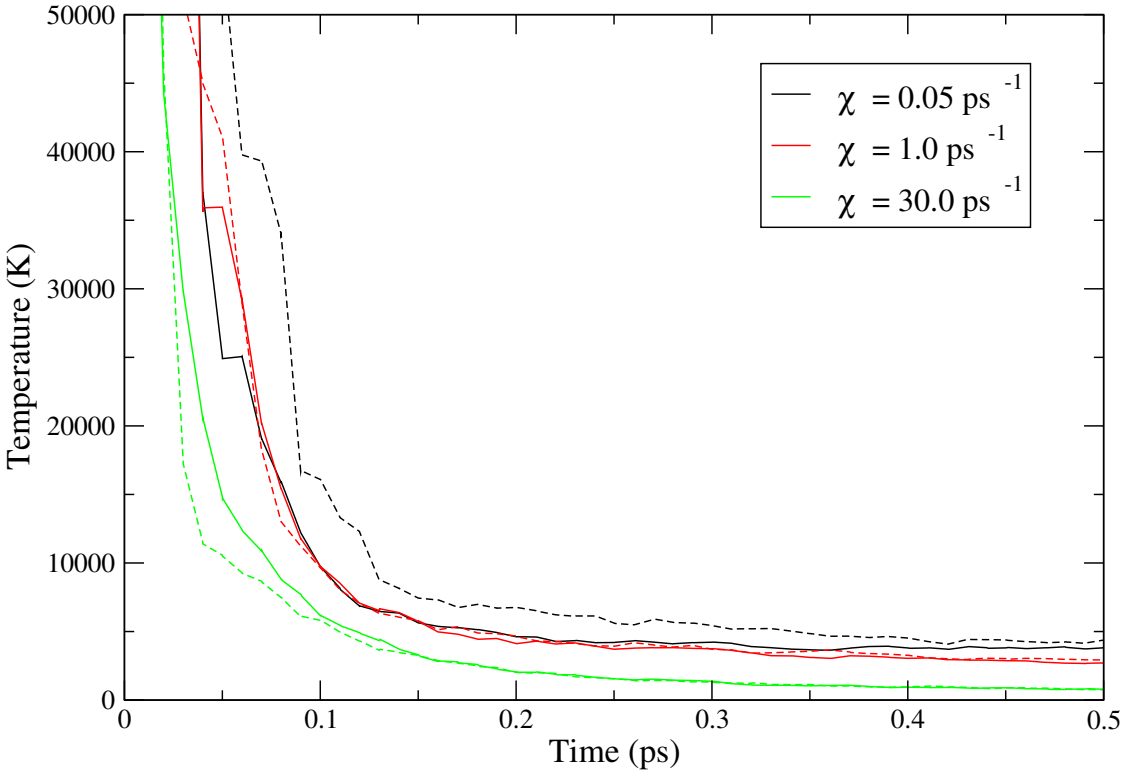

Figure 4.9: Core atomic temperatures with (solid line) and without (dashed line) stopping using inhomogeneous thermostat for 10 keV PKA displacement cascade.

systems, although some differences are seen with and without stopping. However, since stopping is only effective when ions are in a very high energy range, only the collisional phases of high energy events are affected. It is likely that the relative importance of stopping will increase as the PKA energy increases.

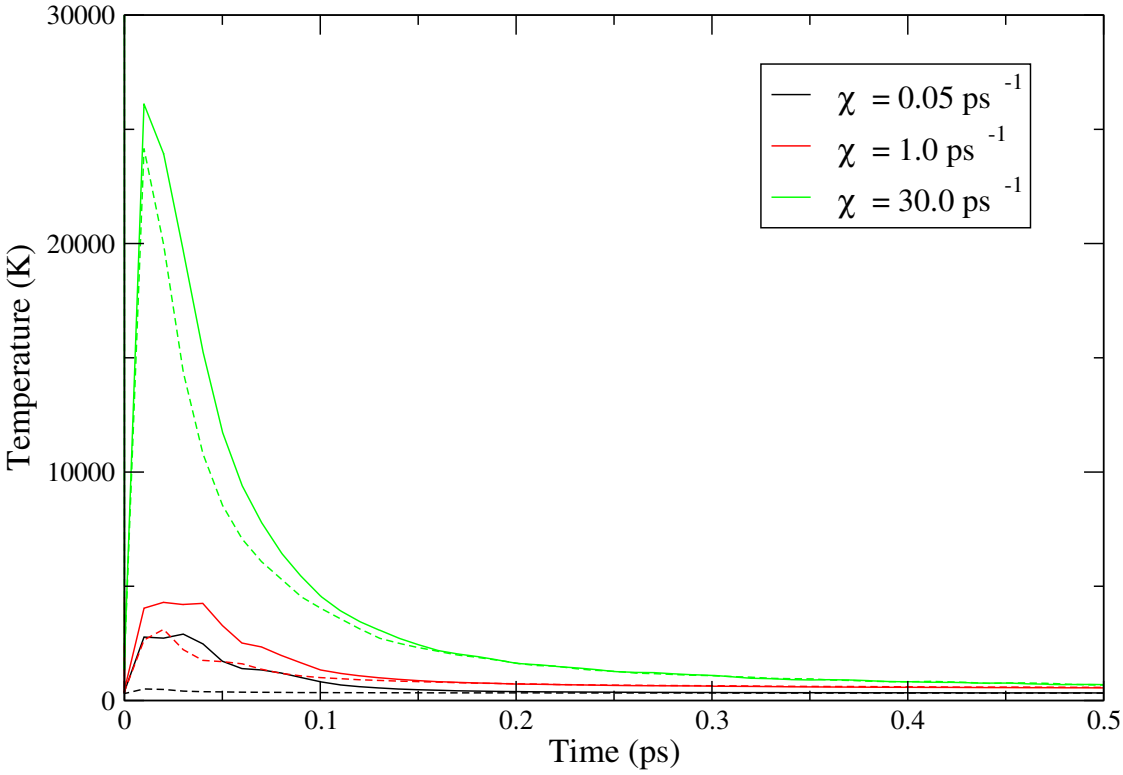

Figure 4.10: Core electronic temperatures with (solid line) and without (dashed line) stopping using inhomogeneous thermostat for 10 keV PKA dispalcement cascade.

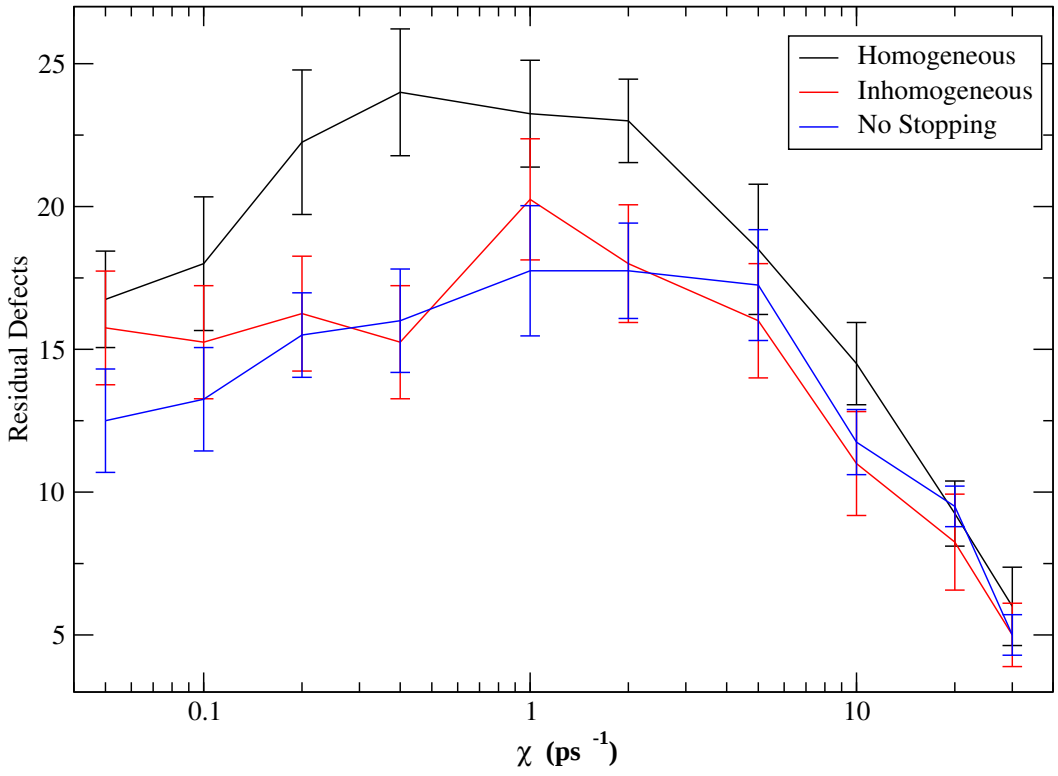

Figure 4.11: Residual defects as a function of coupling strength for 10 keV PKA displacement cascades.

4.2 Low PKA Energy Cascades

The mechanisms we have introduced in our methodology describe processes which must be taken into account above very low energies. In particular electronic stopping, which only acts upon atoms with an individual velocity above a certain threshold, and electronic heating which becomes more significant at higher cascade energies. The simulation of a range of PKA energies allows an estimate of the importance of these mechanisms at different cascade energies. There have been investigations of the scaling of residual defect numbers with energy from large numbers of simulations using traditional simulation techniques with which our results can be compared.

To initiate the thermal spike in the atomic system, a large velocity was given to one atom, the PKA in the centre of the simulation cell. The PKA velocity for energies of $1\,keV$, $2.5\,keV$, $5\,keV$, $7.5\,keV$, $10\,keV$ and $12.5\,keV$ corresponds to $587.91\mathring{A}ps^{-1}$, $929.57\mathring{A}ps^{-1}$, $1314.62\mathring{A}ps^{-1}$, $1610.07\mathring{A}ps^{-1}$, $1859.15\mathring{A}ps^{-1}$ and $2078.59\mathring{A}ps^{-1}$ respectively. The coupling strength was fixed at $\chi = 1.0\,ps^{-1}$

4.2.1 Defect-Energy Relation

According to Bacon *et al* [233], the number of residual defects following a cascade with varying PKA energy is given by (4.2) as discussed in section 1.4.2. Fig (4.12) shows the data and fit

$$N_{FP} = A\,(E_{PKA})^m \tag{4.2}$$

These are compared for the homogeneous thermostat, inhomogeneous thermostat and inhomgeneous thermostat without stopping i.e. with just the effect of coupling to a finite heat capacity heat bath. Each data point represents the average of 8 non-identical starting configurations; positive and negative velocities in the $\langle 110\rangle, \langle 010\rangle, \langle 001\rangle$ and $\langle 110\rangle$ directions. Error bars are calculated from the standard deviation of the defect numbers.

The values found for A and m in (4.2) are presented along with the corresponding R^2 values for the fits which measure how closely the data lie to the fit, a value of 1 representing a perfect fit and 0 no fit. The values for m demonstrate how defect numbers scale with energy and they are of most interest for comparison. This is because the method of classifying and detecting defects, as well as details of simulation technique such as potential stiffening will determine the cascade morphology and so the *absolute* number of defects produced, A. While the pre-factor for the homogeneous fit is considerably lower than that quoted in [233], the exponent is in respectable agreement considering the potential for variation with simulation technique. No measure of scatter is given in [233].

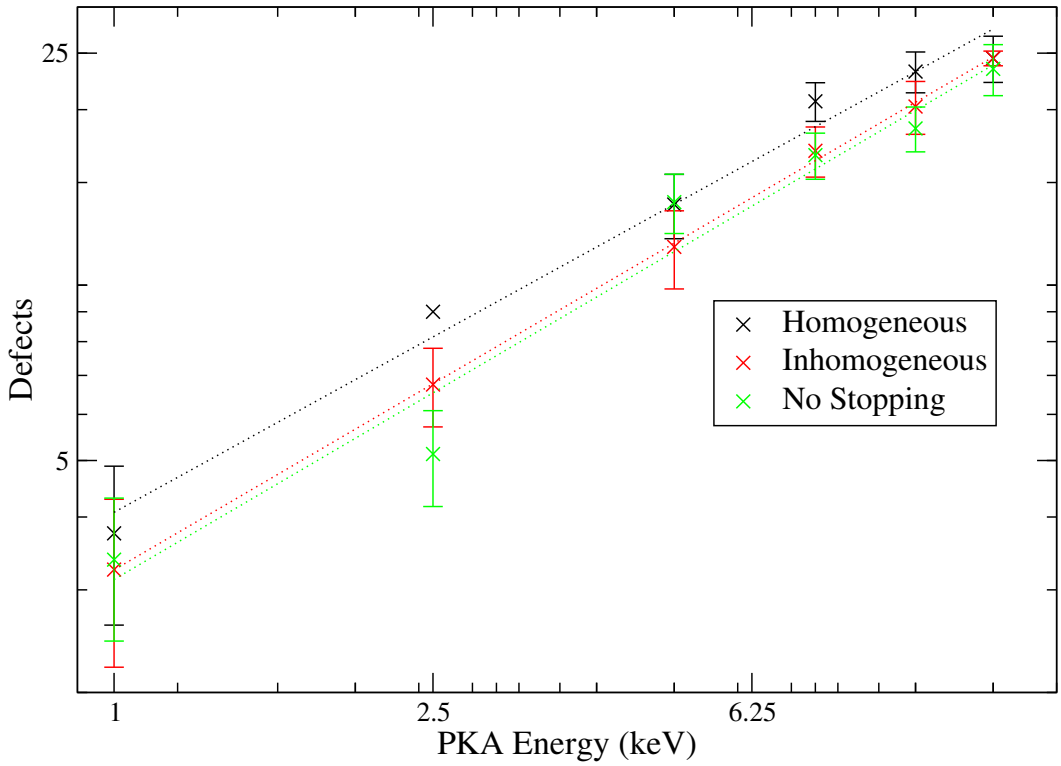

Figure 4.12: Plots of residual defects as a function of PKA energy.

	A	m	R^2
Bacon [233]	5.67	0.779	-
Homogeneous	1.405	0.756	0.9847
Inhomogeneous	1.177	0.802	0.9993
No stopping	1.127	0.824	0.9540

Table 4.2: Parameters of fit to (4.2) as found by Bacon compared to homogeneous and inhomogeneous thermostats

A reduction in the defect production efficiency is found between the NRT formula within the BCA, which cannot describe defect annihilation and annealing, and a full atomistic simulation. This is manifested by a reduction in the energy exponent m from unity to less than 1. It might be expected that a further reduction be observed between an inhomogeneous and homogeneous thermostat as the elevated electronic temperature will encourage annealing; and this is in fact observed as the inhomogeneous data lies below that for the homogeneous. However the data is preferentially fit to a lower m and a higher A.

The fit for the no stopping data lies slightly below that for the full inhomogeneous thermostat. This is counterintuitive as stopping effectively quenches the early stages of a cascade and is equivalent to a reduction in the cascade energy when the dynamics are

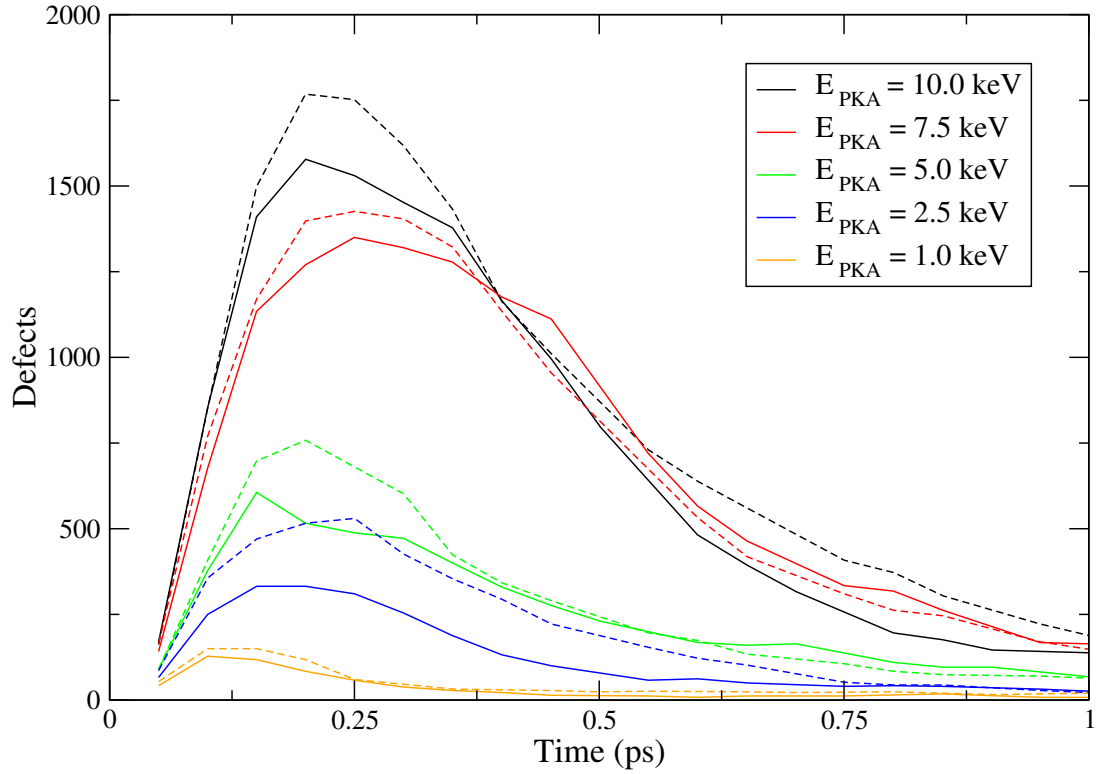

Figure 4.13: Plots of instantaneous number of defects as a function of time for a range of PKA energies using an inhomogeneous thermostat with (solid line) and without (dashed line) electronic stopping.

coupling limited, as energy removed from the atoms via stopping is quickly dispersed. However since there is only a small difference in the fits relative to the size of the error bars, and the individual data points are not consistently above or below one another, it can be concluded that there is no systematic difference. It should be noted that the supression of the formation of a disordered core via stopping increases dramatically with energy since the collisional phase is much longer, as seen in the plot of atomic displacements over time shown in Fig. (4.13). At $E_{PKA} = 10keV$ up to ≈ 100 atoms are in the electronic stopping regime, while at $E_{PKA} = 1keV$ only the PKA lies in the stopping regime. Therefore at higher energies it is likely that some systematic differences will be observed with the inclusion of stopping.

4.2.2 Defect Distribution

Fig. (4.14) shows the average radial distance of interstitial atoms and vacancies from the starting position of the PKA as a function of energy. Spherical symmetry is assumed, although the shape of the disorder more closely resembles an ellipsoid as the early stages of the higher energy events are highly ballistic and the spread of energy is anisotropic. The size of the error bars are given by a standard deviation of the average defect radius in each simulation.

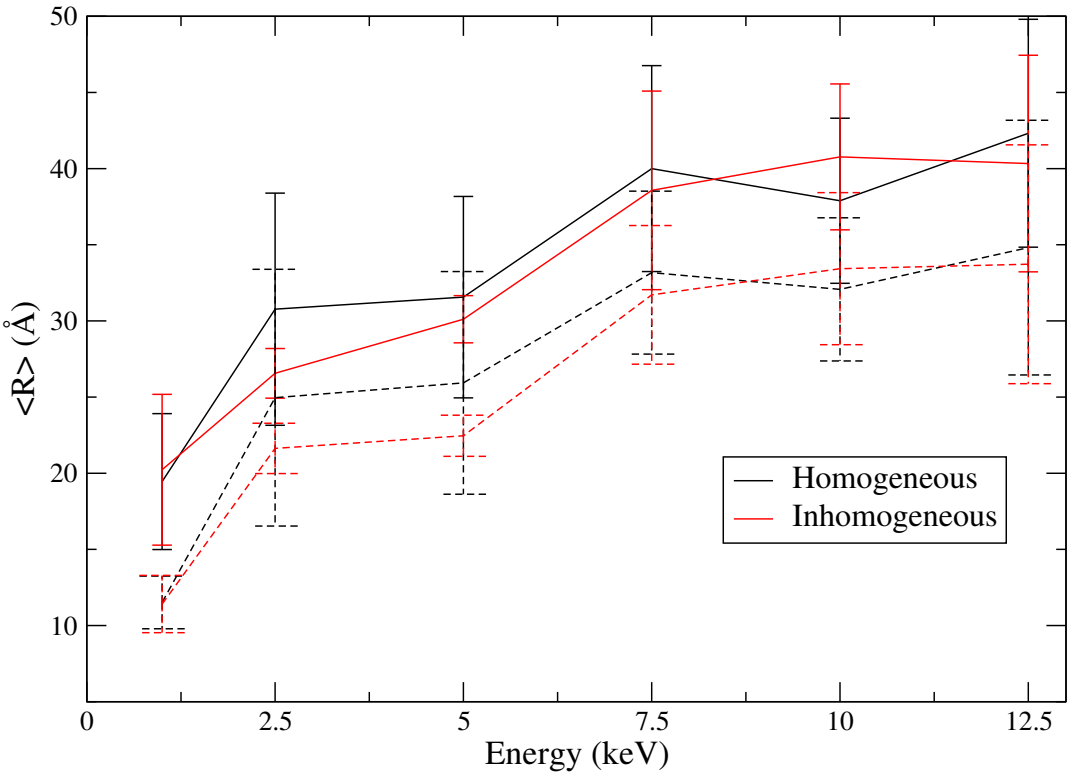

Figure 4.14: Average radius of interstitial atoms (solid line) and vacant sites (dashed line) as a function of cascade energy.

The disparity in mobility can be seen immediately. The interstitials move out from the core leaving vacant sites in the core in all cases. Increasing the cascade energy increases the size of the melted zone and the size and duration of the thermal gradient out of the core which results in increased thermally assisted migration. Also more focussed collision mechanisms are activated allowing rapid mass transport. Little systematic difference is seen, at these energies, with and without stopping given the large spread in results. Therefore these datasets have been omitted for clarity. The inhomogeneous thermostat, in general, lies below the homogeneous dataset. It is possible that this trend is attributable to ballistic damping via stopping, but given the scatter in results this is inconclusive.

In summary, both the mechanisms of electronic stopping and coupling have been investigated in displacement cascades. The strength of the coupling between electrons and phonons emerges as our main parameter and two different regimes are seen. With strong coupling dynamics are determined by the speed with which energy may be removed by electronic diffusion and under weak coupling the relaxation is limited by the rate at which energy may be transferred from the atoms into the electronic system. The presence of electronic stopping acts to damp the ballistic stage of the cascade and so causes the cascade to relax more quickly, by rapidly removing energy in the early stages. As a result of both of these mechanisms, reduced damage is seen over a large range of coupling strength with our inhomogeneous thermostat, in comparison to a homogeneous thermostat. The trend in damage with cascade energy was also investigated. The ballistic stage of a cascade depends strongly on the PKA energy, with the mechanism of stopping becoming more important as energy increases. The degree of residual damage was seen to be consistently lower, compared to previous published results, once a spatially varying electronic temperature was introduced over an energy range $1 - 12.5\,keV$.

Chapter 5

Ion Track Results

5.1 Ion Tracks in Fe

In chapter 4 we investigated displacement cascades, in which the PKAs are of relatively low energy and dynamics dominated by atomic collisions. In this chapter we seek to model events in the other extreme of the radiation energy spectrum, such as irradiation by swift heavy ions. Since the range of the knock on atoms will be large in this case, if such events were to be modelled as a series of atomic collisions the cell size required to contain the cascade would be prohibitively large. Also, under swift heavy ion irradiation, the rate of electronic energy loss is large and nuclear energy loss is negligible. Therefore we model the lattice after the passage of the swift heavy ion; the ion will leave a track of excited electrons in its wake. The swift heavy ion is assumed to have passed through the system in which a track of electrons with cylindrical symmetry is left at an elevated temperature. By varying the electronic thermal parameters and electron-phonon coupling strength the extent to which energy initially deposited in the *electronic* system may be transferred to the *atomic* system, and the resultant damage may be investigated. Further, we attempt to reproduce trends observed in swift heavy ion irradiation experiments in materials with different thermal parameters.

The stopping power corresponding to an excited temperature $T_e^{excited}$ can be calculated according to

$$S = A \int_{300}^{T_e^{excited}} C_e(T_e) \mathrm{d}T_e \tag{5.1}$$

where A is the area of the excited region. The initial electronic excitation in these simulations corresponds to a total initial energy of $\approx 4.38\,keV$ per temperature cell corresponding to a rate of energy loss of $\approx 10\,keV nm^{-1}$ for $T_e^{exc} = 7.5 \times 10^4 K$. The same potential of Dudarev [223] was used as for the previous section.

5.1.1 Temperature Evolution

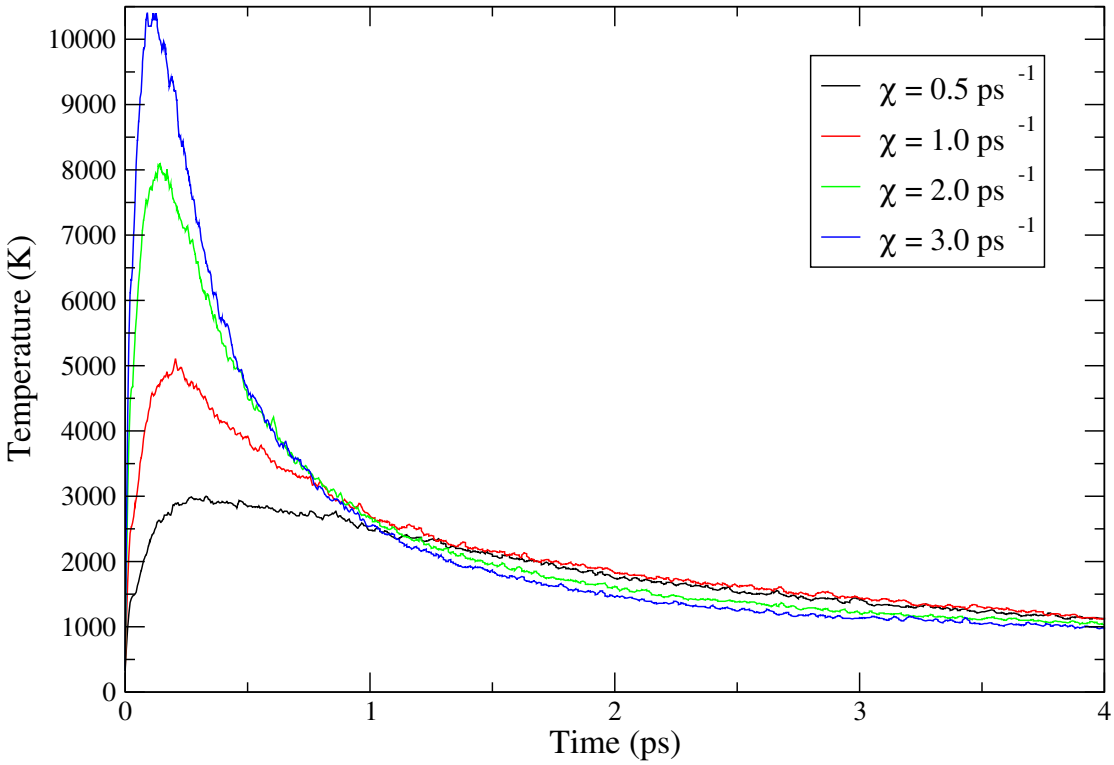

Figure 5.1: Peak atomic temperature in a $10keV\,nm^{-1}$ ion track as a function of time for a range of electron-phonon coupling strengths.

Figs. (5.1) and (5.2) show the evolution of both the peak atomic and electronic temperatures respectively as a function of time for varying coupling strength. The ions are intially cold and are heated by the electrons to a maximum temperature before heat diffuses to the boundary of the electronic system where it is removed. The value of this maximum atomic temperature is very sensitive to the coupling strength. Given that the melting temperature of Fe is $T_m \approx 1500K$, a small change in coupling strength can make the difference between a lattice which emerges undamaged and one in which considerable melting and disorder is seen along the track axis. Fig. (5.2) demonstrates that stronger coupling initially causes faster decay of the electron temperature as energy is removed by both swift diffusion and exchange with the lattice. However after $\approx 1ps$ this trend is seen to reverse. Under weak coupling, although the atoms reach a lower maximum temperature, they cool so slowly that they then act to heat the electrons at later times, which have since cooled. Conversely strong coupling causes more lattice heating when the electron temperature is high, but also allows swift relaxation of the atomic temperature once the electron system has begun to cool resulting in a significant temperature difference between the atomic and electronic systems. This causes faster quenching which may contribute to the higher number of residual defects observed under strong coupling. Thus the electrons can be seen to be acting as a strong heat bath at early times, and a heat sink at later

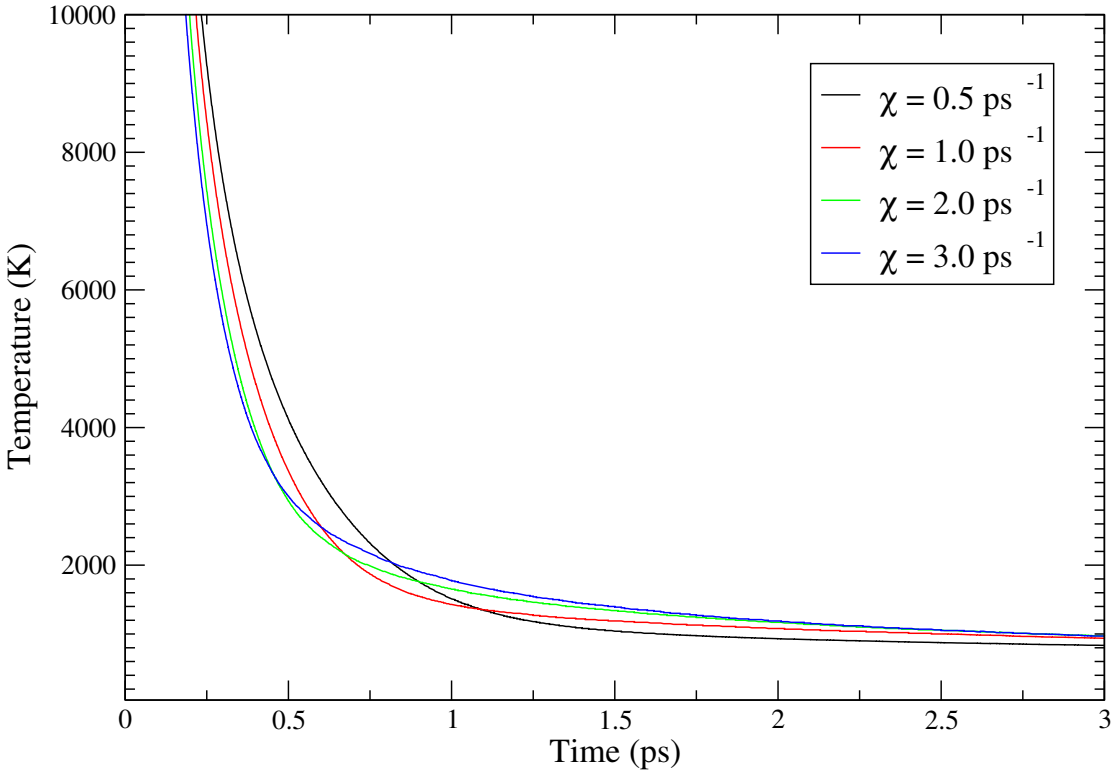

Figure 5.2: Peak electronic temperature in a $10\,keVnm^{-1}$ ion track as a function of time for a range of electron-phonon coupling strengths.

times. These results have been published in [234].

5.1.2 Residual Defects

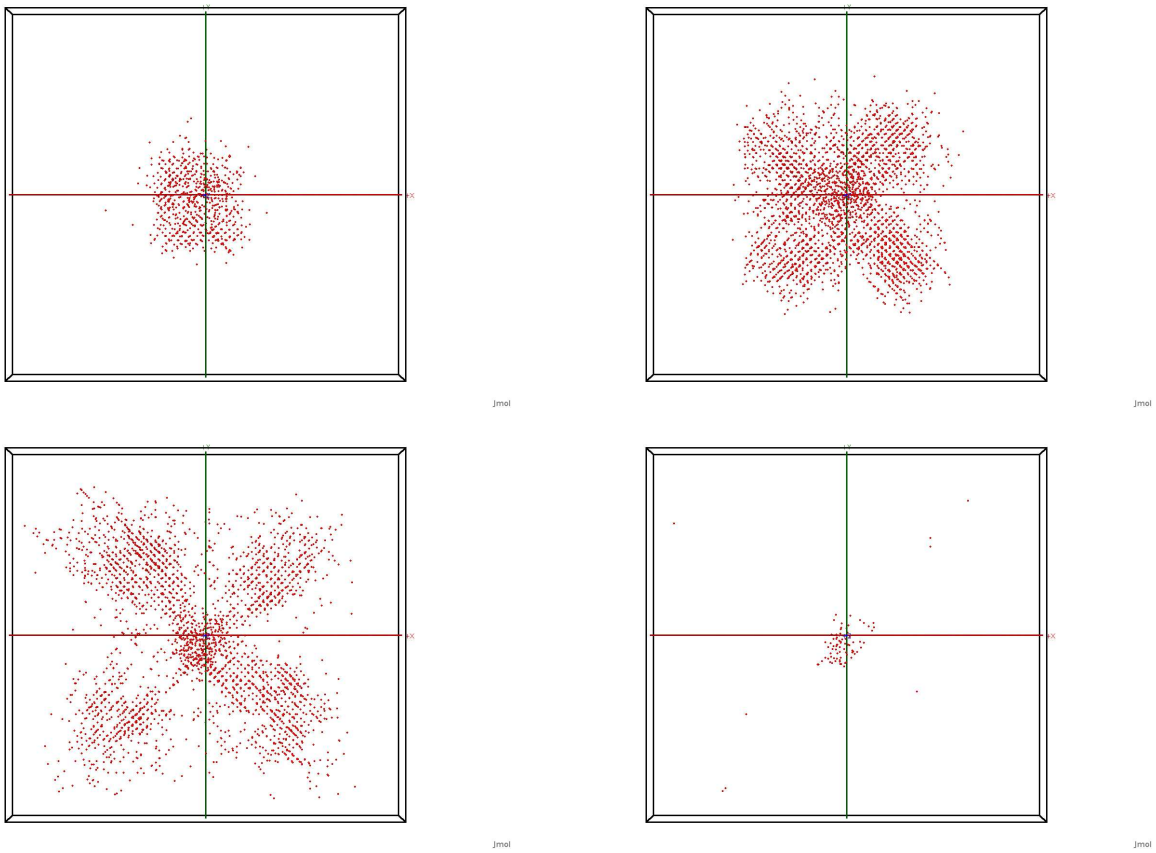

Figure 5.3: A 10 $\mathring{A}$ cross-section through the axis of an ion track in Fe at 0.45, 1.05, 1.65 and 2.25ps, from left to right top to bottom. Only interstitial atoms are shown.

Table (5.1) shows the maximum temperature reached in the lattice along the track axis, the diameter of the melted region and the number of residual defects. The melted region was in this case judged by inspection to be the small cylindrical region around the track axis in which the interstitials do not display any planar symmetry as they are effectively liquid and disordered. This is in contrast to interstitials far from the core which are seen to move coherently under thermal expansion. It can be seen that with each, relatively small, increase in coupling strength the degree of melting and final damage increases. It should also be noted that in the $\chi = 0.5\,ps^{-1}$ simulation, although the atomic temperature rose above the melting temperature of the model potential (see section 2.5.6), no melting was seen. This is likely to be due to both the short time scales for which this temperature persists, which does not allow full melting to take place, and cold matter surrounding the core region which constrains expansion. Both of these effects are physical to some extent although the geometry of the cell does give rise to an artificial 'X' shape (Fig. 5.3) in the displaced atoms since the atoms may expand more readily along diagonal directions in

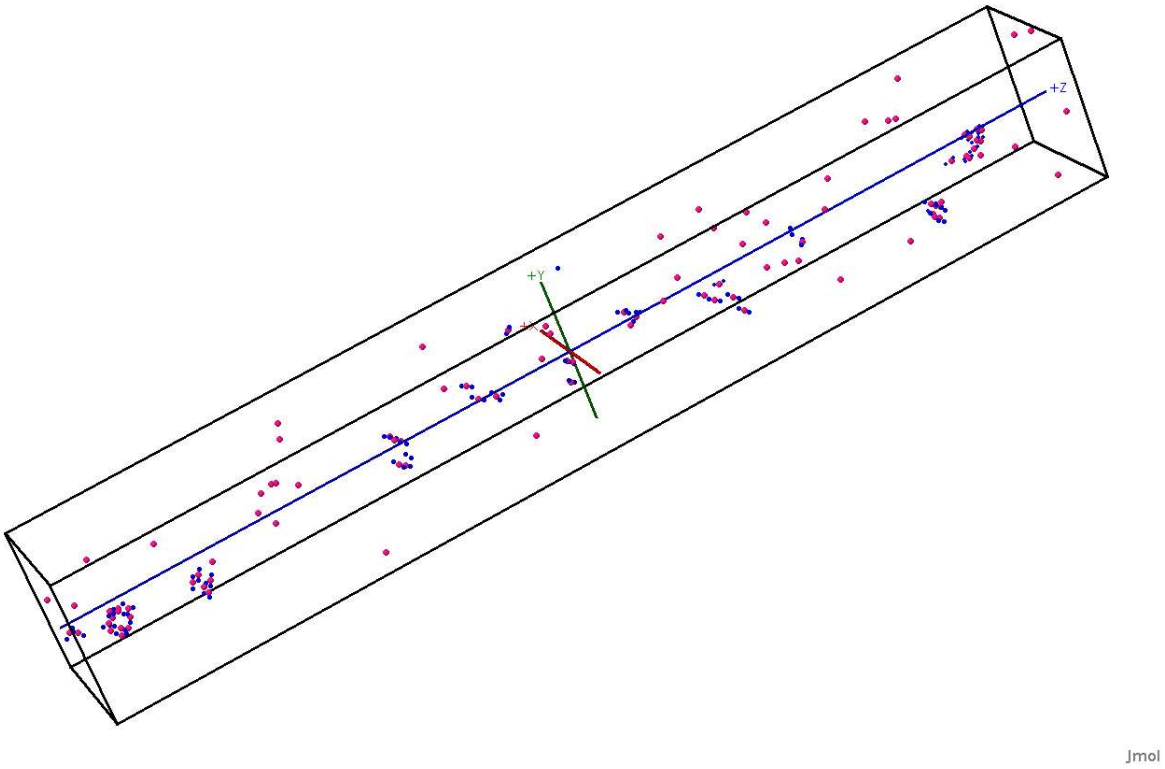

Figure 5.4: Residual defects formed along the axis of an ion track in Fe. Interstitial atoms are shown in blue and vacancies in red. The defects are formed along the length of the MD cell, $\approx 220\mathring{A}$

comparison to vertical and horizontal directions. Although the volume of the cell is fixed through our choice of ensemble, the cell may expand locally as long as it maintains its volume globally. For example the core of the ion track may expand, since it is of a higher temperature, provided the colder material surrounding it is able to compress. This is close to the physical situation in an isolated event where the region of interest is surrounded by a large amount of cold material constraining its expansion. It might be expected that in reality the lattice in the vicinity of the radiation event is somewhere between constant volume and constant pressure; while the cold material far from the event will suppress thermal expansion, it will absorb some of the energy in the pressure wave which leaves the core.

5.1.3 Thermal Parameters

In order to investigate the effect of the thermal parameters, the coupling strength was fixed at $\chi = 1.0ps^{-1}$, and the specific heat capacity and thermal conductivity varied.

$\chi(ps^{-1})$	$T_a^{max}(K)$	D_{melt} (nm)	N_{def}
0.5	3020	0	0
1.0	5100	2.3	46
2.0	8030	3.2	66
3.0	10400	3.6	84

Table 5.1: Maximum atomic temperature, maximum diameter of melted region and number of residual defects as a function of coupling strength in ion the track

Although these new values are unphysical, it allows investigation of the behaviour of the atomic system on these parameters. In particular, different behaviours have been seen in experiments on different metals; some demonstrate defect creation, defect annealing and some show no effect under irradiation. Fig. (5.5) shows this for various metals. High and low thermal conductivity divides metals which are unchanged, and those which see defect creation and annealing respectively, while high and low specific heat coefficient divides those which demonstrate defect annealing and defect creation respectively [24, 235, 236].

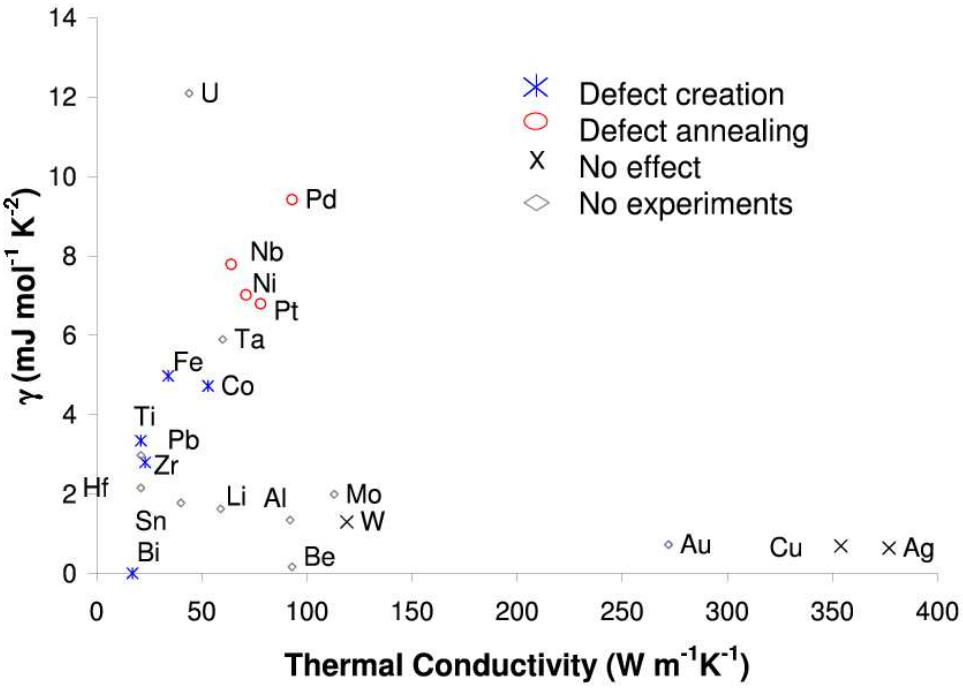

Figure 5.5: Behaviour of various metals under swift heavy ion irradiation.

5.1.3.1 Specific Heat

The specific heat coefficient (γ) was varied, increasing and decreasing the low temperature, linear part of the function and so the temperature of saturation (Fig. (5.6))

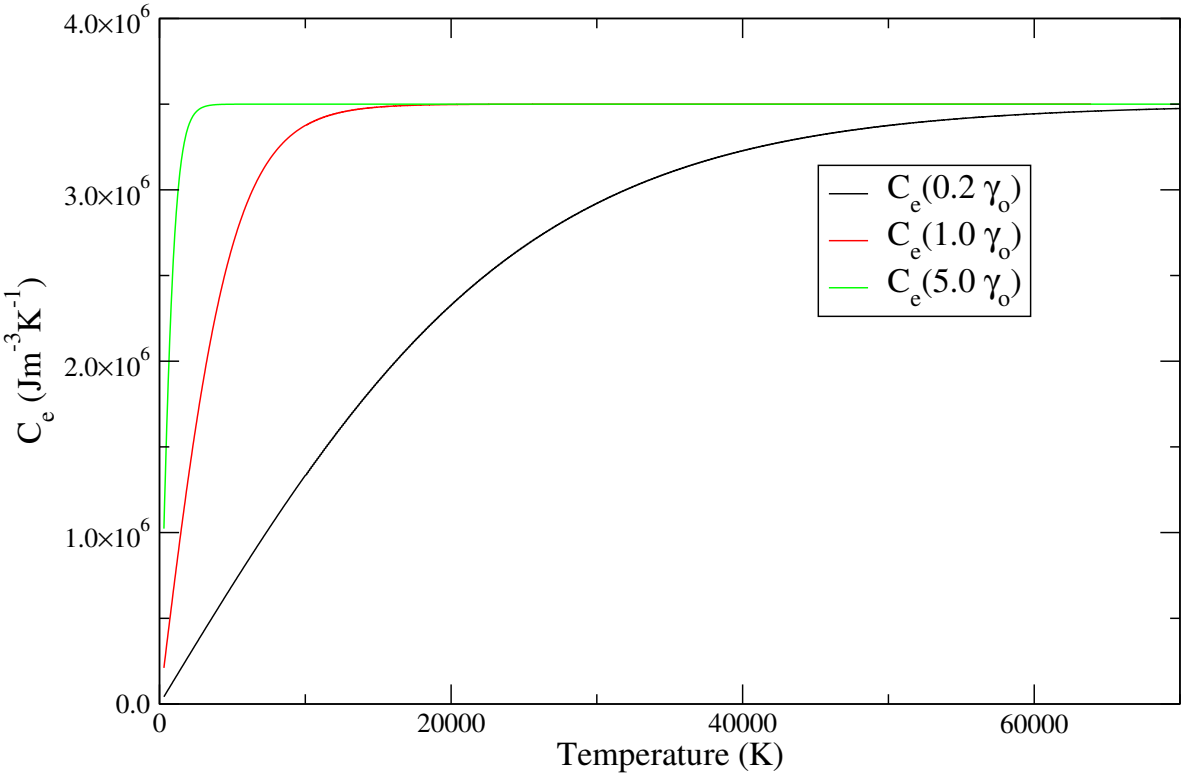

Figure 5.6: Electronic specific heat as a function of electronic temperature with different specific heat coefficients.

according to

$$C_e = \frac{3}{2} k_B \, tanh(\gamma \, T_e / 3k_B) \tag{5.2}$$

A lower value of γ leads to a lower specific heat at low temperatures. The electronic and atomic cooling curves are plotted in Fig. (5.7) and (5.8), and the curves labelled by the multiple of the low temperature specific heat coefficient γ, the values of which are given in table (5.2).

γ	$T_a^{max}(K)$	D_{melt} (nm)	N_{def}
0.2 γ_o(1 $mJ\,mol^{-1}\,K^{-2}$)	5340	3.6	48
1.0 γ_o(5 $mJ\,mol^{-1}\,K^{-2}$)	5100	2.8	46
5.0 γ_o(25 $mJ\,mol^{-1}\,K^{-2}$)	4730	2.0	42

Table 5.2: Maximum atomic temperature (T_a^{max}), maximum diameter of melted region (D_{melt}) and number of residual defects N_{def} as a function of the specific heat coefficient in an ion track

Fig. (5.7) demonstrates a higher peak atomic temperature with a lower specific heat

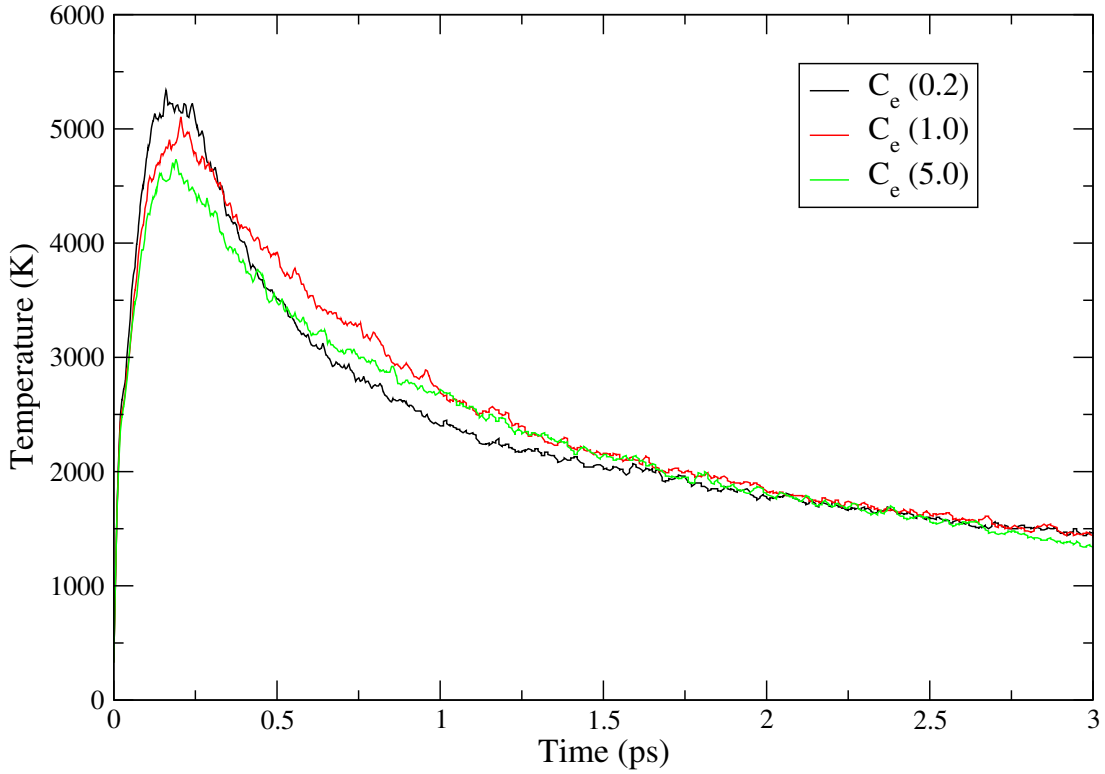

Figure 5.7: Peak atomic temperature in a $10keV\ nm^{-1}$ ion track as a function of specific heat.

coefficient, with faster subsequent relaxation and vice-versa for a large specific heat coefficient. Fig. (5.8) shows that the electron temperature decays significantly faster with a lower specific heat coefficient at intermediate times, yet slower at very short times. Since the electronic diffusivity $\alpha_e = \kappa_e/C_e$ is inversely proportional to specific heat capacity, faster relaxation of the electronic temperature spike would be expected with a lower specific heat capacity at all times. However on further investigation, using simple two-temperature model calculations, this was seen to be attributable to a non-linear effect in the diffusion away from the core as the diffusive profile began to evolve.

The solution of the heat diffusion equation using temperature dependent thermal parameters will be highly non-linear. The electronic temperature profile varies from the extremes of up to $\approx 10^5 K$ at the core when saturation at the classical value might be expected, to $300K$ on the boundary. Within the finite-difference integration scheme, the temperature evolution of a single cell is determined by its nearest neighbours. However, since *these* cell's temperatures are *themselves* determined by *their* nearest neighbours; all the cells are indirectly determined by all the others. As a result, the introduction of anything but simple monotonic temperature dependences will lead to complex behaviour.

There is some difficulty in comparing these simulations since the form of the specific

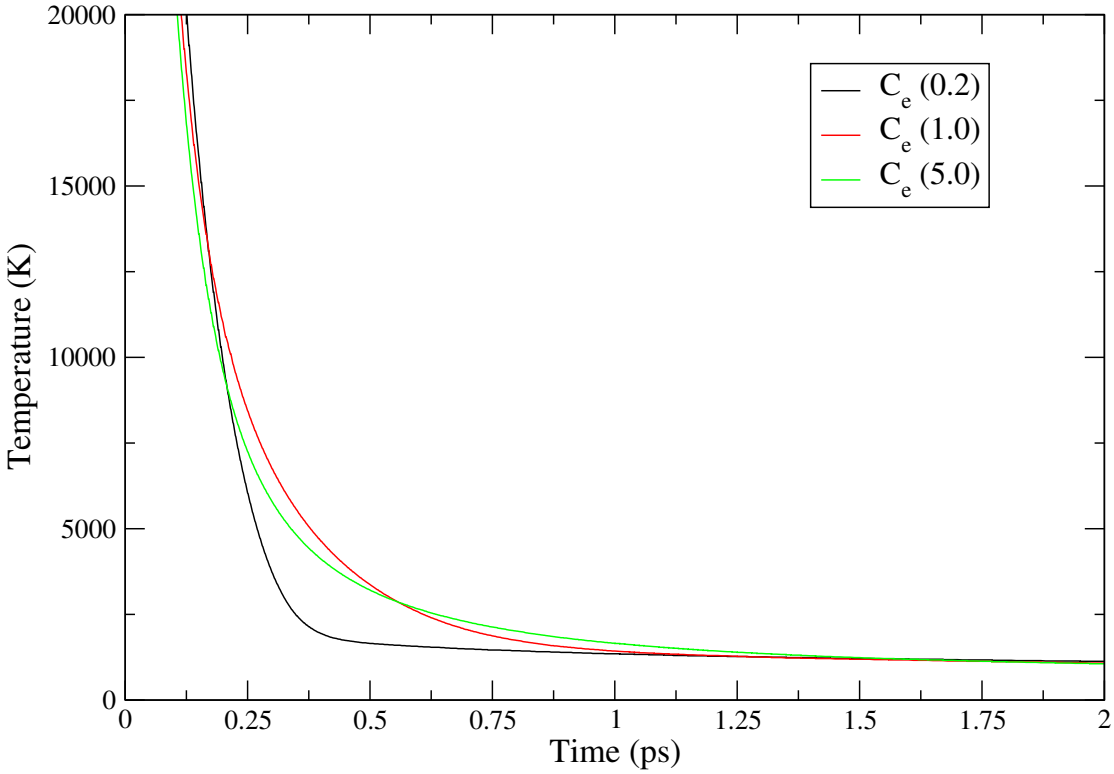

Figure 5.8: Peak electronic temperature in a $10\,keVnm^{-1}$ ion track as a function of specific heat.

heat determines the increase in energy for a given increase in temperature (according to (5.1)). All the different specific heat forms investigated used a fixed value of 7.5×10^4 for the initial electronic temperature, corresponding to a lower value of energy loss for 0.2 γ_o and slightly higher for 5.0 γ_o.

5.1.3.2 Thermal Conductivity

Figs. (5.9) and (5.10) show atomic and electronic cooling curves for a range of thermal conductivities. Fig. (5.9) clearly shows a lesser degree of heating and faster relaxation over all time scales as the thermal conductivity increases. Likewise Fig. (5.10) demonstrates faster relaxation as the thermal conductivity increases, consistent with a larger diffusivity. The residual damage and maximum core temperature observed in the lattice are very sensitive to the thermal conductivity. A relatively small change can mean the difference between a lattice which is left essentially undamaged to a situation where significant melting and residual damage is seen.

Since the degree of damage in an ion track is, unlike a cascade, always dominated by diffusion there is a very sensitive dependence on the thermal parameters of the electron subsystem. The speed with which the initial spike in the electron temperature relaxes by diffusion will determine how much energy energy persists to be transferred to the lattice by

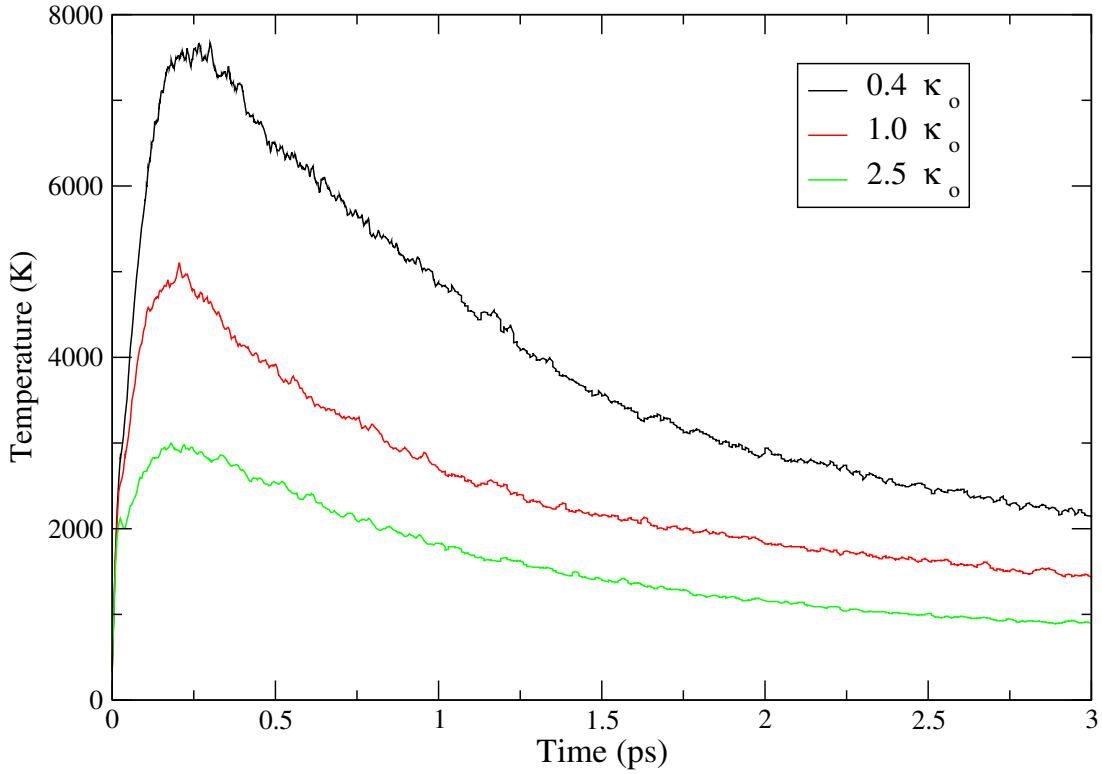

Figure 5.9: Peak atomic temperature in a $10keV\,nm^{-1}$ ion track as a function of time for a range of thermal conductivity.

coupling. Thus the degree of damage will be sensitive to the following ratio $\frac{\chi C_e}{\kappa_e} = \alpha_e \frac{\tau_{diff}}{\tau_{epc}}$.

$\kappa(Wm^{-1}K^{-1})$	$T^a_{max}(K)$	$D_{melt}\ (nm)$	N_{def}
0.2 (20)	9140	11.6	122
1.0 (80)	5100	2.8	46
2.5 (200)	3530	0	0

Table 5.3: Maximum atomic temperature, maximum diameter of melted region and number of residual defects for a range of thermal conductivity in ion track

In summary, we have simulated the track of electronic excitations along the path of a swift heavy ion in Fe. This initial temperature spike diffuses through the electronic system, a proportion of which is transferred into the lattice causing a degree of melting and defect creation, dependent on the coupling strength and electronic diffusivity. Melting is seen only when the temperature rises well above the temperature of melting of the model potential. When melting occurs residual defects are seen up to $\approx 20-40\ \AA$ from the track axis while thermal expansion is seen far from the core giving some atomic displacements which subsequently undergo recombination. The degree of damage is very sensitive to the coupling strength and the electronic diffusivity.

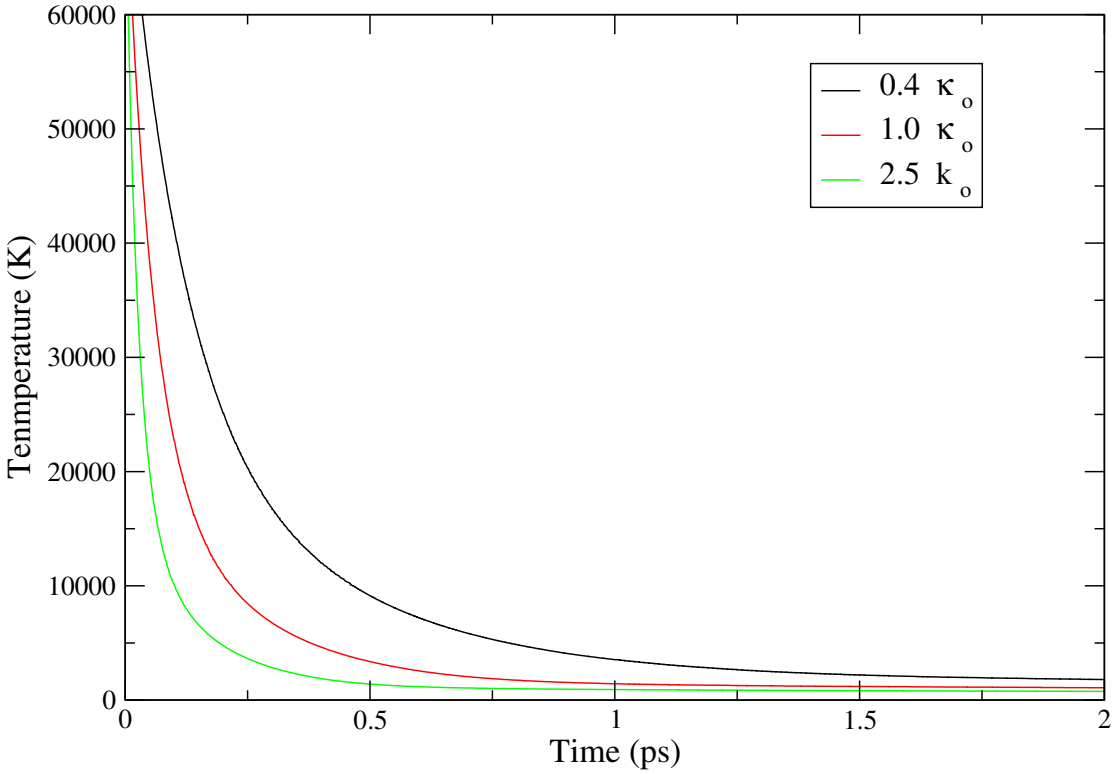

Figure 5.10: Peak electronic temperature in a $10\,keVnm^{-1}$ ion track as a function of time for a range of thermal conductivity.

Our findings are in agreement with the experimental trends in swift heavy ion irradiation shown in Fig. (5.5). Low values of thermal conductivity are seen to encourage defect annealing and creation, while higher values correlate with the irradiation having no effect on the lattice as energy diffuses away very quickly. Our simulations also suggest that a high thermal conductivity leaves the lattice unchanged while a low value causes defect creation. Similarly the trend in specific heat coefficient observed in experiment is seen in our simulations, low values correlate most closely with defect creation. Since our starting configuration was undamaged, we were unable to investigate the parameters required for defect annealing. However we consider the effect of electronic excitation on an initial damage configuration in the next section.

5.2 Radiation Annealing in Fe

Having investigated the degree to which an excitation of the electronic system may produce damage in the lattice, a final damage configuration resulting from a cascade is used as the starting configuration for a subsequent electronic excitation as in section 5.1. The degree of defect creation and and annealing is examined and compared to experimental results, and any effect on the distribution of defects monitored.

In order to investigate the effect of electronic excitation on a pre-existing damage configuration, an initial defect distribution was produced by initiating a $30keV$ cascade in the cell using the method described in section 4. This was allowed to relax for around $5\,ps$ resulting in a distribution of 101 Frenkel pairs, with roughly half in dumbell configurations and the rest producing isolated defects and clusters equally. Fig (5.11) shows the defects resulting from the cascade.

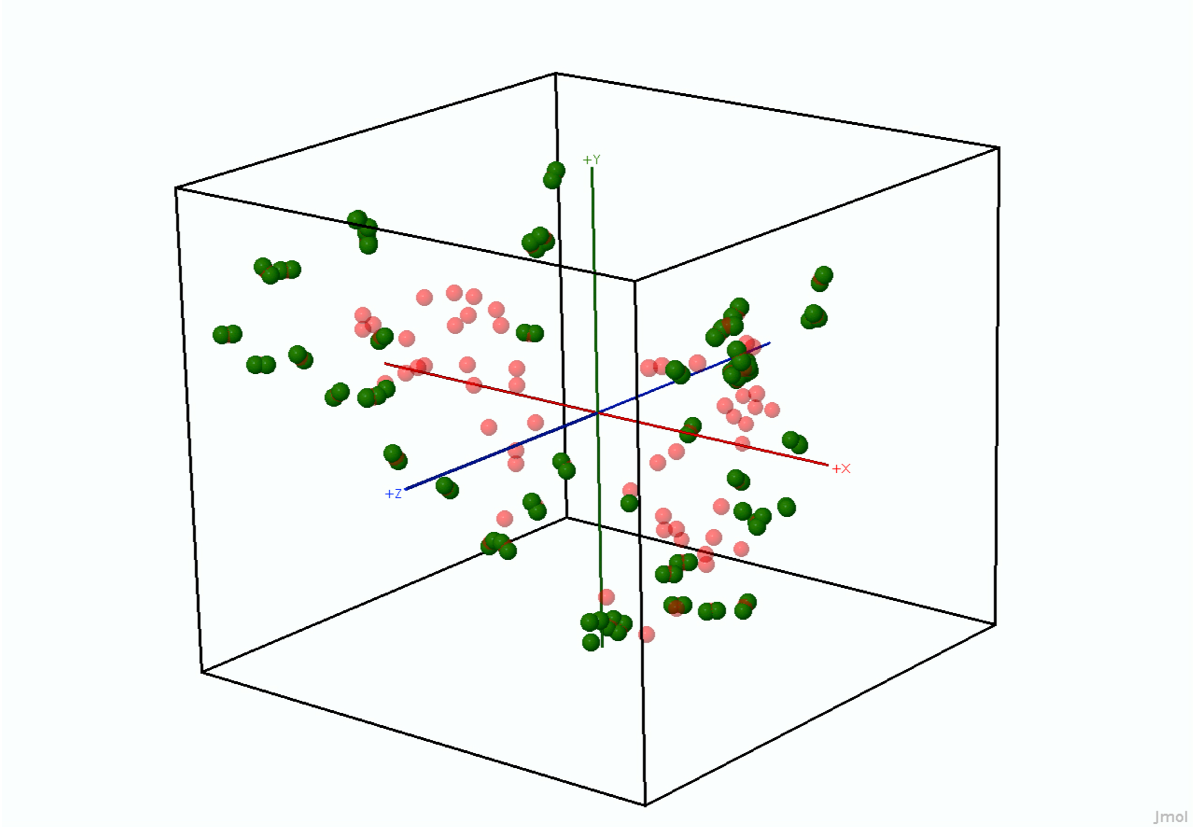

Figure 5.11: Defect distribution after 30 keV cascade initiated in the x-direction. Interstitials are shown in green and vacancies in red. The length scale of the bounding box is $\approx 100\mathring{A}$.

Figure (5.12) shows the temperature evolution following excitation at two different

levels of stopping corresponding to $T_{exc} = 100,000\,K$ and $14,390\,K$ for $14keVnm^{-1}$ and $4keVnm^{-1}$ respectively.

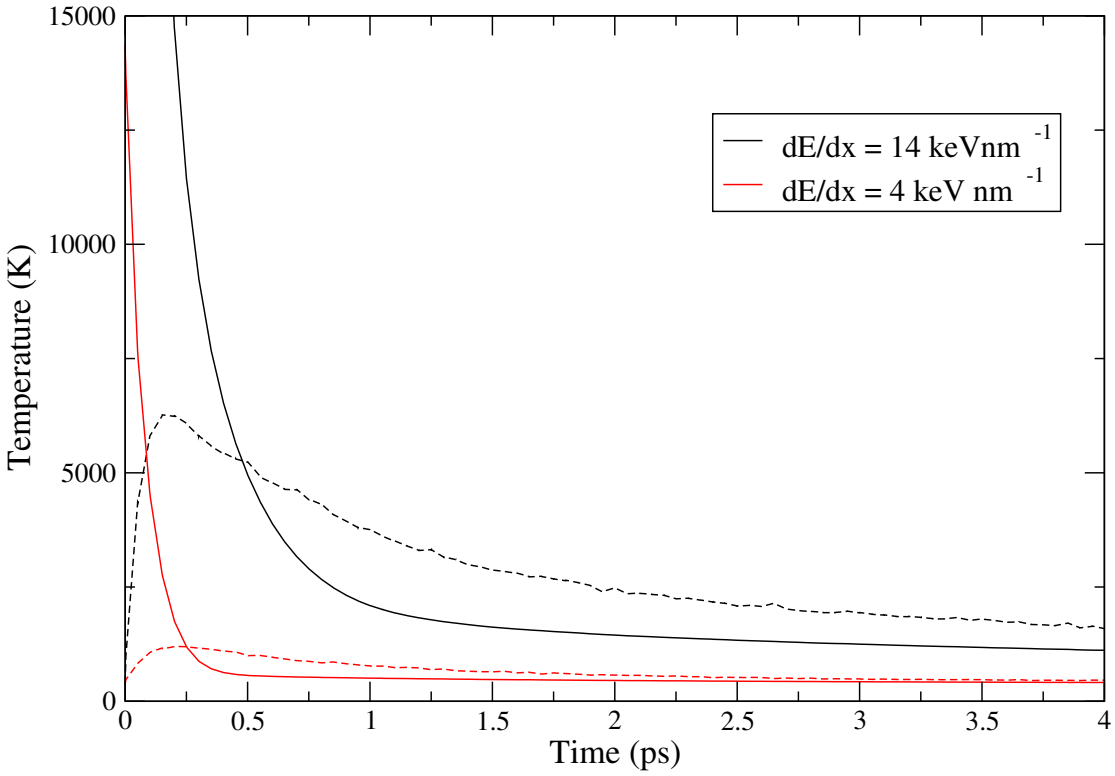

Figure 5.12: Evolution of temperature of electrons (solid line) and atoms (dashed line) in core for a stopping power of 10 and $4keVnm^{-1}$.

5.2.1 Defect Distribution

The defect distribution produced by the initial cascade was modified by the ion track simulation. Some defects remained unchanged, some moved from the original position and some were annihilated. Figure (5.13) shows the defects following electronic excitation with a stopping power of $14keV\,nm^{-1}$. New defects can be seen along the track axis and some defects originating from the initial damage state remain up to $70\mathring{A}$ from the track axis.

The defects from each simulation are summarised in Table (5.4). The initial and final defect configurations were compared to see the effect of the electronic excitation on the cascade defect distribution. These were classified as follows; any atom in an interstitial position in the initial, but not in the final, configuration is said to be *annealed*. Any interstitial which remains within $1.0\,\mathring{A}$ of its starting position in the final configuration is said to be *persisting* and a defect further than $1.0\,\mathring{A}$ is said to have *migrated*. Atoms which occupy interstitial positions in the final configuration, but not the initial, are classified as *new* defects. The number of defects are related as follows

$$\mathrm{N_{final}} = \mathrm{N_{initial}} + \mathrm{N_{new}} - \mathrm{N_{annealed}} \tag{5.3}$$

$$\mathrm{N_{final}} = \mathrm{N_{persisting}} + \mathrm{N_{migrated}} + \mathrm{N_{new}}$$

The number of defects will fluctuate even at $300K$, since single defects will move from isolated configurations to dumbell configurations and may anneal completely, since the spontaneous recombination volume will be small, but non-zero at this temperature but non-zero. The maximum number of defects in the course of the simulation is only quoted in Table (5.4) when this number is above that due to fluctuations in dynamic equilibrium. In order to get a quantitative estimate of the degree of melting, it is necessary to decouple this from replacement and fluctuations between isolated and dumbell configurations, both of which will be interpreted as annealing and new defect creation. In order to do this, the non-mobile, isolated vacancies, which are located more than $1.0\mathring{A}$ from an interstitial, were identified and their evolution monitored. Since these vacancies were isolated, and clustered around the track axis, they could not annihilate with any nearby mobile interstitials. Therefore the only means by which they could annihilate is under local melting. Comparison of the number of these initial vacant sites which did not match between the initial and final configurations gave $\mathrm{N}_{\mathrm{vacancies}}^{\mathrm{isolated,nomatch}}$.

The maximum temperatures reached by the atoms and final defect numbers tabulated in table (5.4) are extremely sensitive to the initial elevated temperature. Consequently, significant melting in a small radius of $\approx 10-15\mathring{A}$, leaving damage along the track, is seen only in the $\frac{dE}{dx} = 14, 10$ and $6keV\,nm^{-1}$ datasets. Fig. (5.14) shows a histogram of defects by cylindrical radius (bin width $6\mathring{A}$). New defect creation is seen up to $R \approx 15\mathring{A}$ in the

$\frac{dE}{dx}(keV\,nm^{-1})$	$N_{defects}^{max}$	T_i^{max} (K)	Migrated	Persisting	Annealed	New	Final	$N_v^{i,nm}$
14	11,265	6,268	0	0	101	235	235	106
10	6,450	4,691	5	2	94	90	97	46
6	165	3,131	8	8	85	64	80	17
4	-	2,197	12	23	66	47	82	5
2	-	1,196	11	54	36	24	89	1
1	-	689	0	70	31	13	83	0

Table 5.4: Table showing; maximum disorder, maximum temperature reached in core T_i^{max}, numbers of migrated, persisting, annealed, new and final defects as a function of stopping rate and the number of unmatched, isolated vacancies.

$\frac{dE}{dx} = 14nm^{-1}$ dataset as a result, and annealing is observed at intermediate distances. There is a trend, observable in all cases, of interstitials moving away from the track axis to occupy radii $> 66.0\mathring{A}$ where no interstitials were found after the cascade. The final radial distribution of the defects is in part determined by the cascade evolution which formed the starting damage.

In displacement cascades interstitials are seen to exit the core swiftly leaving a vacancy rich core (see section (4.2.2)). As a result the starting atomic configuration of the electronic excitation has vacancies at a smaller spherical radius from the inital PKA position than interstitial atoms.

The number of persisting defects decreases as the stopping strength increases because the higher temperatures led to an increased rate of thermal migration. This increased the rate of recombination and resulted in an increased number of annealed atoms. Although significant new defects are formed down to the lowest stopping powers, a simple comparison of the interstitial atom identities is an overly simplistic measure of new damage. In fact the majority of these are due to replacement mechanisms causing the identity of the interstitial atom to change but with no net change in the number of interstitial atoms. The value of $N_{vacancies}^{isolated,nomatch}$ gives a good measure of melting and shows it to be proportional to stopping power.

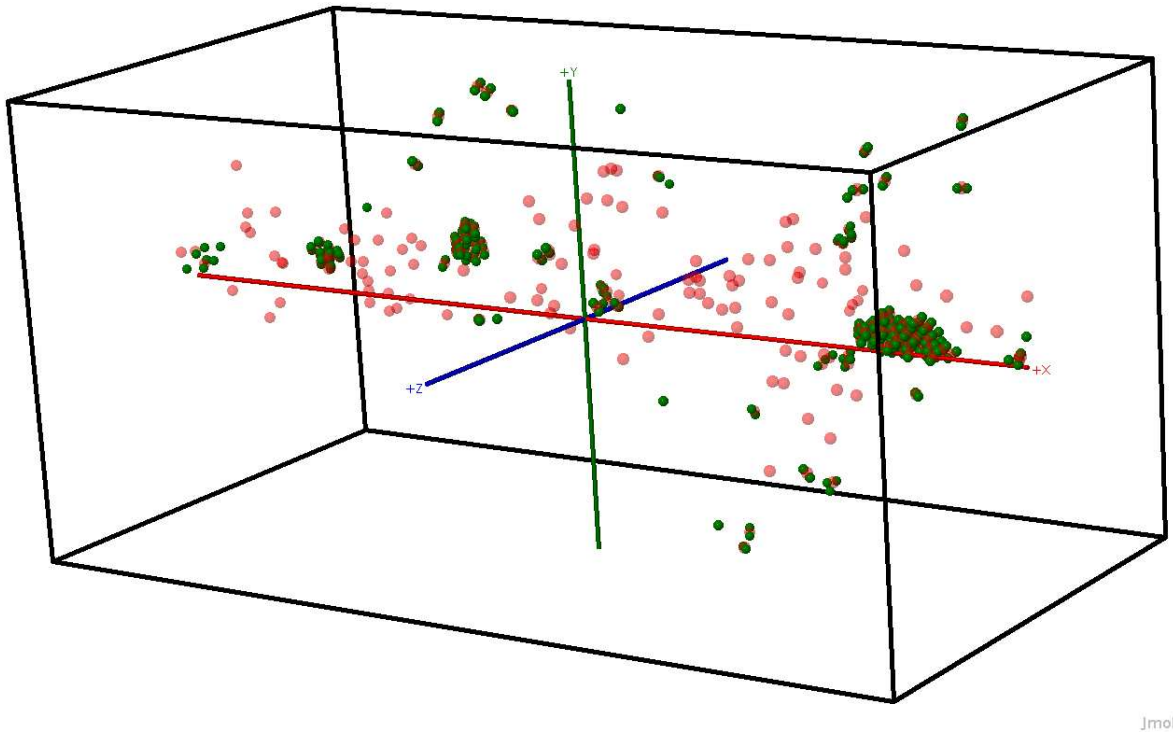

Figure 5.13: Defect distribution following electronic excitation with $\frac{dE}{dx} = 14keV\,nm^{-1}$. Interstitials are shown in green and vacancies in red. Defects are distributed along the length of the MD cell, $\approx 220\mathring{A}$.

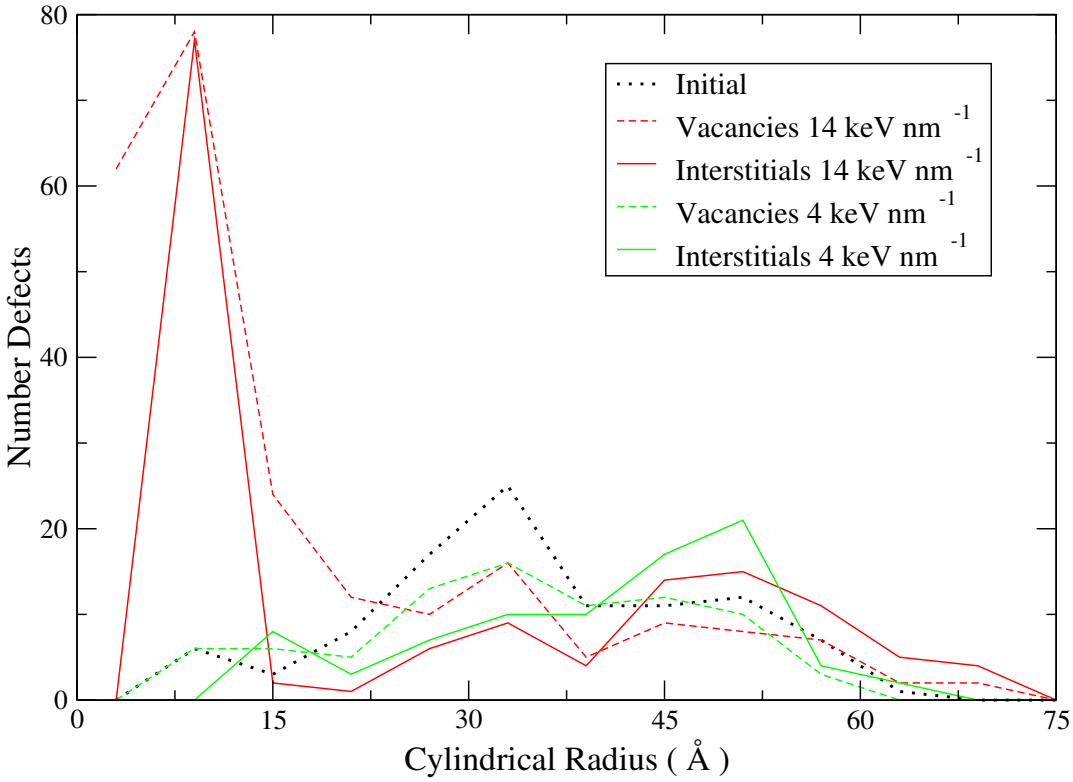

Figure 5.14: Histogram of final and initial vacancies at high and low stopping powers with cylindrical radius from track axis.

Some migration of vacancies takes place, but at a much slower rate than interstitials, leading to a clear separation of interstitials and vacant sites. In the cases where new vacancies are created ($(\frac{dE}{dx})_e > 10keV\,nm^{-1}$) close to the ion's path, the interstitial atoms are immediately transported away leaving a vacancy rich core. The relatively high interstitial mobility is in agreement with quoted values for migration energies using the Dudarev potential [222]; $0.34eV$ and can be an order of magnitude lower for clusters. This separation of intersitials and vacancies means the proportion of Frenkel pairs which can recombine is limited, which is reflected by the fact that the number of final defects is roughly constant for all but the highest energy datasets, suggesting only a fixed number of interstitials are in configurations from which they may find a vacant site to annihilate with.

5.2.2 Replacement Sequences

During the course of the simulations described above with higher stopping powers, sequences of replacement events were observed. Single interstitial atoms were seen to fluctuate between isolated interstitial sites and dumbell configurations, the original interstitial atom may then replace the displaced lattice atoms. Chains of these sequences allow interstitial atoms to leave the track core very efficiently.

Figs. (5.15) and (5.16) shows two chains of replacement mechanisms over time observed during a $14keVnm^{-1}$ irradiation. 400 samples are superimposed over a time period of around $4ps$. Overall motion is in the $\langle\overline{1}\overline{1}1\rangle$ direction.[1]

In addition to chains of replacement sequences, fluctuations between dumbell configurations and isolated interstitials are seen. Both mechanisms cause the number and identity of interstitial atoms to change, but do not represent new damage. As in displacement cascades, these chains of replacement mechanisms are seen along close packed directions. In the case of bcc Fe this corresponds to the $\langle 111\rangle$ directions. Thermal expansion is also likely to encourage migration along the close packed directions in an outward radial direction.

As a result of such mechanisms, the interstitials formed in the primary damage of the cascade and under electronic excitation are seen on average to have migrated away from the track axis in the final configuration. This motion is dominated by replacement mechanisms rather than migration as only a few interstitial atoms are able to move without displacing another atom in a lattice position and undergoing replacement. This is reflected by the lower number of migrating atoms than annealed atoms and the average migration length of $< 2.0\mathring{A}$ which cannot account for the overall movement.

In summary, we have simulated an excitation of the electronic system in a lattice with a pre-existing damage configuration resulting from a displacement cascade. Two distinct effects are seen at extremes of high and low coupling. When a large amount of energy is transfered into the lattice, net damage production is seen with new defects formed along the track axis. Under low levels of excitation some of the original damage is annealed out. This is in agreement with experimental observations of swift heavy ion irradiation in Fe. In all cases considerable movement of defects is observed, this movement is dominated by replacement sequences whereby interstitial atoms displace a nearby lattice atom and occupy its now vacant lattice site along close packing directions. Interstitial atoms are seen to migrate away from the track axis leaving vacant sites in the core.

[1] Videos of these sequences can be accessed in .avi form at http://www.box.net/shared/iv1li1dgcs, http://www.box.net/shared/yqpooecqr1 and http://www.box.net/shared/18qxgl09yv

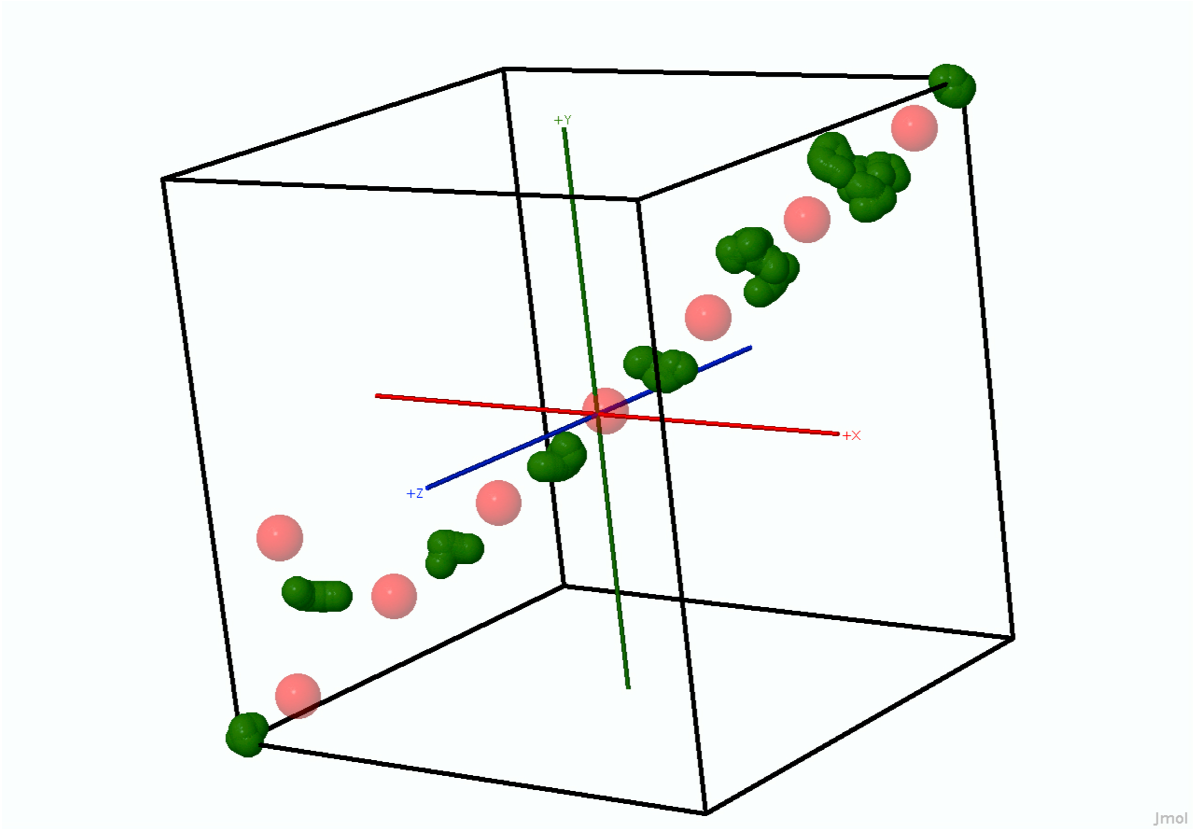

Figure 5.15: Visualisation of a replacement mechanism constructed by superimposing sucessive interstitial and vacancy positions over $\approx 4ps$.

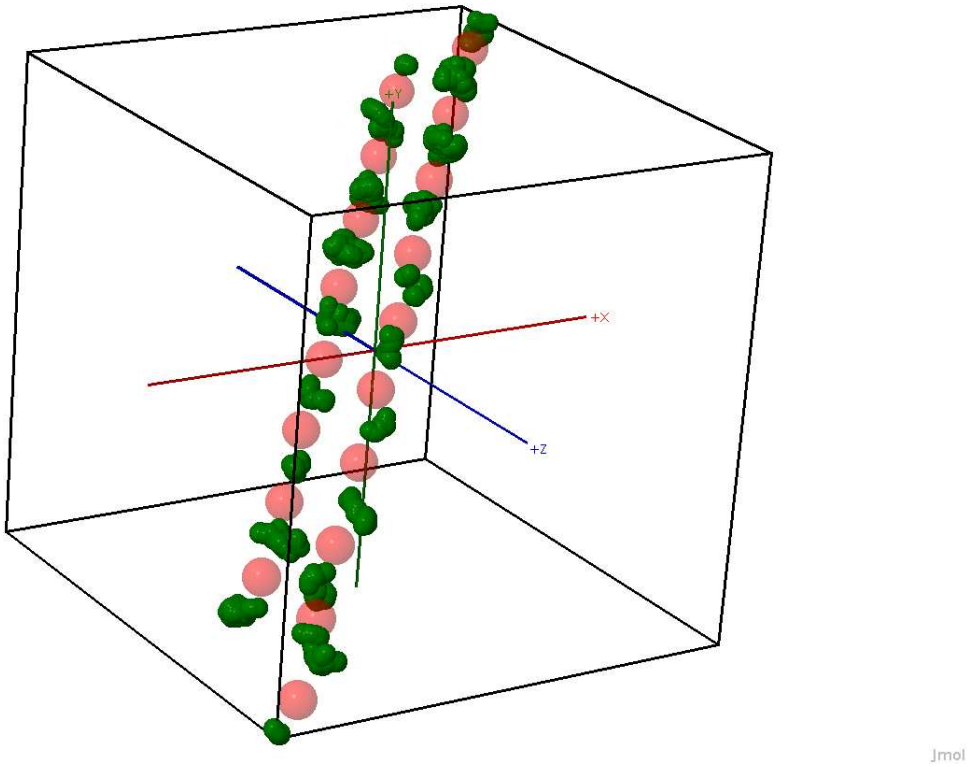

Figure 5.16: Visualisation of a replacement mechanism constructed by superimposing succesive interstitial and vacancy positions over $\approx 4ps$.

5.3 Ion Tracks in W

In this section we present simulations of ion tracks in W using the same method as described for Fe above. Tungsten is of interest as it is a candidate material for fusion reactors, but it also allows some informative comparison with Fe. Some important differences exist between the two materials. Although they are both transition metals, W has considerably higher thermal conductivity and a higher melting temperature, making it much less susceptible to damage than Fe. Three different temperature dependent specific heat functions are investigated and the residual damage configurations are investigated in detail.

No residual damage was found below a stopping power of $30keVnm^{-1}$. A fixed value of $35keVnm^{-1}$ was used as this gave a sufficient number of residual defects for meaningful comparison between simulations. This value is considerably higher than $10keVnm^{-1}$ as used in iron, because of the much stronger bonding and a higher melting point. A coupling strength of $1.0ps^{-1}$ corresponding to $2.6 \times 10^{18} Wm^3K^{-1}$ was chosen and compared to experimental values in the range $5 \times 10^{17} - 1 \times 10^{18} Wm^{-3}K^{-1}$. Two different interatomic potential forms were used.

5.3.1 Specific Heat

In order to investigate the role of the electronic specific heat capacity further, three different temperature dependent specific heat functions were considered. At low temperature the temperature dependence of the specific heat is given by the Sommerfeld expansion (see section 1.5.4), the experimental value of which is given in [123]. A tanh form fit to this value was compared to data derived from DFT calculations by Lin et al [126]; both the precise numerical values and a tanh fit to this data. Saturation was imposed at $\approx 3.23 \times 10^6 \, JK^{-1}m^{-3}$, equivalent to 2.47 electrons per atom participating in heat storage corresponding to the value at which the DFT data saturates. This can be seen in Fig. (5.17), the electronic specific heat capacity is plotted against electronic temperature for a range of different temperature dependences.

The electronic and atomic peak temperatures are shown as a function of time using the Lin and Kittel tanh fits in Fig. (5.18). This shows a considerable difference in the maximum lattice temperature. Since equivalent stopping powers were used, this corresponds to different initial temperatures; $2.41552 \times 10^5 K$ and $2.31714 \times 10^5 K$ for the Kittel and Lin fits respectively. It is seen that the ions are hotter in the first $0.1\,ps$ using the Kittel dataset, although after this time the Lin dataset is hotter, due to slower diffusion of the electronic temperature. Considering the Kittel dataset first; because of the higher initial temperature, the electrons are hotter initially, however this initial spike disperses very

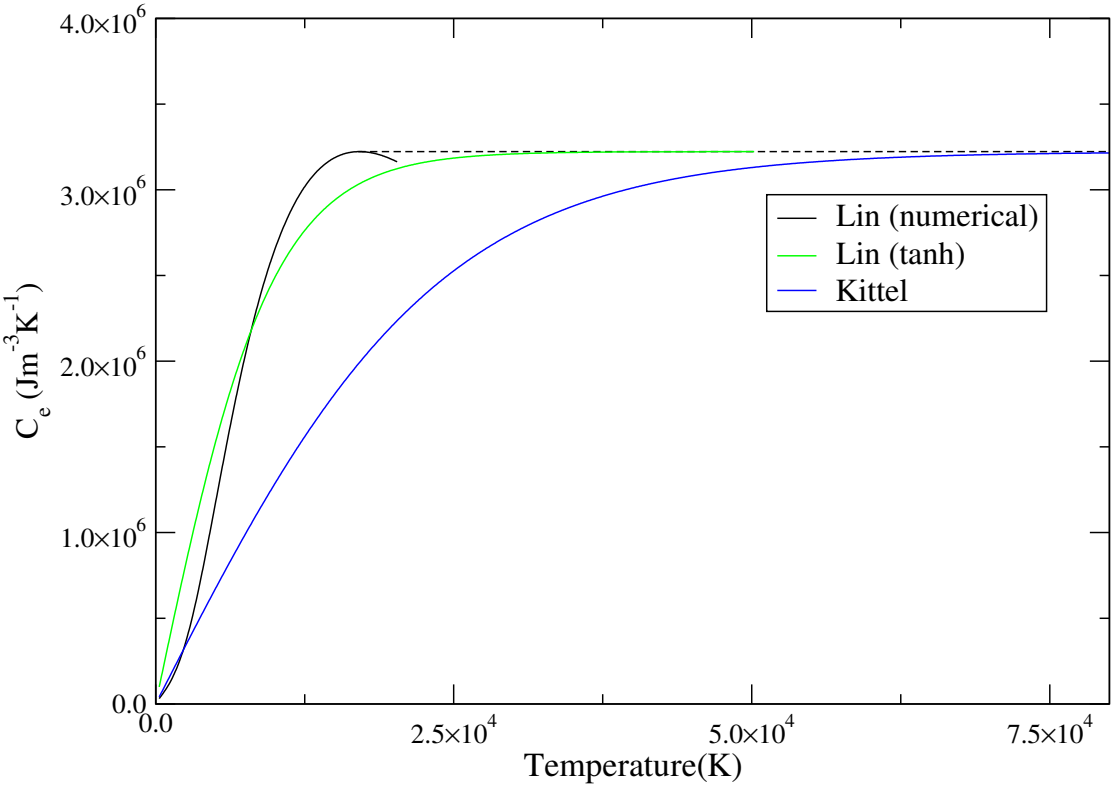

Figure 5.17: Specific heat in tungsten as a function of electronic temperature as fit to DFT data, numerical DFT data and extrapolation of low temperature expansion.

quickly and after $50\,fs$ the electron temperatures are comparable. The rate of diffusion increases steadily as the specific heat capacity begins to drop off linearly with temperature. In contrast, the Lin curve does not begin to diffuse more quickly until the linear section of the specific heat capacity function is reached which occurs later in the simulation as the saturation temperature is considerably lower. That is to say; the differences in low temperature behaviour dominate over the different starting temperatures used to impose equal stopping powers. Thus, more efficient cooling, and so less melting of the lattice, is seen with the form derived from extrapolation of the Kittel coefficient. Fig. (5.19) shows the number of atomic displacements as a function of time for both the simulations. Considerably more peak and residual damage is seen using the Lin fit, which is consistent with the higher atomic temperature obseved.

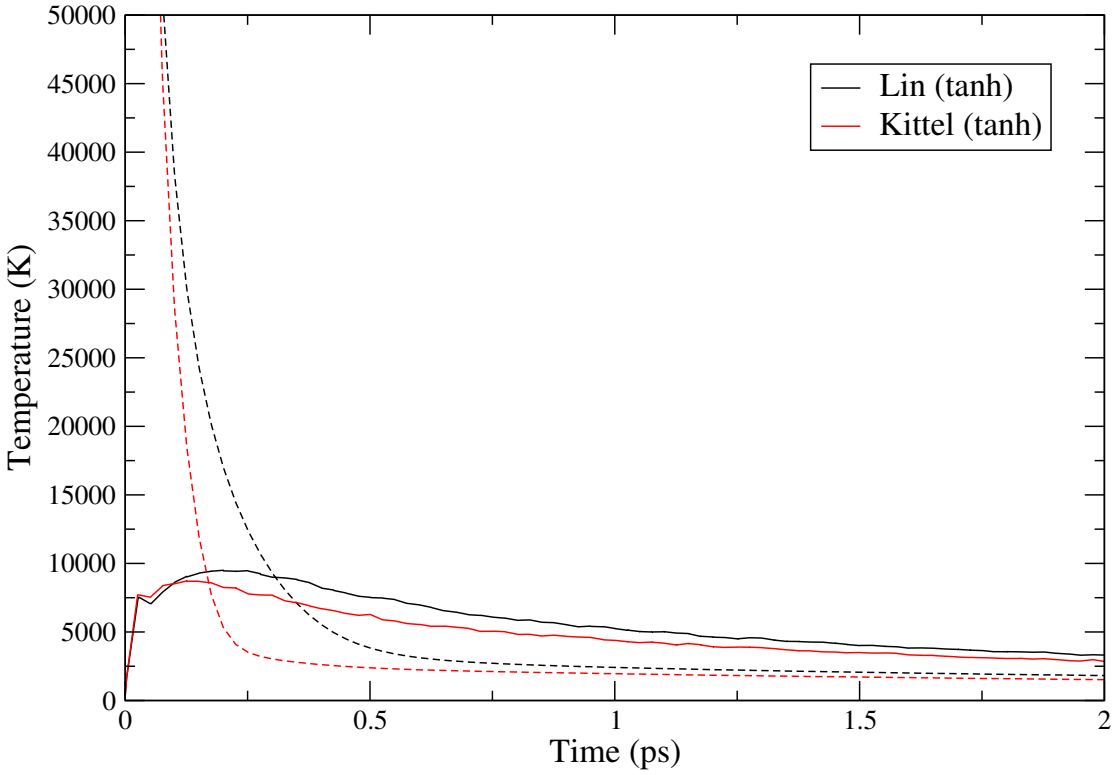

Figure 5.18: Atomic (solid) and electronic (dashed) temperatures as a function of time in $35keVnm^{-1}$ ion track in tungsten.

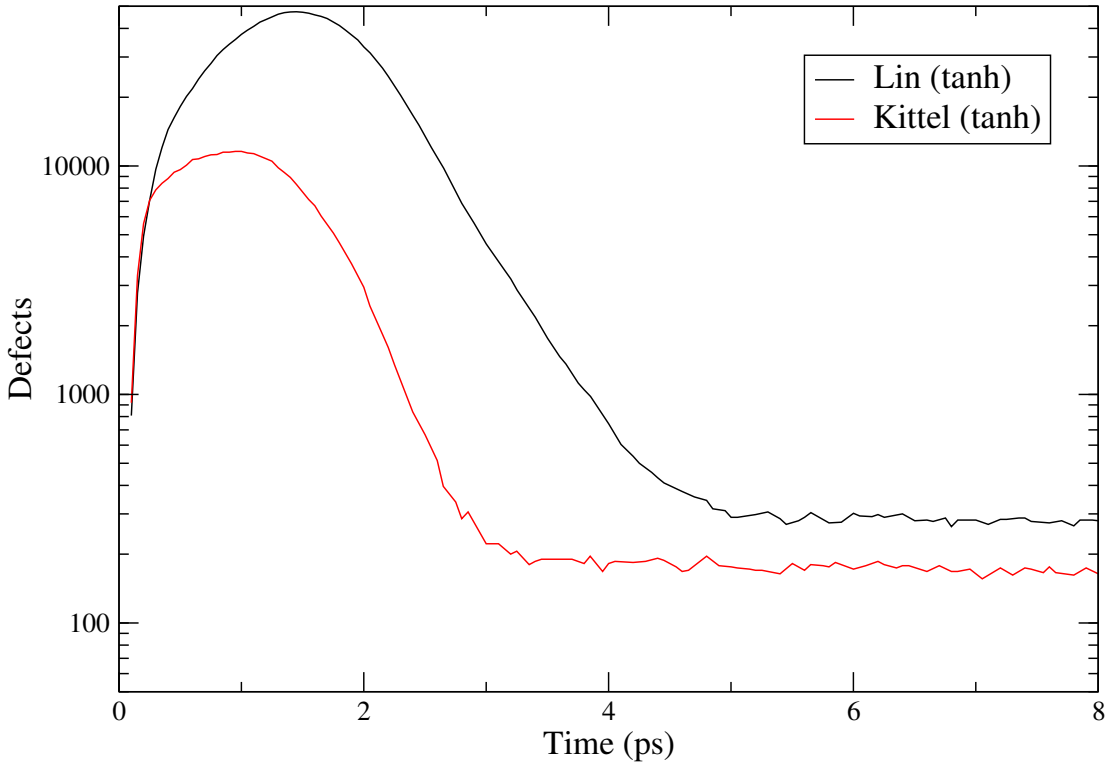

Figure 5.19: Number of displaced atoms as a function of time in $35keVnm^{-1}$ ion track in tungsten.

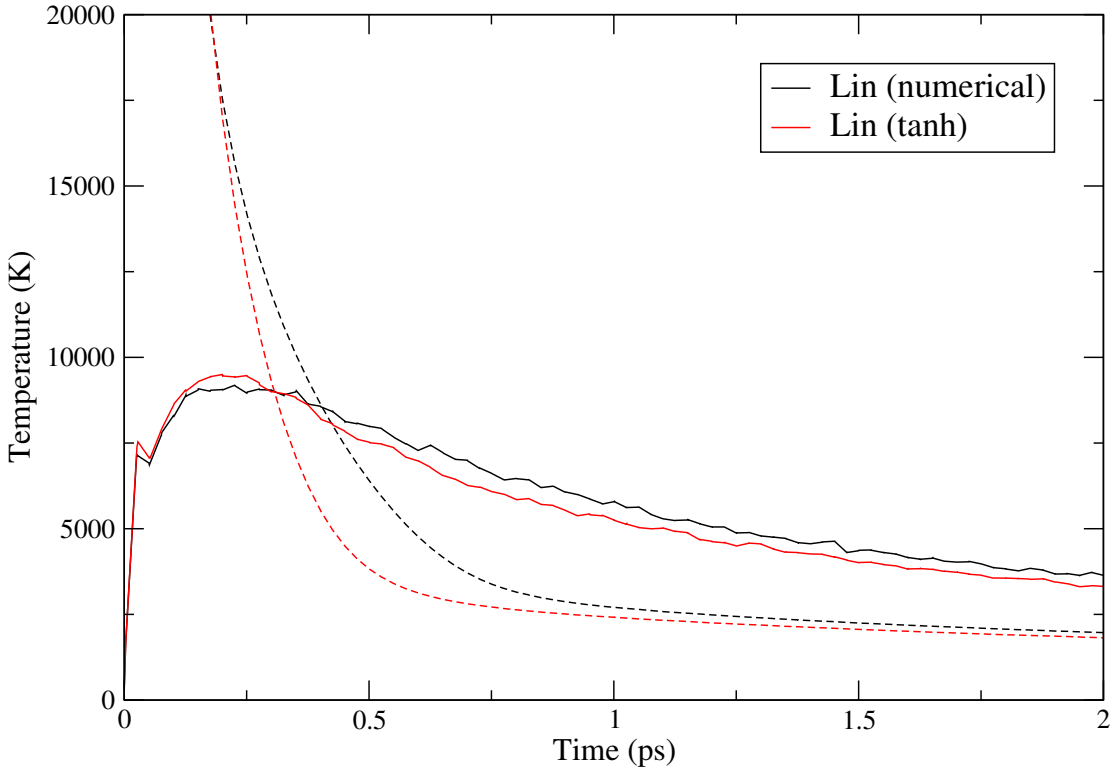

Figure 5.20: Atomic (solid) and electronic (dashed) temperatures as a function of time in $35keVnm^{-1}$ ion track in tungsten.

Figs. (5.20) and (5.21) show the atomic and electronic temperatures and number of atomic displacements as a function of time for both the exact numerical data of Lin et al and a tanh fit to this data. The numerical data is seen to give a slightly lower peak atomic temperature and a much lower subsequent rate of cooling. Despite the lower maximum temperature reached in the core, the numerical data is seen to give considerably more peak damage, however the difference in residual defects is negligible.

The tanh fit to the data of Lin et al captures the qualitative features of the exact results very well. Therefore to impart equivalent energies and so impose the same stopping power, similar excited temperatures are used; $2.31866 \times 10^5 K$ compared with $2.31714 \times 10^5 K$. Therefore any differences in the dynamics may be primarily attributed to differences in the heat capacity at lower temperatures. The slightly higher starting temperature accounts for the slightly higher maximum temperature reached by the atoms in the tanh fit dataset. However faster cooling sets in as electronic temperatures of $1-3\times10^4 K$ are seen to determine the overall diffusion, the fit underestimating the numerical specific heat data in this region. This is the cause of the reversal of the order of atomic temperature curves at around $\approx 0.3ps$. It should be noted that this is despite the tanh fit *overestimating* the DFT data at lower temperatures, below this range.

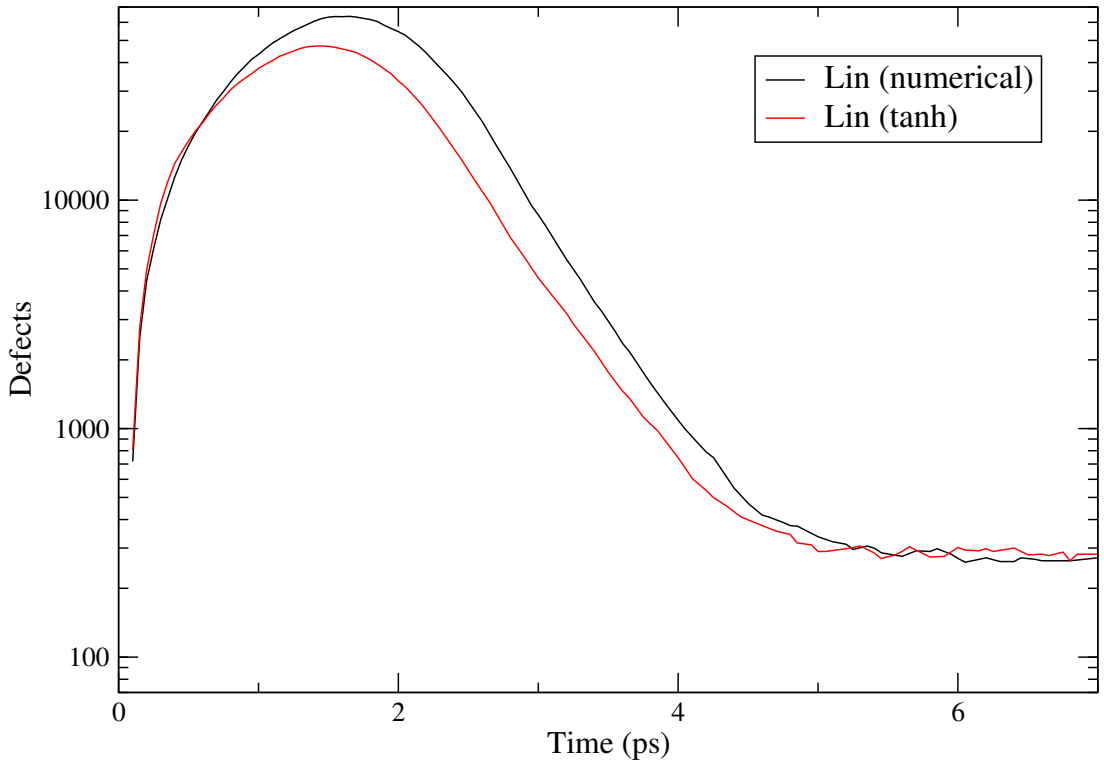

Figure 5.21: Number of displaced atoms as a function of time in $35keVnm^{-1}$ ion track in tungsten.

It is clear that different temperature dependences for the specific heat affect the thermodynamics of the ion track, both in terms of the form of the cooling curve, which will depend sensitively on the temperature dependence, but also the starting temperature corresponding to a given stopping power. It is necessary to integrate the specific heat function to a certain temperature to give a required energy deposition according to (5.1), therefore the excited temperature in the starting state of the system will be determined by the temperature dependence of the specific heat function.

However the initial electronic temperature spike diffuses very quickly, as a result any small initial differences will soon be eliminated. The above results suggest that differences in the temperature dependence at *intermediate* rather than lower temperatures are responsible for differences in the peak lattice temperature and so the degree of melting and damage formation. Unfortunately, it is hard to define where this intermediate temperature range is. Differences in the value of the electronic specific heat when the atomic temperature is at a maximum and melting occuring in the lattice will be most important, as well as the time when this occurs. This in turn is determined by the coupling strength, stopping power and melting temperature. Further, the electronic temperature profile will sample the full range of temperatures from extremes of linear temperature dependence to saturation so, it is not clear on which region of the temperature behaviour diffusion

will depend most sensitively. While these results suggest that differences in the range $T_e = 1 - 3 \times 10^4 K$ which coincide with $T_a = 7 - 10 \times 10^3 K$ (the effective melting temperature under these conditions is $\approx 5000K$) dominate damage formation, a systematic study of specific heat forms which differ in different temperature regimes is necessary to confirm this.

5.3.2 Defect Distribution

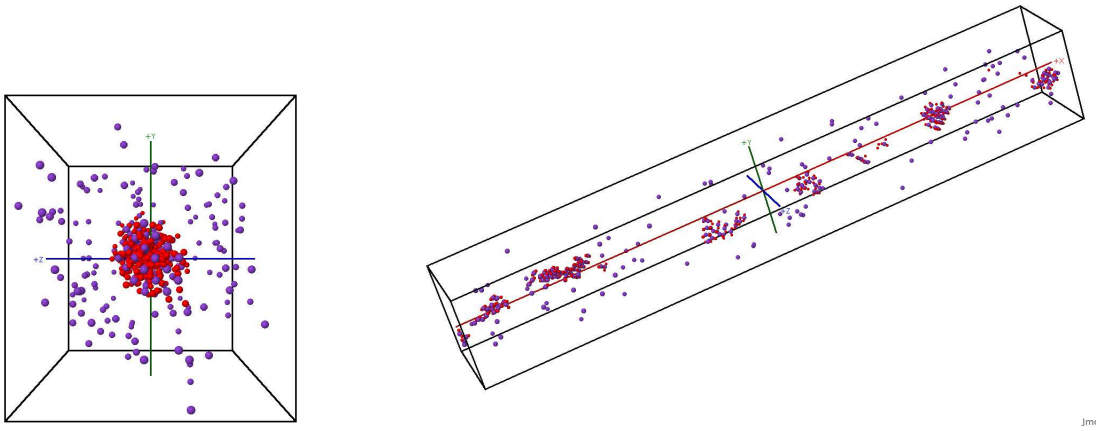

Figure 5.22: Residual defects in an ion track in tungsten using Dudarev potential. Left hand image is down track axis, the length scale is $\approx 30.0\mathring{A}$. Right hand image shows defects along track axis, the length scale is $\approx 250\mathring{A}$. Interstitial atoms are shown in red and vacancies in purple.

Examination of the defect configuration in Fig. (5.22) demonstrates that over the course of the ion track simulation (evaluated using numerical specific heat data from Lin et al), vacant sites are seen further from the core than interstitial atoms. This is in contrast to displacement cascades where interstitials are transported away from the core efficiently via replacement collision sequences, leaving a vacancy rich core. Figs. (5.23) and (5.24) show plots of the radial profiles of vacancies and interstitials for a range of times. These reveal a shock wave propagating from the core with interstitial atoms initially pushed out of their lattice sites to larger radii. While most of this damage at larger radii begins to relax, and vacancies and interstitials begin to recombine after $\approx 3.0ps$, the damage at small radii persists. Interstitial atoms on the periphery of the core migrate *into* the core as the lattice contracts and a proportion of these are unable to recombine with a lattice site as they do so. Initially this was attributed to unphysical contraction of the lattice at high temperatures using the Dudarev potential, as a negative pressure gradient was observed towards the core. Fig. (5.25) shows surface plots, in the plane perpendicular to the track axis, of the pressure, averaged along the track axis, at various times. As the

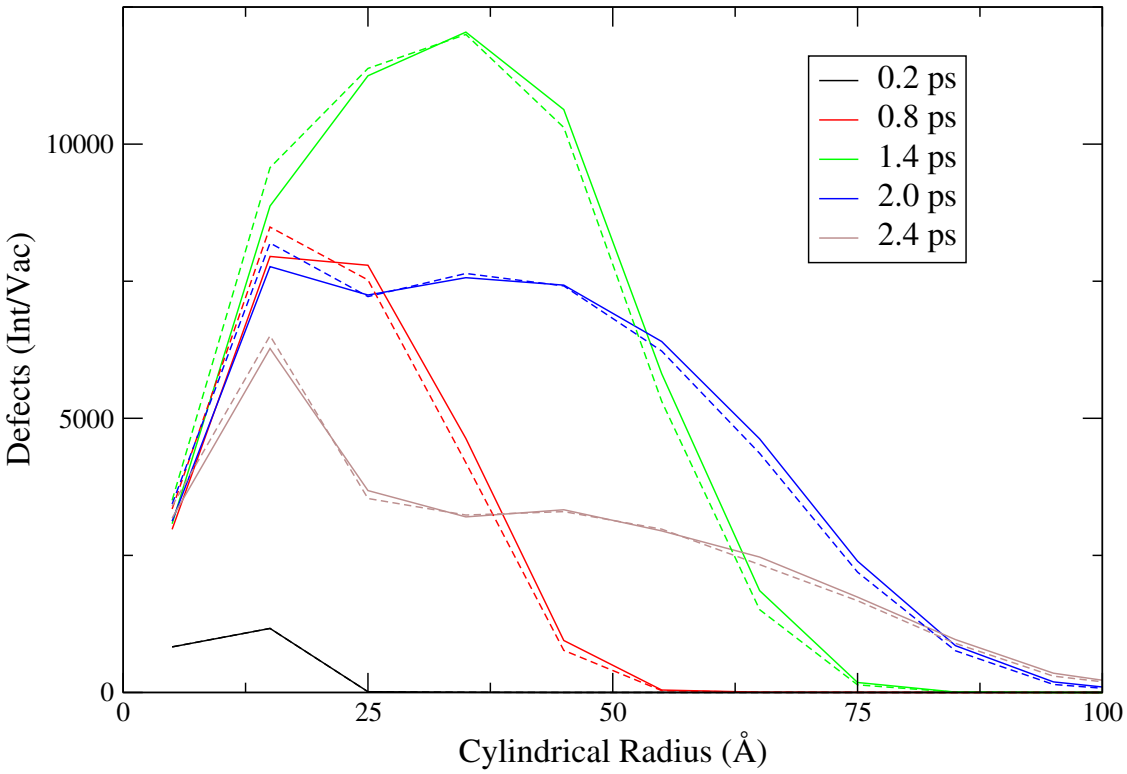

Figure 5.23: Histogram of defect radii over short times using Dudarev potential. Interstitials (solid lines) and vacancies (dashed lines).

lattice cools to the range $300 - 3000K$ the pressure is negative under constant volume, this will encourage migration of interstitials to smaller radii.

This counterintuitive behaviour was considered to be an artefact of the unphysical expansion under heating using the Dudarev potential, and so the same information was compared in an identical simulation using a FS potential. However a negative pressure gradient is observed again, causing interstitials to migrate back towards the core (Figs. (5.27) and (5.28), but it is now less pronounced. Negative pressure gradients appear only for very short times (Fig. (5.29))[2], suggesting that the relaxation of the lattice after the passing of the shock wave which pushes interstitials out of the core is responsible for the final defect configurations seen, rather than anomolous behaviour of the potential. Also the shock wave is seen to dissipate by the time it reaches the edge of the simulation cell, therefore any possibility of the reflection of this wave, due to the periodic boundary conditions, can be eliminated. There are two contributions to the pressure;

$$P(t) = \frac{\overbrace{2E_{kin}(t)}^{1} - \overbrace{W_{atomic}}^{2}}{3V} \tag{5.4}$$

(1) is the contribution from kinetic energy and makes a positive contribution to pres-

[2]Animation of such a sequence can be accessed in .avi form at http://www.box.net/shared/zu5ec0acg2

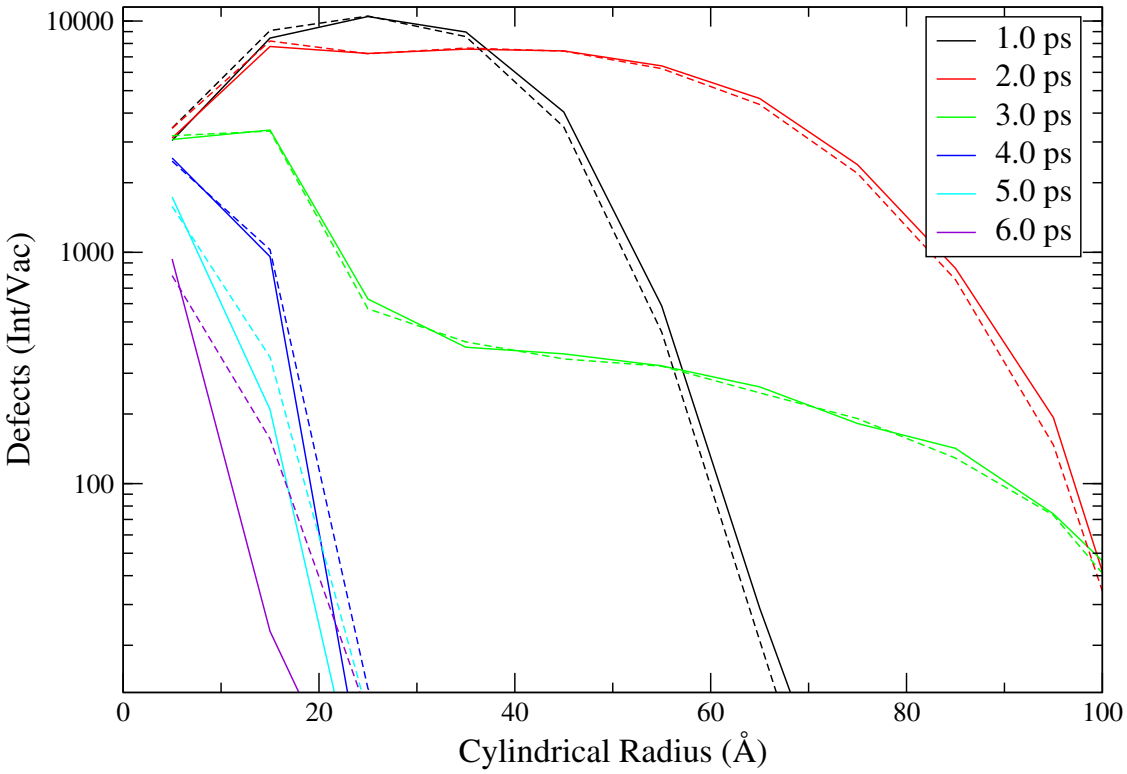

Figure 5.24: Histogram of defect radii over long times using Dudarev potential. Interstitials (solid lines) and vacancies (dashed lines).

sure and increases with temperature, while (2) is the virial term given by

$$W_{atomic} = \sum_{i} \sum_{j>i} -\mathbf{r_{ij}}.\mathbf{f_j} \tag{5.5}$$

The virial is a sum over all forces between atoms and gives a positive contribution to the pressure for repulsive forces and a negative contribution for attractive forces. As the lattice heats up along the core, (1) becomes very large and starts to expand giving a large positive contribution to the pressure overwhelming the negative contribution of (2). Following this local expansion and cooling of the core, the relaxation of the expansion causes (2) to become large while the kinetic contribution decreases as the atomic density in the core is reduced. Therefore the lower pressure seen in the core is due to both (1) decreasing and the size of (2) increasing, both attributable to the initial expansion.

The fact that interstitials are seen to migrate inwards in ion tracks and not in displacement cascades is due to two differences. Firstly the energy is initially partitioned very unequally in the atomic system in a cascade which allows ballistic transport of energy out of the core and the activation of replacement collision sequences. Secondly the constraint of constant global volume, which allows the cell to expand in places and the stress in the crystal to be absorbed elsewhere. In contrast, in an ion track the entire cell is heated

significantly and with a degree of coherence. The choice of a constant volume ensemble may be questioned for simulation of irradiation in which a significant amount of energy is injected into the system which leads to heating and invariably to local expansion. It could be argued that a constant pressure simulation would reflect reality more closely. The site of a radiation event will be surrounded by microns of cold material which may absorb some stress. Following irradiation there will be some local expansion of the damaged region constrained by surrounding material. However the time scale for expansion on micron length scales necessary to find equilibrium of pressure at highly elevated temperatures will be significant. Therefore the use of a barostat with a long pressure relaxation time scale ($\approx 10ps$) may be physical but will be of little significance on the time scales on which events, such as those presented above, proceed. Also, a barostat which imposes a constant global pressure will be inappropriate in a non-equilibrium situation in the same way that a homogeneous thermostat will under damp the core of a cascade and over damp the periphery. An alternative approach would be to couple atoms on the boundary of the cell to a finite element simulation describing the mechanical response of surrounding material and allowing damping of the pressure wave.

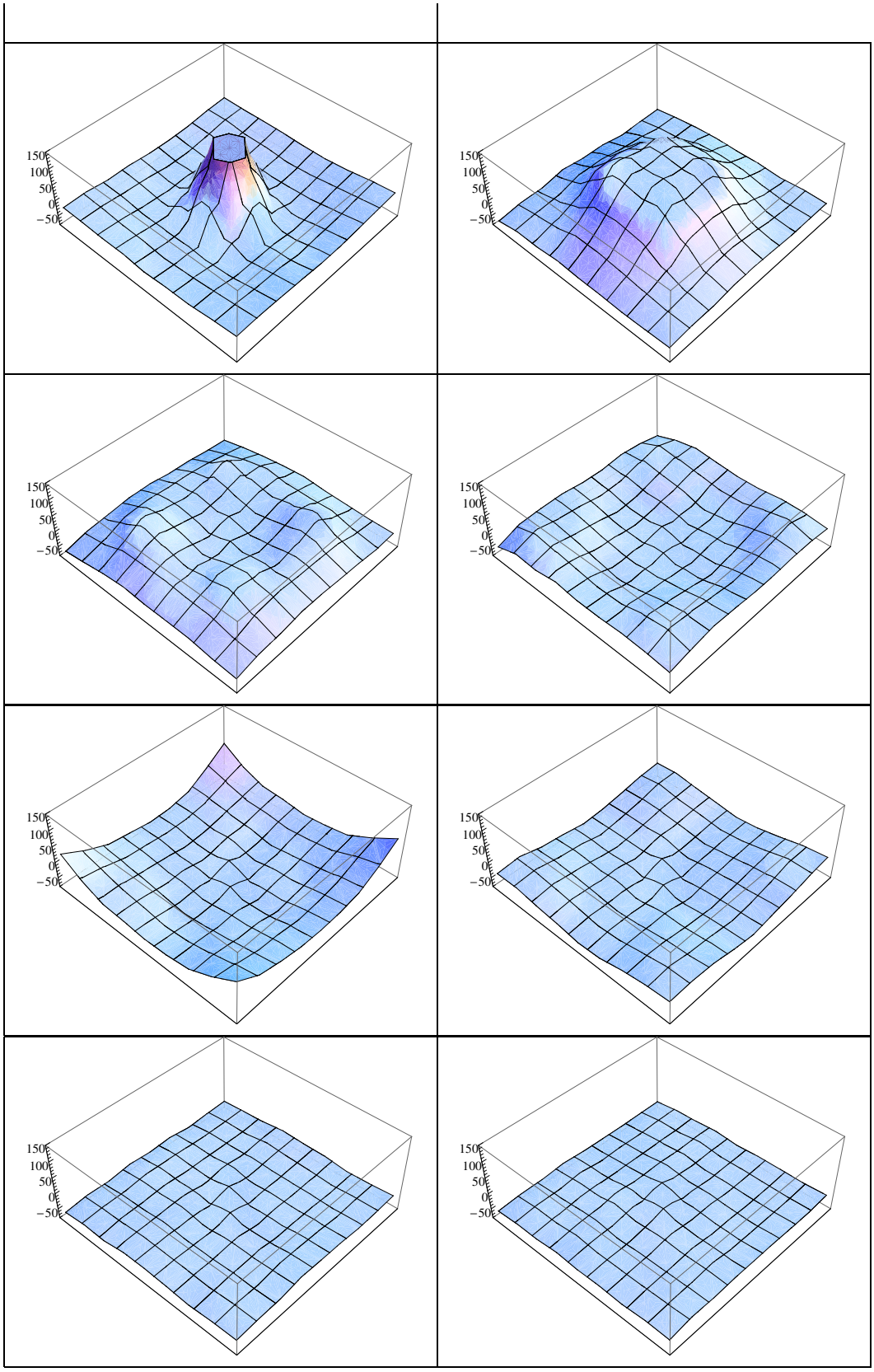

Figure 5.25: Pressure (katms) in the plane perpendicular to the track axis in $35keVnm^{-1}$ ion track in tungsten using the Dudarev potential at $0.2ps, 0.8ps, 1.4ps, 2.0ps, 3.0ps, 4.0ps, 5.0ps$ and $6.0ps$.

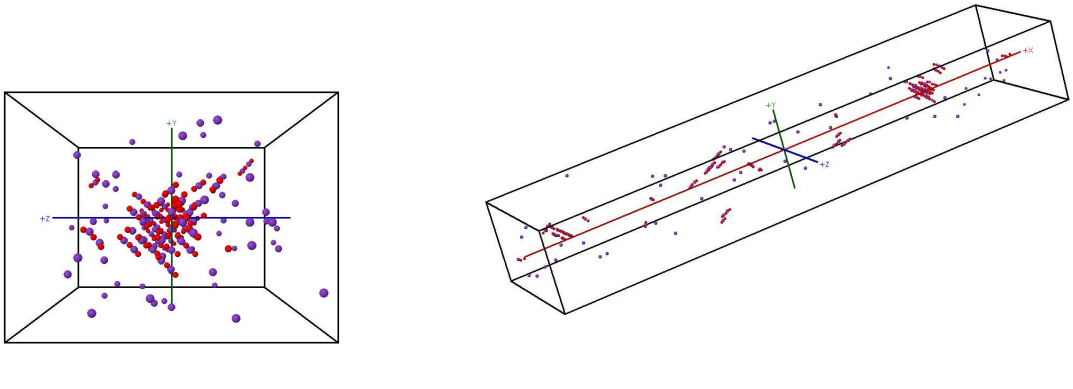

Figure 5.26: Residual defects in an ion track in tungsten using FS potential. Left hand image is down track axis, the length scale is $\approx 30.0\mathring{A}$. Right hand image shows defects along track axis, the length scale is $\approx 250\mathring{A}$. Interstitial atoms are shown in red and vacancies in purple.

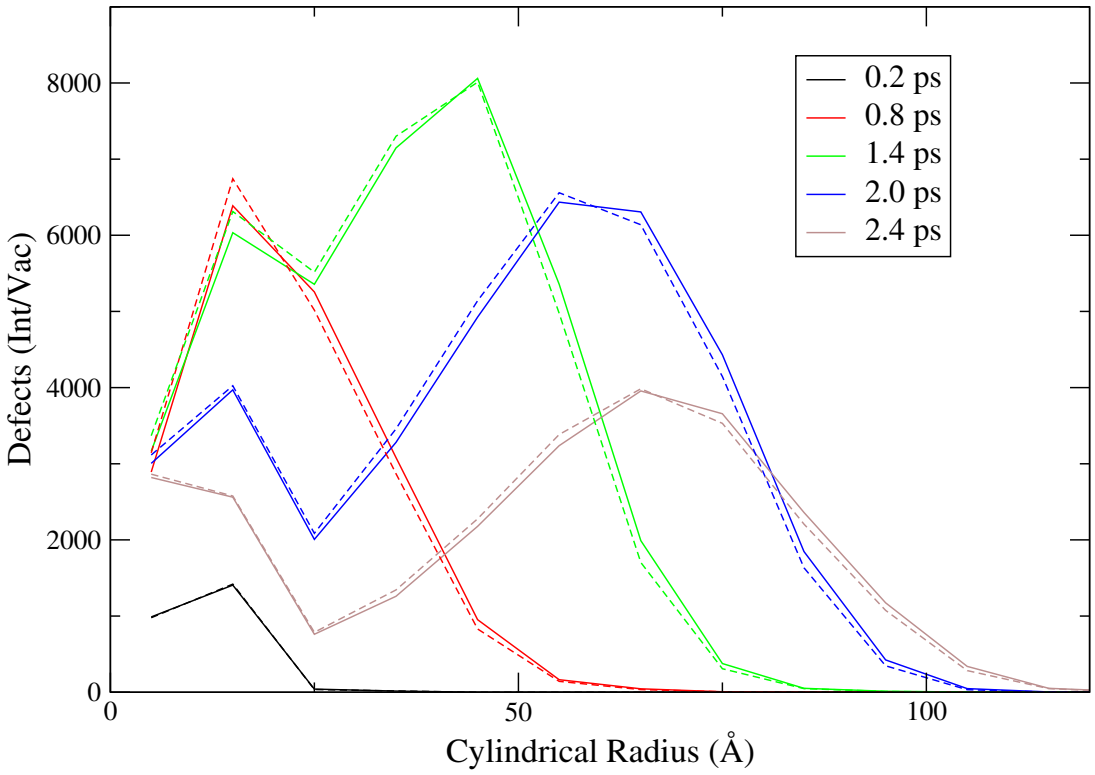

Figure 5.27: Histogram of defect radii over short times using the FS potential. Interstitials (solid lines) and vacancies (dashed lines).

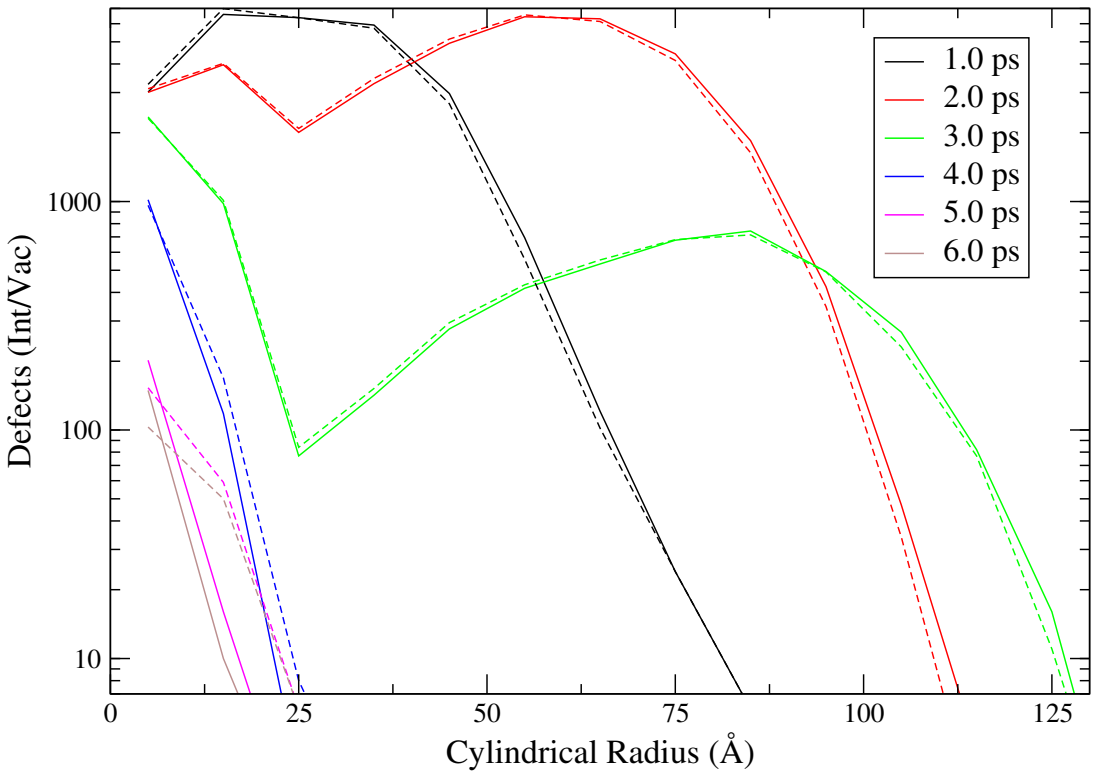

Figure 5.28: Histogram of defect radii over long times using the FS potential. Interstitials (solid lines) and vacancies (dashed lines).

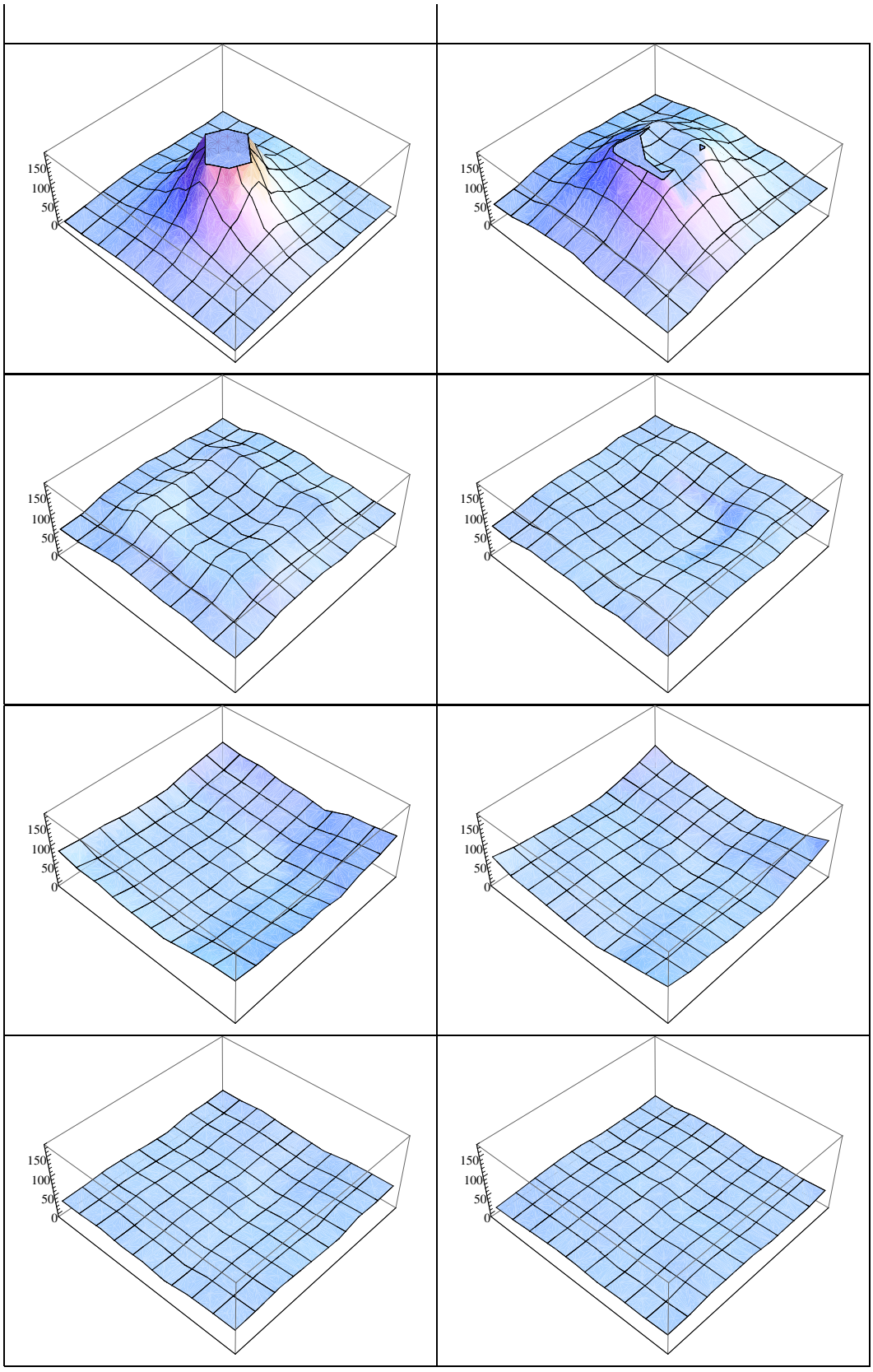

Figure 5.29: Pressure (katms) in the plane perpendicular to the track axis in a $35keVnm^{-1}$ ion track in tungsten using the FS potential at $0.2ps, 0.8ps, 1.4ps, 2.0ps, 3.0ps, 4.0ps, 5.0ps$ and $6.0ps$. Length scale is entire simulation cell, $\approx 250\mathring{A}$.

5.3.3 Comparison of Potentials

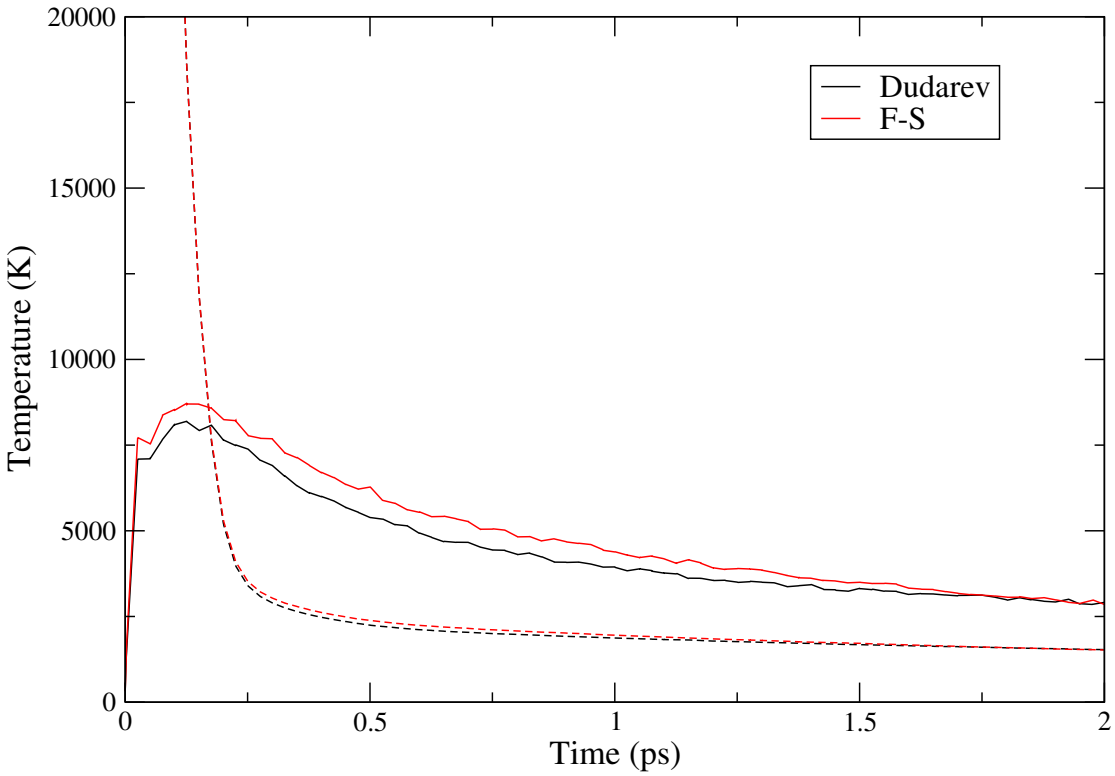

Figure 5.30: Core atomic (solid line) and electronic temperatures (dotted) as a function of time in $35keVnm^{-1}$ ion track in tungsten using the Dudarev and Finnis-Sinclair potentials.

Fig. (5.30) and (5.31) show plots of atomic and electronic temperatures and numbers of displaced atoms over time respectively for both potential functions. Comparison of otherwise identical simulations (the Kittel fit is used) with the two different potential functions shows very different numbers of defects, confirming that the quantitative comparison of damage is limited [90]. The electronic temperature evolution is almost indistinguishable in each case, since this is not directly related to the form of the potential function, however the atomic temperature, which is determined by the forces derived from the potential function are considerably different giving a significantly different damage evolution in terms of both the peak number of atomic displacements and residual damage. Since the atomic interactions are determined by the potential function, this represents the physics of an MD simulation. However useful information may still be derived from these simulations even if the choice of a different, equally valid form may give very different numbers of residual defects. There are many different parameters to be investigated and by fixing the other variable parameters within a simulation and investigating the variation with one, informative trends may be identified. Further, different potential functions capture different aspects with different degrees of success.

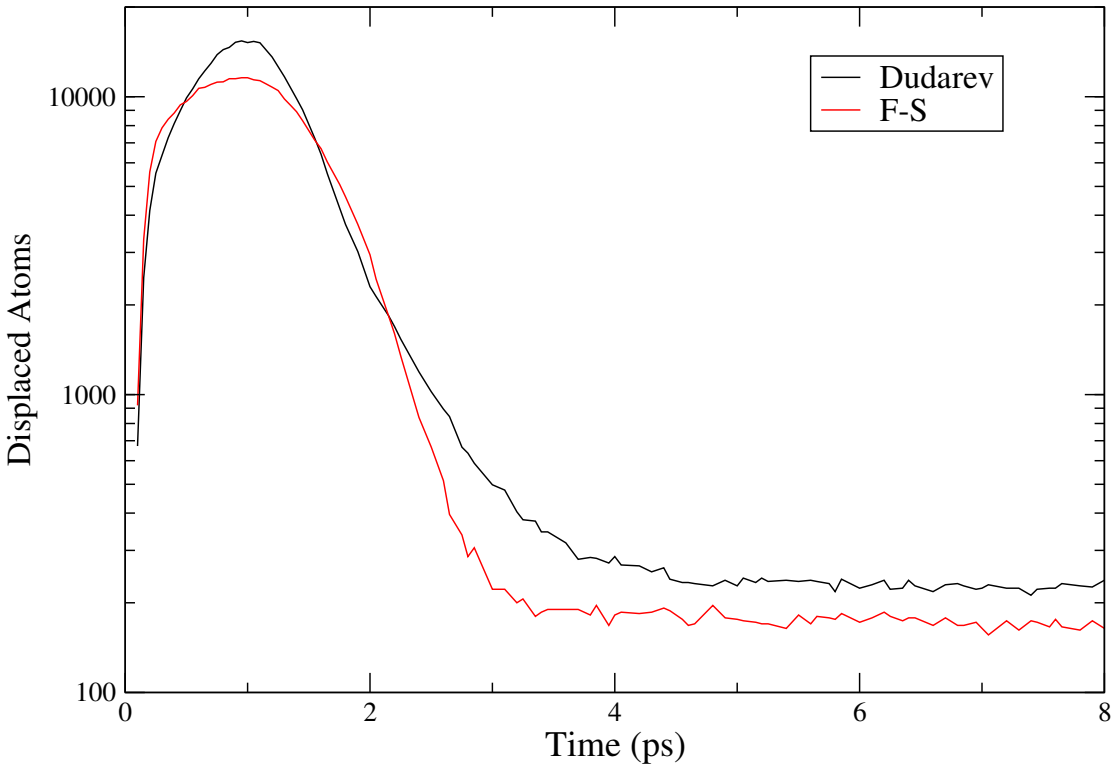

Figure 5.31: Number of displaced atoms as a function of time in $35 keV nm^{-1}$ ion track in tungsten using the Dudarev and Finnis-Sinclair potentials.

Some judgement must, therefore, be employed to determine the most important quantities relevant to the conditions to be simulated, and it must be ensured that any observations are not artefacts of unphysical aspects of the potential. Any observations and conclusions must also be interpreted in light of the assumptions of the model from which they were derived. For example the Dudarev potential has the advantages that the order of the defect formation energies of different dumbell configurations are reproduced and that the regime of $10 - 100\, eV$ governing displacement of atoms, is determined by a physical function rather than an interpolation function between the standard potential regime and the ZBL form. Both of these aspects are crucial for cascade simulations, however the FS form has the advantage of physical expansion at high temperatures which is seen to promote the migration of interstitials into the core as the lattice relaxes.

Iron and tungsten are both important candidate materials for different applications within fusion reactors. Both are transition metals with a high density of states at the Fermi level [3], and some similarities exist between them. However as can be seen from (table 5.5) some important quantities for determining damage are very different.

No significant damage is seen below a stopping power of $35\, keV nm^{-1}$ in tungsten,

	Fe	W
$T_m\,(K)$	1811	3683
$\gamma_e\,(Jm^{-3}K^{-2})$	689.71	136.17
$E^i_{migration}\,(eV)$	0.34	1.78
$\kappa_e\,(Wm^{-3}K^{-1})$	80	178

Table 5.5: Table comparing melting temperature, low temperature specific heat coefficient [123], single interstitial migration energy [222] and electronic thermal conductivity [206] at $300K$ between tungsten and iron.

whereas iron is seen to form residual damage at $10\,keVnm^{-1}$. This is attributable in part to the higher melting temperature. However the significantly higher diffusivity also allows the rapid diffusion of extremely high electronic temperatures before energy may be transferred into the lattice. The radii of the melted zones in iron and tungsten are reflected in the final defect configurations; the average radial distances of residual interstitials and vacancies in the ion tracks considered in iron (section 5.1) and tungsten may be compared. As a result, the effect of interstitials being swept back towards the core in the later stages of an ion track is less pronounced in iron since damage is found so far from the core. The average vacancy and interstitial radii are, respectively, for a $10\,keVnm^{-1}$ event in Fe $64.9\mathring{A}/63.5\mathring{A}$ compared to $8.6\mathring{A}/7.8\mathring{A}$ in a $35\,keVnm^{-1}$ event in W.

In summary, we have simulated ion tracks in tungsten by the same method outlined for iron in the previous section. Tungsten was found to be considerably more impervious to damage in comparison to iron which can be attributed to a higher melting temperature and electronic thermal conductivity. Two different temperature dependent specific heat capacity functions were used and the cooling curves and damage evolution compared. It was found that extrapolation of low temperature specific heat capacity gave significantly different temperature profiles and residual damage, and was in fact a poor approximation to more accurate data derived from DFT. In fact even very small differences in the temperature dependence of the specific heat function were seen to give dissimilar cooling curves, although this did not lead to signficant differences in the residual defect configurations.

Chapter 6

Summary and Conclusions

In this thesis, the effect of electrons on radiation damage has been studied using simulation techniques. The electrons are accounted for in models of bonding, which gives rise to cohesion in condensed phases, however the electrons also represent an energetically coupled system. This interacts energetically with the atomic subsystem which affects the dynamics of a radiation event. Energy is lost to the electrons by moving atoms. This energy loss causes a local temperature rise in the electrons which subsequently diffuses through the system and may be exchanged with the lattice atoms away from the original excitation.

A model incorporating electronic effects into classical MD simulations has been presented. The atomic system is described by a Langevin equation which thermostats the lattice atoms to the local electronic temperature. In this way the coupling of energy and the one-way transfer of energy from ions to electrons via inelastic collisions are described and included in a consistent manner. The electronic temperature evolves according to a heat diffusion equation allowing the electrons to act as a heat sink or a heat bath with an inhomogeneous, time varying temperature.

The model was used to simulate $10\,keV$ displacement cascades in iron. Significant amounts of energy were transferred into the electronic system causing considerable heating above the ambient temperature. This increase in electronic temperature is ignored in traditional simulations which demonstrates the importance of our approach. Our 'inhomogeneous Langevin thermostat' was found to give reduced residual damage in comparison to a traditional Langevin thermostat over the full range of electron-phonon coupling strengths considered. An investigation was made of the strength of the coupling interaction between electrons and atoms on residual damage which identified two broad regimes of *coupling-limited behaviour* and *diffusion-limited behaviour*. Under strong coupling, the time scale for relaxation is limited by electronic diffusivity, while with weak coupling the dynamics are determined by the rate at which energy may be exchanged between energetic

atoms and cold electrons.

We have undertaken the first atomistic simulation of irradiation with swift heavy ions in metals using our new approach. In the past there has been no consistent way to introduce the energy of the initial excitation of the electron system into the atomic simulation. These showed that the degree of melting along the path of a swift ion depends sensitively on the coupling strength and the electronic thermal parameters. Since dynamics in ion tracks are in all cases dominated by diffusion, small changes in these parameters can be the difference between an undamaged lattice and a disordered core of several nanometre dimensions. Despite atomic temperatures well above the melting point of the model potentials, melting was not always observed. This demonstrates the importance of an atomistic treatment over simple two temperature model calculations. The annealing effect of electronic excitation was also investigated. A lattice was irradiated with a single PKA and the defect evolution was monitored under varying levels of electronic excitation. Experimental observations of annealing pre-existing defects and new defect creation at low and high stopping respectively were reproduced. The high interstitial mobility in Fe led to swift separation of vacancies and interstitials via replacement sequences and the electronic excitation was seen to modify the defect configuration significantly.

Ion track simulations were also performed in tungsten. Differences in important quantities such as melting temperature and thermal conductivity meant that the material was much less susceptible to damage under electronic excitation than iron. Several different forms for the electronic specific heat were investigated in tungsten; extrapolation of low temperature behaviour, data derived from DFT calculations, and a close fit to this data were all considered. It was found, since relaxation in ion tracks is dominated by electronic diffusion, that small differences in the temperature dependence of the diffusivity will drastically alter the rate of cooling. This will affect the number of atomic displacements in the course of the event and the number which persist as residual damage, often in complex and unpredictable ways. The later stages of the simulations also highlighted an unexpected trend in the distribution of interstitial atoms and vacant sites. Following the initial spread of a shock wave from the core, interstitials at larger cylindrical radii were seen to migrate *into* the core leaving vacant lattice sites further from the core. This is in contrast to the well understood situation in cascades in which the opposite trend is observed. Following an initial expansion stage, negative pressure gradients are observed. Consequently motion of interstitial atoms formed far from the core is observed towards the track axis.

The model presented has had notable successes. By including electronic effects into molecular dynamical simulations of radiation damage, an understanding of the role of electron-phonon coupling, stopping and energy redistribution has been gained. However

the simplified model of the electrons can be improved upon, in particular the functions used for the electronic thermal parameters must capture the salient features of complex mechanisms over large ranges of phase space and under non-equilibrium of electrons and atoms. The importance of the precise form of the specific heat function has been seen to have considerable effects on subsequent atomic dynamics. The inclusion of realistic electronic and atomic temperature dependent forms for coupling strength and thermal conductivity will likely have significant and unpredictable effects. The assumption of a homogeneous, diffusive continuum is also questionable at high energies. Our model assumes that charge separation is negligible in metals where high electron mobility will lead to swift recombination of electrons and holes recovering spatial homogeneity and leaving the atomic interaction unchanged. This simplification is reasonable given that electron charge neutralisation occurs within $10\,fs$ and atomic dynamics occur on time scales of $\approx 100\,fs$. Tungsten, however, challenges our assumption of diffusive behaviour on length scales of $\approx 10\,\mathring{A}$ due to the extremely large mean free path between collisions. Electron transport is therefore underestimated. The use of a more realistic initial condition in the electron system, such as a smoother form representing a temperature spike which has swiftly relaxed by ballistic transport, may remedy this.

A next logical step in developing an understanding of damage in realistic fusion materials is to simulate Fe-Cr alloys. It is known that small concentrations of atoms of an alloying material can affect displacement energies and consequently will affect the final damage states. While the state of the lattice through the course of an event is of little relevance compared to the final damage state in a *monatomic* material, the number of displacements and the degree of motion and mixing will be significant in alloys. The inclusion of electron dynamics was seen to affect the maximum amount of damage observed as well as the final damage state. While our model will only require the values of several key parameters (coupling strength and diffusivity) which may be measured experimentally or derived from ab-initio techniques, the development of suitable potential forms will be the factor limiting this avenue. Although Fe-Cr alloy potentials are available, special attention must be paid to to fit these closely to properties determining damage and mixing, such as migration and displacement energies of each species.

The construction of a practical fusion reactor remains a long term goal and one in which simulation will be a vital tool; both in understanding basic material properties under hostile conditions and in the choice and testing of individual candidate materials. The non-equilibrium nature of these conditions will always challenge modelling techniques, however we have begun to address a key limitation in classical molecular dynamical models. Our results have aided our understanding of damage formation processes and highlighted the importance of accurate models of parameters of the electronic subsystem. The pursuit of the avenue of research outlined in this work coupled with increasing computational

capability, along with the effort on other fronts, both experimental and theoretical, will bring fusion power on a practical scale closer to reality.

Bibliography

[1] J.Sheffield, A. Gibson, P. Vandenplas, M. Keilhacker, J.F. Davies, K. Lackner, G.H. Wolf, R.D. Gill, P. Thomas, I. Cook, H. Bruhns, M. Watkins, and R.S. Pease. World Population and Energy Demmand Growth: The Potential Role of Fusion Energy in an Efficient World. *Philosophical Transactions: Mathematical, Physical and Engineering Sciences*, 357:377–395, 1999. 4

[2] B.D. Wirth, G.R.Odette, J. Marian, L. Ventelon, J.A. Young-Vandersall, and L.A. Zepeda-Ruiz. Multiscale Modelling of Radiation Damage in Fe-based Alloys in the Fusion Environment. *Nuclear Instruments and Methods B*, 103-111:329–333, 2004. 4

[3] A.M. Stoneham, J.R. Matthews, and I.J. Ford. Innovative Materials for Fusion Power Plant Structures: Seperating Functions. *Journal of Physics C*, 16:2597–2621, 2004. 4, 47, 73, 152

[4] J. Marian L.A. Zepeda-Ruiz, G.A. Gilmer, E.M. Bringa and T. Rognlien. Simulations of Carbon Sputtering in Amorphous Hydrogenated Samples. *Physica Scripta*, T124:65–69, 2006. 5

[5] K. Ehrlich, R. Bullough, A. Kelly, J.Sheffield, P. Vandenplas, C. Windsor, E.A. Little, T.N. Todd, I. Cook, and R.J. Hawryluk. The Development of Structural Materials for Fusion Reactors [and Discussion]. *Philosophical Transactions: Mathematical, Physical and Engineering Sciences*, 357:595–623, 1999. 5

[6] N. Baluc, K. Abe, J.L. Boutard, V.M. Chernov, E. Diegele, S. Jitsukawa, A. Kimura, R.L. Klueh, A. Kohyama, R.J. Kurtz, R. Lasser, H. Matsui, A. Moslang, T. Muroga, G.R. Odette, M.Q. Tran, B. van der Schaaf, Y. Wiu, J. Yu, and S.J. Zinkle. Status of Research and Development Activities on Materials for Fusion Power Reactors. *Nuclear Fusion*, 47:696–717, 2007. 5, 73

[7] A.V. Krasilnikov and V.N. Amosov and P. van Belle and O.N. Jarivs and G.J. Sadler. Study of D-T Neutron Energy Spectra at JET Using Diamond Detectors. *Nuclear Instruments and Methods B*, 476:500–505, 2001. 6

[8] J. Ziegler. http://www.srim.org/. 6, 7, 15, 95

[9] M. Nastasi J. Mayer and J.K. Hirvonen. *Ion-Solid Interactions: Fundamentals and Applications*. Cambridge University Press, 1996. 7, 18

[10] J.A. Brinkman. On the Nature of Radiation Damage in Metals. *Journal of Applied Physics*, 25:961–969, 1953. 7

[11] J.A. Brinkman. Production of Atomic Displacements by High Energy Particles. *American Journal of Physics*, 24:246–267, 1956. 7

[12] S. Matteson and M. Nicolet. Ion mixing. *Annual Review of Material Science*, 13:339–362, 1983. 7, 21

[13] M.W. Guinan and J.H. Kinney. Molecular Dynamics Calculations of Energetic Displacement Cascades. *Journal of Nuclear Materials*, 104:1319, 1981. 8

[14] W. Schilling, E. Erhart, and K. Sonnenburg. Fundamental Aspects of Radiation Damage in Metals Vol P1. In *US Energy Research and Development Adminstration Conference Proceedings 751006 1975*, 1975. 9

[15] P.C.H. Woo and B.N. Singh. Production Bias due to Clustering of Point Defects in Irradiation-Induced Clusters. *Philosophical Magazine*, 65:889, 1992. 10

[16] R.A. Johnson. Interstitials and Vacancies in alpha-Iron. *Physical Review*, 143:1329, 1964. 10

[17] K. Nordlund and R.S. Averback. Collision Cascades in Metals and Semiconductors: Defect Creation and Interface Behaviour. *Nuclear Instruments and Methods B*, 276:194–201, 2000. 10

[18] S. Ishino, N. Sekimura, and H. Abe. Internal Probe to Detect Defects from Cascades - In-situ Ion Irradiation Experiments Revisited. *Journal of ASTM International*, 4:2, 2007. 10

[19] T. Pfeifer, C. Spielmann, and G. Gerber. Femtosecond X-ray Science. *Reports in Progress of Physics*, 69:443–505, 2006. 10

[20] C.W. Siders, A. Cavalleri, K. Sokolowski-Tinten, Cs. Toth, T. Guo, M. Kammler, M. Horn von Hoegen, K.R. Wilson, D. von def Linde, and C.P.J. Barty. Detection of Nonthermal Melting by Ultrafast X-ray Diffraction. *Science*, 286:1340, 1999. 10

[21] A.M. Lindberf, J. Larsson, K. Sokolowski-Tinten, K.J. Gaffney, C. Blome, O. Synnergren, J. Sheppard, C. Caleman, A.G. MacPhee, D. Weinstein, D.P. Lowney, T.K. Allison, T. Matthews, R.W. Falcone, A.L. Cavalieri, D.M. Fritz, S.H. Lee, P.H. Bucksbaum, D.A. Reis, J. Rudati, P.H. Fuoss, C.C. Kao, D.P. Siddons, R. Pahl, J. Als-Nielsen, S. Duesterer, R. Ishebeck, H. Schlarb, H. Schulte-Schrepping, Th. Tschentscher, J. Schneider, D. von der Linde, O. Hognette, F. Sette, H.N Chapman,

R.W. Lee, T.N Hansen, S. Techert, J.S. Wark, M. Bergh, G. Huldt, D. van der Spoel, N. Timmeaunu, J. Hajdu, R.A. Akre, E. Bong, P. Krejcik, J. Arthur, S. Brennan, K. Luening, and J.B. Hastings. Atomic-Scale Visualization of Inertial Dynamics. *Science*, 308:392, 2005. 10

[22] T.L. Daulton and M.A. Kirk and L.E. Rehn. In-situ Transmission Electron Microscopy Study of Ion-Irradiated Copper: Temperature Dependence of Defect Yield and Cascade Collapse. *Philosophical Magazine A*, 80:809, 2000. 10

[23] R. Rauch and J. Peisl and A. Schmalzbauer and G. Wallner. Correlation of Interstitials Within Defect Cascades in Al(Zn) and Cu Observed by Diffuse X-Ray Scattering. *Journal of Nuclear Materials*, 168:101, 1989. 11

[24] A. Dunlop, P. Legrand, D. Leseur, N. Lorenzelli, J. Morillo, A. Barbu, and S. Bouffard. Phonon Soft Modes and Damage Production by High Electronic Excitations in Pure Metals. *Europhysics Letters*, 15:765–770, 1991. 11, 122

[25] G.H. Kinchin and R.S. Pease. The Displacement of Atoms in Solids. *Reports on Progress in Physics*, 18:1–51, 1955. 11, 16, 44

[26] M.J. Norgett, M.T. Robinson, and I.M. Torrens. A Proposed Method of Calculating Displacement Dose Rates. *Nuclear Engineering and Design*, 33:50–54, 1975. 11, 16

[27] F.F. Komarov. Defect and Track Formation in Solids Irradiated by Superhigh-Energy Ions. *Physics Uspekhi*, 46:1253–1282, 2003. 12, 42

[28] A. Barbu, A. Dunlop, A. Hardouin Duparc, G. Jaskierowicz, and N. Lorenzelli. Microstructural Modifications Induced by Swift Ions in the NiTi Intermetallic Compound. *Nuclear Instruments and Methods B*, 145:354–372, 1998. 12

[29] E. Pamier Ch. Dufour and M. Toulemonde. Electron-phonon Coupling and the Sensitivity of Metals to Irradiation with Swift Heavy Ions. *Nuclear Instruments and Methods B*, 122:445–448, 1997. 12

[30] A. Audoard and E. Balanzat and S. Bouffard and J.C. Jousset and A. Chamberod and A. Dunlop and D. Lesueur and G. Fuchs and R. Spohr and J. Vetter and L. Thome. Evidence for Amorphisation of a Metallic Alloy by Ion Electronic Energy Loss. *Physical Review Letters*, 65:875, 1990. 12

[31] M. van Kampen, J.T. Kohlepp, W.J.M. de Jonge, B. Koopmans, and R. Coehoorn. Sub-picosecond Electron and Phonon Dynamics in Nickel. *Journal of Physics C*, 17:6823–6834, 2005. 13, 43

[32] A. Iwase and T. Iwata. Effect of electronic excitation on radiation damage in FCC metals. *Nuclear Instruments and Methods B*, 90:322–329, 1994. 13, 47

[33] A. Dunlop, D. Leseur, P. Legrand, and H. Dammak. Effects Induced by High Electronic Excitations in Pure Metals: A Detailed Study in Iron. *Nuclear Instruments and Methods B*, 90:330–338, 1994. 13

[34] A. Dunlop, D. Leseur, and J. Dural. Damage Production in Iron During High-Energy Ion Iraddiation: Experimental and Theoretical Determinations. *Nuclear Instruments and Methods in Physics Research B*, 42:182–192, 1989. 13

[35] K. Dettmann and G. Leibfried and K. Schroder. *Physica Status Solidi*, 22:423, 1967. 13

[36] A. Dunlop, D. Leseur, G. Jaskierowicz, and J. Schilknecht. Influence of Very High Electronic Energy Losses on Defect Configurations in Self-ion Irradiated Fe. *Nuclear Instruments and Methods B*, 36:412–419, 1989. 14, 47

[37] A.E. Stuchbery and E. Bezakova. Thermal-Spike Lifetime from Picosecond-Duration Pre-equilibrium Effects in Hyperfine Magnetic Fields Following Ion Implantation. *Physical Review Letters*, 82:3637–3640, 1999. 14

[38] N. Itoh and A.M. Stoneham. *Materials Modification by Electronic Excitation*. Cambridge University Press, 2001. 14

[39] M.T. Robinson and O.S. Oen. Computer Studies of the Slowing Down of Energetic Atoms in Crystals. *Physical Review*, 132:2385–2398, 1963. 15

[40] N. Bohr. Velocity-Range Relations for Fission Fragments. *Physical Review*, 40:270–275, 1940. 15, 26

[41] M.T. Robinson and I.M. Torrens. Computer Simulation of Atomic-Displacement Cascades in Solids in the Binary Collision Approximation. *Physical Review B*, 9:5008–5024, 1974. 16

[42] M. Caro, A. Ardelea, and A. Caro. Thermal Behaviour of Radiation Damage Cascades via the Binary Collision Approximation: Comparison with Molecular Dynamcis Results. *Journal of Materials Research*, 5:2652–2657, 1990. 16, 47

[43] M. Jakas and D. Harrison. Influence of Electronic Energy Losses on Atom Ejection Processes. *Physical Review B*, 30:3573–3574, 1984. 16, 47

[44] M. Jakas and D. Harrison. Dependence of Atom Ejection on Electronic Energy Loss. *Physical Review B*, 32:2752–2760, 1985. 16, 95

[45] J. Lindhard and M. Scharff. Energy Dissipation by Ions in the keV Region. *Physical Review*, 124:128–130, 1961. 16, 27, 95

[46] J. Lindhard and V. Nielsen and M. Scharff and P.V. Thomsen. Integral Equations Covering Radiation Effects (Notes on Atomic Collisions III). *Kgl. Danske Videnskab., Selskab. Mat Fys. Medd*, 33:1–42, 1963. 16, 28

[47] J. Lindhard and M. Scharff and H.E. Schioett. Range Concepts and Heavy Ion Ranges (Notes on Atomic Collisions II). *Kgl. Danske Videnskab., Selskab. Mat Fys. Medd*, pages 1–42, 1963. 16, 28

[48] A.S. Nowick. The Golden Age of Crystal Defects. *Annual Review of Material Science*, 26:1–19, 1996. 17

[49] B.J. Alder and T.E. Wainwright. Studies in Molecular Dynamics. I. General Method. *Journal of Chemical Physics*, 31:459–466, 1959. 17

[50] J.B. Gibson, A.N. Goland, M. Milgram, and G.H. Vineyard. Dynamics of Radiation Damage. *Physical Review*, 120:1229–1253, 1960. 17, 18, 19

[51] L. Malerba. Molecular Dynamics Simulation of Displacement Cascades in alpha-Fe: A Critical Review. *Joural of Nuclear Materials*, 351:26–38, 2006. 17, 47, 72, 73, 76

[52] K. Nordlund. Computational Materials Science of Ion Irradiation. *Nuclear Instruments and Methods B*, 188:41–48, 2002. 17, 73

[53] H. Urbassek. Molecular-Dynamics Simulation of Sputtering. *Nuclear Instruments and Methods B*, 122:427–441, 1997. 17

[54] C. Erginsoy, G.H. Vineyard, and A. Englert. Dynamics of Radiation Damage in a Body Centred Cubic Lattice. *Physical Review*, 133:595–606, 1964. 18

[55] K. Nordlund and R.S. Averback. Point Defect Movement and Annealing in Collision Cascades. *Physical Review B*, 56:2421–2431, 1997. 18

[56] K. Nordlund, M. Ghaly, and R.S. Averback. Mechanisms of Ion Beam Mixing in Metals and Semiconductors. *Journal of Applied Physics*, 83:1238–1246, 1998. 19, 21

[57] K. Nordlund, L. Zhong, and R. Averback. Role of Electron-Phonon Coupling on Collision Cascade Development in Ni, Pd and Pt. *Physical Review B*, 57:965–968, 1998. 19, 95

[58] K. Nordlund, M. Ghaly, R.S. Averback, M. Caturla, T. Diaz de la Rubia, and J. Tarus. Defect Production in Collision Cascades in Elemental Semiconductors and fcc Metals. *Physical Review B*, 57:7556–7570, 1998. 20

[59] K. Nordlund, M. Ghaly, R. Averback, M. Carturla, T. Diaz de la Rubia, and J. Tarus. Defect Production in Collision Cascades in Elemental Semiconductors and FCC Metals. *Physical Review B*, 57:7556, 1998. 20

[60] A. Caro and M. Alurralde and R. Slaiba and M. Caro. Heat and Mass Transport in Nanoscale Phase Transitions Induced by Collision Cascades. *Nuclear Beams and Instruments B*, 251:72–76, 1997. 20

[61] D.J. Bacon, F. Gao, and Yu.N. Osetsky. The Primary Damage State in fcc, bcc and hcp Metals as Seen in Molecular Dynamics Simulations. *Nuclear Instruments and Methods B*, 276:1–12, 2000. 20

[62] K. Nordlund, J. Tarus, J. Keinonen, M. Ghaly, and R.S. Averback. Heat Spike Effects on Ion Beam Mixing. *Nuclear Instruments and Methods B*, 164-165:441–452, 2000. 21

[63] T. Diaz de la Rubia, R.S. Averback, and H. Hsieh. Molecular Dynamics Simulation of Displacement Cascades in Cu and Ni: Thermal Spike Behaviour. *Journal of Material Research*, 4:579–586, 1988. 21

[64] D.J. Bacon, A. F. Calder, and F. Gao. Defect Production due to Displacement Cascades in Metals as Revealed by Computer Simulation. *Nuclear Instruments and Methods B*, 251:1–12, 1997. 22, 47

[65] R.E. Stoller and A.F. Calder. Statistical Analysis of a Library of Molecular Dynamics Cascade Simulations in Iron at 100K. *Nuclear Instruments and Methods B*, 283:746–752, 2000. 22

[66] H.F. Deng and D.J. Bacon. Molecular-Dynamics Study of Displacement Cascades in Cu-Au Solid Solutions. *Physical Review B*, 53:11376, 1996. 22

[67] A.F. Calder and D.J. Bacon. Computer Simulation Study of the Effects of Copper Solutes on Cascade Damage in Fe-Cu Alloys. In *Proceedings of the Symposium on Microstructure Evolution During Irradiation vol. 439*. MRS, 1997. 22

[68] F. Gao and D.J. Bacon and P.E.J. Flewitt and T.A. Lewis. A Molecular Dynamics Study of Temperature Effects on Defect Production by Displacement Cascades in alpha Fe. *Journal of Nuclear Materials*, 249:77, 1997. 22, 61

[69] H. Hsieh and T. Diaz de la Rubia and R.S. Averback and R. Benedek. Effect of Temperature on the Dynamics of Energetic Displacement Cascades: A Molecular Dynamics Study. *Physical Review B*, 40:9986, 1989. 22

[70] R.E. Stoller, J.A. Nichols S.J. Zinkle, and W.R Corwin. Workshop on Advanced Computational Materials Science: Application to Fusion and Generation IV Fission Reactors. *Oak Ridge National Laboratory Report*, 2004. 22, 47, 73, 75

[71] K. Nordlund and S.L. Dudarev. Interatomic Potentials for Simulating Radiation Damage Effects in Metals. 50:8016–8019, 1994. 22

[72] A.M. Stoneham. Energy Transfer Between Electrons and Ions in Collision Cascades in Solids. *Nuclear Instruments and Methods in Physics Research*, 48:389–398, 1990. 23

[73] F. Seitz, J.S. Koehler, and D. Turnbull. *Solid State Physics Volume 2*. Academic Press, 1956. 23

[74] M.I. Kaganov, I.M. Lifshitz, and L.V. Tanatarov. Relaxation Between Electrons and Crystalline Lattices. *Soviet Physics - JETP*, 4:173, 1957. 23, 44

[75] D.Duffy. Relaxation Timescales For Electronic Excitations In Metals. *UKAEA Report*, 6, 2005. 23

[76] M. Beuve, N. Stolterfoht, M. Toulemonde, C. Trautmann, and H. M. Urbassek. Influence of the Spatial and Temporal Structure of the Deposited-Energy Distribution in Swift Ion Induced Sputtering. *Physical Review B*, 68:125423, 2003. 24

[77] D.J. Bacon and Yu.N. Osetsky. Modelling Atomic Scale Radiation Damage Processes and Effects in Metals. *International Materials Reviews*, 47:233–241, 2002. 24

[78] Chu-Chun. Fu and J. Dalla Torre and F. Willaime and J.-L. Bocquet and A. Barbu. Multiscale Modelling of Defect Kinetics in Irradiated Iron. *Nature Materials*, 4:68–74, 2004. 24

[79] D.R. Mason, J. le Page, C.P. Race, W.M.C. Foulkes, M.W. Finnis, and A.P. Sutton. Electronic Damping of Atomic Dynamics in Irradiation Damage of Metals. *Journal of Physics: Condensed Matter*, 19:436209, 2007. 24, 30

[80] A.P. Horsfield, D.R. Bowler, H. Ness, C.G. Sanchez, T.N. Todorov, and A.J. Fisher. The Transfer of Energy Between Electrons and Ions in Solids. *Reports in Progress in Physics*, 69:1195–1234, 2006. 24

[81] Yu.N. Osetsky, D.J. Bacon, and B.N. Singh. Statistical Analysis of Cluster Production Efficiency in MD Simulations of Cascades in Copper. *Nuclear Instruments and Methods B*, 307-311:866–870, 2002. 24

[82] B.D. Wirth, M.J. Caturla, T. Diaz de la Rubia, T. Khraishi, and H. Zbib. Mechanical Property Degredation in Irradiated Materials: A Multiscale Modelling Approach. *Nuclear Instruments and Methods B*, 180:23–31, 2001. 24, 25

[83] H.L. Heinisch and B.N. Singh. Stochastic Annealing Simulation of Differential Defect Production in High Energy Cascades. *Nuclear Instruments and Methods B*, 232:206–213, 1996. 24

[84] B. N. Singh, S.I. Golubov, H. Trinkaus, A. Serra, Yu. N. Osetsky, and A.V. Barashev. Aspects of Microstructure Evolution Under Cascade Damage Conditions. *Nuclear Instruments and Methods B*, 251:107–122, 1997. 24

[85] N.M. Ghoniem, D. Walgraef, and S.J. Zinkle. Theory and Experiment of Nanostructure Self Organization in Irradiated Materials. *Journal of computer-aided materials design*, 8:1–38, 2002. 24

[86] M.J. Caturla, N. Soneda, E. Alonso, B.D. Wirth, T. Diaz de la Rubia, and J.M. Perlado. Comparative Study of Radiation Damage Accumulation in Cu and Fe. *Nuclear Instruments and Methods B*, 276:13–21, 2000. 24

[87] T.S. Hudson, S.L. Dudarev, M.J. Caturla, and A.P. Sutton. Effect of Elastic Interactions on Post-Cascade Radiation Damage Evolution in Kinetic Monte-Carlo Simulations. *Philosophical Magazine*, 85:661–675, 2005. 24

[88] N. Soneda and T. Diaz de la Rubia. Migration Kinetics of the Self-Interstitial Atom and its CLusters in bcc Fe. *Philosophical Magazine A*, 81:331, 2001. 24, 25

[89] Z. Wang, Y. Jin, M. Hou, and G. Jin. Modeling of Damage Creation in Metallic Matierals Under Swift Heavy Ion Irradiations. *Nuclear Instruments and Methods in Physics Research B*, 169:98–105, 2000. 24

[90] C.S. Becquart, C. Domain, and A. Legrisand J.C. Van Duysen. Influence of the Interatomic Potentials on Molecular Dynamics Simulations of Displacement Cascades. *Joural of Nuclear Materials*, 280:73–85, 2000. 25, 73, 151

[91] E. Fermi and E. Teller. The Capture of Negative Mesotrons in Matter. *Physical Review*, 72:399, 1947. 27

[92] O.B. Firsov. A Qualitative Interpretation of the Mean Electron Excitation Energy in Atomic Collisions. *Soviet Physics JETP*, 36:1076, 1959. 27

[93] M. Kleman Eds. R. Balian and J-P. Poirier. *Physics of Defects*. North-Holland Publishing Company, 1981. 28

[94] Eds. R.A. Johnson and A.N. Orlov. *Physics of Radiation Effects in Crystals*. North Holland Publishing Company, London, 1986. 28

[95] I. Koponen. Energy Transfer Between Electrons and Ions in Dense Displacement Cascades. *Physical Review B*, 47:14011–14019, 1993. 28

[96] I. Koponen. Thermalisation of an Electron-Phonon System in a Non-Equilibrium State Characterised by a Fractal Distribution of Phonon Excitations. *Physical Review E*, 55:7759–7762, 1997. 29

[97] P.B Allen. Theory of Thermal Relaxation of Electrons in Metals. *Physical Review Letters*, 59:1460–1463, 1987. 29, 44, 92

[98] L. Spitzer Jr. *Physics of Fully Ionised Gases*. Interscience - New York, 1962. 29

[99] L.D. Landau. *Soviet Physics JETP*, 7:203, 1937. 29

[100] G. Tas and H.J. Maris. Electron Diffusion in Metals Studied by Picosecond Ultrasonics. *Physical Review B*, 49:46, 1994. 29, 31

[101] A.E. Volkov and V.A. Borodin. Heating of Metals in Swifty Heavy Ion Tracks by Electron-Ion Energy Exchange. *Nuclear Instruments and Methods in Physics*, 146:137, 1998. 29

[102] M.A. Gilmore and S. Kamal and D.M. Broun and J.S. Dodge. Determination of Electron-Phonon Parameters from Time-Domain Terahertz Spectroscopy. *Applied Physics Letters*, 88:141910, 2006. 30

[103] R.H.M. Groeneveld and R. Sprik and A. Lagendijk. Femtosecond Spectroscopy of Electron-Electron and Electron-Phonon Energy Relaxation in Ag and Au. *Physical Review B*, 51:433, 1995. 30

[104] K. Eidmann, J. Meyer ter Vehn, and T. Schlegel. Hydrodynamic Simulation of Sub-picosecond Laser Interaction with Solid-Density Matter. *Physical Review E*, 62:1202–1211, 2000. 31, 33

[105] J.R. Hook and H.E. Hall. *Solid State Physics (2nd Edition)*. Wiley, 2001. 31, 87

[106] C.P. Flynn and R.S. Averback. Electron-Phonon Interactions In Energetic Displacement Cascades. *Physical Review B*, 38:7118–7120, 1988. 32, 39, 40

[107] G.A. Kobez, I.T. Iakubov, and M.M. Popovich. *Transport and Optical Properties of Non-Ideal Plasma*. Plenum Press, 1995. 32

[108] M. Lampe. Transport Coefficients of Degenerate Plasma. *Physical Review*, 170:306–319, 1968. 32

[109] G.A. Rinker. Thermal Conductivity of a Strongly Coupled Plasma. *Physical Review B*, 31:4220–4229, 1985. 32

[110] G.A. Rinker. Systematic Calculations of Plasma Transport Coefficients for the Periodic Table. *Physical Review A*, 37:1284–1297, 1988. 32

[111] X.Y. Wang, D.M. Riff, Y.S. Lee, and M.C. Downer. Time-resolved Electron-Temperature Measurement in a Highly Excited Gold Target Using fs Thermionic Emission. *Physical Review B*, 50:8016–8019, 1994. 33, 93

[112] A.H. Macdonald. Electron-Phonon Enhancement of Electron-Electron Scattering in Al. *Physical Review Letters*, 44:489–494, 1979. 33

[113] M. Kaveh and N. Wiser. Electron-Electron Scattering in Conducting Metals. *Advances in Physics*, 33:257–372, 1984. 33

[114] N.W. Ashcroft and N.D. Mermin. *Solid State Physics*. Saunders College Publishing, 1976. 33, 93

[115] J.K. Chen, W.P Latham, and J.E. Beraun. The Role of Electron-Phonon Cupling in Ultrafast Laser Heating. *Journal of Laser Applications*, 17:63–68, 2005. 33, 93

[116] A.S. Sandhu, A.K. Dharmadhikari, and G.R. Kumar. Time Resolved Evolution of Structural, Electrical and Thermal Properties of Copper Irradiated by an Intense Ultrashort Laser Pulse. *Applied Physics Letters*, 97:023526, 2004. 33

[117] P. J. Antaki. Importance of Nonequilibrium Thermal Conductivity During Short-Pulse Laser-Induced Desorption From Metals. *International Journal of Heat and Mass Transfer*, 45:4063–4067, 2002. 33

[118] T.Q. Qiu. *Energy Dissipation and Transport During High-Power and Short-Pulse Laser-Metal Interactions*. PhD thesis, University of California, Berkley, 1993. 34

[119] C.J. Powell and A. Jablonski. Evaluation of Electron Inelastic Mean Free Paths for Selected Elements and Compounds. *Surface and Interface Analysis*, 29:108–114, 2000. 34

[120] M.P. Seah and W.A. Dench. Quantitative Electron Spectroscopy of Surfaces: A Standard Database for Electron Inelastic Mean Free Paths in Solids. *Surface ansd Interface Analysis*, 1:2–11, 1979. 34

[121] B. Ziaja, R.A. London, and J. Hajdu. Ionization by Impact Electrons in SOlids: Electron Mean Free Path Fitted Over a Wide Energy Range. *Journal of Applied Physics*, 99:0033514:1–9, 2006. 34

[122] S. I. Abu-Eishah. Correlations for the thermal conductivity of metals as a function of temperature. *International Journal of Thermophysics*, 22:1855–1868, 2001. 34

[123] C. Kittel. *An Introduction To Solid State Physics*. John Wiley and Sons, New York, 2004. 34, 95, 137, 153

[124] D. Nguyen-Manh. Private communication. 35

[125] D. Alfe. Private communication. 35, 37

[126] Z. Lin and L. Zhigilei. Electron-Phonon Coupling and Electron Heat Capacity in Metals at High Temperatures. http://www.faculty.virginia.edu/CompMat/electron-phonon-coupling/. 35, 95, 137

[127] C. R. Phipps, editor. *Thermal Excitation of D Band Electrons in Au: Implications for Laser-Induced Phase Transformations*, volume 6261. SPIE, 2006. 35, 92

[128] Z. Lin and L. V. Zhigilei. Temperature Dependences of the Electron-Phonon Coupling, Electron Heat Capacity and Thermal Conductivity in Ni under Femtosecond Laser Irradiation. *Applied Surface Science*, 253:6295–6300, 2007. 35, 92

[129] A. Caro and M. Victoria. Ion-electron Interaction in Molecular-Dynamics Cascades. *Physical Review Letters*, 40:2287, 1989. 39, 65, 81

[130] M.W. Finnis, P. Agnew, and A.J.E. Foreman. Thermal Excitation of Electrons in Energetic Displacement Cascades. *Physical Review Letters*, 44:567, 1991. 40, 41

[131] V.G. Kapinos and D.J. Bacon. Influence of Ion-Electron Interaction on the Formation Mechanism of Depleted Zones in Displacement Cascades in Metals. *Physical Review B*, 50:194–203, 1994. 40, 104

[132] V.G. Kapinos and D.J. Bacon. Effect of Melting and Electron Phonon Coupling on the Collapse of Depleted Zones in Copper, Nickel and a-Iron. *Physics Review B*, 53:8287, 1996. 41, 104

[133] V.G. Kapinos and D.J. Bacon. Model for Vacancy-Loop Nucleation in Displacement Cascades. *Physical Review B*, 52:4029–4043, 1995. 41

[134] F. Gao, D.J. Bacon, P.E.J. Flewitt, and T.A. Lewis. The Effects of Electron-Phonon Coupling on Defect Production by Displacement Cascades in alpha Iron. *Modelling and Simulation in Material Science Engineering*, 6:543–556, 1998. 41, 92, 104

[135] E. Zhurkin and A. Kolesnikov. Atomic Scale Modelling of Al and Ni (111) Surface Erosion Under Cluster Impact. *Nuclear Instruments and Methods B*, 202:269–277, 2003. 41, 95

[136] M. Spaczer, A. Caro, M. Victoria, and T. Diaz de la Rubia. Computer Simulations of Disordering and Amorphization Kinetics in Intermetallic Compounds. *Nuclear Instruments and Methods in Physics Research B*, 102:81–85, 1995. 41

[137] A. Duvenbeck, F. Sroubek, Z. Sroubek, and A. Wucher. Computer Simulation of Low Energy Electronic Excitations in Atomic Energy Collisions. *Nuclear Instruments and Methods B*, 225:464–477, 2004. 41

[138] E.M. Bringa and R.E. Johnson. Molecular Dynamics Study of Non-Equilibrium Energy Transport From a Cylindrical Spike. *Nuclear Instruments and Methods in Physics Research B*, 143:513–535, 1998. 42

[139] R.L. Fleischer, P.B. Price, R.M. Walker, and E.L. Hubbard. Criterion for Registration in Dielectric Track Detectors. *Physical Review*, 156:353–355, 1967. 42

[140] K. Schwartz and C. Trautmann and R. Neumann. Electronic Excitations and Heavy-Ion Induced Processes in Ionic Crystals. *Nuclear Instruments and Methods in Physics B*, 209:73, 2003. 42

[141] E.M. Bringa and R.E. Johnson. Coulomb Explosion and Thermal Spikes. *Physical Review Letters*, 88:165501–165503, 2002. 42

[142] E.M. Bringa. Molecular Dynamics Simulations of Coulomb Explosion. *Beam Interactions with Materials and Atoms*, 209:1–8, 2003. 43

[143] A.I. Ryazanov, S.A. Pavlov, E.V. Metelkin, and A.V. Zhemerev. Effects of Coulomb Explosion on Track Formation in Metals Irradiated by Heavy Ions. *Electronic Properties of Solids*, 101:139–149, 2005. 43

[144] P.M. Ossi and R. Pastorelli. Structural Changes Induced by Fast Heavy Ion Irradiation of Pure Metals. *Nuclear Instruments and Methods B*, 122:566–570, 1997. 43

[145] D. Alfe S. Khakshouri and D.M. Duffy. Development of an Electron-Temperature Dependent Potential for Molecular Dynamics Simulation of Tungsten Under Electronic Excitation. *Accepted for Publication in Physical Review B*, 0, 2008. 43

[146] Z.G. Wang, C. Dufour, E. Paumier, and M. Toulemonde. The Se Sensitivity of Metals Under Swift-Heavy-Ion Irradiation: A Transient Thermal Process. *Journal of Physics C*, 6:6733–6750, 1994. 44, 92

[147] M. Toulemonde and C. Dufour and E. Paumier. Transient Thermal Process After a High-Energy Heavy-Ion Irradiation of Amorphous Metals and Semiconductors. *Physical review B*, 46:14362, 1992. 44

[148] T.A. Tombrello. Damage in Metals from MeV Heavy Ions. *Nuclear Instruments and Methods in Physics Research B*, 95:501–504, 1994. 45

[149] D. von der Linde, K. Sokolowski-Tinten, and J. Bialkowski. Laser-Solid Interactions in the Femtosecond Time Regime. *Applied Surface Science*, 109-110:1–10, 1997. 45

[150] H.O. Jeschke and M.E. Garcia and K.H. Bennemann. Microscopic Analysis of the Laser-Induced Femtosecond Graphitization of Diamond. *Physical Review B*, 60:3701–3704, 1999. 45

[151] L. Jiang and H. Tsai. Improved Two-Temperature Model and It's Application in Ultrashort Laser Heating of Metal Films. *Journal of Heat Transfer*, 127:1167–1173, 2005. 46

[152] Y. Yamashita, T. Yokomine, S. Ebara, and A. Shimizu. Heat Transport Analysis for Femtosecond Laser Ablation with Molecular Dynamics-Two Temperature Method. *International Journbal of Thermophysics*, 27:627–646, 2006. 46

[153] S.S Wellershoff, J. Hohfeld, J. Gudde, and E. Matthias. The Role of Electron-Phonon Coupling in Femtosecond Laser Damage of Metals. *Applied Physics A*, 69:99–107, 1999. 46

[154] J.K. Chen and J.E. Beraun and C.L. Tham. Comparion of One-Dimensional and Two-Dimensional Axisymmetric Approaches to the Thermomechanical Response Caused by Ultrashort laser Heating. *Journal of Optics A: Pure and Applied Optics*, 4:650–661, 2002. 46

[155] R.S. Averback and M. Ghaly. Fundamental Aspects of Defect Production in Solids. *Nuclear Instruments and Methods B*, 128:1–11, 1997. 47

[156] G.D. Smith. *Numerical Solution of Partial Differential Equations: Finite DIfference Methods*. Clarendon Press, 1985. 52

[157] R. Car and M. Parinello. Unified Approach for Molecular Dynamics and Density Functional Theory. *Physical Review Letters*, 55:2471–2474, 1985. 53

[158] N. Metropolis, A.W. Rosenbluth, M.N. Rosenbluth, and A.H. Teller. Equation of State Calculations by Fast Computing Machines. *Journal of Chemical Physics*, 6:1087–1093, 1953. 53

[159] D.R. Bowler, R. Choudhury, M.J. Gillan, and T. Miyazaki. Recent Progress with Large-Scale ab initio Calculations: the CONQUEST Code. *Physica Status Solidi B*, 243:989–100, 2006. 53

[160] K. Henriksson. Molecular Dynamics Simulation of Ion and Cluster Bombardment of Metal Surfaces-Craters and Sputtered Clusters. Master's thesis, University of Helsinki, 2001. 53

[161] K.Nordlund. Molecular Dynamics Simulation of Ion Ranges in the 1-100 keV Energy Range. *Nuclear Instruments and Methods B*, 3:448–456, 1994. 53

[162] M.P. Allen and D.J. Tildesley. *Computer Simulation of Liquids*. Oxford Science Publications, 1989. 54, 65, 67

[163] B. Cowan. *Topics in Statistical Mechanics*. Imperial College Press, 2005. 54

[164] R.E. Stoller and S.G. Guiriec. Secondary Factors Influencing Cascade Damage Formation. *Journal of Nuclear Materials*, 329-333:1238–1242, 2004. 55

[165] W. H. Press, S. A. Teukolsky, W. T. Veterling, and B. P. Flannery. *Numerical Recipes in C*. Cambridge University Press, 1992. 56

[166] D. C. Rapaport. *The Art of Molecular Dynamics Simulations*. Cambridge University Press, 1995. 56

[167] D. Frenkel and B. Smit. *Understanding Molecular Simulation*. Elsevier, 2002. 56, 57, 62

[168] S.K. Gray, D.W. Nold, and B.G. Sumpter. Symplectic Integrators for Large Scale Molecular Dynamics Simulations: A Comparison of Several Explicit Methods. *Journal of Chemical Physics*, 101:4062–4072, 1994. 57

[169] L. Verlet. Computer Experiments on Classical Fluids. 1. Thermodynamical Properties of Lennard-Jones Molecules. *Physical Review Letters*, 159:98–103, 1967. 57

[170] L. Verlet. Computer Experiments on Classical Fluids. 2. Equilibrium Correlation Functions. *Physical Review Letters*, 165:201–215, 1967. 57

[171] R.W. Hockney. Potential Calculation and Applications. *Methods of Computational Physics*, 9:136–211, 1970. 58

[172] W.C. Swope, H.C. Andersen, P.H. Berens, and K.R. Wilson. A Computer Simulation Method for the Calculation of Equilibrium Constants for the Formation of Physical Clusters of Molecules: Application to Small Water Clusters. *Journal of Chemical Physics*, 76:637–649, 1981. 58

[173] J. R. Beeler Jr. *Radiation Effects, Computer Experiments*. North Holland, 1983. 59

[174] W. Hoover. Non-equilibrium Molecular Dynamics. *Annual Reviews in Physical Chemistry*, 34:103–127, 1983. 60

[175] L.V. Woodcock. Isothermal Molecular Dynamics Calculations for Liquid Salts. *Chemical Physics Letters*, 10:257–267, 1971. 61

[176] W.G. Hoover, A.J.C. Ladd, and B. Moran. High Strain Rate Plastic Flow Studies via Non-Equilibrium Molecular Dynamics. *Physical Review Letters*, 48:1818–1820, 1982. 61

[177] A.J.C. Ladd and W.G. Hoover. Plastic Flow in Close-packed Crystals via Non-equilibrium Molecular Dynamics. *Physical Review B*, 28:1756–1762, 1983. 61

[178] D. J. Evans. Computer 'experiment' for non-linear thermodynamics of Couette flow. *Journal of Chemical Physics*, 78:3297–3301, 1983. 61

[179] S. Nose. A Molecular Dynamics method for Simulations in the Cannonical Ensemble. *Molecular Physics*, 52:255–268, 1983. 61

[180] W.G. Hoover. Cannonical Dynamics: Equilibrium Phase Space Distributions. *Physical Review A*, 31:1695–1698, 1985. 61

[181] H.J.C. Berendsen, J.P.M. Postma, W.F. van Gunsteren, A. DiNola, and J.R. Haak. Molecular Dynamics with Coupling to an External Bath. *Journal of Chemical Physics*, 81:3684–3690, 1984. 61

[182] I.T Todorov and W. Smith and K. Tracjhenko and M.T. Dove. DLPOLY 3: New Dimensions in Molecular Dynamics Simulations via Massive Parallelism. *Journal of Materials Chemistry*, page 51793, 06. 61, 97

[183] S. Pronnecke, A. Caro, M. Victoria, T. Diaz de la Rubia, and M.W. Guinan. The effect of electronic energy loss on the dynamics of thermal spikes in Cu. *Journal of Materials Research*, 6:483–491, 1991. 61, 104

[184] N. Metropolis and S. Ulam. The Monte Carlo Method. *Journal of the American Statistical Association*, 44:335–341, 1949. 63

[185] P. Langevin. On the Theory of Brownian Motion. *C.R. Acad. Sci (Paris)*, 146:530–533, 1908. 63

[186] H. Mori. Transport, Collective Motion and Brownian Motion. *Progress of Theoretical Physics*, 33:423–455, 1964. 63

[187] H. Mori. A Continued-Fraction Representation of the Time-Correlation Function. *Progress of Theoretical Physics*, 34:399–416, 1965. 63

[188] R. Zwanzig. Memory Effects in Irreversible Thermodynamics. *Physical Review*, 124:983–992, 1961. 63

[189] H.C. Andersen. Molecular Dynamics Simulations at COnstant Pressure and/or Temperature. *Journal of CHemical Physics*, 72:2384–2393, 1979. 64

[190] Don S. Lemons. *An Introduction To Stochastic Processes In Physics*. John Hopkins University Press, 2002. 65

[191] F. Mandl. *Statistical Physics*. John Wiley and Sons, 1994. 65

[192] H. Rafii-Tabar. Modelling The Nano Scale Phenomena In Condensed Matter Physics Via Computer-Based Numerical Simulations. *Physics Reports*, 325:239–310, 2000. 67

[193] F. Ercolessi, M. Parinello, and E. Tosatti. Simulation of Gold in the Glue Model. *Philosophical Magazine A*, 58:213–226, 1988. 68

[194] F. Cleri and V. Rosato. Tight Binding Potentials for Transition Metals and Alloys. *Physical Review B*, 48:22–32, 1993. 68

[195] M. Finnis. *Interatomic Forces in Condensed Matter*. Oxford University Press, 2004. 69

[196] M.W. Finnis and J.E. Sinclair. A Simple Empirical N-Body Potential for Transition Metals. *Philosophical Magazine A*, 50:45–55, 1984. 69, 70, 73

[197] A.P. Sutton and J. Chen. Long Range Finnis-Sinclair Potentials. *Philosophical Magazine Letters*, 61:139–146, 1989. 69, 71

[198] M.S. Daw and M.L. Baskes. Semiempirical, Quantum Mechanical Calculation of Hydrogen Embrittlement in Metals. *Physical Review Letters*, 50:1285–1288, 1983. 69

[199] M.S. Daw and M.L. Baskes. Emdedded-atom Method: Derivation and Application to Impurities, Surfaces and Other Defects in Metals. *Physical Review B*, 29:6443–6453, 1984. 69

[200] M.J. Stott and E. Zaremba. Quasi-atoms: An approach to Atoms in Nonuniform Electronic Systems. *Physical Review B*, 22:1264–1583, 1980. 69

[201] J.K. Norskov and N.D. Lang. Effective-medium Theory of Chemical Binding: Application to Chemisorption. *Physical Review B*, 21:2131–2137, 1980. 69

[202] J.K. Norskov. Covalent Effects in the Effective-medium Theory of Chemical Binding: Hydrogen Heats of Solution in the 3d Metals. *Physical Review B*, 26:2875–2885, 1982. 69

[203] R.A. Johnson. Analytical Nearest-neighbour Model for FCC Metals. *Physical Review B*, 37:3924–3931, 1988. 69

[204] Y. Mishin and D. Farkas and M.J. Mehl and D.A. Papaconstantpoulos. Interatomic Potentials for Monatomic Metals from Experimental Data and ab-initio Calculation. *Physical Review B*, 59:3393, 1999. 70

[205] F. Cyrot-Lackman. On the Calculation of Surface Tension in Transition Metals. *Surface Science*, 15:535–548, 1968. 70

[206] Kaye and Laby Natoinal Physical Laboratory. http://www.kayelaby.npl.co.uk/. Online database. 71, 94, 153

[207] J.F. Ziegler, J.P. Biersack, and U. Littmark. *The Stopping and Range of Ions in Matter*. Pergamon, 1985. 72

[208] U. Littmark and J.F. Ziegler. Ranges of Energetic Ions in Matter. *Physical Review A*, 23:64–72, 1981. 72

[209] W. Eckstein, S. Hackel, D. Heinemann, and B. Fricke. Influence of the Interaction Potential on Simulated Sputtering and Reflection Data. *Atoms, Molecules and Clusters*, 24:171–176, 1992. 72

[210] C. Bjorkas and K. Nordlund. Comparative Study of Cascade Damage in Fe Simulated with Recent Potentials. *Nuclear Instruments and Methods B*, 259:853–860, 2007. 73

[211] K. Nordlund, N. Runeberg, and D. Sundholm. Repulsive Interatomic Potentials Calculated Using Hartree-Fock and density-Functional Theory Methods. *Nuclear Instruments and Methods B*, 132:45–54, 1997. 73

[212] R.J. Harrison and S.P. Chen A.F. Voter. *Atomistic Simulation of Materials-Beyond Pair Potentials*. Plenum, 1989. 73

[213] J.C. Turbatte. Master's thesis, Marne la Vallee, 1995. 73

[214] M.I. Haftel, T.D. Andreadis, J.V. Lill, and J.M. Heridon. Surface Relaxation of alpha Iron and the embedded atom method. *Physical Review B*, 42:11540–11552, 1990. 73

[215] R. Vascon. *Doctoral Thesis*. PhD thesis, Universite Paris, 1997. 73

[216] G. Simonelli, R. Pasionat, and E.J. Savino. Lattice Trapping Effects in Fe Using a Potential Based on Experimental Data and Ab-Initio Calculations. *Materials Research Society Symposium Proceedings*, 291:567, 1993. 73

[217] J.M. Raulot. Masters thesis. Master's thesis, University de Marne la Vallee, 1998. 73

[218] A.F. Calder and D.J. Bacon. A Molecular Dynamics Study of Displacement Cascades in alpha Iron. *Journal of Nuclear Materials*, 207:25–45, 1993. 73

[219] J. Wallenius, P. Olsson, C. Lagerstedt, N. Sandberg, R. Chakarova, and V. Pontikis. Modelling of Chromium Precipitation in Fe-Cr Alloys. *Physical Review B*, 69:094103, 2004. 74

[220] L. Malerba, D. Terentyev, P. Olsson, R. Chakarova, and J. Wallenius. Molecular Dynamcis Simulation of Displacement Cascades in Fe-Cr Alloys. *Journal of Nuclear Materials*, 329. 74

[221] J. Wallenius, I.A. Abrikosov, R. Chakarova, C. Lagerstedt, L. Malerba, P. Olsson, V. Pontikis, N. Sandberg, and D. Terentyev. Development of An EAM Potential for Simulation of Radiation Damage in Fe-Cr Alloys. *Journal of Nuclear Materials*, 329. 74

[222] P.M. Derlet, D. Nguyen-Manh, and S.L. Dudarev. Multiscale Modeling of Crowdion and Vacancy Defects in Body-Centered-Cubic Transition Metals. *Physical Review B*, 76:054107, 2007. 74, 133, 153

[223] S.L. Dudarev and P.M. Derlet. A 'Magnetic' Interatomic Potential for Molecular Dynamics Simulations. *Journal of Physics C*, 17:7097–7118, 2005. 75, 76, 97, 117

[224] A. Dunlop, P. Legrand, D. Leseur, N. Lorenzelli, J. Morillo, A.Barbu, and S. Bouffard. Phonon Soft Modes and Damage Production by High Electronic Energy Excitations in Pure Metals. *Europhysics Letters*, 15:765–770, 1994. 78

[225] D.M. Duffy and A.M. Rutherford. Including the Effects of Electronic Stopping and Electron-Ion Interactions in Radiation Damage Simulations. *Journal of Physics C*, 19, 2006. 79

[226] R.C. Weast (Ed.). *Handbook of Chemistry and Physics: A Ready Reference Book of Chemical and Physical Data*. Chemical Rubber Company, 1971. 87, 93

[227] P.H.T. Philipsen and E.J. Baerends. Cohesive Energy of 3d Transition Metals: Density Functional Theory Atomic and Bulk Calculations. *Physical Review B*, 54:5326–5333, 1996. 87

[228] G. Chen. Ballistic-Diffusive Heat-Conduction Equations. *Physical Review Letters*, 86:2297, 2001. 90

[229] S.S Wellershoff, J. Gudde, J. Hohfeld, J.G. Muller, and E. Matthias. The Role of Electron-Phonon Coupling in Femtosecond Laser Damage of Metals. In *Proceedings of International Society of Optical Engineering*. SPIE, 1998. 92

[230] J.G. Fujimoto and J.M. Liu and E.P. Ippen and N. Bloembergen. Femtosecond Laser Interaction with Metallic Tungsten and Nonequilibrium Electron and Lattice Temperatures. *Physical Review Letters*, 53:1837, 1984. 92

[231] A.M. Rutherford and D.M. Duffy. The Effect of Electron-Ion Interactions on Radiation Damage Simulations. *Journal of Physics C*, 19, 2007. 98

[232] D.M. Duffy, S. Khakshouri, and A.M. Rutherford. Electronic Effects in Radiation Damage Simulations. *Submitted to Nuclear Instruments and Methods B*, 2008. 98

[233] D.J. Bacon, A.F. Calder, F. Gao, V.G. Kapinos, and S.J. Wooding. Computer Simulation of Defect Production by Displacement Cascades in Metals. *Nuclear Instruments and Methods B*, 102:37–46, 1995. 112, 113

[234] D.M. Duffy, N. Itoh, A.M. Rutherford, and A.M. Stoneham. Making Tracks in Metals. *Journal of Physics C*, 20, 2008. 119

[235] A. Dunlop and D. Leseur. Damage Creation via Electronic Excitations in Metallic Targets Part 1: Experimental Results. *Radiation Effects and Defects in Solids*, 126:123–128, 1993. 122

[236] C. Dufour and A. Audouard and F. Beuneu and J. Dural and J.P. Girard and A. Hairie and M. Levalois and E. Paumier and M. Toulemonde. A High-Resistivity Phase Induced by Swift Heavy-Ion Irradiation of Bi: A Probe for Thermal Spike Damage? *Journal of Physics C*, 5:4573, 1993. 122